

ABSTRACT

Title of Dissertation: OPTIMIZATION OF PLASMA ASSISTED MOLECULAR BEAM EPITAXY GROWN $\text{Nb}_x\text{Ti}_{1-x}\text{N}$ FOR EPITAXIAL JOSEPHSON JUNCTIONS

Austin Michael Thomas, Doctor of Philosophy,
2023

Dissertation directed by: Dr. Christopher Richardson, Department of
Materials Science and Engineering

This thesis is an investigation into the growth and characterization of NbN_x and TiN transition metal nitrides, along with the alloy $\text{Nb}_x\text{Ti}_{1-x}\text{N}$. These materials are commonly used in many applications ranging from superconducting quantum computing, superconducting conventional computing, high kinetic inductance devices such as single photon detectors, and hard coatings for industrial applications. This thesis will begin with an overview of superconducting quantum computing and superconducting materials, then review the fabrication of Josephson junctions and highlight the need for material improvement. The goal of this work is to grow a superconducting nitride material which can be engineered to lattice match with AlN , the barrier layer in a hypothetical all-nitride, epitaxially grown superconducting quantum computing structure. The alloy $\text{Nb}_x\text{Ti}_{1-x}\text{N}$ is chosen as the superconducting alloy of choice due to the range of lattice constants available, the high critical temperature of these nitrides, and the high quality of material able to be grown using PAMBE. The first aim of this thesis studies the

binary transition metal nitrides NbN_x and TiN to generate endpoints for various properties of the alloy $\text{Nb}_x\text{Ti}_{1-x}\text{N}$. This thesis is one of the first investigations of multi-phase growth of $\epsilon\text{-NbN}$ and $\gamma\text{-Nb}_4\text{N}_3$, and demonstrates control over the phase, crystal orientation, superconducting properties, and surface morphology by changing PAMBE growth parameters. The second aim of this thesis demonstrates the growth of $\text{Nb}_x\text{Ti}_{1-x}\text{N}$ and is the first investigation of tunable material properties for this alloy by adjusting the composition. The last aim of this work is the development of a novel annealing scheme used to prepare $\text{Nb}_x\text{Ti}_{1-x}\text{N}$ thin films for Josephson junction integration. The novel annealing scheme ensures excellent surface roughness of $\text{Nb}_x\text{Ti}_{1-x}\text{N}$ thin films, increases the superconducting critical temperature of this alloy from approximately 14 K to 16.8 K, and improves the crystal quality by way of nitrogen incorporation and improvement of the crystal quality. The results from this work will be crucial in developing $\text{Nb}_x\text{Ti}_{1-x}\text{N} / \text{AlN} / \text{Nb}_x\text{Ti}_{1-x}\text{N}$ Josephson junctions with smooth, uniform interfaces and low-loss, defect free nitride materials. Additionally, this thesis represents an investigation into the relationship between phases of NbN_x and TiN , the role of nitrogen incorporation caused by in-situ annealing, and a useful record of control over this material using PAMBE growth conditions and alloy composition.

OPTIMIZATION OF PLASMA ASSISTED MOLECULAR BEAM EPITAXY
GROWN $\text{Nb}_x\text{Ti}_{1-x}\text{N}$ FOR EPITAXIAL JOSEPHSON JUNCTIONS

by

Austin Michael Thomas

Dissertation submitted to the Faculty of the Graduate School of the
University of Maryland, College Park, in partial fulfillment
of the requirements for the degree of
Doctor of Philosophy
2023

Advisory Committee:

Professor Ichiro Takeuchi, Chair

Dr. Christopher Richardson

Professor Lourdes Salamanca-Riba

Professor Ray Phaneuf

Professor Johnpierre Paglione, Dean's Representative

© Copyright by
Austin Michael Thomas
2023

Acknowledgements

I would like to express my deepest gratitude to Dr. Christopher Richardson for the excellent mentorship and support I received through my graduate studies. Without his advice on matters academic, professional, and personal, I would not be where I am today. This thesis would not be possible without my defense committee, as well as the Department of Materials Science and Engineering and the Department of Physics at the University of Maryland. Additionally, the resources and support from the Laboratory for Physical Sciences were invaluable in conducting the research in this thesis, as well as providing a wonderful working environment.

I am also grateful to many UMD cohort members and LPS coworkers for providing endless moral support, research assistance, and camaraderie. In particular, the Richardson group members were instrumental in my familiarization with the world of quantum information science and MBE growth. I'd also like to thank Dr. Haozhi Wang for his instruction on RF simulations using Ansys, as well as Dr. Hussein Hijazi and the Rutgers University Department of Physics and Astronomy for their RBS measurements, commentary, and analysis.

Finally, I am thankful for the support of both my parents and my sister, who believed in me through this entire process. Their encouragement was exactly what I needed to reach the end of this journey. I am especially grateful for the love and support from my partner, Chris, without which this thesis would have been impossible.

Table of Contents

| | |
|---|-----|
| Acknowledgements..... | ii |
| Table of Contents..... | iii |
| List of Figures..... | vi |
| Chapter 1: Introduction and Background..... | 1 |
| 1.1 Superconducting Quantum Computing and Josephson Junctions | 1 |
| 1.2 Superconducting Material and Device Theory | 4 |
| 1.2.1 Superconductivity Theory..... | 4 |
| 1.2.2 Cooper Pair Tunneling..... | 11 |
| 1.3 Superconducting Circuit Applications..... | 18 |
| 1.3.1 Superconducting Conventional Circuits | 18 |
| 1.3.2 Superconducting Quantum Interference Devices | 19 |
| 1.3.3 Superconducting Quantum Circuits..... | 20 |
| 1.4 Josephson Junction Fabrication | 22 |
| 1.4.1 Double Evaporation Fabrication | 22 |
| 1.4.2 Tri-Layer Designs | 25 |
| 1.4.3 Epitaxial Josephson Junctions..... | 26 |
| 1.5 Superconducting Circuit Materials | 30 |
| 1.5.1 Substrate Selection..... | 30 |
| 1.5.2 Superconducting Materials | 31 |
| 1.5.3 Barrier Materials | 33 |
| 1.5.4 Superconducting Nitrides..... | 33 |
| 1.5.5 Wide-Bandgap Nitrides | 37 |
| 1.6 Content Overview | 38 |
| Chapter 2: Methods..... | 40 |
| 2.1 MBE Growth..... | 40 |
| 2.1.1 UHV, Mean Free Path, and Purity..... | 40 |
| 2.1.2 Sapphire Substrates for Nitride Growth..... | 45 |
| 2.1.3 Growth and Annealing Process for NbTiN Thin Films | 46 |
| 2.1.4 Plasma Cells..... | 48 |
| 2.1.5 Effusion Sources | 49 |
| 2.1.6 Electron Beam Evaporation Sources | 51 |
| 2.2 Growth Mechanics | 53 |
| 2.3 X-Ray Characterization | 55 |
| 2.3.1 Symmetrical X-Ray Diffraction..... | 55 |
| 2.3.2 Reciprocal Space Mapping | 57 |
| 2.3.3 Pole Figures | 60 |
| 2.3.4 X-ray Reflectivity | 61 |
| 2.4 Atomic Force Microscopy | 63 |
| 2.5 Scanning Electron Microscopy | 65 |
| 2.5.1 Imaging | 65 |
| 2.5.2 Energy Dispersive Spectroscopy | 67 |
| 2.6 Rutherford Backscattering Spectroscopy..... | 68 |
| 2.7 Cryogenic Characterization | 71 |

| | | |
|---|---|-----|
| 2.7.1 | Adiabatic Demagnetization Refrigerator | 71 |
| 2.7.2 | Resonator Measurement and Fabrication..... | 75 |
| 2.7.3 | Experimental Kinetic Inductance Measurement..... | 79 |
| 2.7.4 | Calculation of Resonator Center Frequency | 81 |
| 2.7.5 | Resonator Simulation of Center Frequency | 82 |
| 2.7.6 | Direct Current IV Measurements..... | 86 |
| Chapter 3: Binary Transition Metal Nitrides | | 88 |
| 3.1 | Titanium Nitride..... | 88 |
| 3.1.1 | Growth Details | 88 |
| 3.1.2 | TiN Structural Properties | 92 |
| 3.1.3 | Superconducting Properties | 99 |
| 3.2 | Impact of Annealing Titanium Nitride | 104 |
| 3.2.1 | Topographical Changes | 104 |
| 3.2.2 | Structural Changes | 106 |
| 3.2.3 | Superconducting Properties | 110 |
| 3.3 | Niobium Nitride..... | 111 |
| 3.3.1 | Growth Process | 111 |
| 3.3.2 | Phase Identification..... | 115 |
| 3.3.3 | Surface Topography..... | 121 |
| 3.3.4 | Superconducting Properties | 124 |
| 3.4 | Impact of Annealing Niobium Nitride..... | 130 |
| 3.4.1 | Topographical Changes | 130 |
| 3.4.2 | Structural Changes | 131 |
| 3.4.3 | Impact on Superconductivity | 132 |
| 3.5 | Summary | 132 |
| Chapter 4: NbTiN Alloy Development..... | | 135 |
| 4.1 | $(\text{Nb}_x\text{Ti}_{1-x})_{1-y}\text{N}_y$ Alloy Growth | 135 |
| 4.2 | Structural Analysis..... | 138 |
| 4.2.1 | X-Ray Analysis..... | 138 |
| 4.2.2 | Surface Morphology | 142 |
| 4.2.3 | Transition Metal Compositional Analysis | 144 |
| 4.3 | Superconducting Critical Temperature | 148 |
| 4.4 | Resonator Analysis | 150 |
| 4.5 | Summary | 156 |
| Chapter 5: Annealed NbTiN..... | | 159 |
| 5.4 | Impact on $\text{Nb}_x\text{Ti}_{1-x}\text{N}$ Alloys..... | 159 |
| 5.4.1 | Effect of Anneal Temperature Variation | 164 |
| 5.4.2 | Effect of Anneal Time | 172 |
| 5.4.3 | SIMNRA RBS Simulations | 178 |
| 5.5 | Anneal Effects at Depth..... | 181 |
| 5.6 | Summary | 182 |
| Chapter 6: Discussion and Future Work..... | | 185 |
| 6.1 | Binary TiN and NbN_x | 185 |
| 6.2 | NbTiN Alloys..... | 187 |
| 6.3 | Annealed NbTiN..... | 190 |
| 6.4 | Future Work | 194 |

| | |
|-------------------------------|-----|
| Conferences and Posters | 198 |
| Works in Progress | 198 |
| Bibliography | 199 |

List of Figures

| | |
|---|----|
| Figure 1: Computation time compared for conventional and quantum computing. Reproduced from reference 7..... | 2 |
| Figure 2: Two level system example. Higher energy states E_n may exist, but are not used for quantum computation..... | 3 |
| Figure 3: Superconducting transition of a 100-nm thick $Nb_{0.89}Ti_{0.11}N$ thin film..... | 5 |
| Figure 4: Penetration depth of TiN, using theoretical constants from reference 14. | 7 |
| Figure 5: Cooper pair to quasiparticle ratio dependent on temperature of the system. | 9 |
| Figure 6: Josephson junction I-V curve adapted from reference 18..... | 12 |
| Figure 7: Two level system energy diagram. Adapted from reference 28..... | 16 |
| Figure 8: SQUID loop formed of two Josephson junctions. Adapted from reference 37..... | 19 |
| Figure 9: Transmon qubit circuit diagram and image of the device. Adapted from reference 21..... | 21 |
| Figure 10: Diagram of a JJ created using double angle evaporation. Adapted from reference 19..... | 23 |
| Figure 11: Dolan bridge JJ technique. Adapted from reference 50. | 24 |
| Figure 12: Manhattan style deposition technique. Green plane represents the mask offset from the sample in Z, with streets 1 and 2 evaporated with a 90-degree rotation. | 24 |
| Figure 13: JJ structure cross-section using a planar tri-layer design. AlN is used as the barrier layer in combination with TiN, NbN, and NbTiN superconducting layers. Adapted from reference 51. | 25 |
| Figure 14: Atomic arrangement of a rock salt (111) orientated superconductor in blue on each side of an in-plane lattice matched nitride insulating barrier in green. Large circles represent nitrogen in the system, while smaller circles represent the metal atoms. Adapted from reference 55..... | 27 |
| Figure 15: Alloying transition metal nitrides with NbN in the rock salt phase may allow for engineering of the atomic arrangement to match that of AlN in the Wurtzite phase. Adapted from reference 55. | 29 |
| Figure 16: Diagram of a rock-salt unit cell. Silver orbs represent transition metal atoms, while the larger blue orbs are representative of nitrogen atoms..... | 34 |
| Figure 17: Phase diagram of TiN adapted from reference 82..... | 35 |
| Figure 18: Phase diagram of NbN_x from reference 86. | 36 |
| Figure 19: Optimization process flow for materials development..... | 39 |
| Figure 20: Growth chamber pressure and air temperature during bake out of the MBE chamber used in this work. | 42 |
| Figure 21: a) Viscous, b) Intermediate, c) Molecular flow regimes. Adapted from reference 102..... | 44 |
| Figure 22: Growth process for an annealed NbTiN sample. The various anneal temperatures are represented by the dashed lines in the green anneal section. | 47 |
| Figure 23: Nitrogen plasma optical spectra from a Veeco Uni-Bulb RF nitrogen plasma source used at LPS to produce nitride material. | 49 |
| Figure 24: Diagram of an effusion cell. Adapted from reference 106..... | 50 |

| | |
|--|----|
| Figure 25: Cross-sectional side view diagram of an electron beam evaporator. The beam of electrons from the filament to the source material is represented by the red arrow. | 52 |
| Figure 26: Diagram of 2D, 3D, and mixed growth modes. Reproduced from reference 107..... | 54 |
| Figure 27: Symmetric XRD ω - 2θ setup..... | 55 |
| Figure 28: Symmetric XRD measurement of a 100-nm thick Nb _{0.84} Ti _{0.16} N alloy with extensive thickness fringes indicating good crystal quality..... | 56 |
| Figure 29: RSM of a 100-nm thick TiN film grown on sapphire at LPS..... | 59 |
| Figure 30: Pole figure of a 100-nm thick TiN sample rotated about the (113) plane. X ranges from 25° to 35° , while ϕ ranges from 0° to 360° | 60 |
| Figure 31: XRR plot of a NbTiN and AlN heterostructure showing the intensity during measurement (top), and the Fourier transform of the intensity data (bottom) to extract thickness measurements for various interfaces in the sample..... | 62 |
| Figure 32: AFM schematic adapted from reference 112. | 63 |
| Figure 33: AFM image of a NbN _x sample showing evidence of multiple orientations. | 64 |
| Figure 34: XSEM image of a NbN _x sample showing thickness measurements of the nitride layer. | 65 |
| Figure 35: EDS spectra for a NbTiN sample showing Al and O peaks from the substrate as well as Ti, N, and Nb peaks from the thin film. | 67 |
| Figure 36: RBS spectrum from a Nb _{0.72} Ti _{0.28} N sample grown on sapphire. | 69 |
| Figure 37: Simplified RBS apparatus geometry, with the sample depicted as the grey rectangle. Reproduced from reference 114. | 70 |
| Figure 38: Cutaway diagram of the HPD ADR used in this thesis. Reproduced from reference 116..... | 72 |
| Figure 39: ADR resonator measurement wiring diagram..... | 73 |
| Figure 40: RF package made from copper with PCB and coplanar waveguide chip at the center. | 74 |
| Figure 41: Resonator design masks, both the repeatability (left) and width variation (right) designs. | 77 |
| Figure 42: Repeatability type resonator device with a central transmission line feeding 5 resonators. Perforations can be seen in the zoomed view box which assist in trapping magnetic vortices..... | 79 |
| Figure 43: Ansys 2022 simulation structure featuring a sapphire substrate, and multiple resonators which are isolated for determination of resonant frequency. | 82 |
| Figure 44: Simulated resonant frequency and phase for resonator #1 in the design shown in Figure 44..... | 83 |
| Figure 45: a) Calculated and simulated center frequencies for all five resonators on the width variation and repeatability mask designs. b) Difference fraction between the simulated and calculated frequencies. All are < 4 MHz difference. | 85 |
| Figure 46: TiN growth process showing the changes in substrate temperature and chamber pressure as desorb, growth, and cool-down steps are reached..... | 88 |
| Figure 47: RHEED pattern of the Al ₂ O ₃ (1000) pattern pre and post nitridation for 24 hours at 600 °C. Images reproduced from reference 126. | 89 |

| | |
|--|-----|
| Figure 48: AFM (top), and RHEED (bottom) taken of a 100-nm TiN sample grown on sapphire. TiN shows a distinct "river-rock" topography with a RHEED showing a spotty pattern, indicative of a surface with 3D features..... | 91 |
| Figure 49: Symmetric XRD of a 68nm TiN sample with vertical lines denoting reference values for bulk samples in literature. Thickness fringes are evidence of the good crystal quality..... | 92 |
| Figure 50: Lattice constants for TiN samples as a function of growth temperature. A dashed line corresponds to the ideal unstrained TiN lattice for reference..... | 94 |
| Figure 51: Pole figure of the TiN sample shown in Figure 43. Six-fold symmetry is apparent about the (113) plane..... | 95 |
| Figure 52: RBS spectra and fit for a 30-nm TiN film, showing peaks and plateaus for all constituent elements..... | 96 |
| Figure 53: Comparison between RBS titanium peaks fits for stoichiometric TiN and nitrogen-rich TiN. Experimental data is also shown, which matches the nitrogen-rich simulated fit. | 97 |
| Figure 54: TiN on Al ₂ O ₃ schematic representing the virtual structure used to fit the RBS data. | 97 |
| Figure 55: Reflectivity data (left) and thickness analysis (right) for a TiN sample. .. | 98 |
| Figure 56: Superconducting transition for a 68-nm TiN sample. The floor of the data is dictated by the noise of the nanovoltmeter used to perform these measurements. . | 99 |
| Figure 57: RF sweep of a TiN chip featuring five resonators with a common feedline. | 100 |
| Figure 58: R1 from a TiN resonator sample with good fitting at 35-dB applied attenuation. Inverse S ₂₁ and phase are shown..... | 101 |
| Figure 59: Resonator 1 from a TiN sample at an applied attenuation of 65 dB. | 102 |
| Figure 60: Power dependent internal quality factor plot for TiN resonators..... | 103 |
| Figure 61: Surface modification of TiN sample with the addition of an anneal step at 1000 °C after growth at 1150 °C. | 104 |
| Figure 62: RBS and simulated fit for an annealed TiN sample. Growth temperature for this sample is 1150 °C, with an anneal temperature of 1000 °C for a duration of two-hours. | 105 |
| Figure 63: XRD of annealed (in blue) and unannealed (in orange) TiN samples. ... | 106 |
| Figure 64: XRR data from two TiN samples. Blue colored data is the unannealed sample, and the orange data is the sample annealed at T _A = 1000 °C. | 106 |
| Figure 65: RSM from a TiN sample annealed at 1000 °C for two hours. The Al ₂ O ₃ (1129) and TiN (113) asymmetric peaks are seen..... | 108 |
| Figure 66: Gaussian fits of the cross sectional RSM data for an annealed and unannealed TiN sample..... | 109 |
| Figure 67: Superconducting transitions for two annealed and two non-annealed TiN samples..... | 110 |
| Figure 68: Growth process for a NbN _x sample. a) Typical temperature and pressure trends through the growth. b) EIES control and electron gun output power data during the growth..... | 112 |
| Figure 69: RBS data and simulated fit from a 30-nm thick NbN _x sample. | 113 |
| Figure 70: RBS simulation structure for a ~30 nm NbN _x sample. | 113 |

| | |
|--|-----|
| Figure 71: Reflectivity data (left) and thickness analysis (right) for a 32.92-nm thick NbN_x sample. | 114 |
| Figure 72: Symmetric XRD of a $\gamma\text{-Nb}_4\text{N}_3$ sample showing (111) orientation with no evidence of other phases or orientations. | 115 |
| Figure 73: RBS data from a $\gamma\text{-Nb}_4\text{N}_3$ sample with fits using the composition of the gamma phase and the iteratively fit solution giving a composition of $\text{Nb}_{0.52}\text{N}_{0.48}$ | 116 |
| Figure 74: Symmetric XRD ω - 2θ data of several NbN_x films showing peaks from two phases, $\gamma\text{-Nb}_4\text{N}_3$, and $\varepsilon\text{-NbN}$. Data is offset vertically for clarity. | 117 |
| Figure 75: Heatmap of epsilon and gamma phases of NbN_x as substrate temperature and Nb flux are varied..... | 119 |
| Figure 76: Heatmap comparing the two favorable orientations of $\varepsilon\text{-NbN}$ as substrate temperature and Nb flux are varied. | 120 |
| Figure 77: XRD of NbN_x samples grown at 500 °C and 800 °C. The lower growth temperature produces low quality films, setting the lower temperature bound for the phase fraction heatmaps. | 120 |
| Figure 78: $\gamma\text{-Nb}_4\text{N}_3$ AFM (top) and RHEED (bottom), with a "river-rock" topography similar to TiN. $\gamma\text{-Nb}_4\text{N}_3$ surfaces have a lower R_q than TiN samples..... | 121 |
| Figure 79: Comparison between NbN_x samples, each with a dominant phase and orientation. | 122 |
| Figure 80: Superconducting transition for a $\gamma\text{-Nb}_4\text{N}_3$ sample with a thickness of 32-nm. | 124 |
| Figure 81: Superconducting transition for sample A from Figure 80, a multi-phase NbN_x sample. | 125 |
| Figure 82: Superconducting transition for sample C from Figure 80, which is entirely $\varepsilon\text{-NbN}$ | 126 |
| Figure 83: RF sweep of a $\gamma\text{-Nb}_4\text{N}_3$ chip featuring five resonators with a common feedline..... | 127 |
| Figure 84: Power dependent internal quality factor plot for $\gamma\text{-Nb}_4\text{N}_3$ resonators..... | 128 |
| Figure 85: NbN_x samples with and without a post-growth anneal. | 130 |
| Figure 86: NbN_x samples with and without a post-growth anneal. | 131 |
| Figure 87: Growth process chart for a $(\text{Nb}_x\text{Ti}_{1-x})_{1-y}\text{N}_y$ alloy grown at 1000 °C with a two-hour substrate nitridation process. | 136 |
| Figure 88: Waterfall of several XRD plots spanning the $(\text{Nb}_x\text{Ti}_{1-x})_{1-y}\text{N}_y$ composition range as indicated by labels. Reference Bragg angles are shown with vertical dashed lines for planes of interest. | 138 |
| Figure 89: Out of plane lattice constant as a function of $(\text{Nb}_x\text{Ti}_{1-x})_{1-y}\text{N}_y$ composition with two temperature ranges. Reference lines for literature lattice constants are shown, as well as the expected linear and real trends. | 139 |
| Figure 90: RSM peaks for $(\text{Nb}_x\text{Ti}_{1-x})_{1-y}\text{N}_y$ (113) and Al_2O_3 (1129) planes from samples grown at 800 °C across the compositional range x. | 141 |
| Figure 91: RSM peaks for $(\text{Nb}_x\text{Ti}_{1-x})_{1-y}\text{N}_y$ (113) and Al_2O_3 (1129) planes from samples grown at 1000 °C across the compositional range x. | 141 |
| Figure 92: RHEED and AFM evolution as composition of $(\text{Nb}_x\text{Ti}_{1-x})_{1-y}\text{N}_y$ samples changes..... | 143 |
| Figure 93: RBS spectra and simulated fit for a $(\text{Nb}_{0.72}\text{Ti}_{0.28})_{0.55}\text{N}_{0.45}$ sample..... | 145 |

| | |
|--|-----|
| Figure 94: RBS simulated heterostructure for the fit of sample D2G0192, shown in Figure 93. | 146 |
| Figure 95: Selection of $Nb_xTi_{1-x}N$ samples showing abrupt superconducting transitions. | 148 |
| Figure 96: Superconducting critical temperature as a function of composition for two substrate temperatures. | 149 |
| Figure 97: Fractional frequency shift due to changing W_{center} | 151 |
| Figure 98: Fractional frequency shift as a function of composition. Two of the samples with significant variance between the resonators are due to fabrication with the width variation mask. | 151 |
| Figure 99: Average frequency shift, alpha values, and kinetic inductances for $(Nb_xTi_{1-x})_{1-y}N_y$ resonators. | 152 |
| Figure 100: BCS theory predicted kinetic inductances for NbTiN samples using DC measurement results. | 154 |
| Figure 101: RHEED progression as the post-growth anneal progresses. Some images are offset due to rotation of the substrate and interaction of the RHEED beam with the electron beam positioning magnet. | 160 |
| Figure 102: a) AFM of an unannealed NbTiN sample. b) AFM of a NbTiN sample annealed at 850 °C for 2-hours. c) RHEED of an unannealed NbTiN sample. d) RHEED of a NbTiN sample annealed at 850 °C for 2-hours. | 162 |
| Figure 103: Oxidation effects of the NbTiN film after being annealed at 1150 °C, 850 °C, and 650 °C, then left at ambient conditions for 24 hours. | 163 |
| Figure 104: Symmetric XRD ω -2 θ data for annealed NbTiN samples with T_A ranging from 650 °C to 1150 °C. | 165 |
| Figure 105: Peak shift for NbTiN samples annealed at temperatures varying from 650 °C to 1150 °C. | 166 |
| Figure 106: Ratio of thickness obtained from XRD fringes and extracted from XRR data of NbTiN samples annealed. | 167 |
| Figure 107: Nitrogen fraction of annealed $(Nb_{0.84}Ti_{0.16})_{1-y}N_y$ films from RBS simulated fits. | 168 |
| Figure 108: Superconducting transitions for NbTiN samples annealed at varying temperatures. A control sample with no anneal is shown in black. | 169 |
| Figure 109: Superconducting critical temperature as a function of anneal temperature, with a control sample added as a horizontal line. | 170 |
| Figure 110: RRR and transition width for annealed NbTiN samples. An unannealed sample is shown as a horizontal line for reference. | 171 |
| Figure 111: XRD for annealed samples of varying durations at 850 °C. | 172 |
| Figure 112: XRD peak shift as a function of t_{anneal} at $T_{anneal} = 850$ °C. | 173 |
| Figure 113: Thickness ratio of XRD: XRR measurements as a function of t_A | 174 |
| Figure 114: RBS measurements of nitrogen content extracted from simulated fits of the experimental data. | 174 |
| Figure 115: Superconducting transitions for NbTiN samples with varying t_A | 175 |
| Figure 116: Critical temperature of NbTiN alloys as a function of anneal duration. | 176 |
| Figure 117: RRR and transition width for NbTiN samples of varying anneal times, at $T_A = 850$ °C. | 177 |

| | |
|---|-----|
| Figure 118: Simulations of $(\text{Nb}_{0.84}\text{Ti}_{0.16})_{1-y}\text{N}_y$ samples. Nitrogen content of the films is changed, with overall sample density floating and all other parameters fixed. | 178 |
| Figure 119: RBS simulations of isolated nitrogen and niobium peaks for a $\text{Nb}_{0.84}\text{Ti}_{0.16}\text{N}$ sample..... | 179 |
| Figure 120: RBS fit and experimental data for the isolated nitrogen and niobium peaks. Experimental data is not shown for the nitrogen peaks due to influence of the substrate on the experimental data in that region..... | 180 |
| Figure 121: Effect of etching annealed and non-annealed NbTiN alloys..... | 181 |

Chapter 1: Introduction and Background

1.1 Superconducting Quantum Computing and Josephson Junctions

Nearly all modern digital computation uses a binary system, where an on/off paradigm is used to encode data. This binary system is usually macroscopic, using differing levels of voltages for computation. Increasing computational power requires more bits, or in a complementary metal oxide semiconductor (CMOS) device, more transistors. Ideally, these bits have zero information loss, and for modern day computation, can be largely thought of as error-free. Improvement in computation time requires denser device fabrication to increase the number of transistors on a chip or higher clock frequencies for silicon based CMOS. [1] The computing power available with conventional computing generally increases with the number of transistors N , and results in near 100 billion transistors as of 2022. [2]

Quantum computing (QC) aims to offer an alternative to conventional computing for difficult problems such as finding large prime numbers [3], machine learning [4], and simulation of many-particle quantum systems. [5] For some problems, this may result in a “quantum speed-up” due to using fewer steps to generate an output compared to a conventional computing system, visualized in Figure 1. [6], [7]

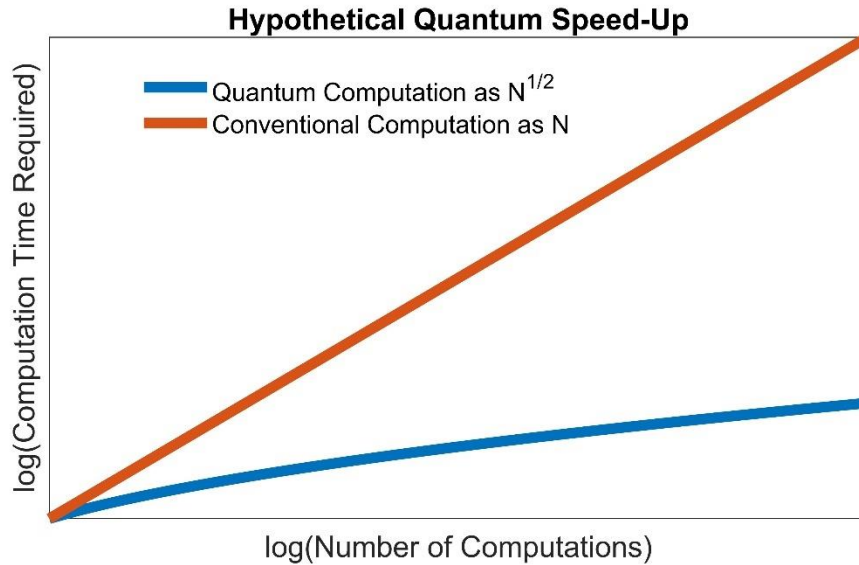


Figure 1: Computation time compared for conventional and quantum computing. Reproduced from reference 7.

The quantum speed up is enabled by the phenomenon of both superposition and entanglement of two or more quantum bits, or qubits. This results in the quantum states of two or more entities becoming mathematically inseparable. Qubits can be held in a superposition of states, $|\psi\rangle = \alpha|0\rangle + \beta|1\rangle$, with α and β are probabilities of being in either the 1 or 0 state. [8]

Qubits characteristics required for stable, controllable computation can be assessed using the DiVincenzo criteria. [6]

1. A well-characterized, scalable physical system with well-defined energy levels, which reduces the possibility of unintended level transitions and allows for precise control of the qubit.
2. The ability to initialize the qubit into a pure state. For two level configurations, the transition energy $E_{|0\rangle \rightarrow |1\rangle}$ needs to be much greater than the thermal noise in the system, where $E_{|0\rangle \rightarrow |1\rangle} \gg K_B T$. K_B is Boltzmann's Constant, and T is the temperature of the system.

3. A universal set of quantum gates consisting of single qubit gates where qubit rotations occur around two axes, as well as two qubit gates such as quantum-XOR or Controlled-NOT gates allow for complete control over a quantum circuit.
4. The capability to measure the qubit state, or each individual qubit in a multi-qubit system.
5. Sufficiently long coherence times to complete quantum computation. The qubit lifetime, or T_1 , is the maximum time available for a measurement of the qubit and is defined as the time needed for the qubit to move from the excited state to the ground state. The coherence time or period where the system is in a predictable state is defined by T_2 and limits the time available for computation.

Above the physical device level, a qubit can be thought of as a two-level system (TLS) where an applied energy E will move the qubit into an excited state $|0\rangle$ from the ground state $|1\rangle$. According to that qubit's T_1 time, the qubit will eventually transition back into the ground state.

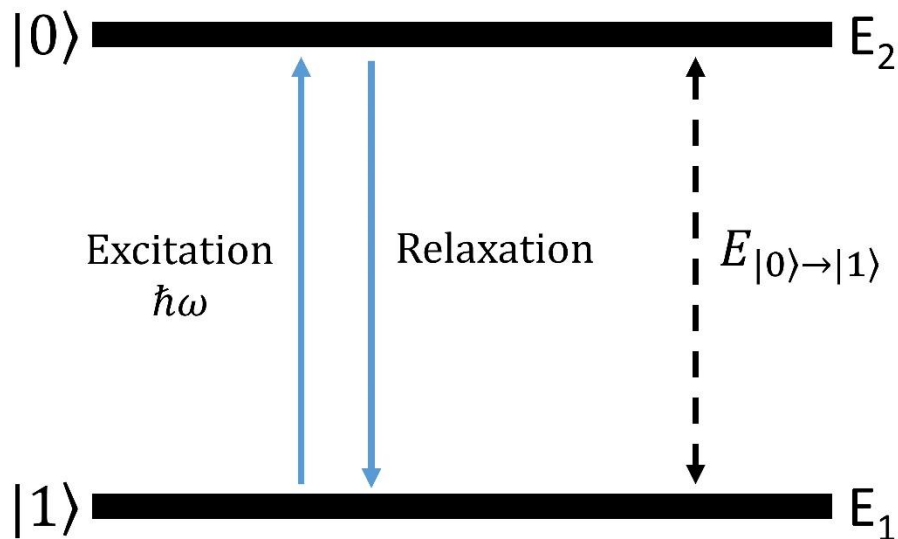


Figure 2: Two level system example. Higher energy states E_n may exist, but are not used for quantum computation.

Below the qubit circuit level, the physical qubit can be composed of many distinct two level systems, often arising from quantum phenomena in microscopic systems such as trapped ions [9], isolated electrons [10], quantum circuits, or topological states. [11] In this work, however, the focus is on superconducting qubits, where a Josephson junction (JJ) is added to an LC circuit composed of an inductor and a capacitor, where the JJ supplies the anharmonicity to satisfy the DiVincenzo criteria.

What this creates in Figure 2 is the elimination of degeneracy between energy transitions, allowing for the application of resonant energy to excite the qubit to distinct, controllable energy levels. This is critical for qubit manipulation and readout to prevent excitations to more than one energy level, or into defect energy levels within the materials used to fabricate the JJ. [12]

Continued advancement of quantum computing is reliant on achieving the DiVincenzo criteria with improvement in the control and readout of these quantum systems. Improvement in these criteria comes from all levels, from the fabrication of the qubit, the creation of a quantum circuit, to new ways of effective control over error correction.

1.2 Superconducting Material and Device Theory

1.2.1 Superconductivity Theory

Superconductivity exists in select materials where below a material-dependent critical temperature T_c , electrons will pair up to form Cooper pairs, which the flow of provides several macroscopic changes to the material characteristics. The most important characteristic for this work is that materials in the superconducting state can produce a current I without any applied voltage V , called a supercurrent. This state possesses zero resistance, where

$$R = \frac{V}{I} = \frac{0}{\infty} = 0. \quad (1)$$

This transition occurs abruptly at the transition temperature and is shown in Figure 3, where a sudden drop in resistance occurs at a temperature of 16.8 K for a NbTiN alloy.

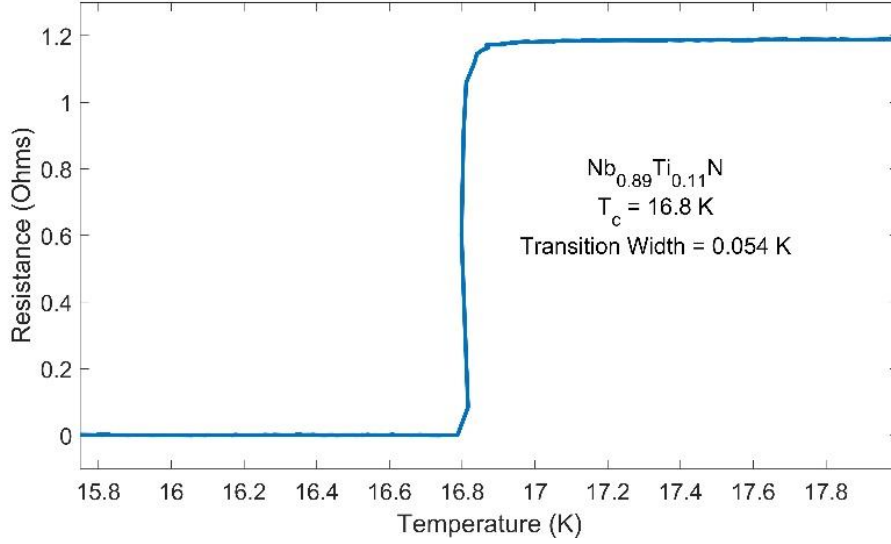


Figure 3: Superconducting transition of a 100-nm thick Nb_{0.89}Ti_{0.11}N thin film.

These macroscopic properties are the result of microscopic changes in the material as it undergoes a transition into the superconducting state, but the macroscopic phenomena can be described by the London equations. [13] The current in the material can be described as

$$\vec{J}(\omega) = \frac{1}{i\omega\Lambda} \vec{E}(\omega), \quad (2)$$

where the current density \vec{J} is a function of the frequency dependent electric field $\vec{E}(\omega)$, the phenomenological London parameter Λ is dependent on current carrying particles (which do not have to be electrons) with a mass m , number n , and charge q . The phenomenological parameter Λ is described as

$$\Lambda = \frac{m^*}{n^*(q^*)^2}. \quad (3)$$

The form of perfect conductivity is then described by the first London equation,

$$\vec{E} = \frac{\partial}{\partial t} (\Lambda \vec{J}). \quad (4)$$

The second London equation is taken from the application of Faraday's law with the first London equation, which describes the Meissner effect where magnetic fields below a certain threshold are expelled from the bulk of the material when below the critical temperature T_c , shown as

$$\nabla \times (\Lambda \vec{J}) = \vec{B}. \quad (5)$$

The second equation can be observed as the superconductor expels magnetic fields from the material within the surface region denoted by the penetration depth (λ) of the magnetic fields as shown below, where

$$\lambda = \sqrt{\frac{\Lambda}{\mu_0}}. \quad (6)$$

Magnetic fields decay exponentially into the material according to the penetration depth. This depth is temperature dependent relative to the critical temperature of the material. For example, it can be shown that the penetration depth of TiN is 22.66 nm in a theoretical 0 Kelvin environment, and is shown in Figure 4. [14]

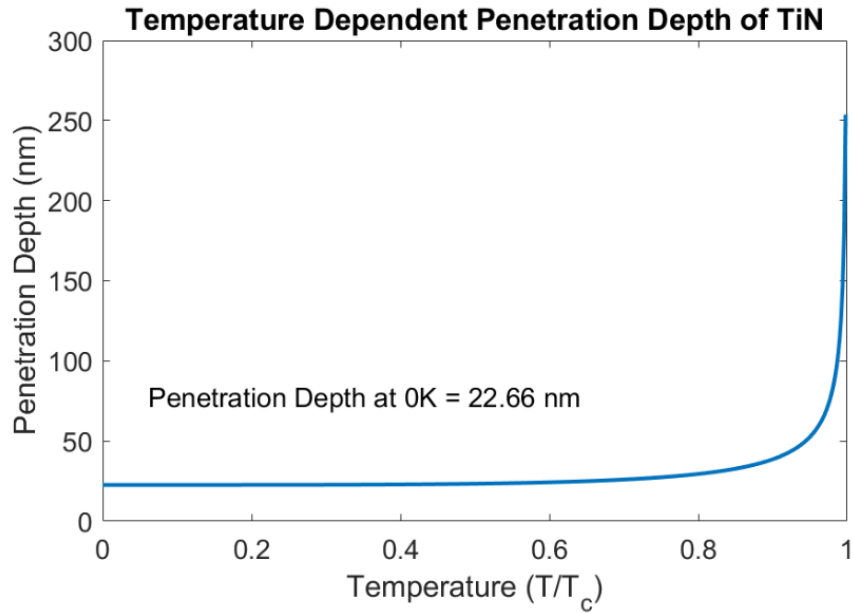


Figure 4: Penetration depth of TiN, using theoretical constants from reference 14.

With the macroscopic characteristics of superconductors described by Meissner in 1933, the London brothers in 1935, and others, a microscopic explanation for the material properties is needed.

The Nobel prize in 1972 was awarded to Bardeen, Cooper, and Schrieffer (BCS) for a microscopic theory explaining the phenomena of superconductivity. In BCS theory, two electrons in the material join into a Cooper pair. Electrons can pair in several forms, which influence the superconducting gap as a function of momentum. Opposite spin electrons can combine into a singlet, which are found in S-wave superconductors and have zero orbital angular momentum. S-wave superconductivity is commonly seen in simple materials such as aluminum and titanium nitride. Electrons with the same spin can also combine into a triplet state, forming a P-wave superconductor. P-wave Cooper pairs are seen in materials such as perovskite oxides like Sr_2RuO_4 . Cooper pairs with spin = 0, but with non-zero angular momentum form a d-wave superconductor, seen in high temperature superconductors.

The superconducting gap Δ indicates the binding energy of the Cooper pairs and is described in BCS theory by

$$\Delta = 2\hbar\omega_D e^{\left(-\frac{1}{\lambda}\right)}. \quad (7)$$

The electron phonon coupling parameter λ is defined by

$$\lambda = |g_{effective}|^2 N(e_F), \quad (8)$$

where λ describes how easily electrons move through a field of charged nuclei in an ordered crystal lattice. The Debye frequency ω_D is a cutoff for the phonon frequency in a material, \hbar is the Planck constant, and $N(e_F)$ is the density of states at the Fermi level. These electrons interact with lattice vibrations, or phonons, with an effective coupling coefficient,

$$g_{effective} = |g|^2 \frac{1}{\omega^2 - \omega_q^2}. \quad (9)$$

Where ω is the frequency of the electron, ω_q is the frequency of phonons in the material, and g is the electron-phonon coupling coefficient. This bandgap is formed with magnitude 2Δ , and is related to the critical transition temperature of the material by

$$2\Delta = k_B T_c \text{ when } T = 0 \quad (10)$$

and

$$\Delta(T) = \Delta_0 \sqrt{\left[1 - \frac{T^4}{T_c^4}\right]} \text{ when } T \neq 0. \quad (11)$$

Cooper Pairs are thermodynamically stable, and as such are the dominant carriers when the material is below its critical temperature. When the binding energy of the copper pairs is exceeded, the broken pair generates unbound electrons with enough energy to elevate them into a different energy band. These unbound electrons are called quasiparticles.

The generation of quasiparticles is thermally dependent, with the number of cooper pairs and quasiparticles described by

$$n_{Cooper\ Pairs} = n_0 \left(1 - \left(\frac{T}{T_c}\right)^4\right) \quad (12)$$

and

$$n_{Quasiparticles} = n_0 \left(\frac{T}{T_c}\right)^4 \quad (13)$$

where n_0 is the total number of conducting particles. The amount of both are shown as a function of temperature below T_c in Figure 5.

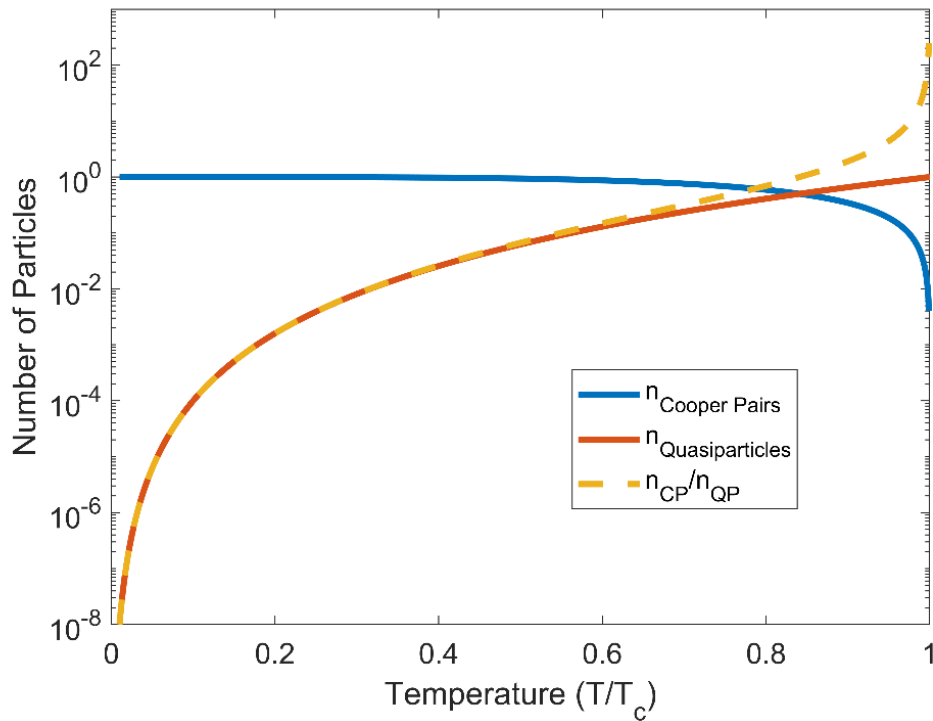


Figure 5: Cooper pair to quasiparticle ratio dependent on temperature of the system.

The coherence length of the cooper pairs is derived from the Ginzburg-Landau theory of superconductivity, and helps describe the type of superconductivity expressed by a material. [15]

The coherence length, or phenomenon describing the decay of a magnetic field in the superconductor is written as

$$\xi(T) = \sqrt{\frac{\hbar^2}{4m^*|\alpha(T)|}}. \quad (14)$$

The temperature dependent term $\alpha(T)$ describes the critical field of the material, and m^* is the effective mass of the carriers. The Ginzburg-Landau parameter κ compares the coherence length above with the London penetration depth as

$$\kappa = \frac{\lambda(T)}{\xi(T)}, \quad (15)$$

where κ is used to describe the boundary between a type I ($\kappa < \frac{1}{\sqrt{2}}$) and type II ($\kappa > \frac{1}{\sqrt{2}}$) superconductor. Type I superconductors such as aluminum typically have lower critical transition temperatures and have a single critical field threshold where all magnetic field is expelled. Type II superconductors do not have an abrupt transition into the superconducting state when exposed to a magnetic field and some field lines will penetrate the superconductor when the magnetic field reaches H_{c1} . Once the magnetic field reaches an upper threshold, H_{c2} , the material loses all its superconducting properties. The region between the two levels is called the mixed state. Some type II superconductors have a relatively high upper critical field ($H_{c1} > 1$ T), these materials can be used for superconducting magnets in a myriad of applications.

Superconducting material properties such as critical temperature and critical field play a large part in material selection when designing a superconducting device for a specific use case. For example, the proximity of large permanent magnets or the requirement to have superconducting properties at a certain temperature will influence the use of a type I or type II superconductor.

1.2.2 Cooper Pair Tunneling

Superconducting quantum circuits rely on the ability of Cooper pairs to tunnel through an insulating barrier. The probability of tunneling from one side of a Josephson junction to the other is determined from the incident and transmitted wavefunctions of the Cooper pairs and is described by,

$$P_{I \rightarrow T} \propto R(k, \kappa) e^{-\frac{2d\sqrt{2m(E-V_0)}}{\hbar}}. \quad (16)$$

Where R is dependent on the probability of reflection from the interface, and associated electron wave numbers inside the barrier, κ , with incident/transmitted propagating Cooper pair k , thickness of the barrier, d , mass of the Cooper pair, m , and height of the barrier, $E - V_0$. [16] The most important feature of this relationship is that the tunneling probability is exponentially dependent on the barrier thickness and height.

Without a voltage bias on the junction, the energy difference between sides is not large enough to stimulate current. To cause electrons to flow across the junction, the applied voltage must be larger than the energy gap of the device, as shown in Figure 6. [17], [18]

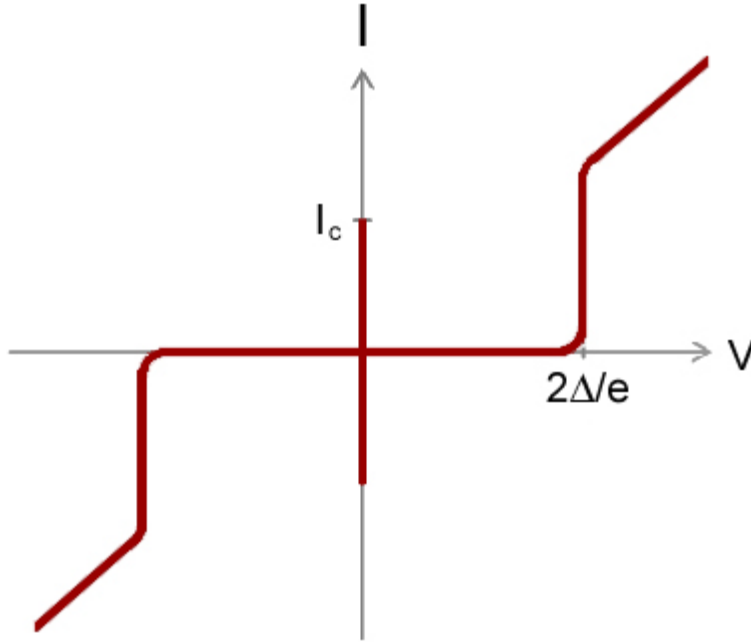


Figure 6: Josephson junction I-V curve adapted from reference 18.

In Figure 6, exceeding the gap energy 2Δ causes Cooper pairs to split, and a linear IV curve emerges, similar to a normal metal. However, at zero applied voltage, there is a supercurrent, or flow of Cooper pairs across the Josephson junction. This supercurrent can be explained using Schrodinger's equations for both sides of the junction as

$$i\hbar \frac{\partial \psi_1}{\partial t} = \frac{qU}{2} \psi_1 + \hbar T \psi_2 \quad (17)$$

for the right moving wavefunction, with the left moving wavefunction described by

$$i\hbar \frac{\partial \psi_2}{\partial t} = \frac{-qU}{2} \psi_2 + \hbar T \psi_1. \quad (18)$$

Here, ψ_1 and ψ_2 are the wave functions for the right and left moving wave functions, and U is the applied voltage bias at the tunneling barrier. q is the charge of the tunneling particle. The tunneling probability is represented by $\hbar T$ and links the two equations so that the equations take the solutions of

$$\psi_1 = \sqrt{n_1} e^{i\theta_1} \quad (19)$$

and

$$\psi_2 = \sqrt{n_2} e^{i\theta_2}. \quad (20)$$

Here θ is the phase of the wave function of Cooper pairs on either side of the junction, and n is the number density of Cooper pairs. Using these solutions in Schrodinger's equation reveals that a supercurrent can exist when there is zero applied voltage, as long as there is a phase difference δ between the two sides of the junction, where $\delta = \theta_1 - \theta_2 \neq 0$. This phenomenon is the DC Josephson effect. The current and voltage are expressed using

$$I = I_c \sin(\delta) \quad (21)$$

and

$$V = \frac{\hbar}{2e} \frac{\partial \delta}{\partial t} = \Phi_0 \frac{\partial \delta}{\partial t}. \quad (22)$$

Here, I_c is the critical current of the Josephson junction, which is the maximum current across the JJ barrier that can be maintained before resistance is encountered. The inductance resulting from this flow across the junction is described by the flux quanta Φ_0 and critical current, where

$$L_J(0) = \frac{\Phi_0}{2\pi I_c}. \quad (23)$$

1.2.3 Effect of Material Properties

Many variants of the Josephson junction have been successfully tested since the first aluminum-based devices developed in the late 1960's by Giaever. [19] The most commonly used structure is the superconductor-insulator-superconductor stack, but both superconductor-normal

metal-superconductor and superconductor-“weak-link” superconductor-superconductor material systems have been fabricated. Regardless of the material selection, the critical current of the junction is the most important parameter. The materials chosen also affects the surface states available and can result in detrimental effects on the Josephson junction.

The most predominantly used barrier material is the native oxide produced by the material used as the superconductor. This is mainly due to the ease of fabrication, as simple exposure to air before depositing the second layer of material will grow an oxide. For example, aluminum forms a very stable but amorphous oxide which allows for easily fabricated junctions with reliable thicknesses of the barrier. Niobium and tantalum are materials of recent interest for junction fabrication, but come with their own set of multiple oxidation states, forming amorphous oxide barriers of varying quality and thickness. [20], [21]

Material selection affects the energy barrier height ($E - V_0$) of the junction, and the thickness of the barrier drastically changes the critical current, which affects the frequency of the qubit. [22] Material selection also may affect the energy loss in the finished device. One of the major hindrances for superconducting qubits is decoherence caused by the junction barrier. [23] Since most barriers used since the introduction of the Josephson junction are amorphous, material defects exist in significant densities within the barrier. These defects can consist of dangling bonds, contaminants from imperfect deposition techniques, and incoherent interfaces with the superconducting material. These defects may create what are known as two level systems (TLS), which can have an activation energy on the scale of the energy needed to switch states in the qubit. By losing energy to these defects, the coherence and lifetime of the qubit diminishes. [24]

For superconducting qubits with resonators for state readout and manipulation, the lifetime the qubit depends on the quality factor of the resonator used to propagate and extend the state memory. In a resonator, photons reflect off the ends of the resonator, with the number of reflections determined by the quality factor of the material. Energy loss in the resonator is a function of the loss tangent, $\tan \delta$, and is a measure of how much a material or component deviated from its ideal characteristics. Loss tangent is inversely proportional to the quality factor by $Q = \frac{1}{\tan \delta}$. The total quality factor of a resonator is a function of both the internal quality factor, Q_i , of the materials and various loss mechanisms, as well as the coupling quality factor Q_c between the resonator and other components, described by

$$\frac{1}{Q_T} = \frac{1}{Q_i} + \frac{1}{Q_c}. \quad (24)$$

Internal energy loss in superconducting qubits is the sum of various sources of loss where

$$\frac{1}{Q_i} = \frac{1}{Q_{TLS}} + \frac{1}{Q_{Quasiparticle}} + \frac{1}{Q_{Radiation}} + \frac{1}{Q_{Vortex}}. \quad (25)$$

These sources of loss are generally independent from each other. Radiative loss arises from the loss due to dissipation of energy from the resonator into the surrounding vacuum. Quasiparticle loss originates from interactions of quasiparticles with various electromagnetic fields in the material. Interaction of quasiparticles in these fields dissipates energy by ohmic heating. Reductions in loss due to quasiparticles can be accomplished by proper thermalization of superconducting components, which reduced the likelihood of Cooper pairs separating. [25], [26] Dilution refrigerators used in the operation of superconducting qubits generally maintain a temperature of a few milliKelvin, well below the critical temperature of material used in superconducting circuits. Vortex loss is due to magnetic fields penetrating the material. Modern

superconducting qubit systems have significant magnetic shielding and preventative circuit design to minimize this effect. [27]

Two level systems (TLS) create loss from both the natural properties of materials used in the qubit system as well as defects in the material. TLS reside in dielectrics, and can act as an energy absorbing site. [28] The conventional model, as shown in Figure 7, can have a transitional energy, E , resulting from energy difference of the two potentials, ε , and tunnel coupling, Δ . When E is close to the transition energy of the qubit, ($E_{|0\rangle\rightarrow|1\rangle}$) or resonant energy of a resonator, energy can be absorbed from the qubit.

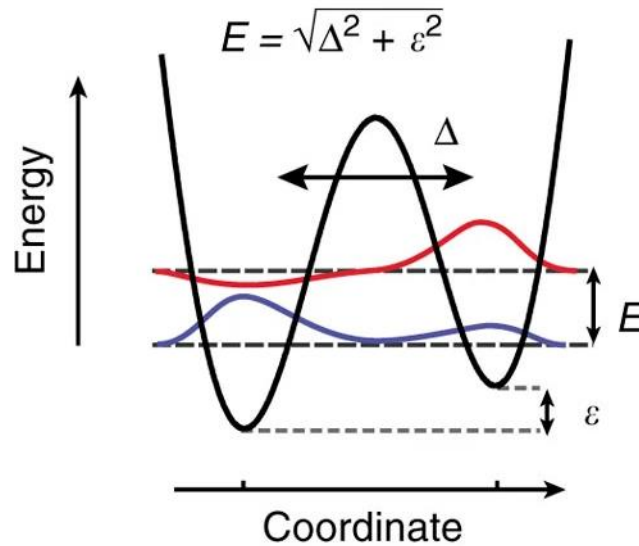


Figure 7: Two level system energy diagram. Adapted from reference 28.

Superconducting devices are most strongly affected by TLS defects in regions of high electric field. Classifying these regions results in three main interaction areas:

1. Metal to air interfaces
2. Substrate to air interfaces
3. Metal to substrate interfaces

In thin film growth using molecular beam epitaxy, the metal to substrate interface is dictated by the in-situ environment, wafer preparation, and growth parameters. The type of substrate cleaning and etching, as well as the contaminants present in the chamber during growth will be reflected in this interface. The other two interaction areas, substrate to air and metal to air, are affected by the fabrication process of the qubit after growth, with the etching steps, oxidation of surfaces, and quality of resist removal all dictating the characteristics of these regions. [29]

Two-level systems generally have a uniform distribution of transition energies, so TLS loss tends to be frequency independent. Additionally, TLSs have a low saturation power that is governed by relaxation rate of the TLS after it has absorbed a resonant photon. For this reason, superconducting resonators are usually tested for power dependence with the goal of evaluating the unsaturated loss from TLSs that occurs near the single photon regime.

Identifying the root cause of TLS loss can be difficult, and much research has been performed to both find the sources and identify remedies. [29] Interstitial contaminants in materials as well as vacancies caused by damage due to ion milling can also generate TLS. Defects are of a particular concern in amorphous materials such as native oxides. Due to the amorphous nature, the density of dangling bonds and vacancy sites can be high. This has prompted researchers to use crystalline materials for the insulating barrier as well as developing better control over oxide growth, as the crystalline order reduces the prevalence of such dangling bonds. [27], [30], [31]

The interfaces mentioned prior might be engineered to possess less loss-producing states. Cleaning procedures for reducing contaminants, as well as passivation techniques are extensively studied in literature to prevent the formation of TLS at these interfaces. [32]–[34]

1.3 Superconducting Circuit Applications

1.3.1 Superconducting Conventional Circuits

Josephson junctions can be used to create conventional binary logic circuits such as Rapid Single Flux Quantum (RSFQ) architecture. Binary information is stored as magnetic flux quanta, in superconducting loops that contain multiple JJs and are used with Boolean logic arithmetic identical to conventional CMOS circuits in consumer products. The overall power consumption for an RSFQ logic circuit is much lower than for conventional room temperature CMOS circuits, even considering superconducting cooling requirements. Additionally, the switching speed of these devices is typically around 100 GHz and has been shown in laboratory experiments to approach speeds of 1000 GHz. Moreover, the power required does not follow the same scaling as CMOS devices.[35], [36]

In conventional CMOS circuits, a detriment to efficiency is the need to move data from one processing unit to the next using interconnects made from metals with a finite resistance. RSFQ does not suffer from this inefficiency because all the interconnects are superconducting. While in principle RSFQ circuits possess superior speeds compared to CMOS circuits, the fabrication technology and achievable circuit complexity are less advanced. Currently, Josephson junctions and the surrounding superconducting circuit cannot be reliably manufactured with the same device density and thin linewidth as conventional circuits. Deviations in the critical current due to material imperfections and uncertain insulating widths due to RSFQ's thin-film-based fabrication can make these junctions useless for RSFQ logic. Without reliable yields during fabrication, commercial success of RSFQ is made more difficult. [35]

1.3.2 Superconducting Quantum Interference Devices

The DC Superconducting Quantum Interference Device (SQuID) is made by connecting two JJs in parallel to form a superconducting loop, as shown in Figure 8.

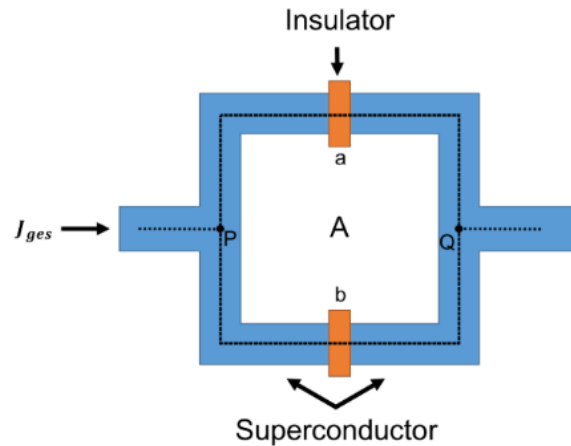


Figure 8: SQuID loop formed of two Josephson junctions. Adapted from reference 37.

When an externally applied magnetic field is applied, a current is induced in the SQUID that reduces the total magnetic flux passing through the center of the loop. This current circulates in the loop formed by the two JJs, and results in a phase difference across the junctions and a change in supercurrent that can flow through the loop. The magnitude of this difference can be used to measure magnetic fields, with detection of fields as low as 1×10^{-18} T. [37] A common commercial use for SQUIDs is the measurement of magnetic properties of materials. Magnetic susceptibility meters use superconducting electro-magnets to apply an external magnetic field to a sample and use a SQUID to detect changes in sample magnetization. These devices are also used in low-power magnetic resonance imaging (MRI) to image biological structures. The use of SQUIDs in this case allows for lower magnetic fields to be used in the milliTesla range, reducing the cost and power usage when compared to high-field MRI tools. [38]

1.3.3 Superconducting Quantum Circuits

Qubits store information in quantum states using many different phenomena, such as electron spins, quantum dots, or nitrogen vacancy centers. Coplanar waveguides are used commonly in superconducting qubits, as a photon in the resonator can be strongly coupled to a qubit. The use of low-loss superconducting materials like aluminum ensures that the captive photon in the resonator persists for long enough to perform manipulations of the qubit. In the last two decades, quantum computing has grown from theory and single qubit experiments, to working systems made up of a hundred functioning qubits. Researchers at IBM, Google, and Rigetti have all reported work on superconducting quantum computers.

Josephson junctions, superconducting wires, capacitors, and inductors can be combined to create a quantum circuit that manifests quantization of charge or flux. One of the more common qubit designs is the transmon, a modified form of the Cooper pair box, where a capacitor in parallel with a Josephson junction creates a circuit where the junction energy is much greater than the energy of the capacitor, providing reduced sensitivity to charge changes in the circuit. The quantum-mechanical Hamiltonian for a transmon qubit can be written as

$$\mathcal{H} = 4E_C(n - n_g)^2 - E_J \cos(\varphi) = \frac{Q^2}{2C}(n - n_g)^2 - \frac{I_C \Phi_0}{2\pi} \cos(\delta). \quad (26)$$

Here, E_C is the energy stored in the capacitor, and E_J is the Josephson energy. The conjugate variables, n and φ , vary with respect to each other in a manner to ensure that the total energy of the system is conserved in the Josephson junction system. The conjugate variables are the Cooper pair density difference, n , and the Josephson phase φ . The offset charge due to the applied voltage is n_g , the electron charge on the capacitor is Q , the capacitance of the device is

C , and the flux quantum is Φ_0 . The critical current is denoted as I_c , and δ is the phase difference across the junction.

The non-linearity of the JJ, as well as the relative energies of the capacitor and Josephson junction are design criteria that can affect the operation and charge sensitivity of the circuit, creating qubits which balance energy level nonlinearity and charge noise sensitivity. There is currently no consistent mitigation strategy for flux noise or device uniformity. Transmon qubits are typically coupled to a readout resonator leveraging circuit quantum electrodynamic concepts to isolate the qubit from the environment. [39] A transmon qubit, along with the circuit diagram, is shown in Figure 9. [21]

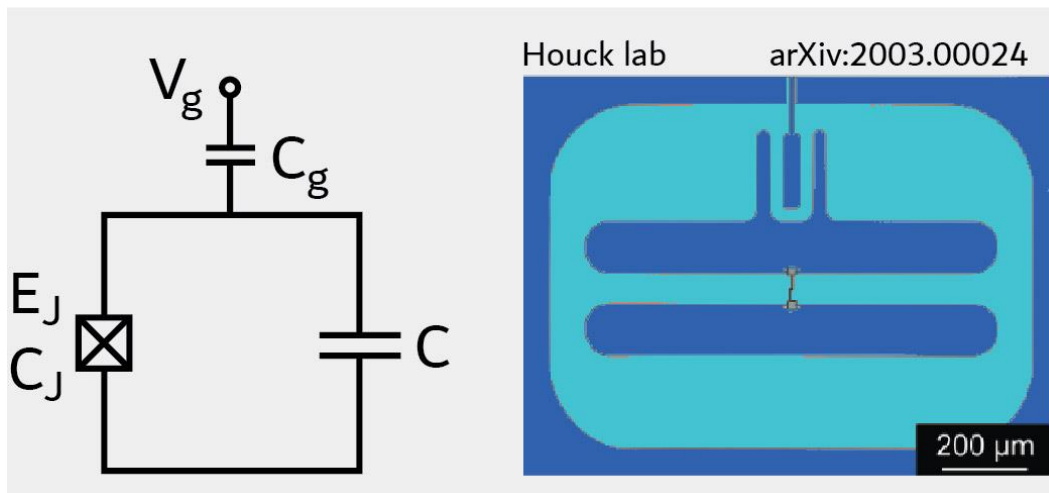


Figure 9: Transmon qubit circuit diagram and image of the device. Adapted from reference 21.

Superconducting quantum circuits must be run at cryogenic temperatures well below the critical temperature of the superconducting material. In a cryogenic environment, superconducting qubits provide the potential for long coherence times due to the non-dissipative properties of superconductors. [40], [41] This cryogenic environment is required to reduce noise, thermal excitation of the qubit, and to keep the quasiparticle density low. [42]

From a materials perspective, advancement in qubit lifetime is one of the more important research objectives. Material defects may cause “charge noise” or “flux noise”, which both affect the T_2 of the qubit. Both types of noise are responsible for affecting energy relaxation and decoherence that directly causes errors in quantum circuits. Charged traps residing within the JJ interface may couple to the qubit, increasing the rate of energy loss [43], while undercoordinated bonds may produce spin defects in dielectrics and interfaces. Further research suggests that up to 60% of the conventional dielectric loss at these junctions can be attributed to atomic scale defects. [44] These defects may be formed from the random ordering of these materials that create parasitic quantum TLS, that can couple to the device’s oscillating electric field through resonant dipole interactions and affect the T_1 of the qubit. [12] To minimize the effects of these defects, engineers have found that reducing the device active area to less than $1 \mu\text{m}^2$ is effective. Frequency stability in JJ circuits is also an important engineering figure of merit when large circuits are produced. Current atomic scale variations in thickness [45], and variations in bond-coordination in barrier dielectrics frustrate device designers. [46]

1.4 Josephson Junction Fabrication

1.4.1 Double Evaporation Fabrication

Josephson junction fabrication can be traced back to the first double angle evaporation techniques used by Giaever. [19] After attempts using alternate materials such as thermoplastics as a barrier between aluminum contacts, Giaever realized that the more effective approach was to use naturally occurring aluminum oxide as the junction barrier. By evaporating aluminum within

a Bell jar, then exposing the aluminum strip to air, a $\sim 30 \text{ \AA}$ layer of amorphous AlO_x was grown, which was then capped with a cross strip of aluminum.

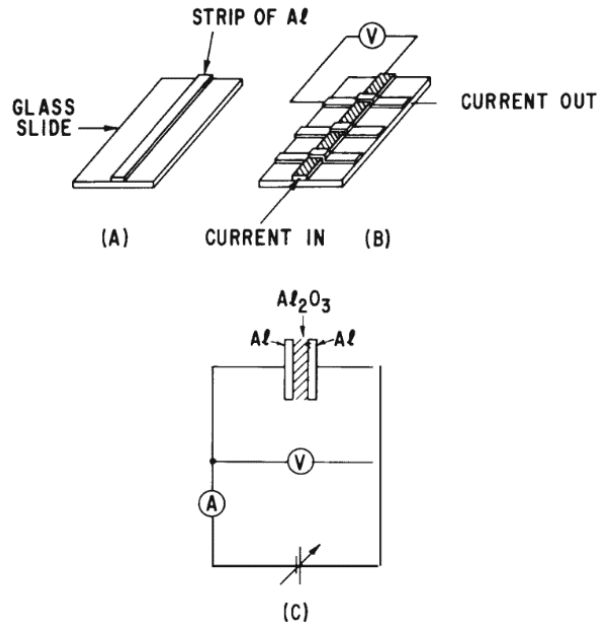


Figure 10: Diagram of a JJ created using double angle evaporation. Adapted from reference 19.

The results from these first experiments showed a DC current at zero applied volts, evidence of the Josephson effect. Refined with modern metal deposition tools and fabrication processes, this technique is still used today. [47], [48] Modern applications of the oxidation method use high purity oxygen or a low power oxygen plasma in the growth chamber to minimize contaminants in the insulating barrier, as well as having more control over the tunnel barriers thickness. Pioneered by G. Dolan in 1977 [49], the Dolan bridge technique uses a strip of suspended resist patterned with an electron beam with multiple angles of evaporation to form an overlapping metal structure with oxidized metal in between. This is similar to the shadow mask technique, in that windows in a layer above the substrate are used with rotated evaporation sources to deposit multi-layer structures. [50] Figure 11 shows the technique where an initial

layer of aluminum is deposited through a mask, which is oxidized, forming a native oxide layer. A second aluminum layer is deposited from an offset direction, creating the JJ.

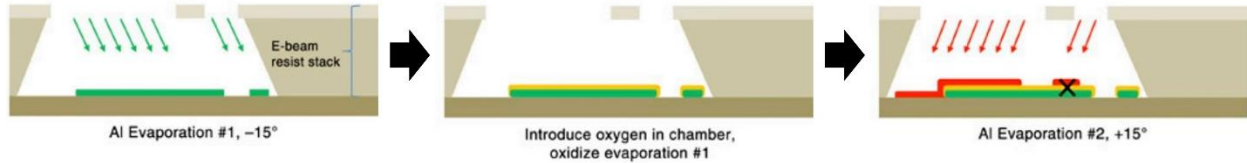


Figure 11: Dolan bridge JJ technique. Adapted from reference 50.

Another method to create oxide-based Josephson junctions is with “Manhattan-style” fabrication. In this technique streets are etched into photoresist at 90-degree angles. Evaporated metal is deposited down one street, then allowed to oxidize. Turning the sample 90 degrees around its surface normal enables the second street to be deposited, forming a junction where the streets intersect.

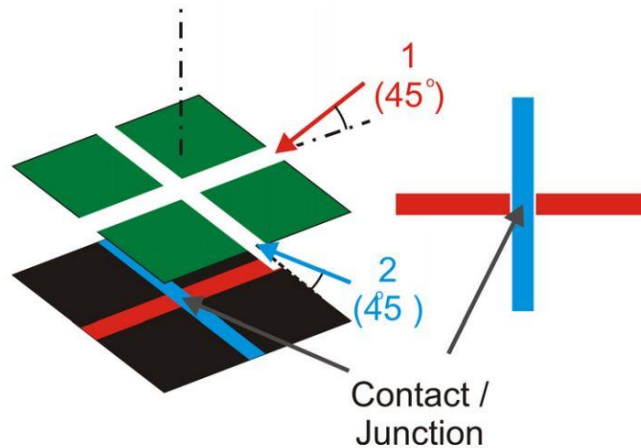


Figure 12: Manhattan style deposition technique. Green plane represents the mask offset from the sample in Z, with streets 1 and 2 evaporated with a 90-degree rotation.

1.4.2 Tri-Layer Designs

Tri layer designs differ from the traditional multi-deposition step fabrication techniques in that the entire heterostructure is grown prior to any fabrication steps. The wafer scale planar device is then etched down from the top of the material stack with wiring layers added to form the Josephson junction. Figure 13 shows a simplified cross-sectional diagram of a JJ test structure, where areas of the heterostructure are etched away to allow leads to be attached to the bottom superconductor, completing the circuit through the JJ barrier. [51]

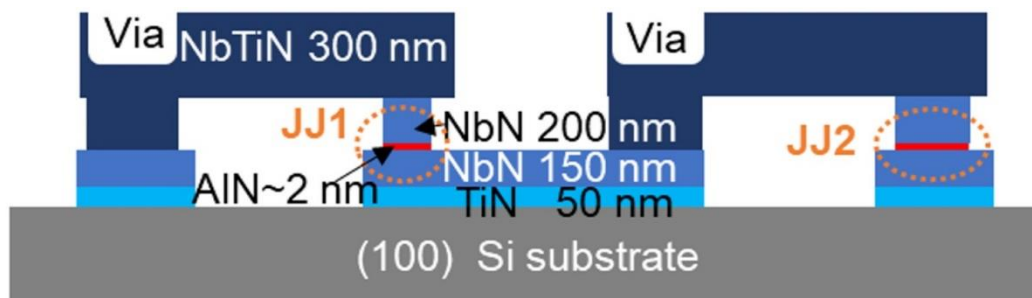


Figure 13: JJ structure cross-section using a planar tri-layer design. AIN is used as the barrier layer in combination with TiN, NbN, and NbTiN superconducting layers. Adapted from reference 51.

Tri-layer designs offer several advantages when compared to oxidation techniques.

1. Growing the tri-layer generally takes place all in-situ, reducing the interaction of the bottom superconductor and the insulating material with atmosphere. This has the potential to keep the interfaces contaminant-free.
2. The use of epitaxial nitride materials throughout the structure may lower the loss generated from TLS usually due to traditional oxide-based barrier layers.
3. Oxidation techniques typically produce amorphous oxide layers. A tri-layer heterostructure benefits from much more choice in barrier material, from crystalline oxides produced with plasma to entirely different material systems which can be grown in crystalline form.

Early examples of using tri-layer material systems include Uzawa et al, who found that not only were they able to fabricate NbN/AlN/NbN Josephson junction on MgO substrates using radio-frequency (rf) magnetron sputtering with current densities as high as 100 kA/cm^2 , the sub gap leakage denoted by the ratio of the normal resistance and the resistance at 3 mV below the inflection point in the I-V curve was superior to junctions created using Al/AlO_x and Nb metal. [52] With nitride-based based material systems, the Fujimaki and Lichtenberger groups used rf magnetron sputtered NbTiN deposited on oxidized silicon substrates with an AlN barrier layer to create successful JJs with performance on par with traditional devices. [53] [54] Lichtenberger et al. points out that higher T_c material systems are attractive for qubit operation at temperatures around 10 K. It was also found that the NbTiN based junctions possessed higher critical current density compared to aluminum-based devices. Likewise, Fujimaki et al. also finds high gap voltages and junction critical current densities of 4.3 mV and 6.2 kA/cm^2 . [55]

1.4.3 Epitaxial Josephson Junctions

Epitaxial Josephson junctions, heterostructures grown layer by layer with coherent, single crystal order throughout the structure, may be the next evolution of planar JJ fabrication. While planar tri-layer devices attempt to solve many of the problems created in traditional oxidation type junction fab, there is still the issue of defects arising at the barrier interface due to an incoherent bonding arrangement.

To form an epitaxial junction with coherent interfaces, the atomic arrangement at the interface must be similar enough between the superconductor and the crystalline insulating barrier so as to prevent a mismatched bonding arrangement, as in Figure 14. [56]

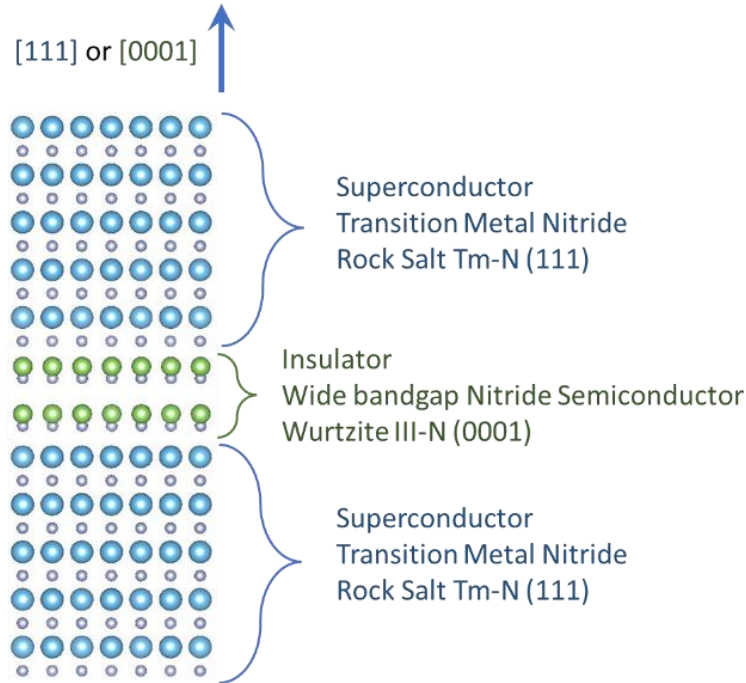


Figure 14: Atomic arrangement of a rock salt (111) orientated superconductor in blue on each side of an in-plane lattice matched nitride insulating barrier in green. Large circles represent nitrogen in the system, while smaller circles represent the metal atoms. Adapted from reference 55.

The in-plane crystal structure at the interface can have some strain between the two layers, but must be low enough, typically less than 1 %, to prevent defects from forming. To accomplish this, the crystal structure of the superconductor and the barrier must have near identical in-plane atomic arrangements at the interface. For example, Figure 14 shows a face centered cubic TmN (111) oriented superconductor with a hexagonal barrier layer. The in-plane atomic arrangement in this scenario is similar with a relationship $((11\bar{2}0)_{Al_2O_3} || (110)_{TiN})$, with only a difference in the vertical stacking order. Since most used junction materials will not lattice match perfectly to the superconducting layers, engineering of the interface is required to form coherent bonding. This engineering can consist of strain engineering to force the bonding to

match by straining the film a few percent, or by forming an alloy of two different material, with the intention to create a specific lattice constant which may match that of the surrounding layers. This can take the form of an alloyed barrier layer matching the surrounding superconductor, or an alloyed superconducting material matched to the barrier. [57]

When engineering the lattice constant through composition, the two binary constituents of the alloy generally must grow in the same crystal structure, with similar dominant orientations to each other. This ensures a stable alloy with predictable properties which can be modeled as a linear or near-linear fit between binary compounds. Much research has been done into the alloying of III-V materials following Vegard's law. [58], [59] Typically, these materials do not follow a perfectly linear trend, and possess some bowing parameter which changes the specific alloy composition needed to achieve a desired lattice constant. For example, in Figure 15, several alloys are shown using dashed lines between rock salt structured transition metal nitrides. [56] Intersection of the alloy lines with the in-plane lattice spacing of AlN represents an alloy of a particular composition which could in theory be used to form a coherent interface in a JJ.

The transition metal nitrides are of significant interest in modern superconducting qubit systems mainly due to the fabrication of low-loss resonators. Much of this research has focused on niobium nitride and titanium nitride compounds, as well as some success using tantalum nitride. [21], [60]–[62] Earlier examples continue to use oxidized aluminum or similar grown oxides as the barrier due to the ease of fabrication. This material system does not create the epitaxial nature desired in order to reduce defects, so aluminum nitride has been chosen as the material of choice. [45], [51]

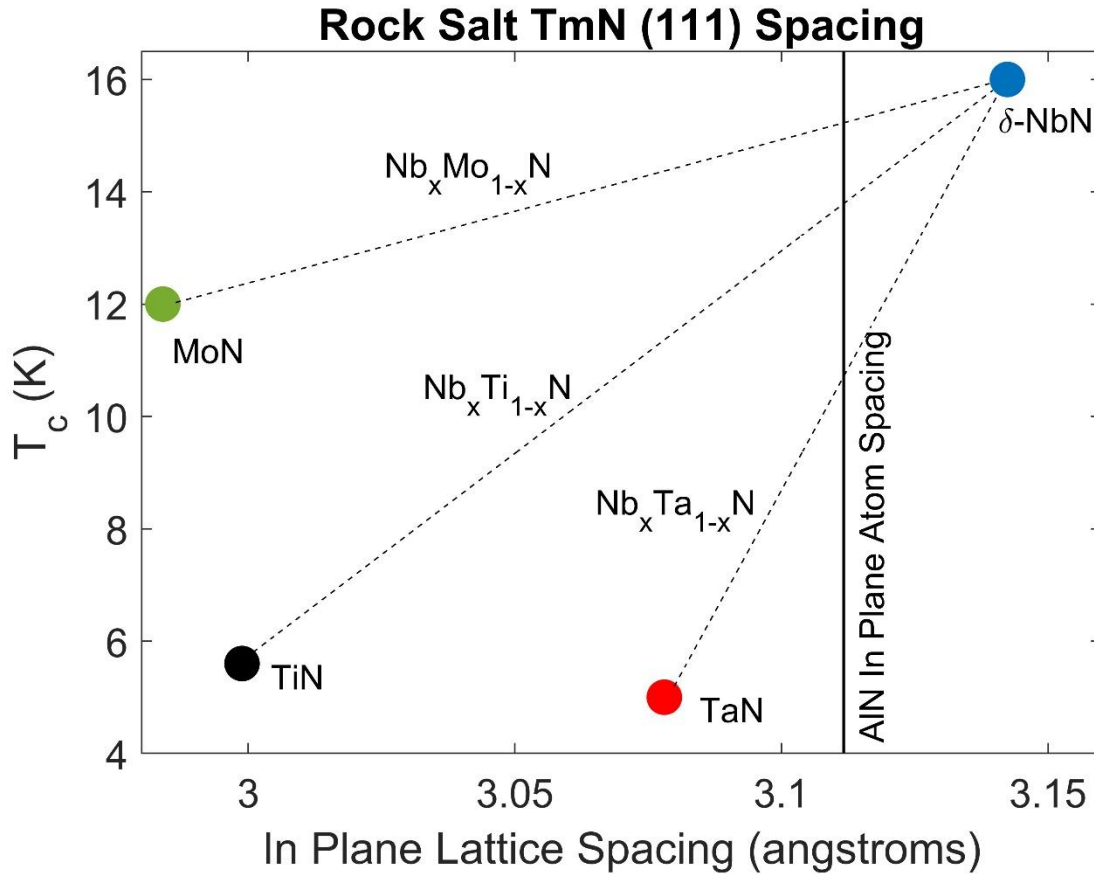


Figure 15: Alloying transition metal nitrides with NbN in the rock salt phase may allow for engineering of the atomic arrangement to match that of AlN in the Wurtzite phase. Adapted from reference 55.

The transition metal nitrides and their alloys in Figure 15 form a rock-salt cubic structure, which when orientated in the [111] direction forms an in-plane atomic arrangement identical to wurtzite aluminum nitride (0001) at the interface. While the spacing between atoms is not perfect, some alloying of these binary nitrides indicated by the dotted lines can theoretically form a lattice constant matching that of aluminum nitride.

These epitaxial Josephson junctions are thought to possess much less loss due to fewer TLS at the interface, as well as much improved oxidation resistance. [51] By using crystalline aluminum oxide instead of amorphous AlO_x , Oh et al. showed the density of TLS defects could be reduced by 80 %. [24] By transitioning to a material system where all layered elements are

grown in a clean environment, using crystalline materials, and with coherent interfaces, material losses may be greatly reduced. Additionally, the use of an epitaxially grown crystalline barrier improves the thickness uniformity of the layer, improving the uniformity of the critical current. This may allow for more repeatable fabrication of JJs with a predictable critical current.

The use of nitride materials may allow for reduced aging of materials, as oxide layers have been shown to change properties over time, and can be dependent on the vacuum conditions during growth. [63] Increased stability of the crystalline nitride may reduce diffusion into the superconducting layers, while growth in UHV conditions may reduce contaminants incorporated into the interface. Nitride material such as NbN also offer a higher critical temperature over aluminum-based devices, potentially increasing the operating temperature of the device.

1.5 Superconducting Circuit Materials

1.5.1 Substrate Selection

Substrate selection for growth of superconducting circuits depends on several factors, namely the loss tangent of the material, reactions between the substrate and the grown layers, and effect on the orientation of the grown film. Common substrates used for superconducting qubit fabrication include MgO, Al₂O₃, and Si.

While high quality transition metal nitride films have been shown to grown on MgO substrates [64], the loss tangent of MgO is high (2×10^{-5}) [65] when compared to sapphire (6.3×10^{-8}) [66] and high-resistivity Si (2×10^{-6}). [67] This limits the use of MgO as a viable substrate due to its high absorption of microwave energy. The orientation of the substrate also

plays a role in the orientation of the grown layer, with Si (001) producing TiN (001) films and Si (111) producing TiN (111) films. [68] This is important when uniform interfaces are desired for heterostructure growth since different orientations will possess different surface morphologies and roughness. In addition, for epitaxial growth with AlN, the rock salt (111) orientation is required, limiting usage of silicon substrates to the (111) orientation.

Unfortunately, Nb grown on silicon forms an inhomogeneous niobium silicide at temperatures greater than 400 °C, which hinders the crystal quality, limiting the thermal budget for any further growth or processing steps. [69] Due to the high loss tangent of MgO and the reaction between niobium and silicon, sapphire substrates were chosen for all samples grown in this work.

1.5.2 Superconducting Materials

In the pursuit of lower loss materials as well as materials with more advantageous electrical and structural characteristics, many material systems have been used for successful Josephson junctions.

The first and still most commonly used material is aluminum, which is attractive due to its ease of deposition and fabrication of devices. Aluminum grows in a face centered cubic structure regardless of the substrate it is grown on, further enhancing its ease of use by device fabricators. There are downsides to using aluminum as a junction material however, namely its low mechanical stability, low critical temperature, high reactivity, and aggressive oxidation of the surface when exposed to atmosphere.

When working with aluminum thin films, extreme care must be taken so as to not deform or disturb the smooth aluminum surface. Aluminum thin films have a tendency to be extremely

soft when compared to other superconducting materials such as Nb. Aluminum also forms a native oxide after just a few hours in atmosphere. At room temperature and standard pressure, aluminum exposed to an oxygen rich environment will form an oxide layer ~ 4 nm thick. [70] While this is a reliable process, the amorphous nature of the oxide and lack of fine control over the continued growth of this oxide once exposed to atmosphere results in an aging qubit where the properties change over time. Lastly, aluminum has a relatively low critical temperature of approximately 1.2 K. This is detrimental to Josephson junction performance as quasiparticle density increases the closer a material is to the T_c . When compared to higher T_c material such as niobium or tantalum, this results in a four order of magnitude increase in quasiparticle density at 90 mK.

Alloys of lead were also used in the earlier days of Josephson junction fabrication. Pure lead has a critical temperature of 7.2 K but has low mechanical stability and possesses several oxidation states. These oxidation states can generate significant loss due to TLS in the material.

With a similar ease in fabrication to aluminum, the transition metal materials niobium and tantalum have emerged as successful superconducting materials for capacitive and inductive circuit elements that are paired with an Al/AlO_x/Al Josephson junction. [21] Both elements have been shown to grow in the body centered cubic structure and have relatively high critical temperatures of 9.3 K for Nb and 4.4 K for Ta. [71] All metals readily form a native oxide which can be lossy. In the case of niobium, several phases of oxide grow with preference for the Nb₂O₅, and Nb₄O₆ varieties [71], while tantalum typically only grows a single oxide, Ta₂O₅. [72] It is a common practice to take steps to passivate metal surfaces during fabrication to control the formation of oxides with decreased TLS loss. [21], [74]

1.5.3 Barrier Materials

Due to the lack of pinholes in native aluminum oxide, it is seen commonly in literature as a barrier layer material. [47], [75], [76] The downsides to using these oxides are mainly the loss associated with an amorphous compound, and the lack of uniformity in thickness.

Deposited oxides, such as crystalline Al_2O_3 and SiO_2 are also used, especially when trying to improve loss mechanisms in the junction. Contrary to native oxide growth, thickness control is typically very good with deposited oxides when grown using CVD or sputtering. MgO has been used with some success, and was attractive due to its relatively high gap voltage of 5.1 eV, making it an attractive material for higher frequency qubit systems. [60], [77] Early Josephson junction research into loss neglected to include contributions from the barrier layer. However, Yu et al. showed that loss contributions due to TLS in the barrier are a dominant decoherence mechanism, and less lossy oxides, or different material systems are needed. [78] Negation of the loss due to oxide must come from naturally less lossy materials, or by reducing the participation of the junction, resulting in conventional qubit designs with JJ areas below $1 \text{ } \mu\text{m}^2$, to reduce the number of TLS affecting the decoherence of the qubit in the barrier volume.

1.5.4 Superconducting Nitrides

Superconducting transition metal nitrides encompass many compounds, all generally highly crystalline, tough materials with enhanced critical temperatures when compared to their pure metal counterparts. Notably, compounds such as TiN , NbN , TaN , and VN fall into this category. Outside of quantum computation, these materials have been used extensively as hard-coating materials due to their hardness and chemical resistance. These materials are also

chemically stable, forming thin oxide layers, and are resistant to bulk impurities when grown with PAMBE. While several of these transition metal nitrides have multiple stable crystal structures, most only form, or dominantly form in the rock-salt cubic phase. This structure is a face centered cubic lattice with a two-atom basis, where the nitrogen atoms for another FCC lattice are distanced $\frac{1}{2}$ a lattice parameter from the metal atoms, as in Figure 16.

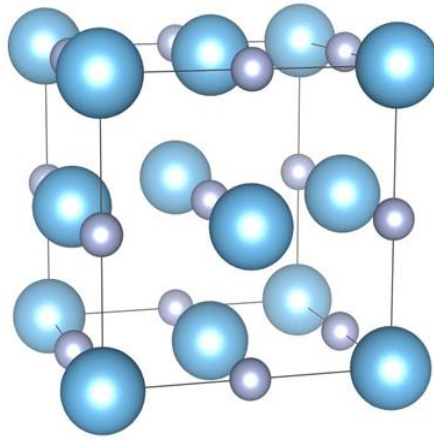


Figure 16: Diagram of a rock-salt unit cell. Silver orbs represent transition metal atoms, while the larger blue orbs are representative of nitrogen atoms.

Titanium nitride has been well studied in literature due to its use in hard coatings [79], superconductivity [80], and microelectromechanical devices (MEMS). [81], [82] TiN grows almost exclusively in a rock-salt structure, as seen in the large region of stability in the phase diagram in Figure 17. [83]

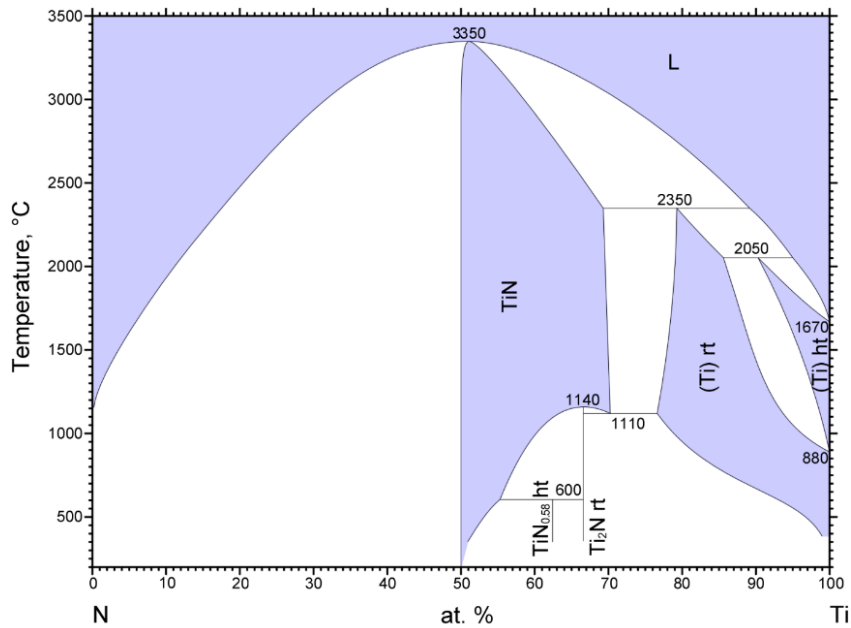


Figure 17: Phase diagram of TiN adapted from reference 82.

In Figure 17, TiN has a large central region labeled “TiN”, but the material of interest is the stoichiometric 1:1 Ti:N rock salt phase that occurs on the left side of this region. The rock salt phase is also stable across a wide range of temperatures, given the films are not grown in a titanium rich manner. Other undesirable phases are visible, notably the Ti₂N phase, a hexagonal, titanium rich phase, as well as phases of Ti where nitrogen isn’t incorporated in meaningful amounts. [84]

Niobium nitride has also been well studied, mainly due to its high superconducting critical temperature of near 17 K, though various research groups report T_c down to 4.5 K when grown under certain growth conditions. [85] This large variation in T_c is due to several factors, namely stoichiometry and phase. Transition metal nitride T_c can be altered by adjusting the stoichiometry in the film, while still remaining stable. [86] Niobium nitride possesses several

different stable crystal structures. In Figure 18, a phase diagram shows several different regions of NbN_x , which correspond to different crystal structures and compositions. [87]

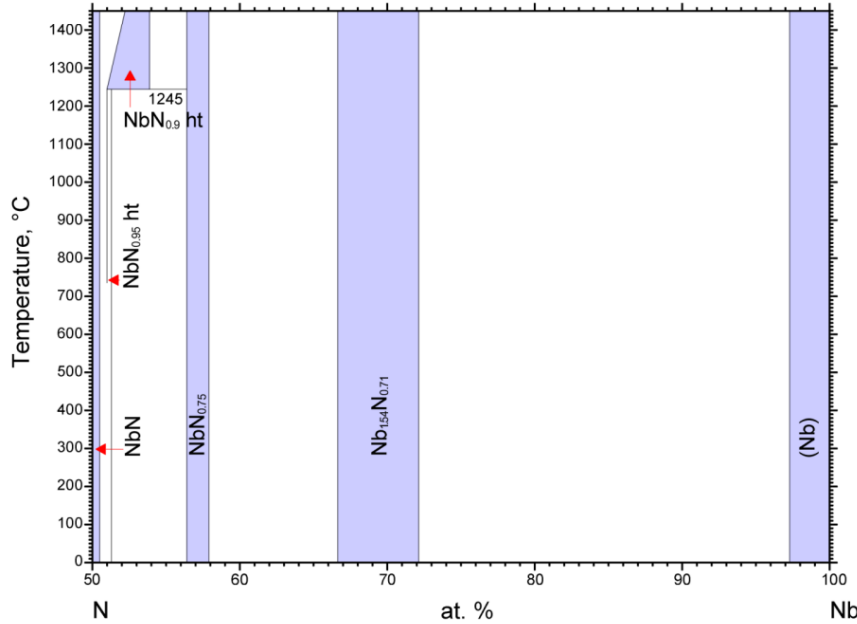


Figure 18: Phase diagram of NbN_x from reference 86.

Off to the left of the diagram is the δ -NbN phase, a rock-salt cubic structured material with a critical temperature of ~ 17 K, and a lattice constant of 4.444 \AA . This phase occurs near 50 % nitrogen content and has been shown to be stable with some reduction in the nitrogen content before encountering a more stable allotrope of NbN_x . In the diagram, $\text{NbN}_{0.75}$ refers to the tetragonal γ - Nb_4N_3 phase of NbN_x , which has a critical temperature of ~ 11 K. [88] This phase has a rock-salt like structure, which has the same metal sub-lattice as δ -NbN, but with ordered nitrogen vacancies. $\text{Nb}_{1.54}\text{N}_{0.71}$ refers to the hexagonal β - Nb_2N phase, which is less well studied than the rock-salt phase, but does have some use in JJ material growth when paired with an AlN barrier which experiences some strain from the superconducting layer. [89], [90] Not shown directly in the phase diagram is the ϵ -NbN phase, a hexagonal phase with recently discovered superconductivity properties. [91] Several other nitrogen rich phases are stable, but

are not well studied in the field. [92] In MBE growth, many of these phases are successfully grown, and due to the closeness of the growth conditions, can coexist together, forming complicated, multi-phase thin films.

Basic electrical, structural, and mechanical material parameters for the transition metal nitrides of interest in this thesis are collected in Table 1. [93], [94], [95], [96]

Table 1: Collected material parameters for the transition metal nitrides TiN and phases of NbN_x.

| | Space Group | Structure | Lattice Constants (Å) | T _c (K) | E (GPa) | v |
|--|---|--------------------|-----------------------------|--------------------|---------|-------|
| TiN | <i>Fm</i> $\bar{3}$ <i>m</i> # 225 | Cubic Rock-Salt | $a = 4.231$ | 5.3 | 287 | 0.35 |
| δ -NbN | <i>Fm</i> $\bar{3}$ <i>m</i> # 225 | Cubic Rock-Salt | $a = 4.444$ | 17.1 | 298 | 0.331 |
| γ -Nb ₄ N ₃ | <i>I4/mmm</i> # 139 | Tetragonal | $a = 4.231$ $c = 8.632$ | 11.5 | 354.2 | 0.289 |
| ϵ -NbN | <i>P6</i> ₃ / <i>mmc</i> #194 | Hexagonal | $a = 2.960$ $c = 11.250$ | 0.2 | 501.1 | 0.274 |

1.5.5 Wide-Bandgap Nitrides

Aluminum nitride is an attractive choice for a non-oxide Josephson junction barrier due to its high crystal quality, and chemically stable nature. [97] Aluminum nitride forms readily in the hexagonal wurtzite crystal structure, though there are reports that thin layers can cause the formation of cubic zinc blende structured AlN. [55] Wurtzite AlN has a lattice parameter of 3.112 Å with a c/a ratio of 1.60. The zinc blende structure has a calculated parameter of 4.421 Å using first-principles simulation, but few experimental results exist in literature. [98]

Regardless of the structure, AlN can work well as a lower loss barrier material. Hexagonal AlN possesses piezoelectricity, the ability of a material to physically deform when exposed to an electric field. [99] This property can be used in applications such as energy harvesting, MEMS development, or microwave filters for telecommunications, but may cause abnormal effects when introduced into a qubit system, potentially changing thickness and subsequently the critical current as the electric fields in the JJ interact with the barrier. [100] [101] This effect specifically on JJs has not been well studied.

1.6 Content Overview

In this thesis, a structure first approach is used to demonstrate improved materials for Josephson junction performance. Materials are grown using plasma assisted molecular beam epitaxy, then have the structural, interfacial, and electrical properties characterized. From the information gained from varying growth parameters such as substrate temperature, metal or nitrogen flux, and post-growth analysis of the thin film, optimization towards the ideal JJ material can be achieved. The knowledge from each analysis technique allows for refining of material growth parameters for further improvement of the material performance. This optimization process is performed in a deliberate manner, modifying a single growth parameter at a time to investigate changes due to that parameter, and how it may interact with other growth conditions.

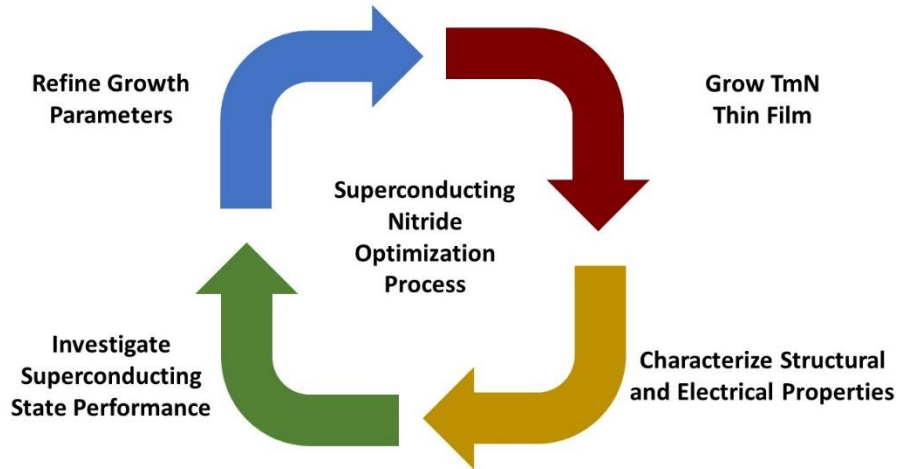


Figure 19: Optimization process flow for materials development.

In Chapter 2, the methods used for growth of transition metal nitride films, and analysis methods for electrical and structural properties will be discussed. Methodology will also be described for both Rutherford Backscatter Spectroscopy and Ansys resonator simulation, which serve to provide theoretical insight into material composition and resonator performance.

Chapter 3 will cover the investigation into TiN and NbN_x thin film growth on sapphire to give insight into the material property endpoints that should be expected from Nb_xTi_{1-x}N alloys, along with the effects of annealing these films. Chapter 4 will cover the growth of Nb_xTi_{1-x}N thin films, with description of the crystal structure changes seen through the composition range, as well as the impact of composition on resonator performance and kinetic inductance. Chapter 5 will describe results for annealing Nb_xTi_{1-x}N samples, which provides significant surface roughness and structural quality improvement. In addition, the effects of annealing on the nitrogen content of Nb_xTi_{1-x}N will be discussed, as well as the implications for the material characteristic improvements due to this change.

Chapter 2: Methods

2.1 MBE Growth

Crystal growth by molecular beam epitaxy (MBE) is regarded as one of the foremost methods for explorative thin film growth with excellent material purity and control over sample composition. MBE allows for material growth with very low defect densities, complicated heterostructures with abrupt interfaces or graded compositions, and low contaminant concentrations due to the ultra-high vacuum (UHV) conditions. These advantages come at a cost, in that MBE requires specialized hardware and expert professionals to operate the system. Researchers performing MBE must maintain strict cleanliness protocols to keep the chamber as contaminant-free as possible. In this thesis, $\text{Nb}_x\text{Ti}_{1-x}\text{N}$ samples are grown using plasma-assisted MBE (PAMBE) because low-loss materials with low defect density and contaminant levels are critical for superconducting quantum computing devices requiring high coherence times and qubit lifetimes. Using PAMBE also allows for the in-situ growth of AlN, the barrier layer used for all-nitride Josephson junctions without the complications and material challenges associated with removal from the chamber and need for a second deposition tool.

2.1.1 UHV, Mean Free Path, and Purity

Molecular beam epitaxy is recognized in the crystal growth community largely by its operation within UHV conditions. Growth in UHV is attractive due to the large mean free path of particles, enabling extremely low interaction rates between desired atomic species and contaminants. This has the effect of allowing for highly directed beams of atomic flux to be

directed at a substrate, as well as ensuring ultra-high material purity, since sources are typically 5N+ purity elemental sources instead of precursor gases used in chemical vapor deposition (CVD) or sintered pucks in the case of alloy growth using sputtering.

UHV is defined by pressure lower than 7.5×10^{-9} Torr and requires significant effort to attain and maintain. [102], [103] Instead of sealing with Viton O-rings as in most vacuum systems, UHV systems rely on deformed copper gaskets with tight-tolerance stainless steel flanges to contain UHV pressures. While the types of dry vacuum pumps used are similar to those used in high vacuum systems, in order to improve pressure from the high vacuum range (7.5×10^{-4} to 7.5×10^{-9} Torr), lengthy baking of the growth chamber must be performed to increase the outgassing rate of contaminants introduced when the chamber was exposed to air or contaminant species native to material used within the chamber such as stainless steel. The primary contaminant removed during bake-out is water, which physisorbs onto all exposed surfaces.

During baking of the chamber used in this thesis, the entire apparatus is shrouded in thermally insulating blankets, with a heater that reaches an air temperature of 150 °C and a temperature of over 100 °C for the steel chamber. This temperature is maintained for around a week until the pressure inside the chamber stabilizes. Figure 20 shows a progress diagram for one such bake-out.

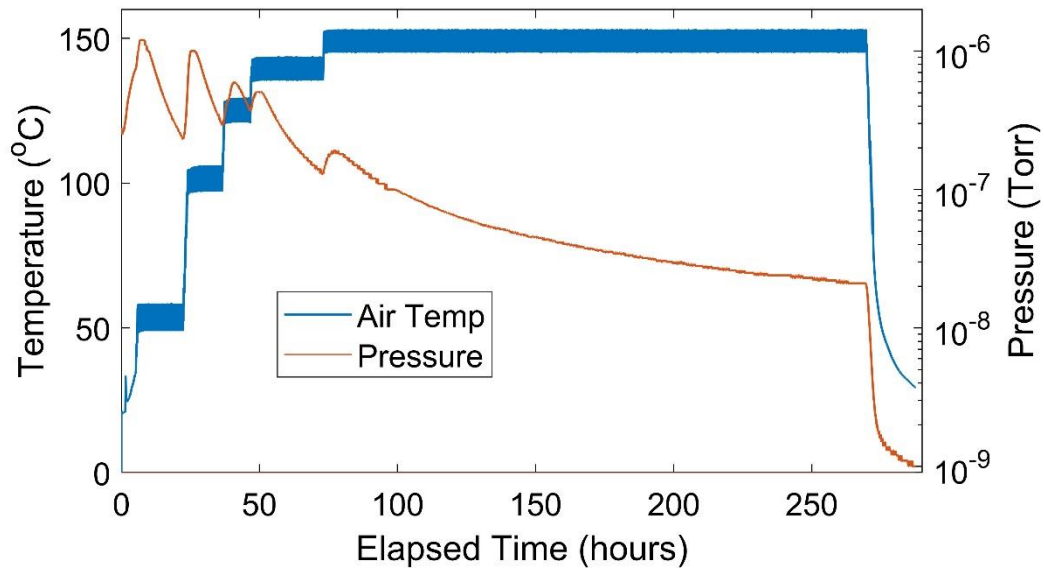


Figure 20: Growth chamber pressure and air temperature during bake out of the MBE chamber used in this work.

Maintaining UHV conditions with a properly baked chamber still requires high performance vacuum pumps, which in most UHV systems is maintained by a combination of cryogenic pumps and sputter ion pumps. The nitride chamber in this thesis is evacuated using three pumps. The first is a Pfeiffer High-Pace 1200 turbo pump, which works well on the large amount of nitrogen injected into the chamber during nitride growth. A large momentum transfer pump such as the Pfeiffer enables very fast initial pump down times, which can be helpful after venting a chamber for maintenance. Additionally, a Brooks Cryo-Torr cryopump is brought online once the chamber pressure is less than 1×10^{-4} Torr and freezes contaminants onto a set of vanes cooled using compressed helium. This pump is particularly effective at removing water from the system, which is a large component of contamination introduced during venting of the chamber. Lastly, a Gamma Vacuum ion pump is used to maintain UHV pressures and is only used once the pressure is well into the high vacuum range. Entrapment style pumps such as the ion pump excel in trapping gases such as N_2 and O_2 due to the reactive titanium cathode used in the pumping process.

The mean free path,

$$\lambda = \frac{RT}{\sqrt{2}\pi d^2 N_A P}, \quad (27)$$

of particles in UHV is derived from an assumption that an atom or molecule with diameter d follows a straight path approximated by a cylinder and can be determined from kinetic theory. Here, R is the universal gas constant, N_A is Avogadro's number, d is the diameter of the particle cross section, with the environmental variables temperature, T , and pressure, P . For example, at UHV conditions where $P = 1 \times 10^{-10}$ Torr, nitrogen molecules have a mean free path of approximately 110 km, which is much greater than the distance from the source to the substrate. For comparison, in normal atmospheric conditions where $P = 760$ Torr, the mean free path of nitrogen molecules is 100 nm. To estimate the rate of interaction of two particles, the average velocity of particles in the chamber is described by

$$\langle v \rangle = \sqrt{\frac{8kT}{\pi m}}, \quad (28)$$

where k is Boltzmann's constant, T is temperature of the particle, and m is the mass of the particle. The collision rate can be determined using

$$\tau = \frac{\lambda}{\langle v \rangle}. \quad (29)$$

For a room temperature nitrogen molecule in UHV, with an average velocity of 470 m/s and a mean free path of 110 km, the collision rate is approximately 15 collisions per hour.

Three types of flow can be defined for a vacuum system: viscous, molecular, and Knudsen, and are differentiated with the dimensionless Knudsen number, K_n , described by

$$K_n = \frac{\lambda}{D}, \quad (30)$$

where D is the diameter of the chamber. In the viscous regime flow, K_n is less than 0.01. In this case, the flow can be directed, and its speed is greatly influenced by chamber geometry and pumping speed. Molecular flow is only seen in high vacuum and UHV environments, where the mean free path is such that interaction between particles in the confines of the chamber is improbable and K_n is greater than 0.5. No ordered flow is possible, and particles generally move in straight lines until impacting the chamber wall or a piece of hardware. The intermediate region, or Knudsen regime, is where particle movement is influenced by both wall collisions and intermolecular interaction and is defined as having K_n between 0.01 and 0.5. A simplified diagram showing different flow regimes is shown in Figure 21. [103]

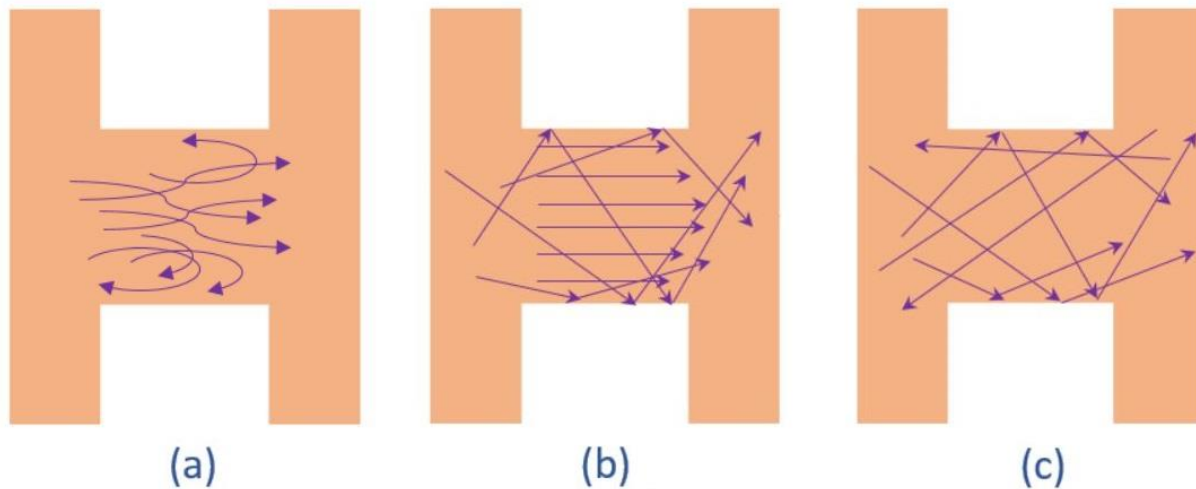


Figure 21: a) Viscous, b) Intermediate, c) Molecular flow regimes. Adapted from reference 102.

2.1.2 Sapphire Substrates for Nitride Growth

PAMBE growth on sapphire begins with rigorous cleaning of the bare wafers to remove grease and contaminants from the manufacturing process. 2” single crystal sapphire wafers from Kyocera are used as substrates for transition metal nitride growth. These wafers are C-plane orientated sapphire which have been polished on one side, providing a rough underside for ease of wafer handling. The hexagonal unit cell substrate has lattice parameters of $a = 4.763 \text{ \AA}$ and $c = 13.003 \text{ \AA}$, with a bulk dielectric loss tangent of 6.3×10^{-8} . [66] Sapphire is chosen for growth of these materials due the low loss of these substrates during measurement of RF devices, as well as its relative cost effectiveness when compared to materials such as SiC. Conveniently, sapphire is much tougher than commonly used substrates such as silicon, making handling and fabrication with these wafers less prone to breakage.

Cleaning of the wafers begins with sequential baths of trichloroethylene, acetone, methanol, isopropyl alcohol (IPA), and finally deionized water. The wafer is soaked in each bath for one minute. In between soaks, the wafer is sprayed with the previously used bath chemical from a clean squirt bottle. This removes any remaining contaminants adhered to the wafer from the removal of the wafer through the top surface of the fluid. After the final deionized water rinse, the wafer is rinsed with IPA and blown dry with filtered nitrogen.

After cleaning, the wafers are loaded into a load lock using molybdenum and silicon carriers which have been cleaned with a 3:1 HCL:HNO₃ acid etchant before their first use for one minute on each side, then ultrasonicated in deionized water for five minutes before being dried with filtered nitrogen. The load lock is pumped down to the 1×10^{-7} Torr range, then the chamber is ramped to 200 °C. The load lock is baked for four hours, then allowed to cool. The bake out in the load lock removes any residue from the wafer cleaning procedure and any

moisture from the atmosphere while waiting for the load lock pressure to stabilize. Once room temperature has been reached, the pressure inside the load lock is in the 1×10^{-9} Torr range, and the wafers are transferred into the growth chamber. Prior to each growth, the wafers are ramped to 800 °C, held for 15 minutes, then ramped to 1000 °C. Once reaching 1000 °C, the wafer is cooled back down to 800 °C and the growth commences. All ramps are performed at 20 °C/min. The baking of the wafers once in the growth chamber further removes any contaminants on the wafer before the growth begins.

2.1.3 Growth and Annealing Process for NbTiN Thin Films

After wafer preparation and cleaning, the sapphire substrates are loaded into the growth chamber and $\text{Nb}_x\text{Ti}_{1-x}\text{N}$ thin films are deposited on the substrate. After growth, the nitrogen plasma overpressure is maintained at 500 W at a flow of 1.8 sccm while the substrate temperature (T_A) is changed to the annealing temperature. The sample is held at this temperature for a time t_A until the substrate temperature is ramped down, nitrogen plasma generation is stopped, and nitrogen is evacuated from the chamber. Anneal temperatures vary between 650 °C and 1150 °C, with all samples being grown at 1000 °C. Anneal duration was investigated at 30-minutes, 2-hours, and 4-hours. Figure 22 shows the growth scheme for the annealed samples.

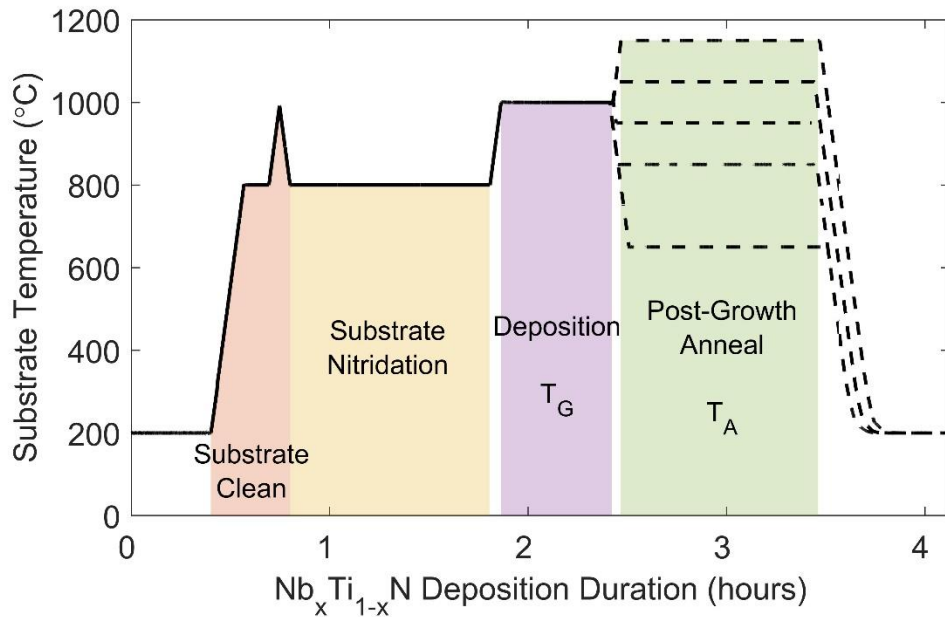


Figure 22: Growth process for an annealed NbTiN sample. The various anneal temperatures are represented by the dashed lines in the green anneal section.

All the samples for the annealed Nb_xTi_{1-x}N series start with a wafer cleaning process involving a thermal desorb to 800 °C with a spike to 1000 °C before returning to 800 °C for the two-hour substrate nitridation. Deposition occurs in the purple highlighted region in Figure 22, in which the substrate is held at 1000 °C. After deposition is completed, the substrate temperature is adjusted to the anneal temperature indicated by the dashed lines. The sample is held under nitrogen plasma overpressure for the duration of the anneal. Post-anneal, the nitrogen plasma is shut off and the sample is cooled down to 200 °C.

For samples without a post-growth anneal, the green annealing area in Figure 22 is omitted, and the sample is cooled down from T_G at a rate of 20 °C/min immediately after deposition.

2.1.4 Plasma Cells

Nitrogen is incorporated into the grown thin films using a radio frequency (rf) plasma source. Plasma sources ionize the nitrogen gas to excite and break apart gas molecules, thus generating a plume of ionized molecular and atomic nitrogen. It has been shown that higher a dissociated fraction in the plasma is beneficial in both lowering defect density and increasing growth rates. [104], [105] The relative amount of molecular nitrogen to various ionized species is affected by several engineering design parameters, including aperture size, gas flow rate, and RF power applied to the cell.

Aperture size and gas flow largely determine the pressure in the active plasma producing region of the cell, which needs to be raised to such a point that the mean free path in the cell is decreased enough to cause a high rate of collisions. RF power scales linearly with the number of collision events, and typically is maximized within the constraints of the hardware to encourage a higher atomic:ionic species ratio. Figure 23 shows an optical spectrum taken of the nitrogen plasma cell used in PAMBE at LPS to produce nitride material. A triplet of peaks is seen corresponding to various ionized molecular species along with a single sharp peak from the atomic nitrogen split from N_2 .

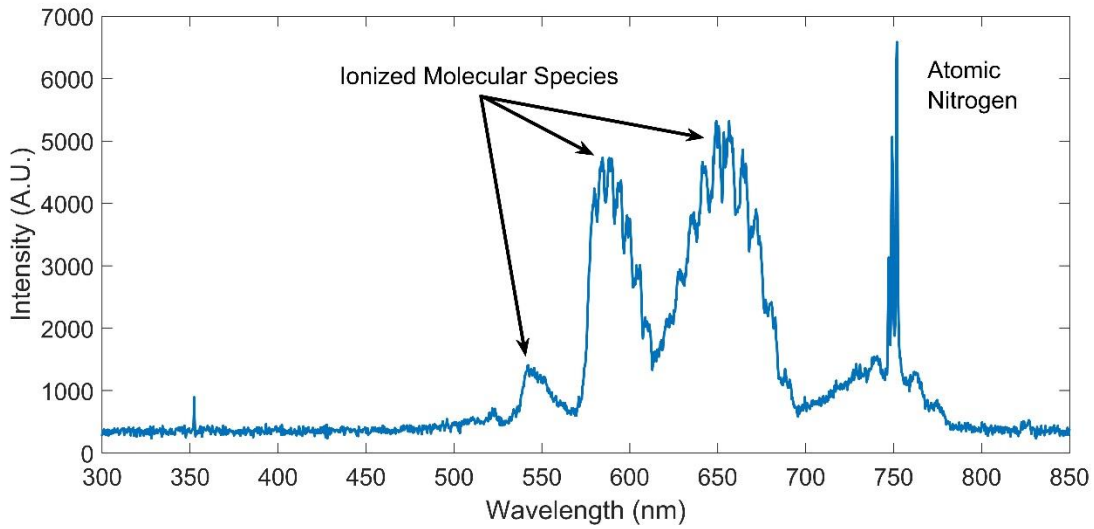


Figure 23: Nitrogen plasma optical spectra from a Veeco Uni-Bulb RF nitrogen plasma source used at LPS to produce nitride material.

2.1.5 Effusion Sources

The most commonly used source in MBE growth is the effusion cell, or thermal evaporation cell. Effusion cells provide reliable, repeatable elemental flux in a beam facing the deposition target. Inside an effusion cell is a crucible made of a high melting point, chemically inert material. Source material with high purity is placed inside the crucible, where a wound filament heats the crucible, shown in Figure 24. The crucible is heated to the point where the vapor pressure of the source material increases until the desired elemental flux is emitted from the cell. [106], [107]

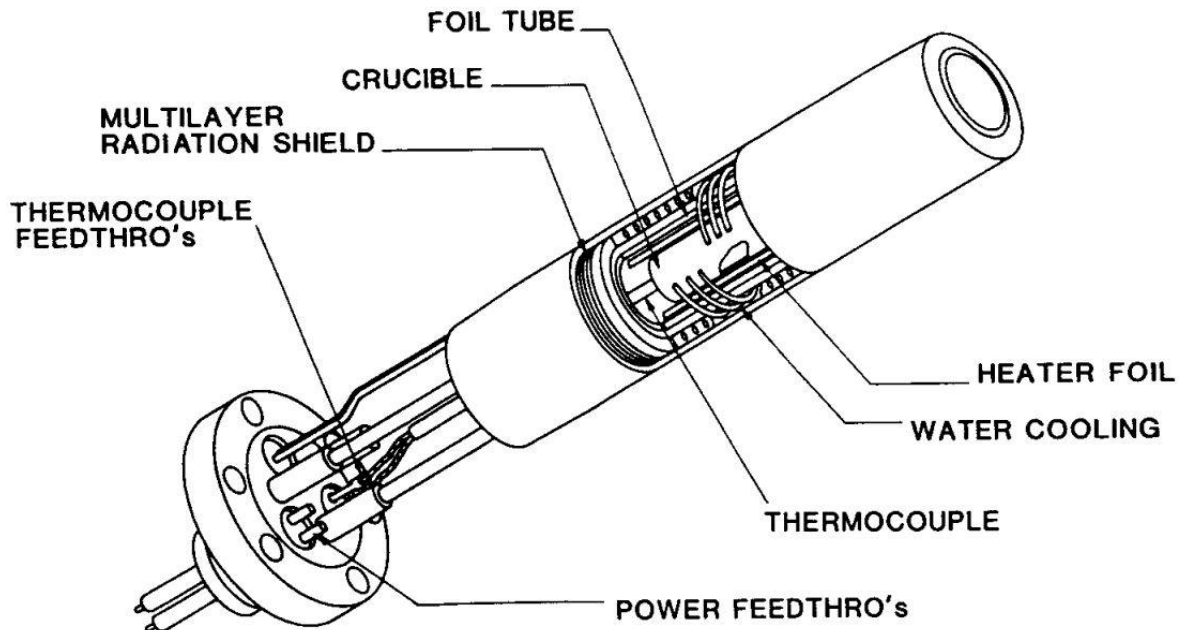


Figure 24: Diagram of an effusion cell. Adapted from reference 106.

This flux is commonly measured using beam equivalent pressure (BEP). BEP is a measure of the local pressure, typically directly in front of the substrate, created by a particular elemental flux. This is used as a calibration for flux or growth rate, as BEP is directly proportional to elemental flux, and is described as

$$J = 4.62 \times 10^{22} \frac{pr^2}{L^2(MT)^{0.5}} \quad (31)$$

The flux density, J , is a function of the vapor pressure of the cell material, p , the effusion aperture radius, r , the distance from the source, L , the cell temperature, T , and the molecular weight of the source material, M . The prefactor $4.62 \times 10^{22} \frac{s\sqrt{T}}{cm\sqrt{kg}}$ gives J the units of $\frac{\text{molecules}}{\text{cm}^2\text{s}}$.

BEP during MBE is generally taken before each growth to ensure accurate flux control, since the elemental flux can drift over time due to shifting of the source material within the crucible or depletion of source material.

A shutter over the cell opening acts as a switch for flux control, covering the source to stop the elemental flux while keeping the source hot for future use. In this fashion, deliberate and precise control of layer thicknesses and heterostructure growth can be performed. The shutter can be actuated in a fraction of a second, providing quick flux control for abrupt material transitions during growth. With the DCA system used at LPS, the entire shutter system is coordinated by computer-controlled recipes, which can be more precise than older manually operated growth systems.

2.1.6 Electron Beam Evaporation Sources

MBE is largely used to grow III-V materials, which function well with effusion cells operating under 1300 °C. For higher melting point material, such as transition metal nitride growth, electron beam evaporators are required to generate appreciable elemental flux. Electron beam evaporators use several thousand volts to accelerate electrons that are emitted from a tungsten or tantalum filament. The beam of electrons is arced using permanent magnets and adjustable electromagnets onto a pocket containing source material, as shown in Figure 25.

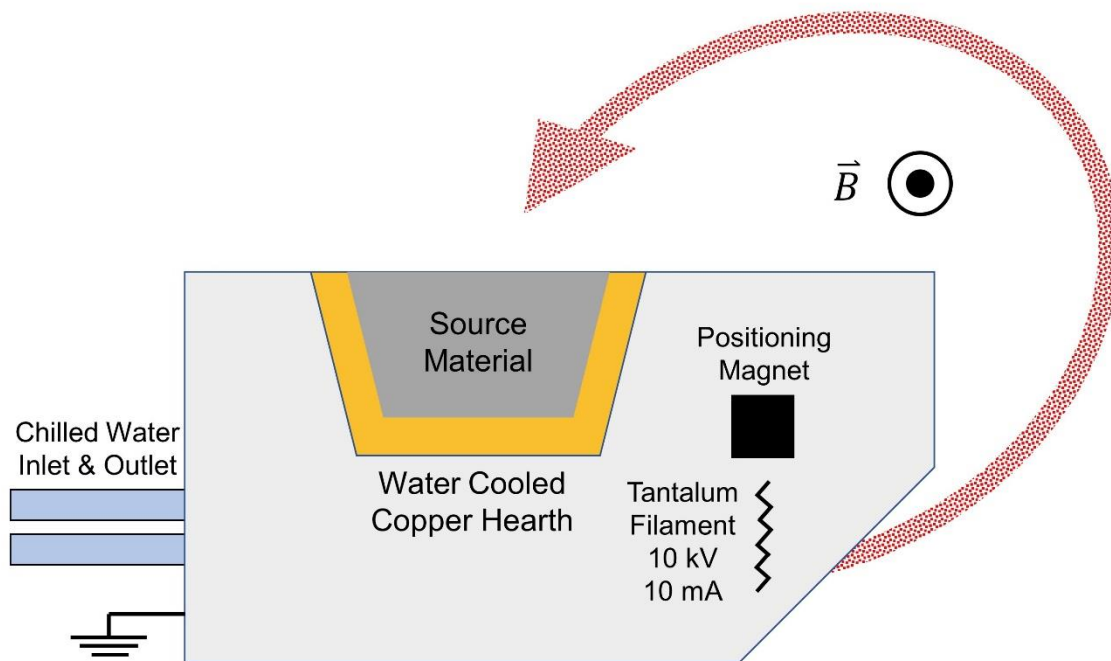


Figure 25: Cross-sectional side view diagram of an electron beam evaporator. The beam of electrons from the filament to the source material is represented by the red arrow.

This pocket is in a hearth made of water-cooled copper that dissipates heat from the system, while keeping the source material hot. This electron beam can heat materials to over 3000 °C, which is sufficient to evaporate nearly any material including tantalum or niobium. This beam is rastered across the source material to melt or sublimate the charge evenly. To prepare for a growth, the Nb source is ramped to a power about 50 % higher than the needed growth power to observe a melt pool on the source material, with the shutter over the source closed, then cooled down to the operating power.

Determination of material flux and calibration of the source is performed using Electron Impact Emission Spectroscopy (EIES). Electrons emitted from the EIES filament interact with evaporated atoms from the source material, which excites valence electrons in the atoms passing through the sensor. The excited electrons lose their energy and emit a characteristic wavelength photon as a result. This photon is collected using a photomultiplier tube after being passed

through an optical filter corresponding to the wavelength expected from the material being evaporated. The intensity of this signal is indicative of the density of atoms passing through the sensor, and functions similarly to the BEP measurement previously mentioned when calibrating sources. A second sensor out of sight of the source is used to measure the background signal, and is subtracted from the primary sensor signal, allowing for accurate flux measurement with a high nitrogen background during a nitride growth.

2.2 Growth Mechanics

During MBE growth, the ideal path of an atom starts in the effusion cell or electron beam evaporator. Once evaporated from the source material, atoms adsorb onto the substrate, and migrate across the surface until a low energy site is found. The likelihood that these atoms either stick to the substrate surface or desorb is known as the sticking coefficient, $0 < \sigma < 1$. As atoms arrive on the surface, they will undergo surface diffusion at a rate that is determined from a combination of factors, including temperature of the growth surface, local surface energy, and topographic features. Some of these factors also affect the physisorption and chemisorption rates as well as the desorption rate. MBE crystal growth is a kinetic process and can be categorized into three different growth modes: 2D layer-by-layer growth, or Frank-Van der Merwe mode; 3D mounded growth, or Volmer Weber growth mode; and the hybrid Stranski-Krastanov growth mode. [108]

The Frank-Van der Merwe mode consists of smooth layers of deposited atoms and nucleated atomic clusters for each layer growing laterally instead of upwards. This creates a

situation where atoms on the surface stick well and preferentially settle into low energy sites on the surface, forming a complete layer before a second layer forms.

In contrast, Volmer Weber growth forms islands of atoms that minimize contact area with the surface to reduce the total energy of the nucleated cluster. Once adatoms have been adsorbed, migrated across the surface, and nucleated into islands, these islands coalesce into larger and larger areas until complete coverage is achieved. Volmer Weber growth mode typically results in rougher surfaces with a distinct texture.

Stranski-Krastanov growth mode is a mix of the previous two, where an initial smooth 2D film changes into 3D islands after a certain thickness is grown. This transition is frequently observed during the growth of strained thin film growth. It occurs when the film can reorganize from a smooth, strained film to a rough, partially relaxed film that increases the surface area (energy) and decreases the strain energy in order to achieve a lower energy state. Figure 26 shows a simplified sketch of the different growth mode types.

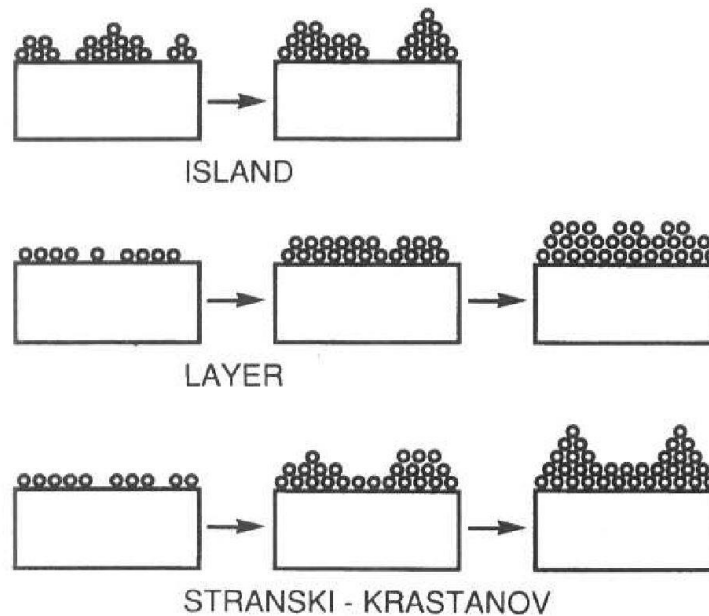


Figure 26: Diagram of 2D, 3D, and mixed growth modes. Reproduced from reference 107.

2.3 X-Ray Characterization

2.3.1 Symmetrical X-Ray Diffraction

X-ray diffraction (XRD) data is collected using either a Panalytical MRD Pro or Empyrean diffractometer. Both systems use a copper K_{α} x-ray source. The incident beam optics for both systems is a hybrid, 2-bounce Ge monochromator and mirror assembly. A proportional detector and $1/4^{\circ}$ slit are used for the diffraction optics for ω - 2θ scans, while a PIXcel imaging detector is used for all space maps.

Diffraction of the incident x-rays occur when atomic planes within a crystal cause incident x-ray to diffract, forming a pattern of constructive interference at specific angles of incidence corresponding to the spacing between crystal planes. [109] In the symmetric case, the incident beam and diffracted beam are measured at equal angles from the sample surface normal, shown in Figure 27.

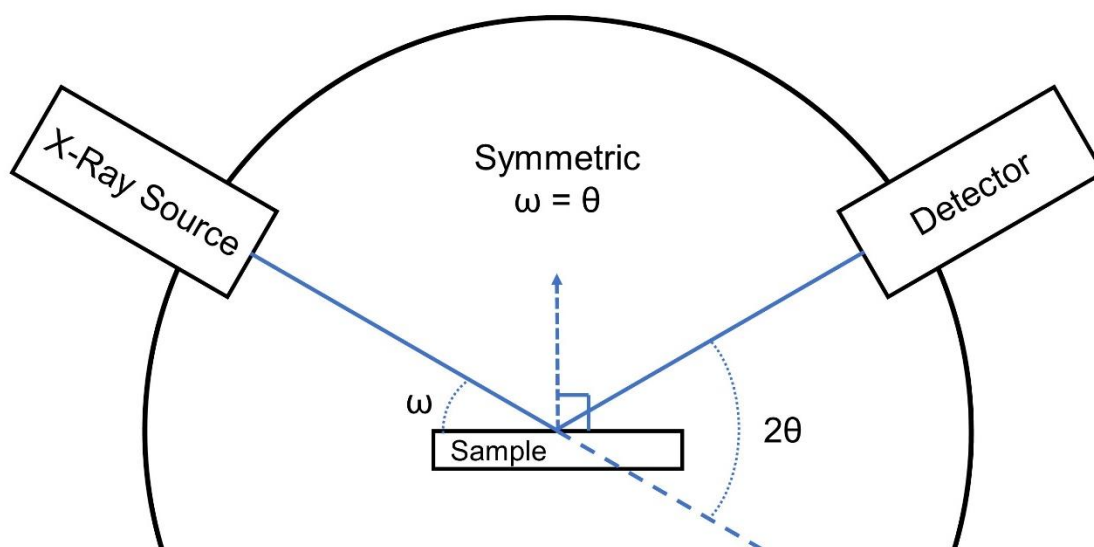


Figure 27: Symmetric XRD ω - 2θ setup.

These peaks of constructive interference occur at angles corresponding to Bragg's Law as

$$n\lambda = 2d\sin(\theta), \quad (32)$$

where λ is the wavelength of the incident photons, d is the spacing between the atomic planes in the crystal, and θ is the angle of incidence from the sample surface. [109]

XRD is a non-destructive technique that allows for identification of crystalline phase, orientations of those phases, and the structural properties of the material such as lattice strain, composition, and thickness. Peaks found using a properly calibrated XRD tool can be compared to standard values for known materials, with deviations from the norm providing information into strain of the material as well as subtle differences in atomic arrangement.

XRD Measurements can be calibrated using the substrate that a thin film is grown on, since the bulk substrate crystal is known and is not affected by strain or inhomogeneities. Figure 28 shows a PAMBE grown sample of a $\text{Nb}_{0.84}\text{Ti}_{0.16}\text{N}$ alloy with a thickness of 100 nm on a c-plane sapphire substrate.

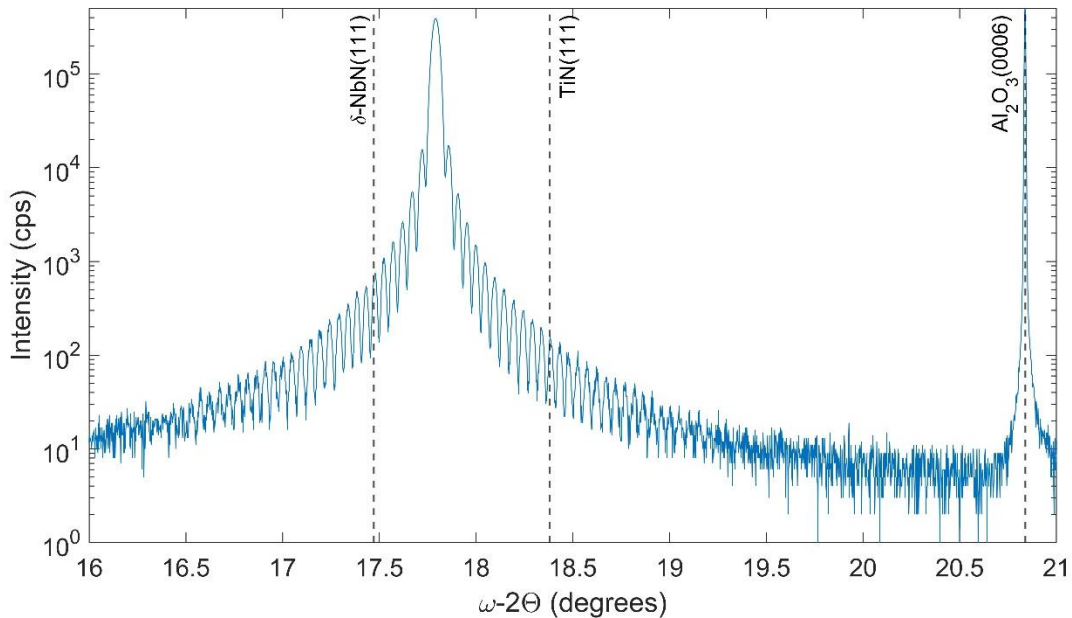


Figure 28: Symmetric XRD measurement of a 100-nm thick $\text{Nb}_{0.84}\text{Ti}_{0.16}\text{N}$ alloy with extensive thickness fringes indicating good crystal quality.

With symmetric XRD, the preferred orientation of the film with respect to the surface normal is inferred from the atomic plane spacing d in Equation 32. For this material, the [111] crystal direction is the growth direction when c-plane Al_2O_3 is used as a substrate. The 430- μm -thick substrate produces a sharp, strong peak which is used as a reference for the rest of the measurement. The alloy film produces a peak in between the reference lines for the binary constituents of the alloy. The film peak is broader than that of the substrate because of the size of the crystal that is diffracting the x-rays. For single crystal thin films, the broadening increases with decreasing film thickness. [109]

The fringes observed on either side of the main film peak are thickness fringes, also called Pendellösung fringes or Laue fringes. [110] These fringes are indicative of the number of complete, finite unit cells within the film, and occur when the area being measured contains a large density of these identical cells throughout the measured volume. Generally, the presence of these features represents a single crystal film with good uniformity, good homogeneity, with smooth surfaces and interfaces. In addition, the thickness of the film can be estimated from the frequency of these fringes and is an accurate measure of the thickness specifically from the ordered crystal in the film.

2.3.2 Reciprocal Space Mapping

The reciprocal space is a recording of diffracted x-rays at across a range of incident and diffracted beam angles. This allows for measurement of atomic planes that are not parallel to the surface normal, allowing for measurement of in-plane and out-of-plane lattice constants. The advantage of using this method for diffraction is that features of atomic planes not parallel to the

surface normal can be measured, as well as information regarding mosaic spread and strain of the sample.

The relationship between omega and theta during measurement can be converted into reciprocal lattice units, Q_x and Q_z calculated using

$$Q_x = \frac{2\pi}{\lambda} [\cos(\omega) \cos(2\theta - \omega)] \quad (33)$$

and

$$Q_z = \frac{2\pi}{\lambda} [\sin(\omega) \sin(2\theta - \omega)]. \quad (34)$$

where λ is the wavelength of x-rays, θ is the angle of the diffracted beam, and ω is the angle of the incident beam. From these relations, in-plane dimensions of the crystal lattice can be examined with changes in Q_x , while out of plane dimensions can be determined using Q_z .

While peak location is used to determine the in-plane and out-of-plane lattice constant, broadening of the peaks can result from biaxial strain, variation in the lattice constant in the film, and artifacts from the instrument. Figure 29 shows an asymmetric RSM of the TiN (113) and Al_2O_3 ($11\bar{2}9$) peaks of an annealed 100-nm-thick TiN film grown on sapphire sample that is discussed in Chapter 3.

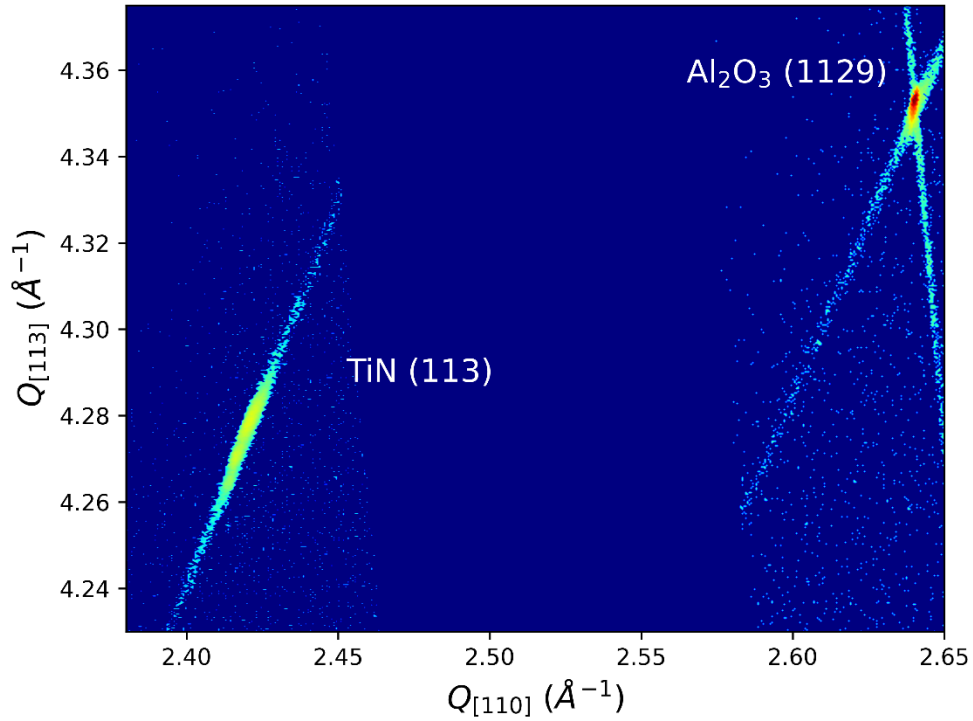


Figure 29: RSM of a 100-nm thick TiN film grown on sapphire at LPS.

The TiN reference point indicates the expected peak for a relaxed TiN film. Drawing a line from the reference peaks to the origin shows the peak broadening that may be due to changes in lattice constant through the thin film.

Several artifacts can be seen around the substrate peak, where the vertical intensity line is due to the Panalytical PIXcel detector, and the more horizontal line is due to the monochromator on the incident beam side of the measurement apparatus. More information on the applications of RSMs can be found in *Reciprocal Space Mapping* by Paul F. Fewster. [111]

2.3.3 Pole Figures

Pole figures are a measurement technique mainly used to investigate crystal texture, or the rotation of grains within a sample. The x-ray diffractometer is positioned around an off-normal crystal plane. Sample rotation, ϕ , and tilt, χ , are varied so that high intensity peaks form from the crystal plane when Bragg's Law is satisfied. The sample rotation angle is rotated 360° for each sample tilt angle, where a map is produced showing rotations of the crystal plane. Figure 30 shows the pole figure from a 100-nm-thick TiN sample around the TiN (113) plane, where $25^\circ \leq \chi \leq 35^\circ$.

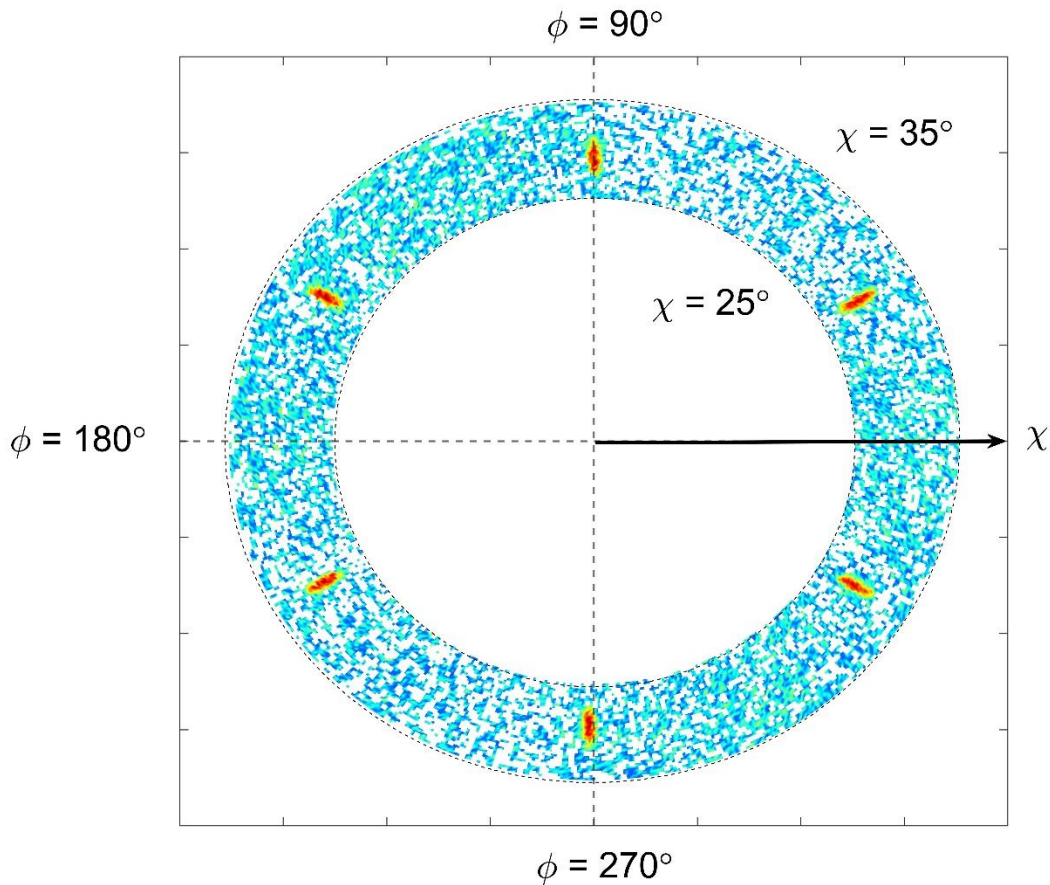


Figure 30: Pole figure of a 100-nm thick TiN sample rotated about the (113) plane. χ ranges from 25° to 35° , while ϕ ranges from 0° to 360° .

Ideally, a cubic crystal such as this TiN sample would only possess three peaks in the pole figure, corresponding to the {113} family of planes 120° apart. Due to twinning in the sample, some regions of the lattice are rotated 60° with respect to others, forming a set of 6-peaks in the pole figure that are created from two intermixed 3-fold patterns.

2.3.4 X-ray Reflectivity

X-Ray reflectivity (XRR) is a technique where glancing angle incident x-rays reflect from the interfaces within a sample composed of stacked thin films. Kiessig fringes, or oscillations from the reflections off each interface are caused by constructive and destructive interference similar to interference fringes in optical multilayer dielectric mirrors. The intensity of these oscillations will decrease at angles greater than the critical angle θ_c and is dependent on the roughness of the interface and relative indices of refraction at x-ray wavelengths. Specifically, oscillation periodicity can be used to calculate a layer thickness, while the angle dependence of the fringes can be used to extract density of the layer as well as roughness of the surface. Figure 31 shows the reflectivity data of a 100-nm NbTiN / 9-nm AlN / 25-nm NbTiN heterostructure used for preliminary JJ fabrication.

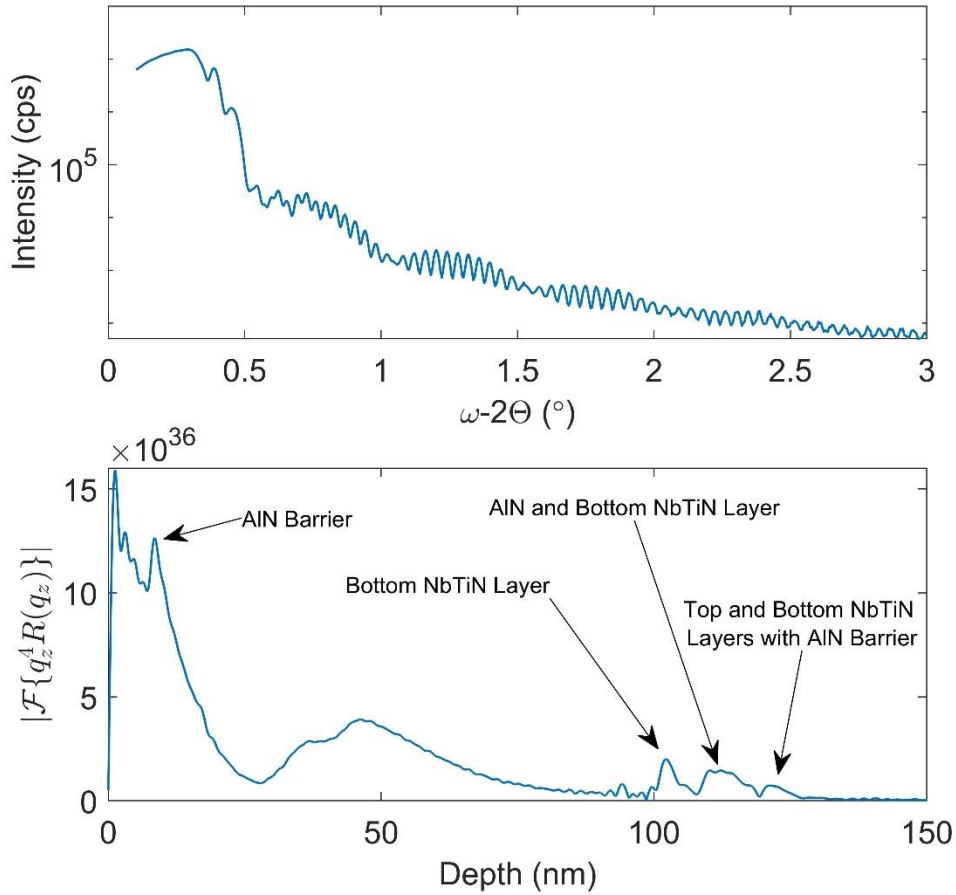


Figure 31: XRR plot of a NbTiN and AlN heterostructure showing the intensity during measurement (top), and the Fourier transform of the intensity data (bottom) to extract thickness measurements for various interfaces in the sample.

The top plot in Figure 31 shows the intensity as a function of angle during the reflectivity measurement, with several distinct oscillation periods visible. The longer oscillations are formed from thinner layers, such as the AlN barrier layer. The thicker NbTiN layers cause the shorter period oscillations. From Fourier analysis, various thicknesses can be extracted, with notable values at 9-nm for the AlN barrier, 102-nm for the bottom NbTiN layer, 111-nm for the bottom layer and AlN layer together, and 124-nm for the whole heterostructure. [112] XRR is an important technique for thin film heterostructure growth if the samples are of high quality with clearly defined interfaces.

2.4 Atomic Force Microscopy

The surface topography of samples is measured using atomic force microscopy (AFM) with a Bruker Icon system using conventional silicon cantilever tips. This technique is important for analysis of surface features, and inspection of fabrication steps in the case of wafer-based device creation. In AFM, a silicon tip is etched from a cantilever, which is attached to a piezoelectric positioner for vertical and horizontal movement. In this work, non-contact mode is used exclusively, though there are other modes of operation. The cantilever oscillates at a set frequency in free space, which is altered when the tip encounters the sample surface. This deflection is measured with a laser and position sensitive detector which is used to form a 3D image of the surface topography. Figure 32 shows a simplified schematic of an AFM tool scanning a sample. The laser is reflected off the back of the cantilever into the photodetector, where the position is used to extract the vertical deflection of the cantilever tip. [113]

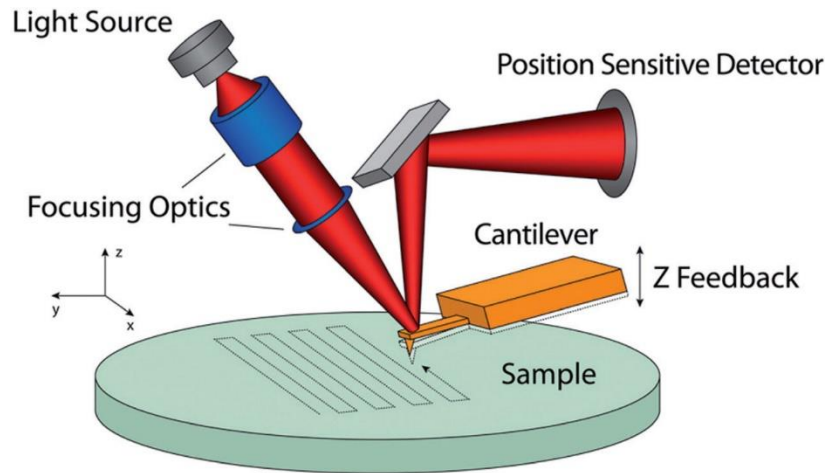


Figure 32: AFM schematic adapted from reference 112.

The use of AFM allows the detailed imaging of surface features down to near nanometer scales. Figure 33 shows a NbN_x sample with various surface features associated with different orientations of the sample crystal structure.

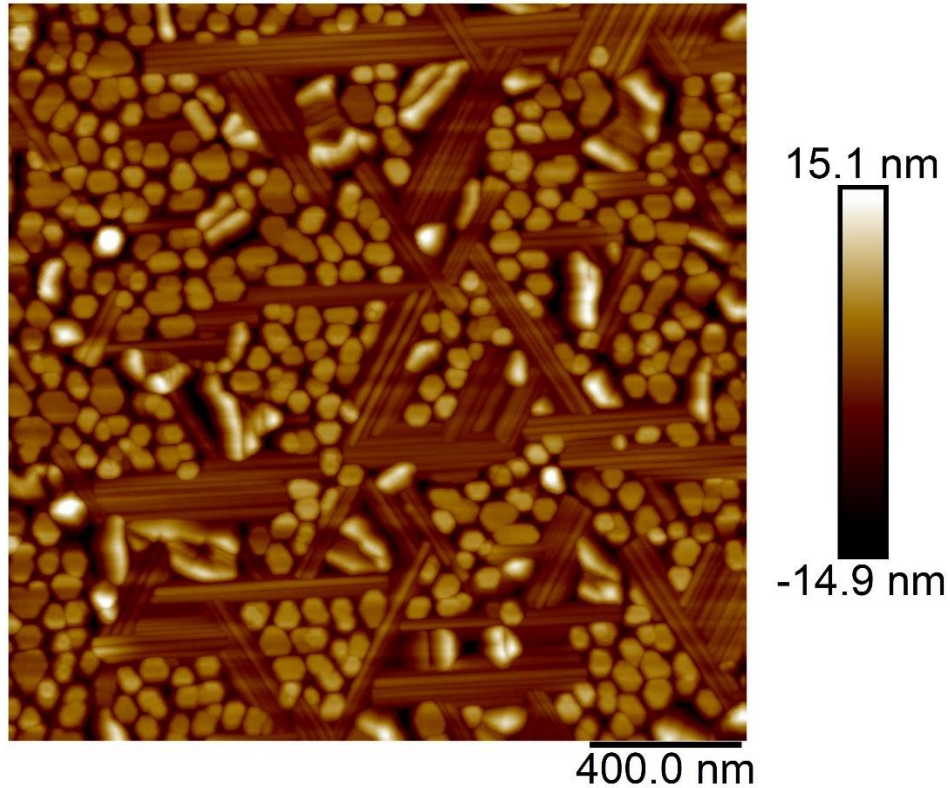


Figure 33: AFM image of a NbN_x sample showing evidence of multiple orientations.

In Figure 33, clusters of columnar structures, each approximately 50 nm in diameter, are interspersed with smoother striated regions. These smoother regions have clear steps about 15-nm apart. By using AFM with the samples in this thesis, valuable surface roughness and crystal phase information can be extracted.

For measurements taken in this thesis, a 2- μm wide scan was used to get an overall picture of the surface of each sample. This wider scan is generally taken at a scan rate of 0.5 mm/sec, with PID control values (integral and derivative gain) set to values just prior to the beginning of oscillations in the phase measurement. A more detailed scan is taken with a width of 500 nm and a scan rate of 0.5 mm/sec at points of interest on the sample surface.

2.5 Scanning Electron Microscopy

2.5.1 Imaging

Scanning electron microscopy is a very common analysis and imaging technique used in materials science, where a focused beam of electrons interacts with a sample. Various detectors are used to measure the intensity from different interactions within the material. A Zeiss Gemini SEM is used with several detectors that are positioned to measure secondary electrons, backscattered electrons, and characteristic x-rays. Figure 34 shows an SEM image taken with a secondary electron InLens detector of a cross section of a NbN_x sample used to measure the thickness of the nitride layer.

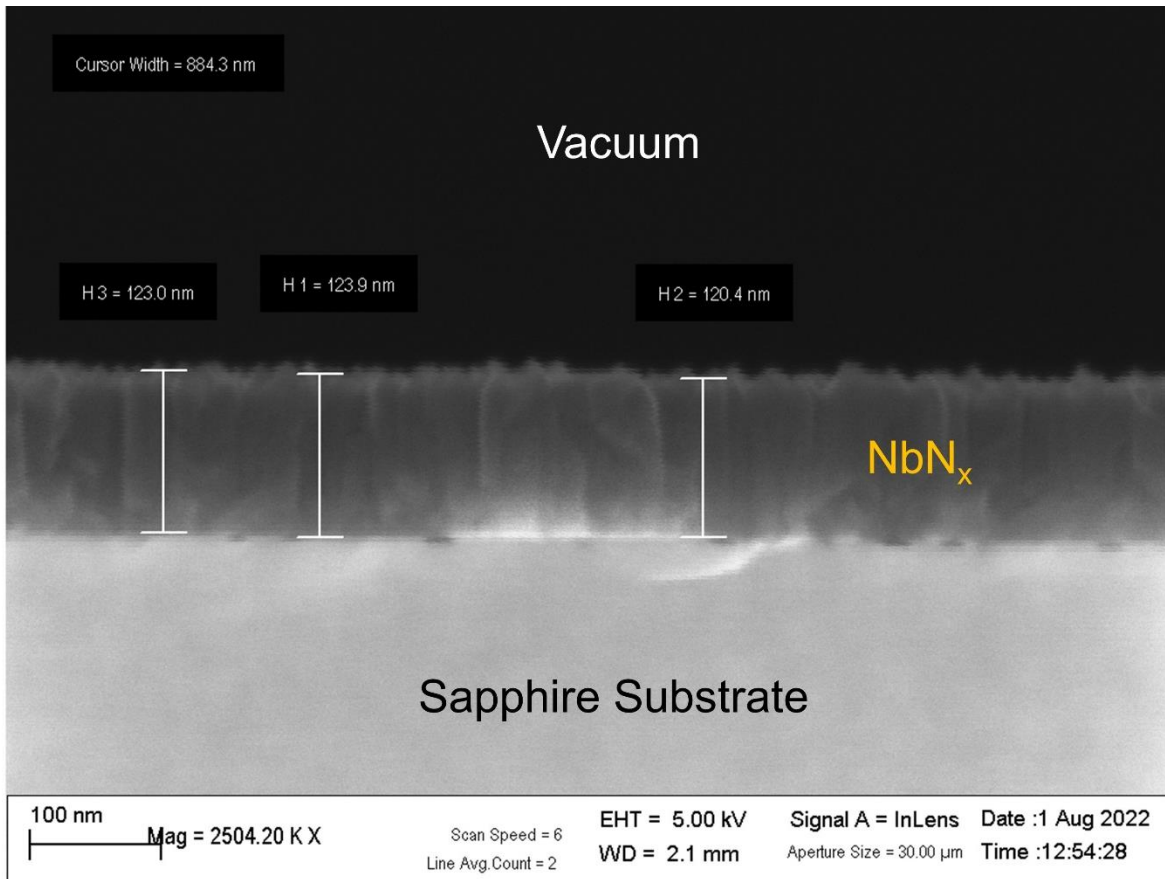


Figure 34: XSEM image of a NbN_x sample showing thickness measurements of the nitride layer.

This particular sample was approximately 120-nm-thick, and the contrast difference between the upper and lower layers helps distinguish the sapphire substrate from the nitride layer. Roughness seen in Figure 34 makes hand-drawn thickness measurements less precise than other methods such as XRR, but averaging multiple measurements can help with precisely reporting a layer thickness.

Secondary electrons occur from interaction of an incident electron and an electron in the material. The interaction is inelastic, and the excited electron from the sample is ejected at a lower energy, potentially making an exit from the sample into vacuum. This excited electron is detected. These electrons are relatively low energy (< 50 eV) and deliver valuable surface topography information about the sample.

Backscattered electrons provide information from deeper within the sample, as primary electrons from the beam interact with atoms in the material and are scattered elastically, retaining much of their original energy. These primary electrons are deflected due to this interaction, potentially being ejected back into vacuum. Due to the higher energy, these electrons have a longer mean free path within the material and can be used to image deeper than secondary electrons. Additionally, due to the elastic scattering, backscattered electrons can be used to identify atomic species in the material through Z-contrast. The higher the atomic number of the atomic species is, the higher the number of electrons the primary electron can interact with, leading to variations in image brightness with high atomic number atoms appearing brighter than a species with a low atomic number.

2.5.2 Energy Dispersive Spectroscopy

Energy Dispersive X-Ray Spectroscopy (EDS) uses characteristic x-rays emitted by electron transitions excited by the primary electrons interacting with the sample to identify atomic species in the material. As primary electrons excite and eject core shell electrons from the atoms in the sample, the resulting hole is filled by a higher-level electron. This transition emits a photon in the form of an X-ray of a wavelength corresponding to that atomic species and particular transition. **Error! Reference source not found.** shows an EDS spectrum from a N

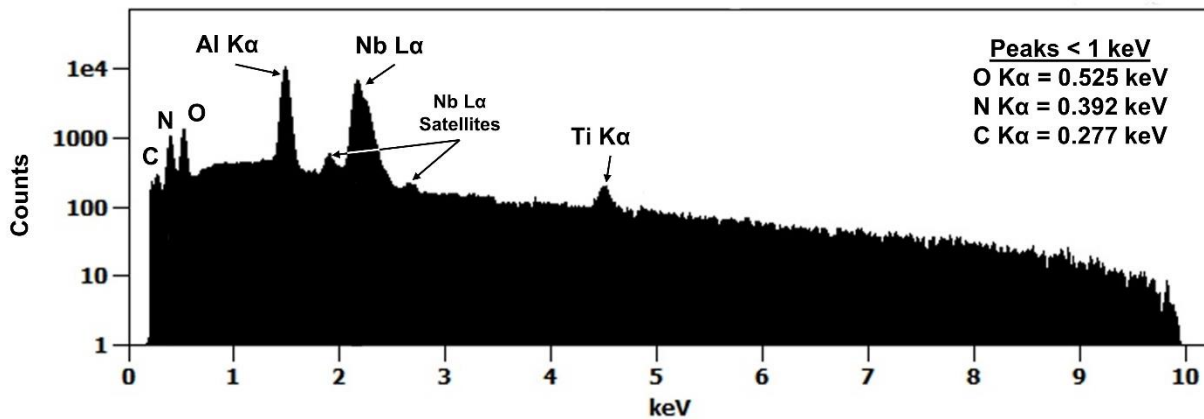


Figure 35: EDS spectra for a NbTiN sample showing Al and O peaks from the substrate as well as Ti, N, and Nb peaks from the thin film.

bTiN sample.

Peaks from the transition metals in the film can be seen at 2.2 and 4.5 keV, along with a strong aluminum peak from the substrate at 1.5 keV. The lighter elements are at lower energies, with peaks from oxygen, nitrogen, and carbon found. EDS measurements are more sensitive to heavier elements, allowing for accurate alloy fraction analysis of the niobium and titanium in this sample. Unfortunately, lower atomic number materials ($Z \leq 7$) are generally not as sensitive, limiting accurate calculation of the total atomic percent in the sample, and subsequently the metal-to-nitrogen ratio.

The background in the EDS data is due to continuum x-ray production, which occurs from a decrease in incident electron energy as they interact with the positive nuclei of the sample. The interactions between the electrons and the sample are random, and the electron may lose its energy up to the original energy, resulting in an emitted photon. The mass production of these photons forms the bremsstrahlung, or continuum background. [114]

In Error! Reference source not found., low intensity satellite peaks can be seen on either side of the Nb $L\alpha$ peak are primarily the result of secondary energetic transitions due to vacancies produced from ejected electrons, or subshell transitions. [114]

In this thesis, an Oxford EDS system is used, with accelerating voltage of 10 keV. Using double the energy required to observe the highest energy peak (in this case, Ti $K\alpha$ at 4.5 keV) is required to obtain appreciable intensity from higher energy peaks. A working distance of 8.5 mm was used for all EDS measurements, set by the optimal geometry of the tool. A live time for detection of 2 minutes was used for all scans to ensure adequate time for collection of sufficient photons and to establish enough counts to minimize noise in the calculated composition.

2.6 Rutherford Backscattering Spectroscopy

Rutherford Backscattering Spectroscopy (RBS) is a materials analysis technique generally used to measure thickness and composition, where ions are launched at a sample and are backscattered off nuclei within the sample. Since the initial kinetic energy of the ion is known, the energy of the backscattered ion will be at a lower energy dependent on the mass of the target nucleus that it is scattered from. This energy is characteristic of a specific atomic species, and the resulting spectra of various energies can be numerically fit, and properties of the

material extracted. In this work, RBS measurements were performed by Dr. Hussein Hijazi in the Department of Physics & Astronomy at Rutgers University. In Figure 36 below, the spectrum from a NbTiN sample is shown. Thicker layers in the sample produce wider peaks, resulting in

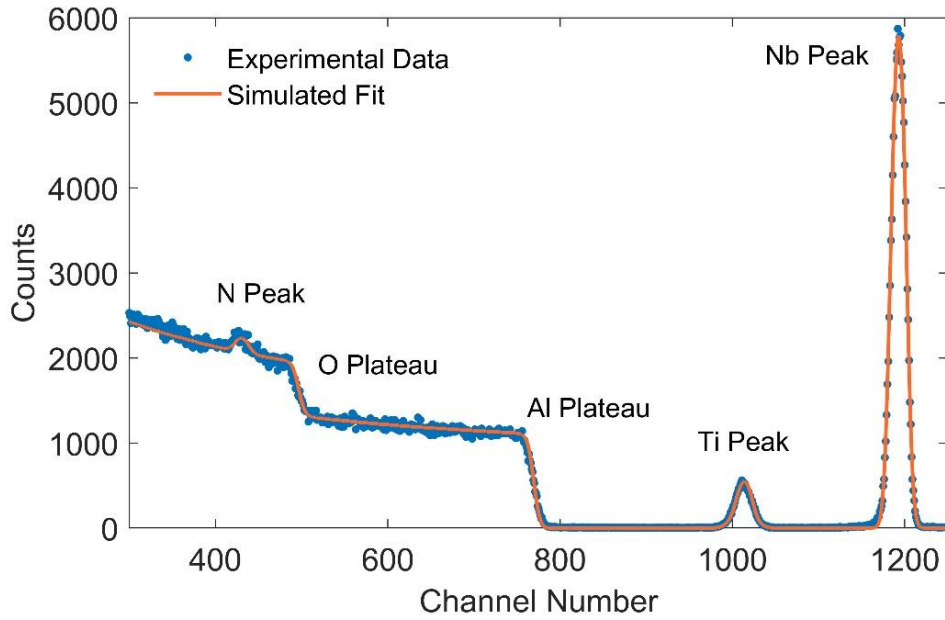


Figure 36: RBS spectrum from a $\text{Nb}_{0.72}\text{Ti}_{0.28}\text{N}$ sample grown on sapphire.

plateaus for elements contained in the substrate, which is much thicker than the nitride film grown.

Peaks are fit using the SIMNRA software package, which extracts the thickness and composition. [115] The simulation used to create the fit begins with an environmental setup, where the type of incident projectile (He^4) and energy of the incident particles (2.3 MeV) are declared. The geometry of the apparatus is also set up, as the incident angle will affect the depth of penetration. Figure 37 shows a simplified geometry of the RBS setup.

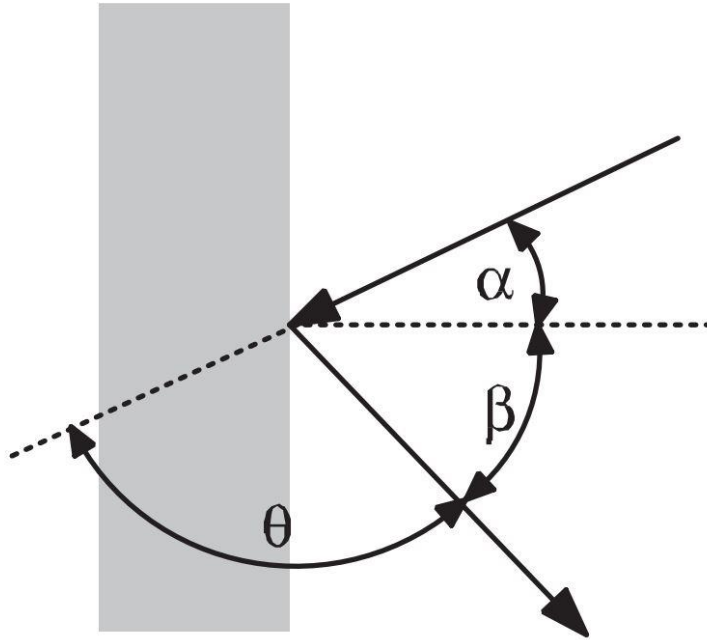


Figure 37: Simplified RBS apparatus geometry, with the sample depicted as the grey rectangle. Reproduced from reference 114.

In Figure 37, α is the angle of incidence for the He^4 particles, β is the exit angle of particles, and θ is the scattering angle of the ions. For the experimental geometry, the exit angle β is set to 17° , with the scattering angle θ equaling 163° . The resolution of the simulated detector is 18 keV, while the calibration parameters, energy per channel and energy offset are set to near 1.4 keV/channel and between 5-10 keV, respectively. These parameters are optimized during fitting and will generally settle to a constant value while the composition and thickness parameters continue to change during the fit.

The simulated structure consists of three layers for each sample, an Al_2O_3 substrate, a $\text{Nb}_x\text{Ti}_{1-x}\text{N}$ layer, and a thin oxygen containing layer on top. Oxygen is set to a composition fraction of 0.05 and allowed to vary during the fit. Layers in SIMNRA are described in terms of thickness-atomic density product, with units of 10^{15} atoms/cm².

Once the environment is set up, and the target material stack is created, the fitting routine is run. For the purposes of this thesis, the convergence value for the fitting was set to 1×10^{-5} . No foil or window was used in the environment creation. SIMNRA used the Simplex algorithm for minimizing variation between the simulated fit and the measurement data. [115], [116]

2.7 Cryogenic Characterization

2.7.1 Adiabatic Demagnetization Refrigerator

The adiabatic demagnetization refrigerator (ADR) used for the DC and RF measurements in this thesis is a High Precision Devices Model 103 Rainier system. This type of cryogenic refrigeration uses both a pulse tube refrigerator and an adiabatic demagnetization system to cool samples and components to less than 90 mK. The pulse tube refrigerator consists of a remote compressor to move helium in the system and is attached to a cold head where the helium expands. As the expanding helium absorbs heat from the environment, it is passed back to the compressor. This closed loop system provides constant cooling down to 3 K.

For further cooling, the ADR system uses magnetocaloric cooling with a 4 T superconducting magnet along with both Gadolinium Gallium Garnet (GGG) and Ferric Ammonium Alum (FAA) paramagnetic salt pills. An ADR uses these salt pills to convert thermal energy to magnetic energy. The increasing magnetic field aligns the magnetic dipoles of the atoms in the salt pills which decrease the materials magnetic entropy that heats the salt pill. The salt pills are thermally connected to the cold stage of the ADR through an actuatable heat switch. This heat is removed with the pulse tube refrigerator while the magnetic field is maintained. The heat switch then decouples, and the magnetic field is reduced, causing the

magnetic moments to de-align, which absorbs heat from the sample. The two different salts have different minimum temperatures, with the GGG salt cooling to 500 mK, and the FAA salt cooling to 50 mK. Once the magnetic spins are randomly aligned, the salts cannot absorb any more heat and the cycle is repeated.

The ADR refrigerator uses a series of temperature stages which become progressively cooler from the top of the tool to the bottom, and a diagram is shown in Figure 38. [117]

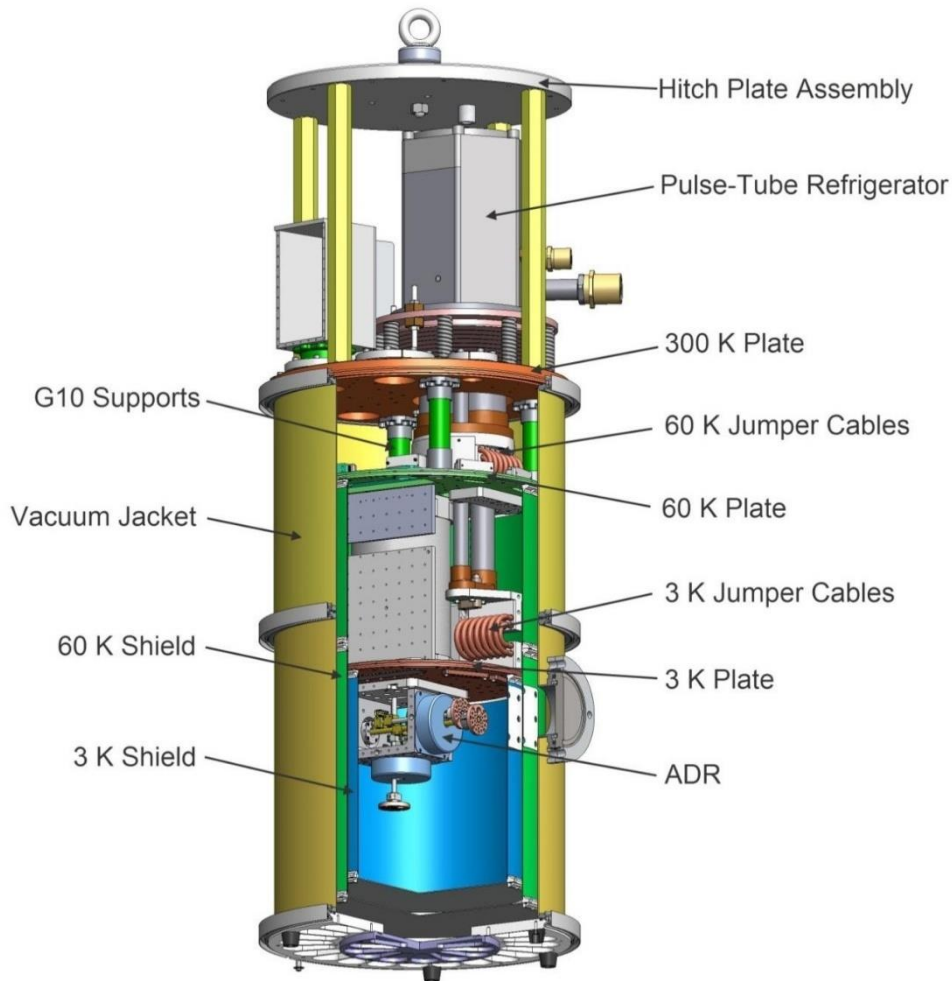


Figure 38: Cutaway diagram of the HPD ADR used in this thesis. Reproduced from reference 116.

The cooling stages are encased in a series of vacuum and radiative shielding, which prevents the transfer of heat to the lowest stages. The stages for the 103 Rainier consist of a room temperature stage, then a 60 K stage, a 3 K stage, a 1 K stage, and a 50 mK stage. These last two stages are

thermally isolated from the rest of the system by a Kevlar suspension. The three stages mentioned are visible in the diagram, along with the helium pulse tube for refrigeration down to 3 K. The 1 K and 50 mK stages are contained in the section labeled ADR.

Figure 39 shows an RF wiring diagram for the ADR as set up at the laboratory.

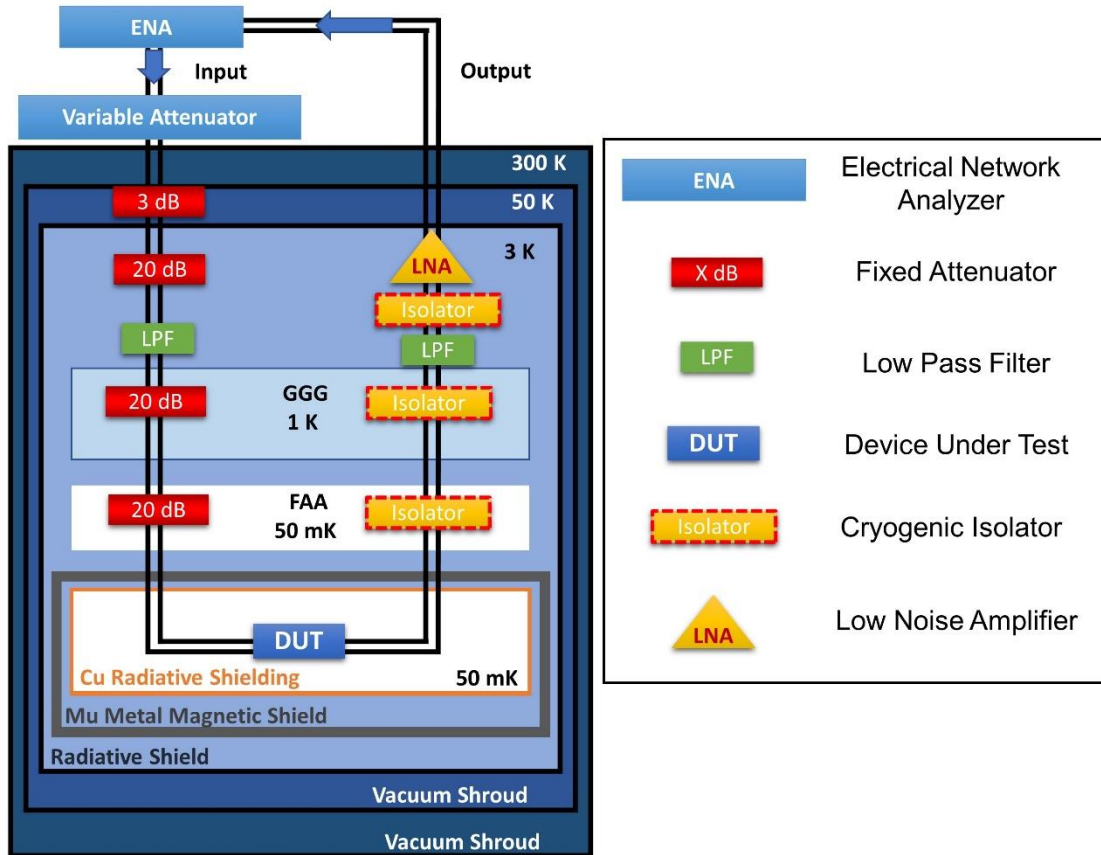


Figure 39: ADR resonator measurement wiring diagram.

The input lines going down the left side of the diagram in Figure 39 consist of a series of fixed attenuators which eliminate thermal noise induced from warmer stages and the outside environment. A low pass filter is also present which eliminates frequencies above 13 GHz. On the output lines, isolators are placed at both the 50 mK and 1 K stages help eliminate frequencies less than 4 GHz and higher than 12 GHz, which reduces low frequency noise from the

environment. The low noise amplifier built by Cosmic Microwave Technology amplifies the outgoing signal by approximately 30 dB to improve the signal to noise ratio and enable measurement at low power levels. RF wiring in this system consists of superconducting NbTi wire between stages below the 3 K stage. This is done to both reduce thermal conduction between stages due to the low thermal conductivity of NbTi, and to reduce attenuation in the output lines. At the 50 mK stage, copper coaxial cables are used to improve thermalization of the device under test (DUT).

The resonator sample is packaged in a custom copper container. The package has bolted-on SMA coaxial connectors which are soldered to a PCB. The LPS designed PCB connects the SMA connector to the coplanar waveguide on the device. The ground plane has an array of vias to reduce asymmetric ground plane modes. Figure 40 shows one of the packages used to measure resonators.

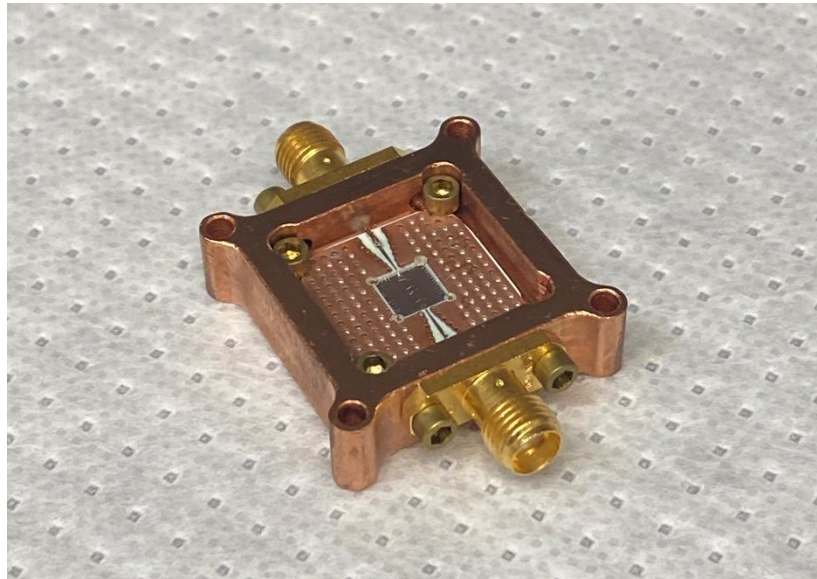


Figure 40: RF package made from copper with PCB and coplanar waveguide chip at the center.

RF measurements are performed using an Agilent Technologies E5072A spectrum analyzer, a variable attenuation unit, and DC power supplies to power the bias connection on the

low noise amplifiers. The variable attenuation unit is used to test the resonators at different power levels and reach the single photon regime without introducing excessive noise.

2.7.2 Resonator Measurement and Fabrication

Resonators are structures that exhibit standing waves when the wavelengths match the effective length of the structure, resulting in a change in the transmitted and reflected signal. These waves can be electromagnetic in nature, as in RF resonators, vibrational, as in phonon-based resonators, or mechanical, as in pendulums. In this thesis, coplanar waveguide resonators are fabricated from superconducting $\text{Nb}_x\text{Ti}_{1-x}\text{N}$ thin films with radio-frequency resonance frequencies near 5 GHz. The resonance frequency is a function of the resonator inductance, L , as well as the capacitance, C , of the circuit, written as

$$f_0 = \frac{1}{2\pi\sqrt{LC}} \quad (35)$$

Resonator measurements in the ADR are performed at base temperatures below 100 mK. Resonator frequencies are identified using a broad transmission sweep (S_{21}) from 3 GHz to 7 GHz. The numerical derivative of the phase signal produces sharp peaks that are automatically identified using the peak finding functions in MATLAB. Subsequent scans using a tighter sweep around each individual resonator are measured at varying photon powers by increasing the attenuation applied to the incoming RF signal.

For each resonator measurement, the real and imaginary parts of the S_{21} transmission are fit using a circle fit to minimize measurement artifacts. A seven parameter fit is used to extract the internal and coupling quality factors as described in Chapter 1. [62] The internal power dependent quality factor can be described by the conventional TLS model,

$$\frac{1}{Q_i} = \frac{1}{Q_A} + \frac{1}{Q_{TLS}^0} \frac{1}{1 + \frac{n}{n_c}^a}. \quad (36)$$

Here, Q_i is the internal quality factor of the material. All power independent loss is contained within Q_A , and the TLS quality factor is Q_{TLS}^0 . The average photon number in the resonator is n_c , and a is a fitting parameter to accommodate power dependence of the TLS defects.

Careful fabrication of the resonator devices using superconducting NbTiN is important for reliable, repeatable results. All resonator fabrication is performed in the LPS cleanroom, and consists of wafer pre-cleaning, lithography, pattern development, etching, and wafer post-cleaning processes with a total of more than 50 individual steps.

Prior to fabrication, wafers are diced into 15 mm x 15 mm pieces. Each of these pieces contains four 5 mm x 5 mm resonator chips, each with a central transmission line attached to 5 individual resonator devices. Figure 41 shows two designs used for fabrication with the “repeatability” mask on the left and the “width variation” design on the right. The first design, denoted as the “repeatability” design, features a gap width and the resonator trace width which are identical at $W_{\text{center}} = 6 \mu\text{m}$ and $W_{\text{gap}} = 3 \mu\text{m}$. The length of the resonators changes to separate the center resonance frequencies from one another. The second mask, denoted as the “width variation” design, features the same length changes, but W_{center} ranges from 3- μm to 22- μm , with W_{gap} always being equal to one half the center width. This mask was used to examine the changes in quality factor with respect to the varying degrees of TLS interaction with the electric field, which can vary in strength based on changes in the gap and center conductor widths. Ideal center frequencies and resonator lengths are shown on the right in Figure 41, while the left design shows the changing center widths and gap widths for each resonator. Lengths of

resonators in the “width variation” design are identical to the respective resonator in the repeatability design.

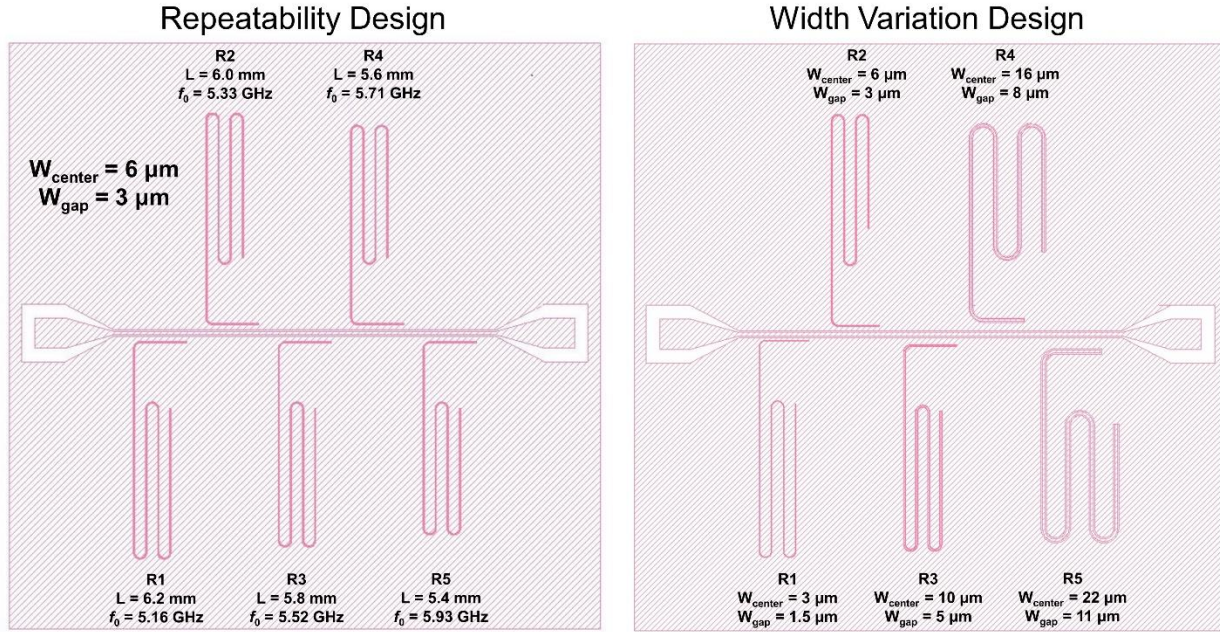


Figure 41: Resonator design masks, both the repeatability (left) and width variation (right) designs.

Pre-cleaning of the wafers involves sequential 3-minute ultrasonication in room temperature acetone, methanol, isopropyl alcohol, deionized water, then a rinse in isopropyl alcohol before blow drying with nitrogen. These steps remove contaminants that are on the surface of the sample after removal from the chamber. Micrographs are taken of the bare surface to ensure no remaining contaminants are visible before a resist layer is spun on, where stuck residue can significantly impact the uniformity and thickness of the resist layer.

The single lithography step consists of spinning Fujifilm OiR906-10 resist at 3000 RPM for 60 seconds, to a target thickness of 1.1 μm . The resist layer is pre-baked at 90 °C for 60 seconds before the pattern is exposed. OiR906-10 is a multi-purpose mid-UV sensitive photoresist intended for high-resolution patterns with critical dimensions greater than 500 nm. The pre-bake removes most of the solvent and creates a semi-hard resist layer, which preserves

the resist polymer without significant crosslinking, contamination incorporation, and prevents bubbles from forming during UV exposure. Exposure is performed using a GCA i-line (365 nm) stepper, with 45-ms exposure time after an autofocus step is done.

After exposure, the sample is post-baked at 120 °C for 60 seconds to finish the crosslinking of the polymer initiated during exposure. The baked sample is developed in room temperature OPD 4262 for 60 seconds with manual agitation to ensure consistent removal of material and uniform development. The wafer is then soaked in a deionized water bath with manual agitation to stop development. Micrographs are taken to ensure the sample is contaminant free, with no bubbles or defects in the remaining resist pattern.

Etching of the samples takes place in an Oxford PlasmaPro 100 Cobra system, where the sample is mounted to a thick sapphire substrate using thermally conductive vacuum grease. The recipe used etches NbTiN at a rate of 2.4 nm/sec using a gas mixture of 22.5:49.5 BCl₃:Cl₂, a forward power of 400 W, and a sample temperature of 40 °C. Thicknesses obtained using XRR measurements are used to determine the total etch time. After etching, the samples are cleaned of vacuum grease using trichloroethylene and swabs. The resist is removed using a bath of heated Electronic Materials Microposit Remover 1165, an NMP based solvent solution. The bath is heated to 80 °C, and the sample is soaked for 10 minutes, then sonicated in that solution for 5 minutes. The soak and sonicate steps are repeated using fresh 1165 to ensure no resist contaminants are re-deposited on the sample. Sonication in deionized water is performed after the cleaning to removal residual 1165, then blow dried.

After cleaning, micrographs are taken to ensure clean sidewalls and good depth of the etch. Figure 42 shows a micrograph of one TiN sample. Clean edges around all features can be

seen, indicative of a successful fabrication process particularly evident on the smaller perforations used to trap magnetic vortices, which have sharper corners.

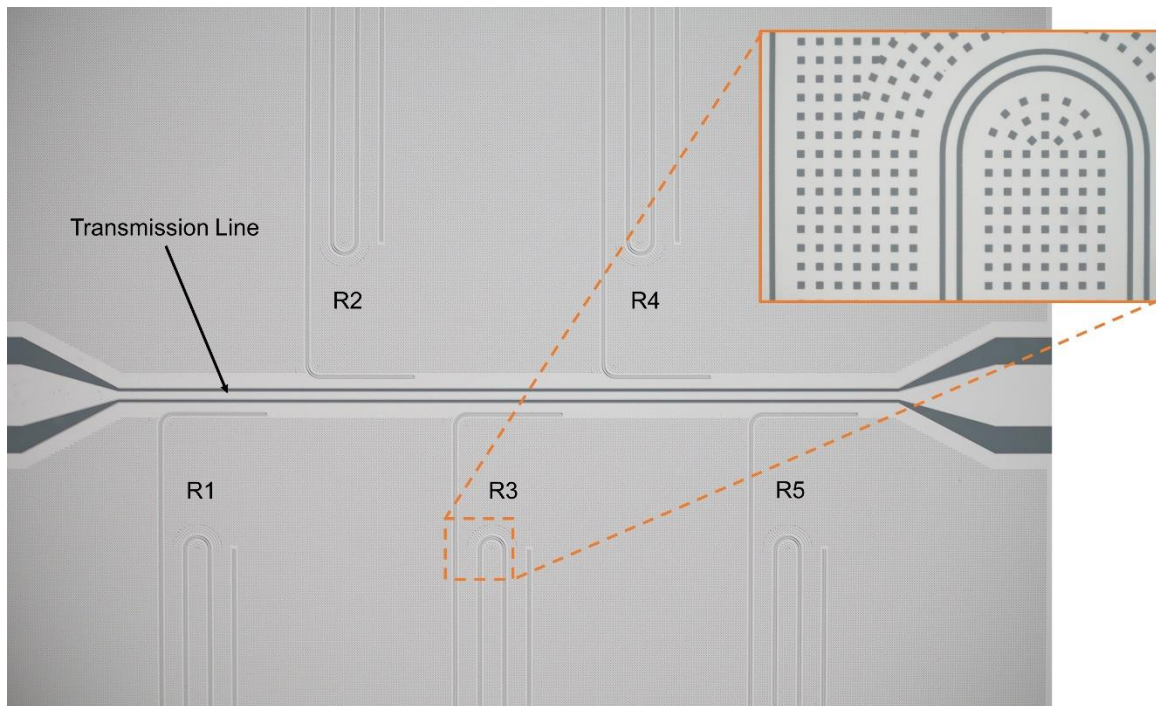


Figure 42: Repeatability type resonator device with a central transmission line feeding 5 resonators. Perforations can be seen in the zoomed view box which assist in trapping magnetic vortices.

2.7.3 Experimental Kinetic Inductance Measurement

Kinetic inductance of Cooper pairs in coplanar waveguide resonators can be calculated from the difference in measured resonant frequency and design resonant frequency, as well as the geometry of the resonator. To calculate the geometric inductance of the resonator, which is established by the cross section of the resonator, the characteristic impedance of each device must be found. The characteristic impedance is calculated using

$$Z_0 = \frac{30\pi}{\sqrt{\epsilon_{eff}}} \frac{K(k'_0)}{K(k_0)}, \quad (37)$$

where ϵ_{eff} is the effective dielectric constant, and $K(k'_0)$ and $K(k_0)$ are the complete elliptic integrals. [118] For calculations in this work, an ideal geometry where the center resonator width is twice that of the gap on either side is assumed, along with an effective dielectric constant of 10 for the sapphire substrate. Using the calculated Z_0 , the geometric inductance L of each resonator can be calculated using

$$Z = R + 2\pi fL. \quad (38)$$

Here, R is zero due to the superconducting state of the resonator, and f is the resonant frequency of each resonator. [119] This results in a characteristic impedances and geometric inductance for each resonator shown in Table 2.

Table 2

Table 2: Characteristic impedances and geometric inductances calculated for all resonators in the repeatability and width variation designs.

The fraction of the kinetic inductance, L_{ki} , to the total inductance, L , of the device is defined as

$$\alpha = \frac{L_{ki}}{L}, \quad (39)$$

and α can be calculated from the change in measured resonant frequency to the simulated resonator frequency as

$$\alpha = 1 - \left(\frac{f_0^m}{f_0}\right)^2. \quad (40)$$

Here, f_0^m is the measured resonant frequency, and f_0 is the ideal resonant frequency, assuming only geometric inductance contributions. [120] Since $L = L_{ki} + L_g$, Equation 39 can be rearranged to form

$$L_{ki} = \frac{\alpha L_g}{1-\alpha}. \quad (41)$$

This gives the total kinetic inductance of the resonator in Henrys. To remove the geometry of the resonator from consideration so that only the material properties are considered, L_{ki} is multiplied by a geometric aspect ratio to give inductance per square, written as

$$L_{ki\blacksquare} = L_{ki} \frac{w}{l}, \quad (42)$$

where w is the width of the resonator center line, and l is the length of the resonator. [121]

2.7.4 Calculation of Resonator Center Frequency

The resonant frequency of each resonator can be calculated using the geometry of the mask design, as well as the effective dielectric constant using

$$f_0 = \frac{1}{4L\sqrt{\varepsilon_0\varepsilon_e\mu_0}}, \quad (43)$$

where L is the length of the resonator, μ_0 is the vacuum permeability, ε_0 is the vacuum permittivity, and ε_e is the effective dielectric constant between vacuum and sapphire. The effective dielectric constant is calculated using

$$\epsilon_e = \frac{(\epsilon_s + \epsilon_v)}{2}, \quad (44)$$

where ϵ_s is the dielectric constant of the substrate ($\epsilon_{sapphire} = 10$), and ϵ_v is the dielectric constant of vacuum ($\epsilon_{vacuum} = 1$). [122] This results in an effective dielectric constant of 5.5. Ideally, the resonant frequency of each resonator should be identical between the two mask designs, influenced only by non-geometric losses in a physical device.

2.7.5 Resonator Simulation of Center Frequency

To ensure accuracy of the calculated resonant frequencies, simulation of the resonators from both mask designs was performed using Ansys 2022. Figure 43 shows the structure used to perform the Ansys simulation with the repeatability mask design.

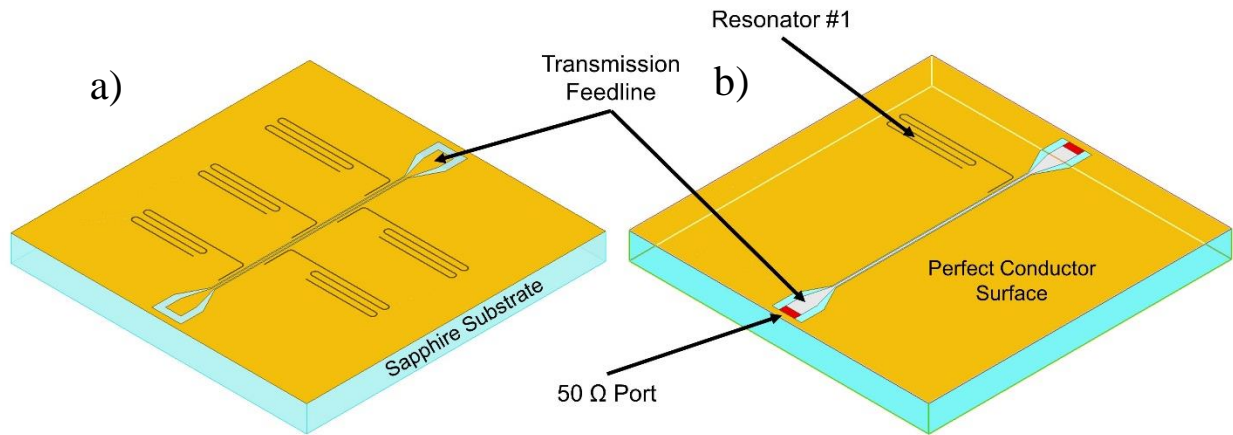


Figure 43: Ansys 2022 simulation structure featuring a sapphire substrate, and multiple resonators which are isolated for determination of resonant frequency.

Here, the entire chip with 5 coplanar quarter wavelength resonators is shown in Figure 43(a), each with a different trace length and resonant frequency. The substrate in teal is modeled as sapphire with a dielectric loss tangent of 1×10^{-6} , and a thickness of $430 \mu\text{m}$. A 3-mm thick top

layer is added and is modeled as vacuum. To isolate each resonator and extract an accurate resonant frequency, all resonators but the one being tested are removed from the model, shown in Figure 43(b). The sides, bottom and top faces are modeled as perfect conductors which simulate a superconducting material perfect grounding. A $50\ \Omega$ port is added at each end of the transmission feedline to provide the RF excitation and are shown in red in Figure 43(b).

S_{21} through resonator #1 is simulated and plotted in Figure 44.

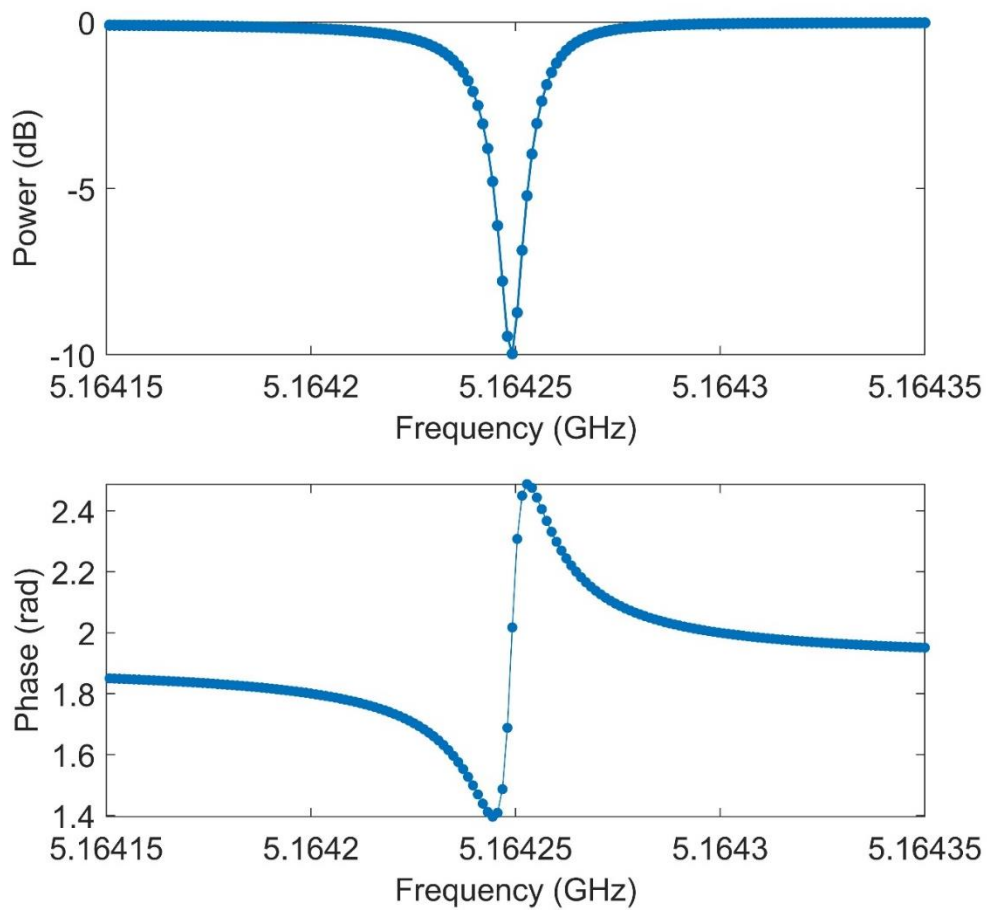


Figure 44: Simulated resonant frequency and phase for resonator #1 in the design shown in Figure 44.

This resonance is simulated first in a broad sweep from 5 to 7 GHz, then refined until the resonant peak contains more than 20 simulated points. The peak is then fit with a spline curve in MATLAB, and the peak of the curve is used as the resonant frequency.

Table 3 lists the simulated resonant frequency for each resonator for the device design used for the NbTiN devices fabricated.

Table 3: Simulated resonant frequencies for both designs used to fabricate resonators from $\text{Nb}_x\text{Ti}_{1-x}\text{N}$ samples.

| Resonator Number | Repeatability Simulated Resonant Frequency (GHz) | Width Variation Simulated Resonant Frequency (GHz) |
|------------------|--|--|
| 1 | 5.164 | 5.150 |
| 2 | 5.328 | 5.351 |
| 3 | 5.521 | 5.530 |
| 4 | 5.697 | 5.705 |
| 5 | 5.928 | 5.941 |

These results are plotted in Figure 45 for both the geometrically calculated resonant frequencies and the simulated values. Ideally, the resonances should follow a linear line with a slope of one, but some variation exists in both sets of data.

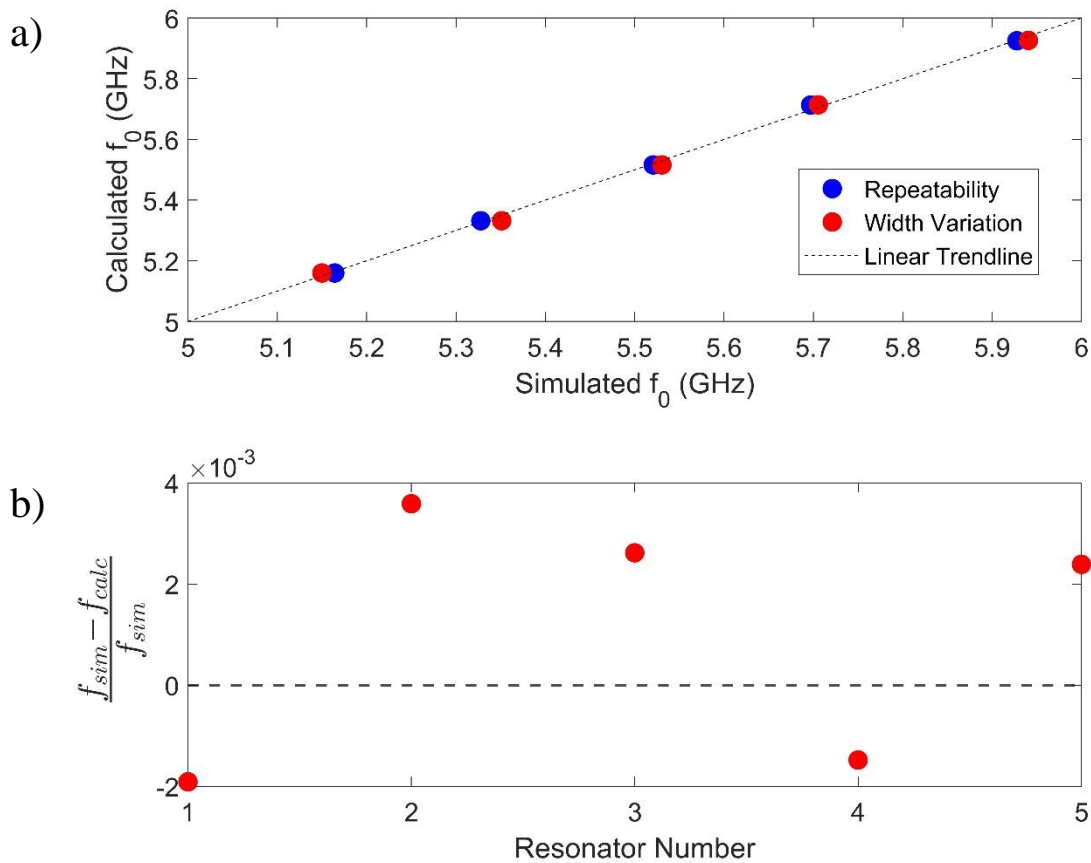


Figure 45: a) Calculated and simulated center frequencies for all five resonators on the width variation and repeatability mask designs. b) Difference fraction between the simulated and calculated frequencies. All are < 4 MHz difference.

The data in Figure 45 follows with the ideal resonator behavior, where the resonant frequency should be dependent only on the trace length and the dielectric constant associated with the substrate and vacuum above the device. This shows that the capacitive coupling to the transmission line, as well as the cross-sectional geometry, does not impact the expected resonant frequency.

2.7.6 Direct Current IV Measurements

DC resistance measurements are completed with a delta mode measurement system consisting of a Keithly 2182A nanovoltmeter to measure the voltage from the DC samples and a 6220 current source to supply a set current of 10 mA to the sample. The delta mode system sequentially applies positive and negative current biases to eliminate voltage offset artifacts. An LPS-designed, custom PCB with attached 20-pin connector is bolted to a copper plate, and wire bonds are used to connect copper pads to the 4 mm x 4 mm squares cut from whole wafers. The wire bonds deliver a 10-mA current as the temperature of the ADR varies. It was found that warming up the ADR is a slower process than cooling it down in the range of interest for NbTiN superconductivity ($4 \text{ K} < x < 17 \text{ K}$). This slower process allows for more accurate measurement of the superconducting critical temperature and is used for all measurements reported in this thesis.

The critical transition temperature of many of the NbTiN films in this thesis are abrupt. For these samples, the sampling rate of the DC measurement apparatus and temperature ramp of the ADR while warming establish an upper bound on the width of the superconducting transition. To extract T_c from superconducting samples, the 90% and 10% resistances of the normal state resistance immediately above the superconducting transition are averaged, and the corresponding temperature for that average resistance is reported as the T_c . [123] Superconducting transition width is also reported from between the 90 % and 10 % resistance thresholds. [124] These are described with

$$T_c = \frac{T_{0.9R_N} + T_{0.1R_N}}{2} \quad (45)$$

and

$$\Delta T = T_{0.9R_N} - T_{0.1R_N}. \quad (46)$$

The residual resistance ratio (RRR) is a qualitative assessment of the ease that electrons flow through a material, described by

$$RRR = \frac{R_{RT}}{R_N}, \quad (47)$$

where R_{RT} is the resistance of the sample at room temperature, and R_N is the normal state resistance just above T_c . For insulating materials, the resistance of the sample increases as temperature is decreased due to the reduced number of electrons in the conduction band, resulting in $RRR < 1$. For metals, a reduced temperature decreases phonon scattering resulting in a smaller R_N and larger RRR. Smaller values of RRR also indicate a lower relative contribution from phonon scattering and larger contribution from temperature independent features such as impurities, defects, and grain boundaries.

Chapter 3: Binary Transition Metal Nitrides

To begin an evaluation of NbTiN alloy for all-nitride epitaxial Josephson junctions, the binary compounds must be studied to form bounds on the properties that should be observed with alloys of any composition. To this end, PAMBE described in Chapter 2 was used to produce TiN and NbN_x thin films on C-plane sapphire substrates. These films are evaluated with respect to their structural properties, electrical characteristics, and surface morphology.

3.1 Titanium Nitride

3.1.1 Growth Details

TiN growth on sapphire begins with the wafer preparation process described in Methods section 2.1.2 before being loaded into the load lock. A typical TiN growth is shown in Figure 46.

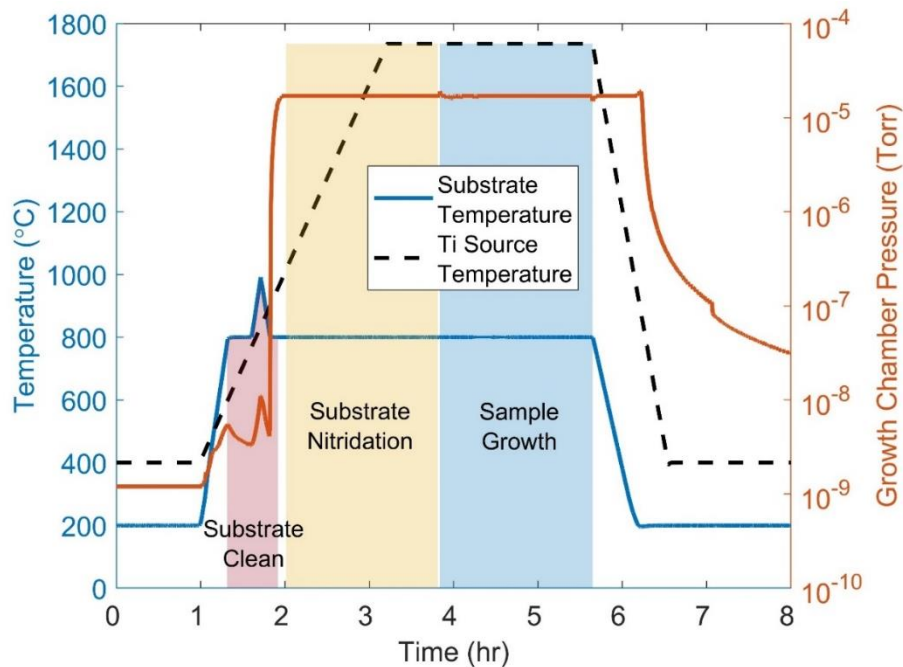


Figure 46: TiN growth process showing the changes in substrate temperature and chamber pressure as desorb, growth, and cool-down steps are reached.

During substrate desorb, the source temperature is ramped to the operation temperature for that growth. At the same time, the nitrogen plasma source is lit with an ultra-high purity nitrogen flow of between 0.6 and 1.8 sccm, depending on the source diffuser plate installed and the cell geometry. These variables influence the backpressure within the cell, which requires a specific pressure range to light the plasma. The substrate is held at 800 °C under operational nitrogen plasma flow for two hours to nitride the surface of the sapphire substrate. Nitridation of c-plane sapphire substrates has been shown to form a thin layer of $\text{AlO}_x\text{N}_{1-x}$ on the surface of the substrate after just a few minutes in a nitrogen overpressure. [125], [126] This is shown in Figure 47, where a sapphire substrate was held at 600 °C under nitrogen plasma overpressure for 24 hours. [127]

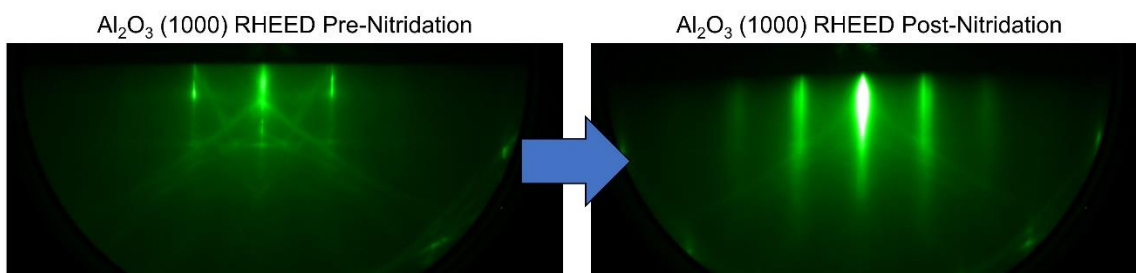


Figure 47: RHEED pattern of the Al_2O_3 (1000) pattern pre and post nitridation for 24 hours at 600 °C. Images reproduced from reference 126.

After the desorb and substrate nitridation steps are complete, the titanium cell is at operating temperature and the shutter over the Ti cell is opened and growth begins. Titanium flux is generated with a DCA high-temperature effusion cell run between 1600 °C and 1900 °C depending on the flux required and the age of the source material. Figure 46 shows a growth process for a TiN sample grown at 800 °C with a cell temperature of ~1700 °C. Typical growth rates for TiN samples are between 0.001 and 0.005 nm/second which has an upper limit dictated by the high temperature effusion cell.

Pressure during growth ranges from base pressure ($\sim 1 \times 10^{-10}$ Torr) to 5×10^{-5} Torr when ultra-high purity nitrogen is flowing. Pressure changes in Figure 46 are due to several factors. The initial rise and subsequent double spikes in pressure between hours one and two occur from the heating of the bare substrate. Contaminants from the wafer are desorbed for a pristine growth surface. The small pressure drop at hour seven is due to the opening of the gate valve to the ion pump after the growth is complete. This valve is closed during growth to prevent the pump from overheating due to a large influx of nitrogen.

Once the growth duration is finished, the cell shutter is closed, and the cell is cooled down. The nitrogen overpressure is shut off and the substrate is ramped to 200 °C at 25 °C/min. Once the pressure in the chamber has fallen below 5×10^{-9} Torr, RHEED is performed on the sample before removal from the PAMBE chamber. Pumping down the chamber post-growth before collecting RHEED may help optimize the image by reducing the scattering of electrons from gas molecules left in the chamber by the nitrogen plasma source. [128]

RHEED of the TiN sample shows a spotty pattern with distinct vertical lines, indicating a highly crystalline material with a surface structure composed of mainly 3D features, typically seen in Volmer-Weber crystal growth. In Figure 48, the AFM corroborates the spotty RHEED pattern with a topography referred to as “river-rock”, which is composed of small spherical nodules. TiN samples with this topography typically have a root-mean-squared roughness (R_q) of 2-4 nm, dependent on the sample thickness and growth rate.

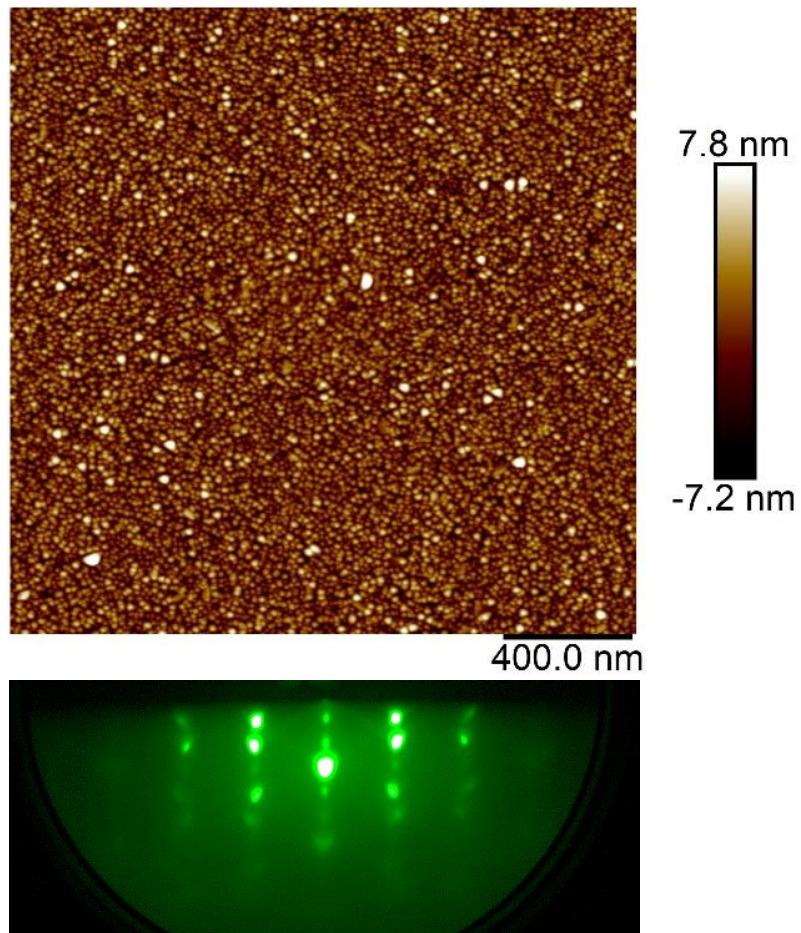


Figure 48: AFM (top), and RHEED (bottom) taken of a 100-nm TiN sample grown on sapphire. TiN shows a distinct "river-rock" topography with a RHEED showing a spotty pattern, indicative of a surface with 3D features.

3.1.2 TiN Structural Properties

The symmetric XRD of TiN films show a single film peak corresponding to the (111) orientation of the rock salt structure. Extended scans across the hardware limited range of ω - 2θ were performed and show the (222) peak at higher ω - 2θ values. Figure 49 shows a 68-nm-TiN sample. Vertical dashed reference lines are present for both the substrate and TiN film.

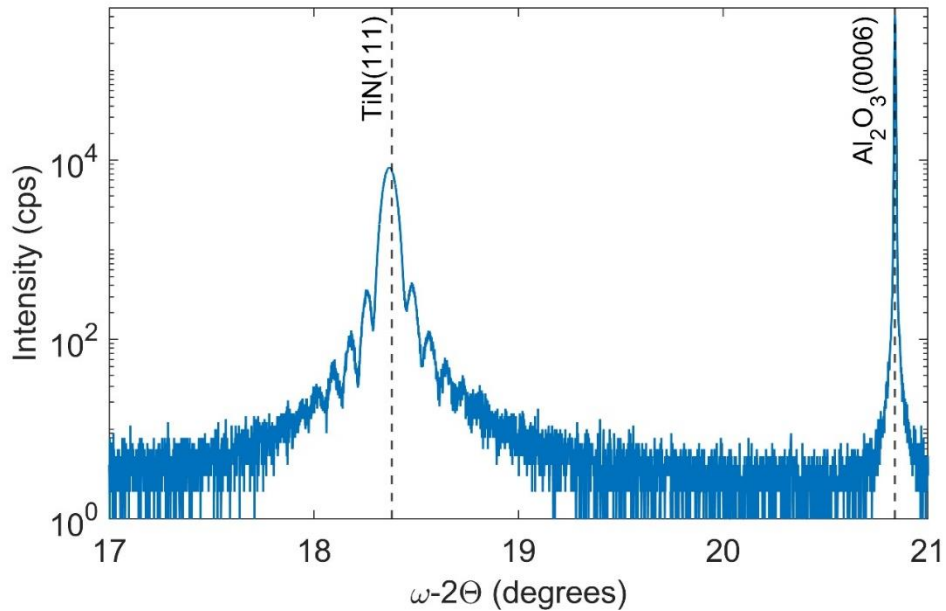


Figure 49: Symmetric XRD of a 68nm TiN sample with vertical lines denoting reference values for bulk samples in literature. Thickness fringes are evidence of the good crystal quality.

Reference peak locations are calculated from bulk lattice values in literature, where

$a_{bulk} = 4.231 \text{ \AA}$. [80] Thickness fringes are evident on both sides of the TiN peak, indicating high crystalline quality.

With a peak angle of 18.368° , this representative sample has a lattice constant of 4.234 \AA , assuming no distortion in the cubic lattice, which is a 0.07 % change in the out-of-plane lattice constant from a bulk lattice. A slight deviation of the TiN (111) peak from the reference value to a lower ω - 2θ indicates an increase in the out of plane direction. This elongation could be caused by several factors, namely growth stress from the thermal expansion mismatch between the film

and the substrate, mosaic spread from misfit dislocations, or compressive stress caused by interstitial nitrogen.

Since lateral strain of the film is constrained by the substrate, growth stress causing out-of-plane distortion for TiN films on sapphire can be estimated using their coefficient of thermal expansion (CTE) mismatch. The CTE for sapphire is $7 \times 10^{-6} \text{ }^\circ\text{C}^{-1}$, for TiN it has been shown to be 9.4×10^{-6} . [129] The growth stress is

$$\sigma_T = E \varepsilon_T = E \Delta T \Delta \alpha, \quad (48)$$

where the thermal stress (σ_T) is calculated from the difference in expansion from the change in coefficient of thermal expansion ($\Delta\alpha$) and difference between the highest temperature experienced by the thin film and room temperature (ΔT). The strain due to thermal expansion is ε_T . The Young's modulus, E , for TiN is 590 GPa. For the TiN sample grown using PAMBE with a growth temperature of 800 °C as in Figure 49, the growth stress is 1.10 GPa, corresponding to an in-plane strain of 0.186 %. Calculating the lattice constant from several TiN samples as a function of growth temperature results in Figure 50. TiN sample lattice constants show no trend which may have been caused by thermal strain in the film.

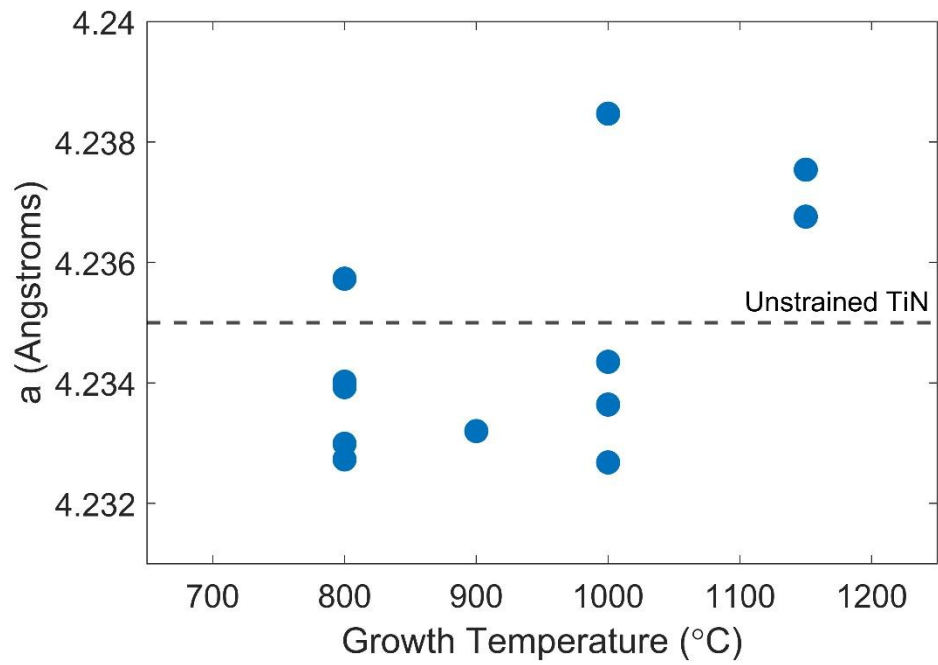


Figure 50: Lattice constants for TiN samples as a function of growth temperature. A dashed line corresponds to the ideal unstrained TiN lattice for reference.

Pole figures of the TiN (113) peak reveal six-fold symmetry that is likely caused by twinning in the material. [130], [131] Figure 51 shows this 6-fold symmetry at a χ value of approximately 30° , with the span from $25^\circ < \chi < 35^\circ$ to show the entirety of the TiN {113} peaks.

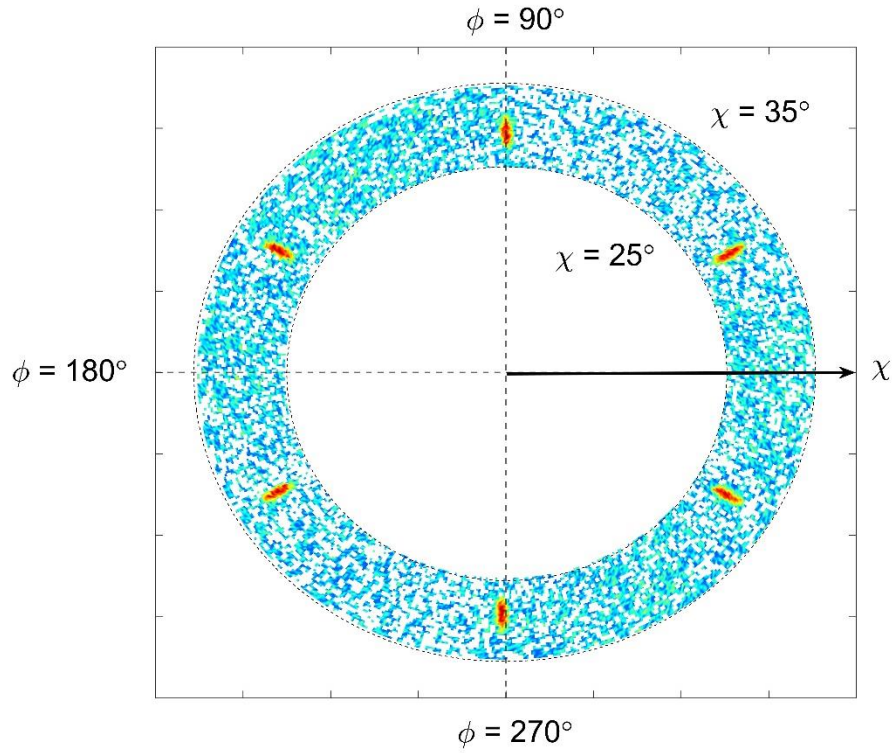


Figure 51: Pole figure of the TiN sample shown in Figure 43. Six-fold symmetry is apparent about the (113) plane.

Compositional analysis was performed using RBS, with fitting of the spectra done in SIMNRA. Figure 52 shows the TiN spectra, with a strong peak for titanium and a weaker peak for nitrogen. Plateaus in the spectra are seen for oxygen and aluminum from the Al_2O_3 substrate.

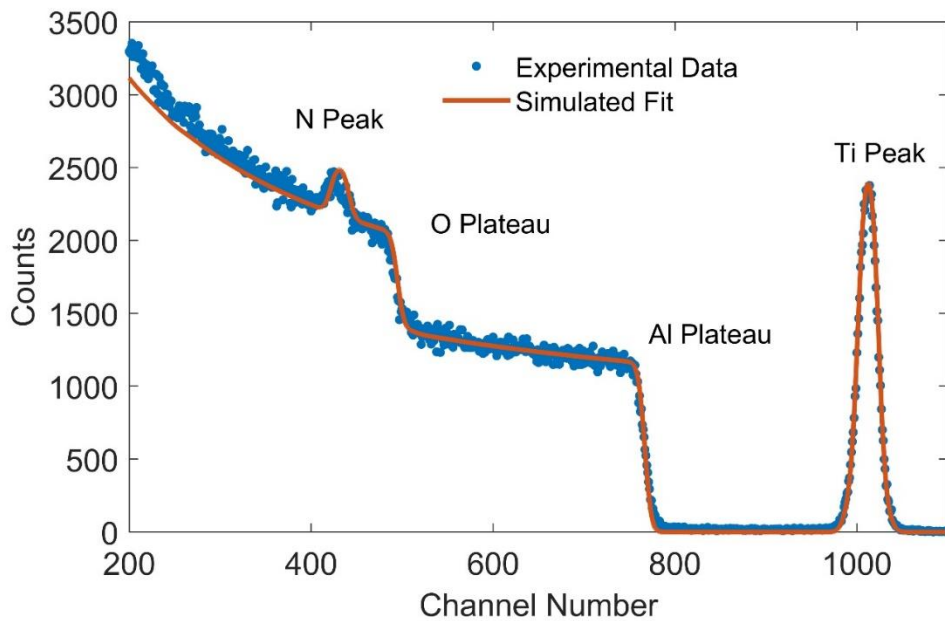


Figure 52: RBS spectra and fit for a 30-nm TiN film, showing peaks and plateaus for all constituent elements.

A thin oxide layer was added to the simulation and allowed to be fit for both composition and thickness to better match the data. This oxide layer addition does not significantly affect the composition calculated for the main TiN film. Side to side shifts in the fit as seen around the nitrogen peak can be caused by changes in the energy scaling used to fit the data, while still maintaining an accurate peak shape and intensity. Composition for the TiN film was determined to be nitrogen rich at $\text{Ti}_{0.45}\text{N}_{0.55}$. To compare with stoichiometric TiN, a simulation was run forcing the composition of the sample to be $\text{Ti}_{0.5}\text{N}_{0.5}$, shown in Figure 53.

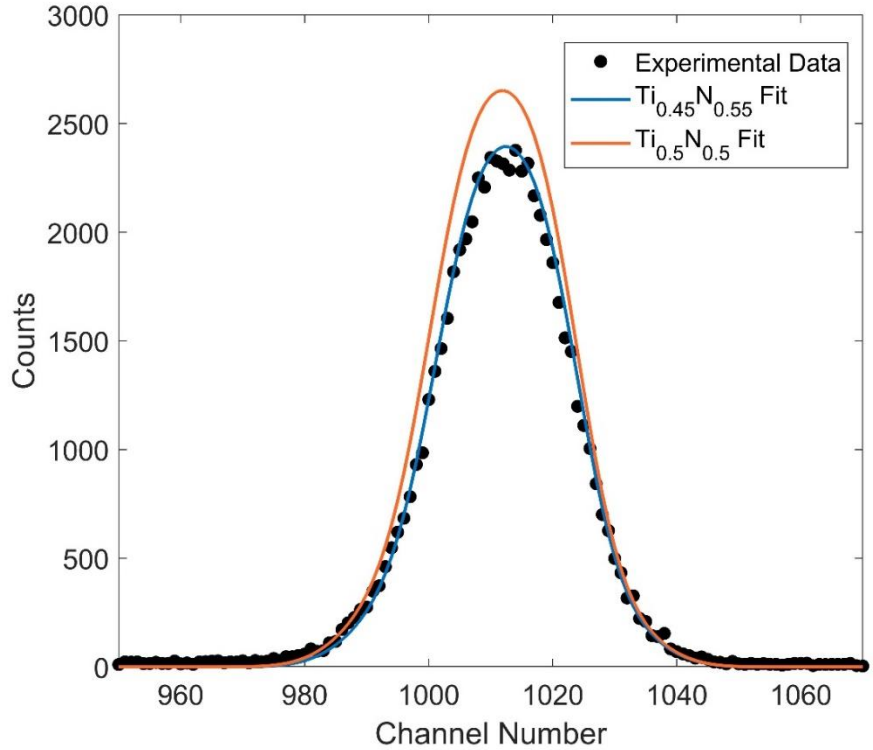


Figure 53: Comparison between RBS titanium peaks fits for stoichiometric TiN and nitrogen-rich TiN. Experimental data is also shown, which matches the nitrogen-rich simulated fit.

The simulation in Figure 53 confirms that the nitrogen content change causes a noticeable shift in the titanium peak. The heterostructure used for fitting the experimental data is shown as a schematic in Figure 54.

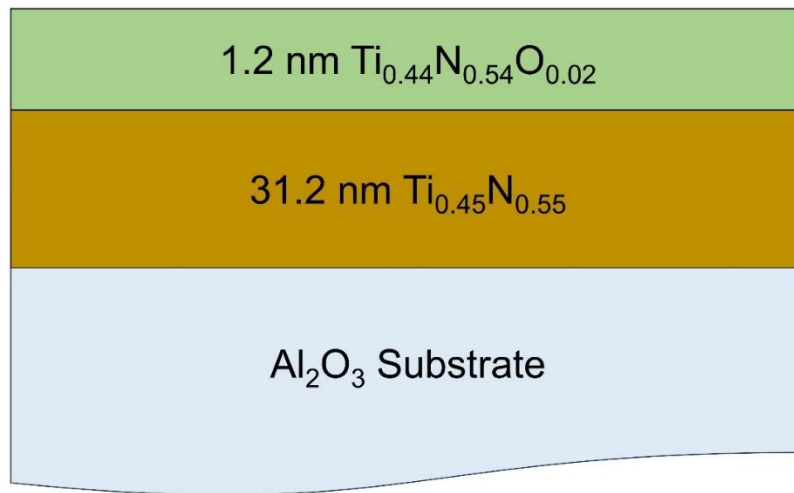


Figure 54: TiN on Al₂O₃ schematic representing the virtual structure used to fit the RBS data.

RBS simulation for the TiN sample converged to a thickness of 31.2 nm, which is similar to the thickness calculated from X-ray reflectivity data at 29.4 nm, as shown in Figure 55.

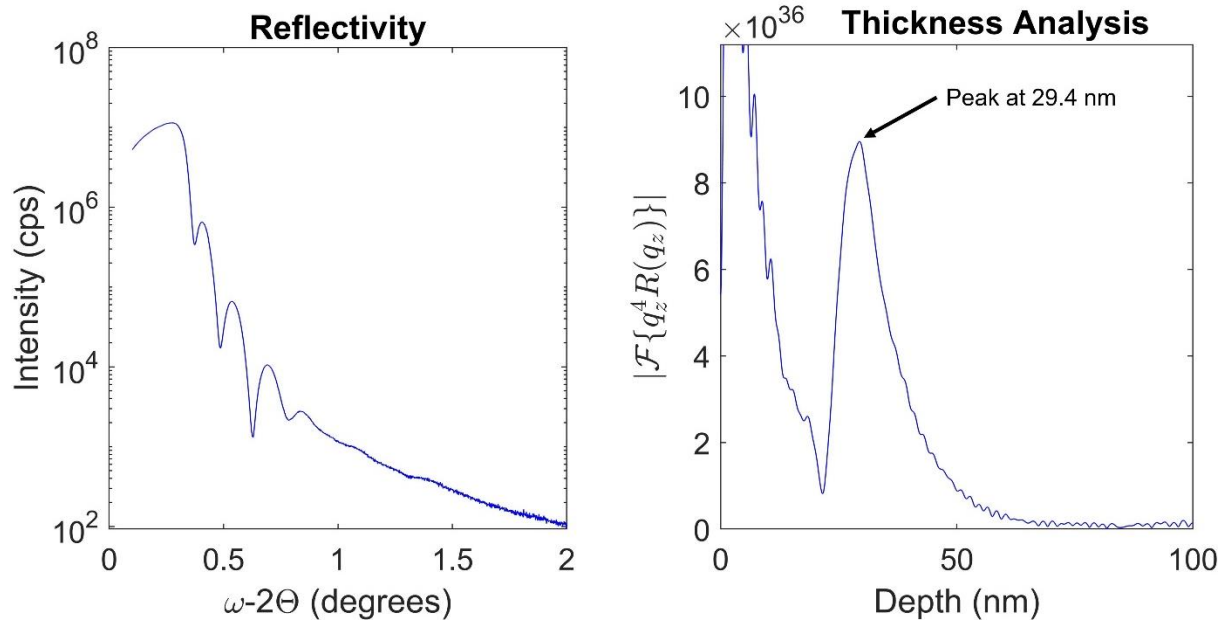


Figure 55: Reflectivity data (left) and thickness analysis (right) for a TiN sample.

3.1.3 Superconducting Properties

TiN films produced with PAMBE display a superconducting transition between 4-5 K and were fabricated into resonators to measure the quality factor and kinetic inductance of the material. Figure 56 shows the superconducting transition of a 68-nm thick TiN sample with an abrupt transition at 4.4 K. The transition width for this sample is a maximum of 0.02 K. The uncertainty in the transition width is due to the sampling interval during the measurement. RRR for this sample was 2.79, indicating metallic character.

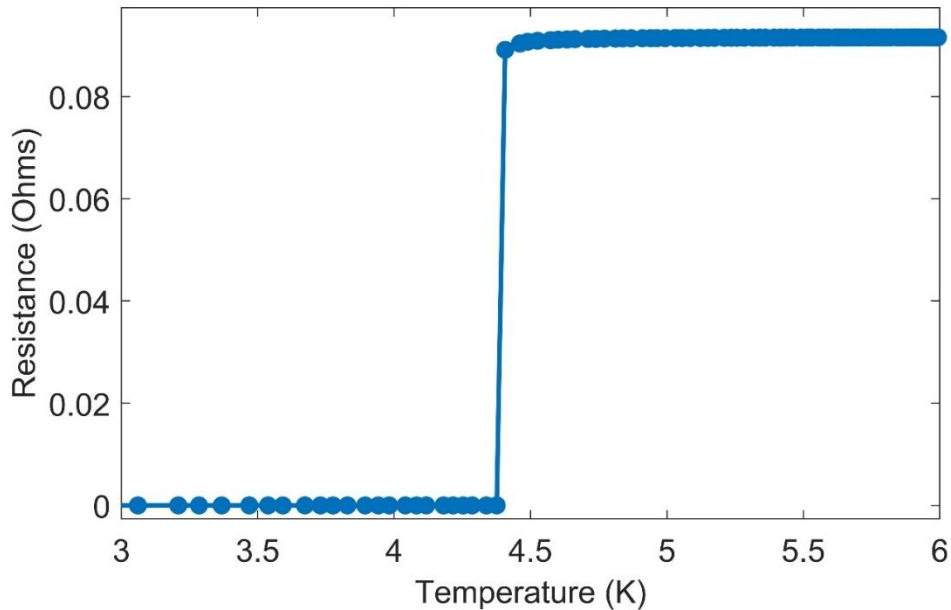


Figure 56: Superconducting transition for a 68-nm TiN sample. The floor of the data is dictated by the noise of the nanovoltmeter used to perform these measurements.

Resonators are initially found using a broad survey of the frequency range, looking at the S_{21} characteristics of the chip. Five co-planar waveguide resonators are fabricated on each chip, and so five resonances are found in the survey. Figure 57 shows the frequency range from 3.3 GHz to 4.3 GHz. Resonances are marked in red. Other less distinct features are found in the

frequency sweep and are likely caused by package modes or imperfect impedance matching of the chip to the 50- Ω cables and connectors.

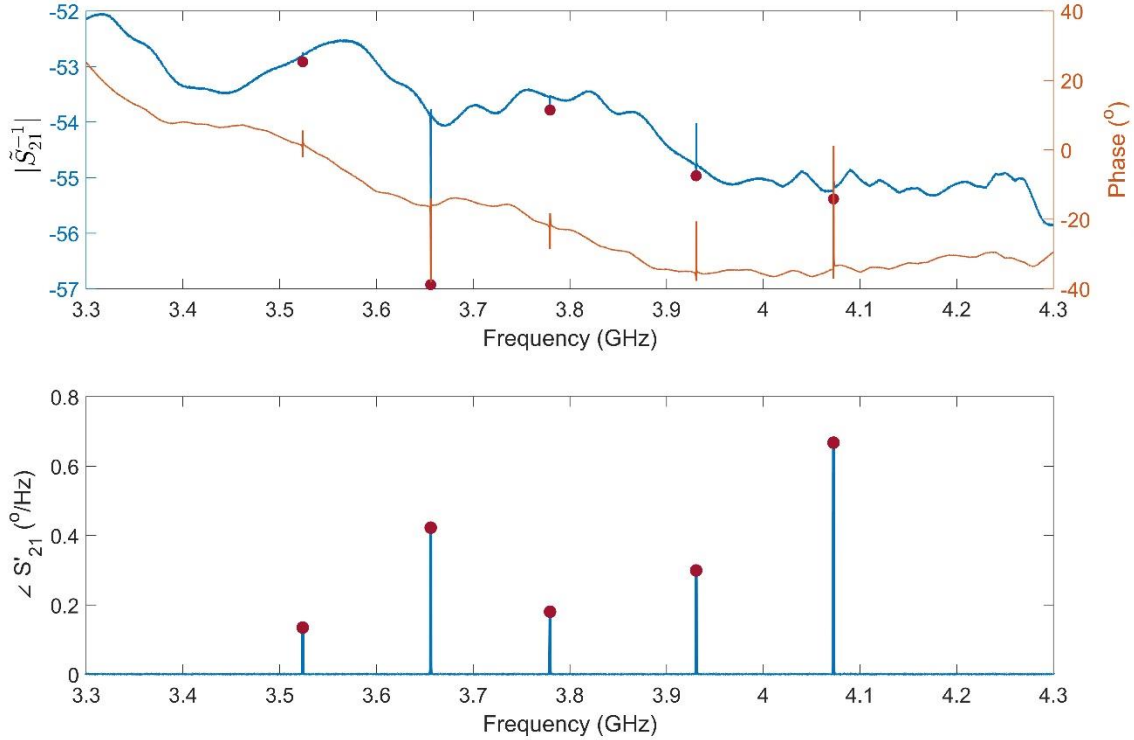


Figure 57: RF sweep of a TiN chip featuring five resonators with a common feedline.

Centering around a single resonator and decreasing the sweep range allows for finer analysis of the resonance peak. Figure 58 shows the circle fit from the real and imaginary parts of the S_{21} data. The resonator in the figure is R1 from a repeatability design mask as described in Methods section 2.7.3. This fit was performed at 35-dB of applied attenuation at a temperature of 51 mK.

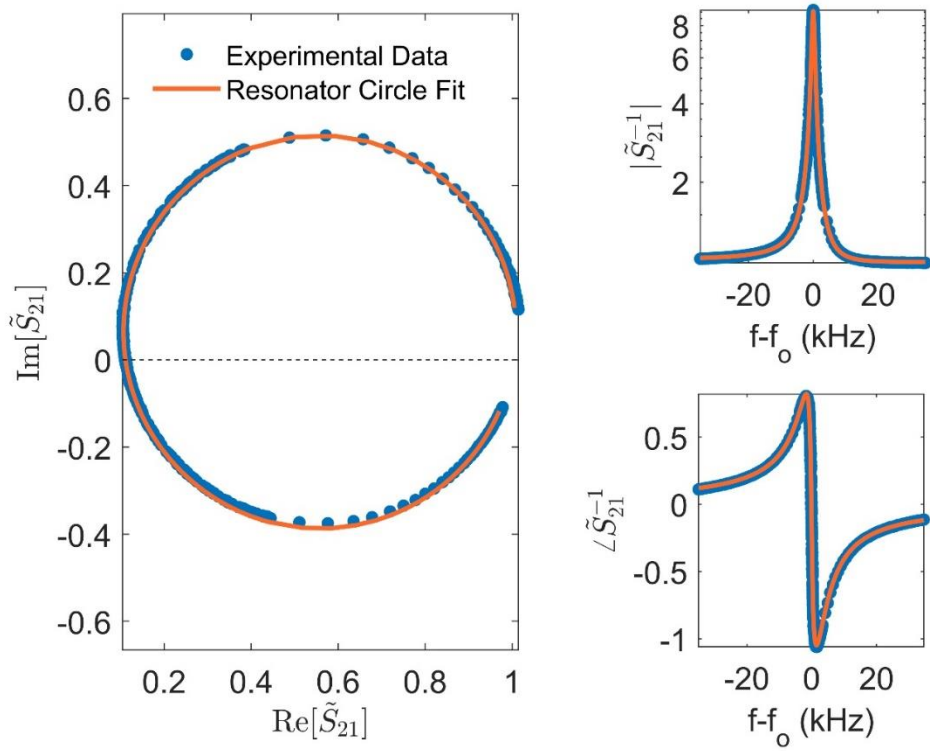


Figure 58: R1 from a TiN resonator sample with good fitting at 35-dB applied attenuation. Inverse S_{21} and phase are shown.

As the attenuation increases to reach single photon levels, the noise from the system starts to dominate and the resonator character begins to devolve. Figure 59 shows the same resonator at 65-dB of applied attenuation and shows much more spread in the data as the resonance peak loses intensity.

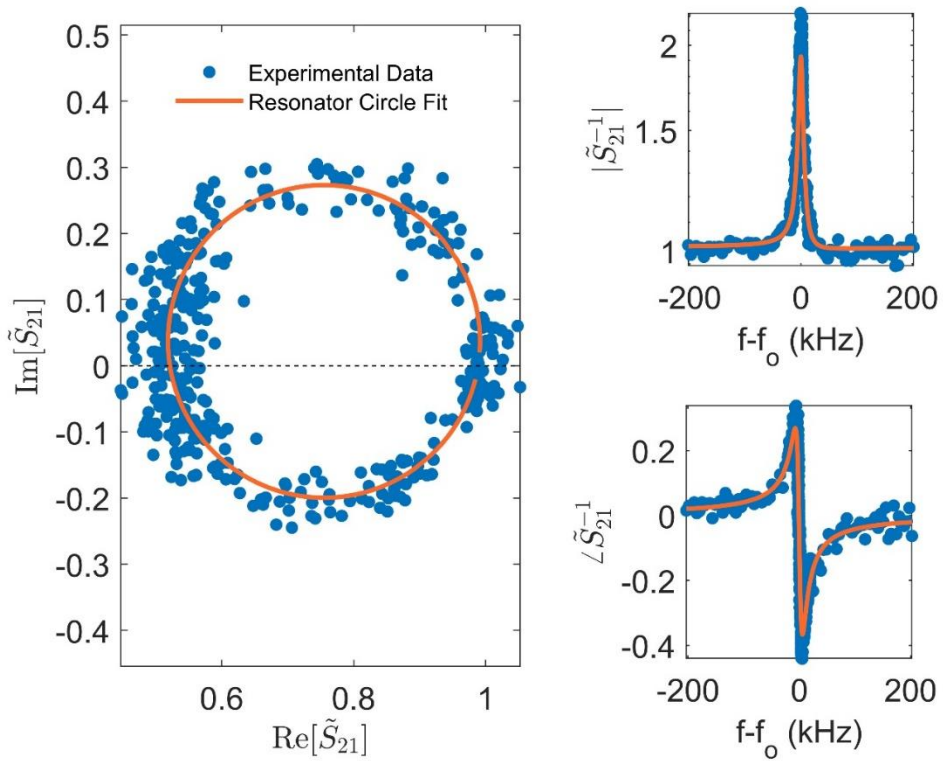


Figure 59: Resonator 1 from a TiN sample at an applied attenuation of 65 dB.

At low powers (attenuation > 75 dB), the data generally cannot be fit properly due to excessive noise in the data.

Resonators fabricated from PAMBE grown TiN show high-power internal quality factors approaching 20 million but have a much lower internal quality factor of between 200-400 thousand at the single photon level, indicated by the vertical line in Figure 60.

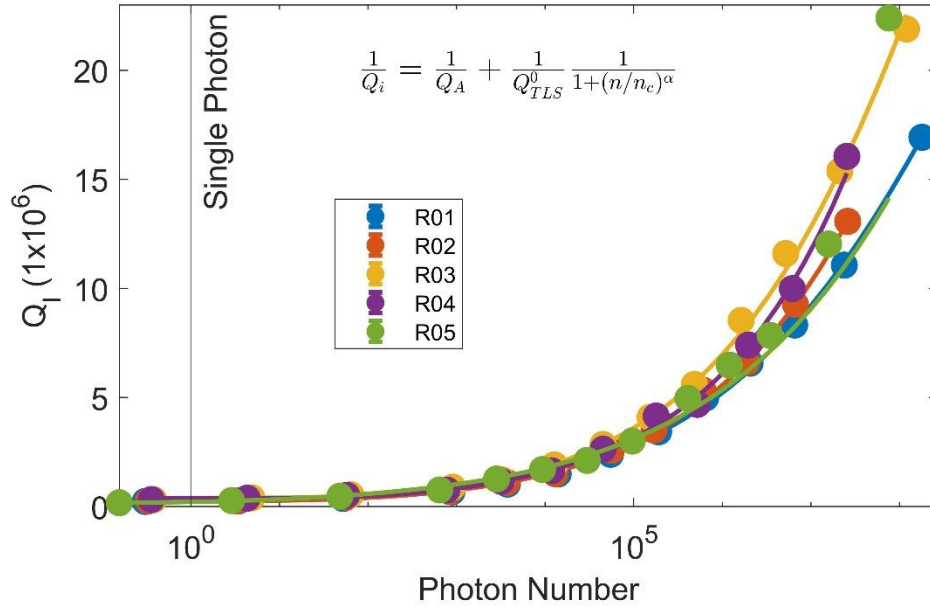


Figure 60: Power dependent internal quality factor plot for TiN resonators.

None of the resonators on this TiN chip saturate at higher powers, reaching quality factors of over 20 million at high photon numbers.

Table 4 shows the resonant frequency for the resonators fabricated on this chip, along with the variables used to fit the power dependent data.

Table 4: Values used to fit the power dependent resonator data, with the internal quality factors at single photon power as well as the maximum power during that measurement.

| Resonator | f_0 (GHz) | Q_A | Q_{TLS} | a | n_c | Q_i ($n = 1$) |
|-----------|-------------|-----------------------|-----------------------|------|-------|--------------------|
| 1 | 3.5238 | 2.11×10^{-8} | 4.01×10^{-6} | 0.29 | 18.5 | 2.52×10^5 |
| 2 | 3.6561 | 1.43×10^{-8} | 3.80×10^{-6} | 0.30 | 29.2 | 2.65×10^5 |
| 3 | 3.7795 | 1.54×10^{-8} | 2.52×10^{-6} | 0.31 | 68.3 | 3.97×10^5 |
| 4 | 3.9306 | 3.09×10^{-8} | 2.67×10^{-6} | 0.29 | 69.1 | 3.76×10^5 |
| 5 | 4.0727 | 9.40×10^{-8} | 5.71×10^{-6} | 0.25 | 0.7 | 2.16×10^5 |

3.2 Impact of Annealing Titanium Nitride

3.2.1 Topographical Changes

TiN samples exposed to the anneal process described in Methods section 2.1.3 experience a change in surface topography, evidenced by both RHEED and AFM. Figure 61 shows the RHEED of two different TiN samples both grown at 1000 °C, but with and without the anneal step. The non-annealed sample in Figure 61(a) has the typical “river-rock” surface morphology, and possesses a spotty RHEED pattern in Figure 61(c), expected for 3D growth. The sample in Figure 61(b) with the anneal step shows clear, smooth triangular domains on the surface, with interspersed pockets in the surface. These recesses form deep channels, which are several nanometers deep and cannot be accurately measured due to the size of the AFM tip.

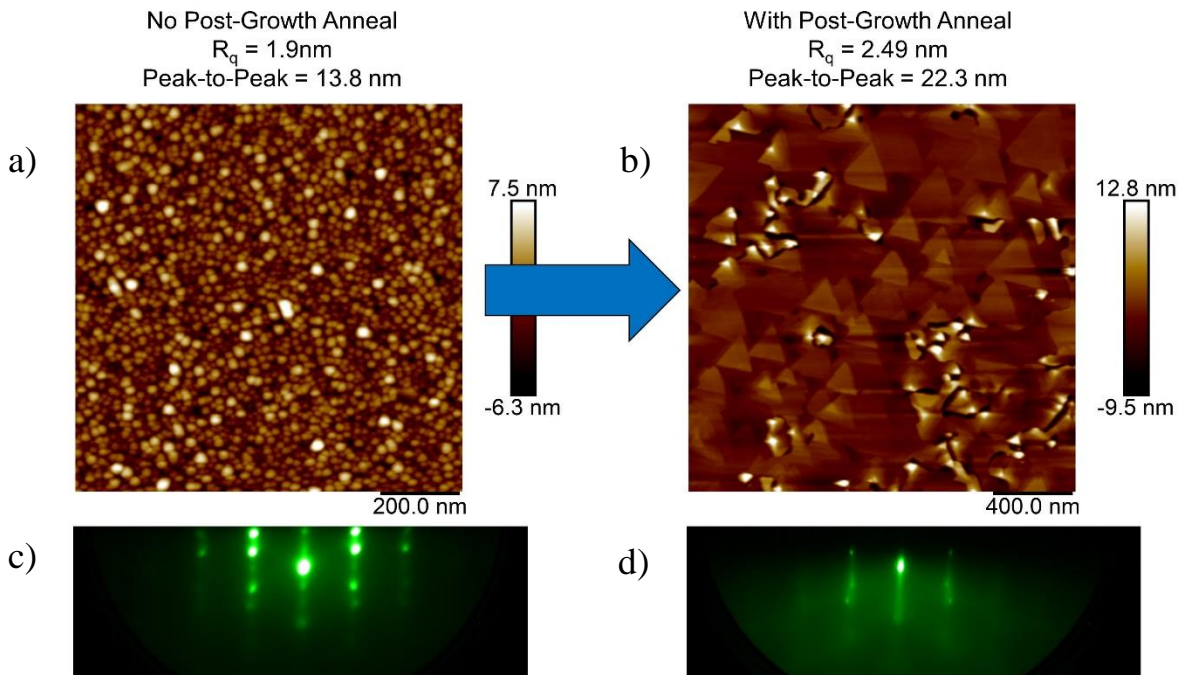


Figure 61: Surface modification of TiN sample with the addition of an anneal step at 1000 °C after growth at 1150 °C.

The RHEED pattern for the annealed sample in Figure 61(d) becomes more streaky than the unannealed sample, with some weak spots. This change in surface structure is dramatic, but due to the trench-like features, the film is not smoother than non-annealed films. The peak-to-peak roughness increases with the anneal. RMS roughness for the TiN samples increases from 1.9 nm to 2.5 nm when the trenches are included. For the smoother triangular regions, the RMS roughness is lower at 1.3 nm. The step height between triangular domains on the surface is approximately 1 nm.

RBS measurements of an annealed TiN sample show little change from the unannealed sample, with a calculated composition of $\text{Ti}_{0.46}\text{N}_{0.54}$. Similar to the non-annealed sample, TiN grown using PAMBE produces a nitrogen rich TiN sample. Figure 62 shows the RBS data with a simulated fit using the previously listed composition.

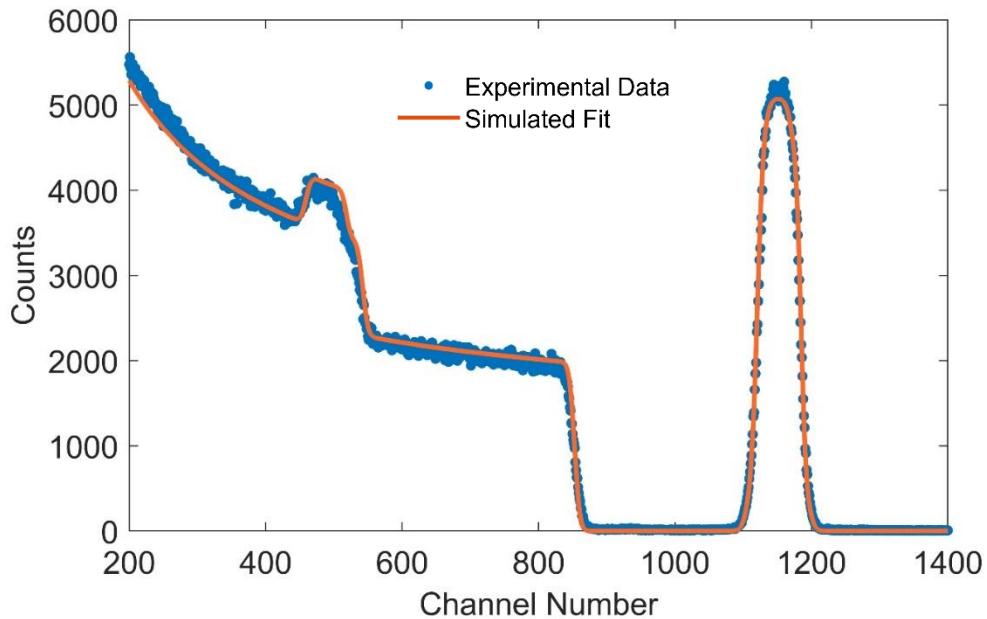


Figure 62: RBS and simulated fit for an annealed TiN sample. Growth temperature for this sample is 1150 °C, with an anneal temperature of 1000 °C for a duration of two-hours.

3.2.2 Structural Changes

Annealing TiN results in more extensive and more clearly defined thickness fringes compared to the non-annealed sample. Figure 63 shows the symmetric XRD ω - 2θ data for both the non-annealed TiN and annealed TiN with the AFM shown in Figure 61. The orange-colored sample data in Figure 63 was annealed with $T_A = 1000$ °C for a duration of 2 hours.

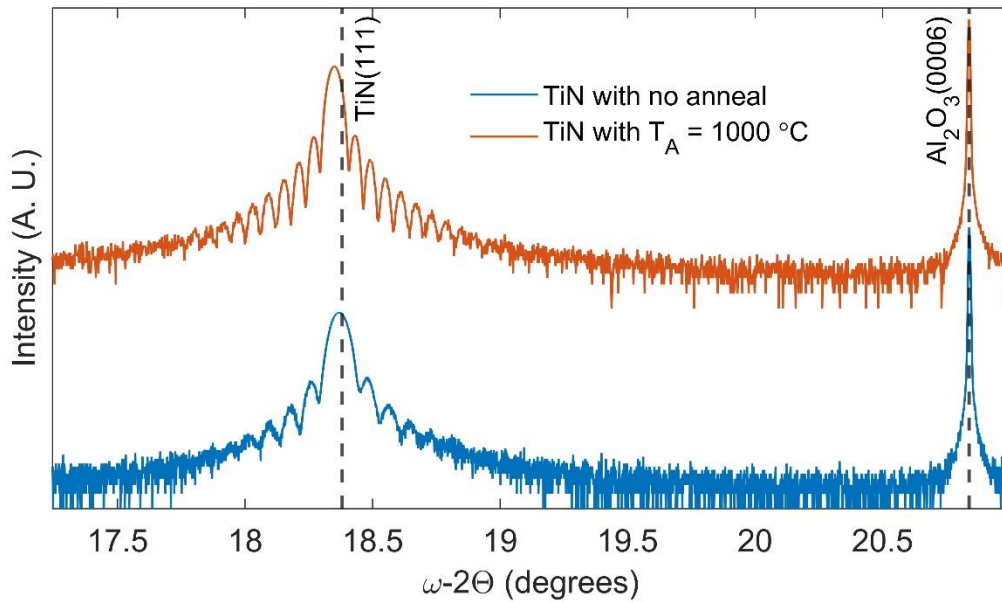


Figure 63: XRD of annealed (in blue) and unannealed (in orange) TiN samples.

Figure 64 shows x-ray reflectivity data for the two TiN samples.

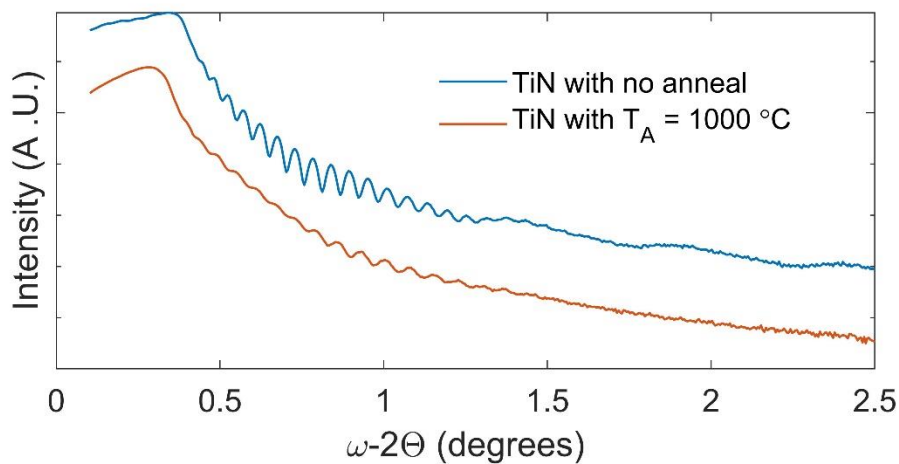


Figure 64: XRR data from two TiN samples. Blue colored data is the unannealed sample, and the orange data is the sample annealed at $T_A = 1000$ °C.

The annealed sample in orange has a thickness of 67.1 nm, while the non-annealed sample in blue has a thickness of 68.3 nm. XRR oscillations may show a decrease in intensity for the annealed sample due to the increase in surface roughness when compared to the unannealed sample.

While the presence of thickness fringes on the non-annealed sample is evidence of good crystal quality, the additional fringes seen in the annealed sample may be due to improved crystal quality of the film. The non-annealed sample possessed a lattice constant $a = 4.234 \text{ \AA}$, while the annealed sample had an increase of 0.07 % over the non-annealed sample with a lattice constant $a = 4.237 \text{ \AA}$.

Investigating the RSM data collected from the annealed TiN (113) asymmetric peak results in the map shown in Figure 65. The magenta line represents the streaking that might be seen for a TiN sample with an undistorted cubic lattice constant variation of $\pm 1 \%$. The red line represents the horizontal shift that should be seen in a sample due to biaxial strain from a difference in coefficient of thermal expansion between the TiN film and the sapphire substrate when grown with $T_G = 1000 \text{ }^\circ\text{C}$.

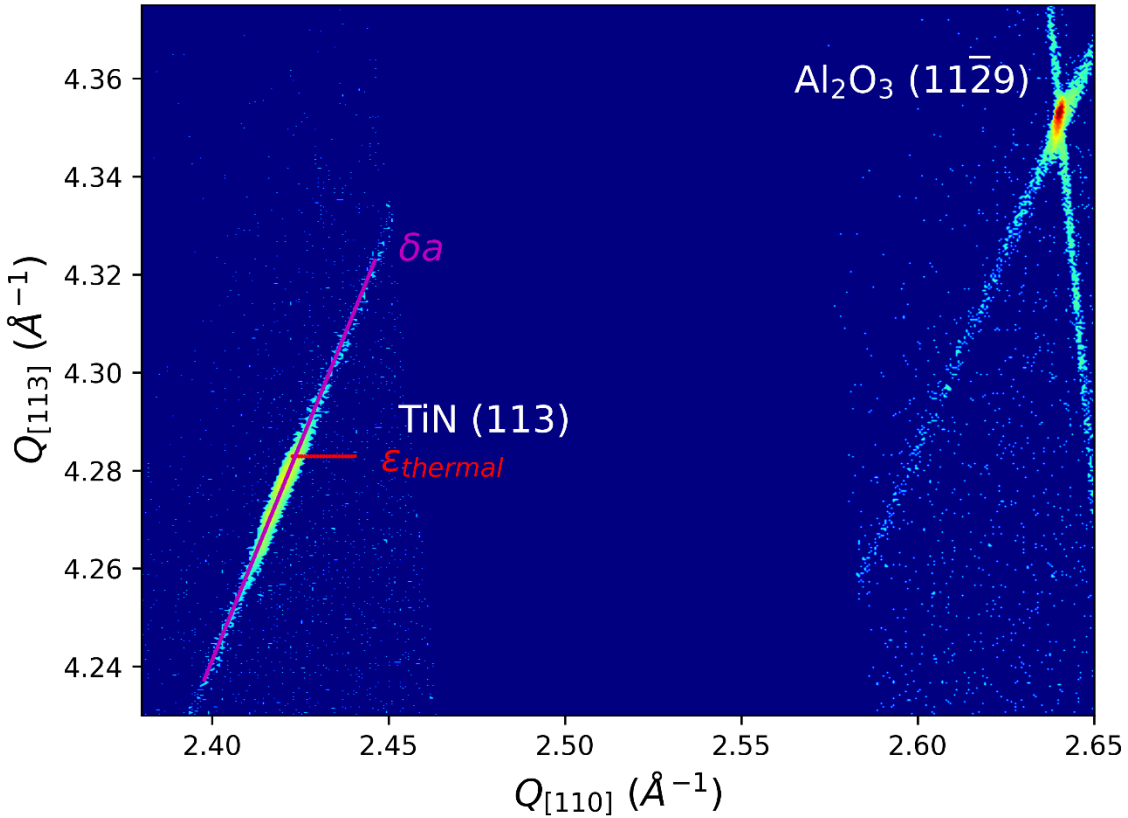


Figure 65: RSM from a TiN sample annealed at 1000 °C for two hours. The Al_2O_3 ($11\bar{2}9$) and TiN (113) asymmetric peaks are seen.

Taking the intensity cross section through the magenta line for both the annealed and unannealed sample shows the width of the peak, and variation in lattice constant between samples. Both samples show similar spreading along δa , with minimal spreading along the thermal strain line. The data of this cross section is fit with a Gaussian curve, then normalized and shifted so the peaks are lined up with each other. This is shown in Figure 66.

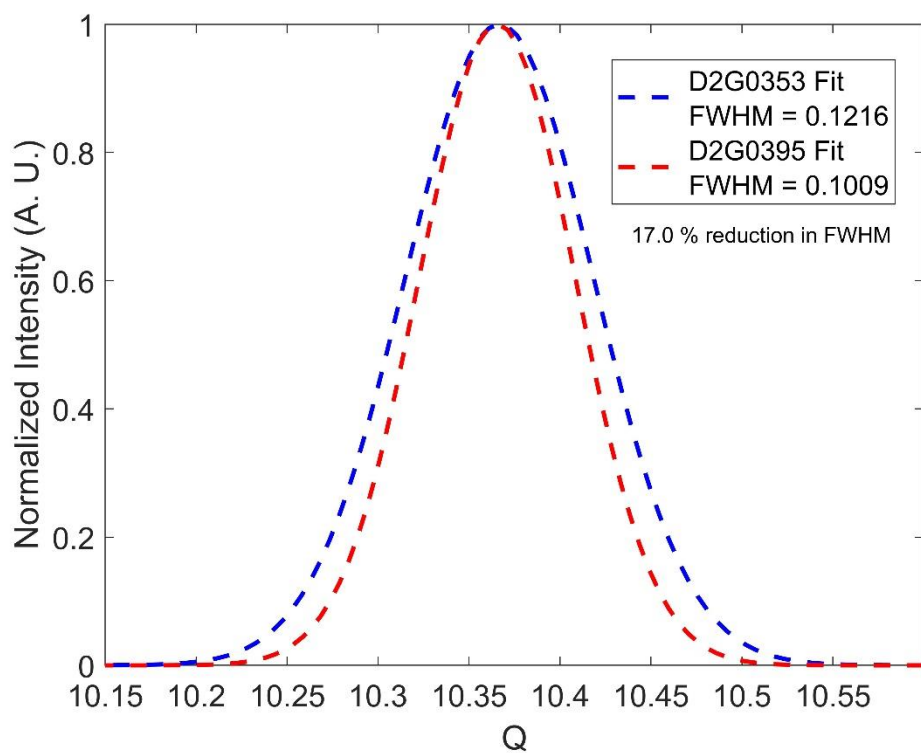


Figure 66: Gaussian fits of the cross sectional RSM data for an annealed and unannealed TiN sample.

The FWHM of the Gaussian fit shows a 17 % reduction for a TiN sample with the annealing process.

3.2.3 Superconducting Properties

The superconducting transition temperature of TiN samples produced with an anneal step post growth show improvement over an unannealed sample. The topography change seen in a TiN sample grown at 1150 °C does not occur in a similarly grown sample with $T_G = 1000$ °C, but both samples experience an increase in T_c over non-annealed samples. Figure 67 shows a selection of TiN samples, with the orange line denoting an unannealed sample. The yellow and purple lines are from measurements made from annealed TiN samples.

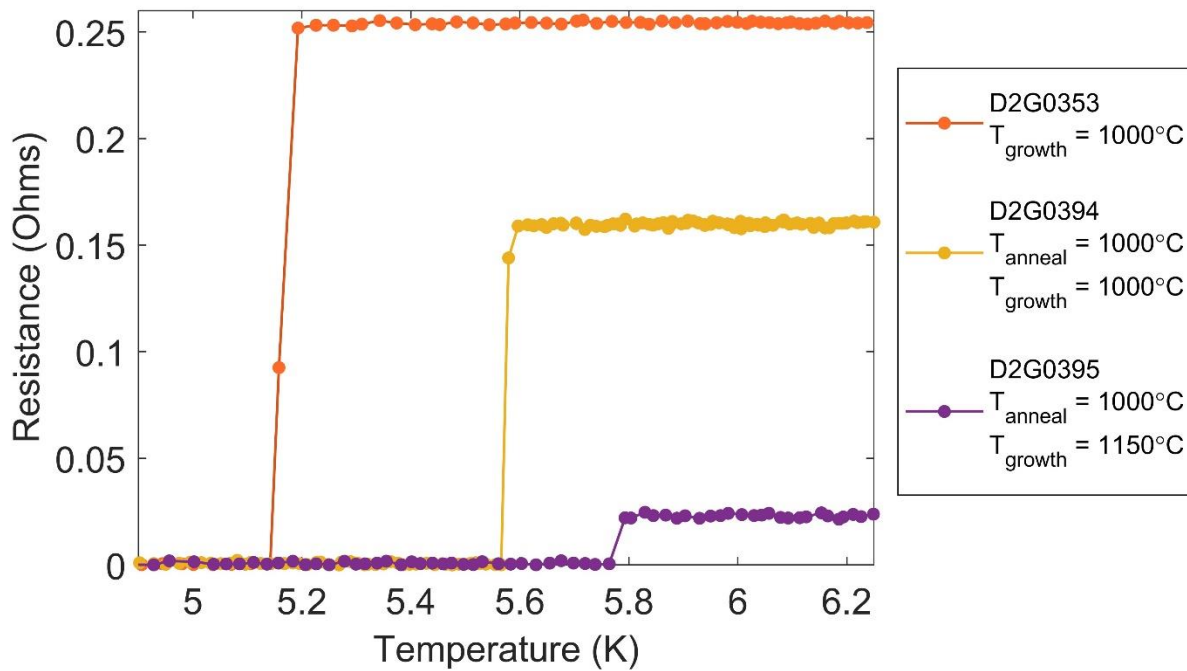


Figure 67: Superconducting transitions for two annealed and two non-annealed TiN samples.

Table 5 shows the superconducting properties of the three samples shown in Figure 67.

Table 5: Superconducting characteristics of annealed and non-annealed TiN samples.

| Sample Number | T _G (°C) | T _A (°C) | T _c (K) | Maximum ΔT (K) | RRR |
|---------------|---------------------|---------------------|--------------------|----------------|-------|
| D2G0353 | 1000 | N/A | 5.167 | 0.047 | 3.426 |
| D2G0394 | 1000 | 1000 | 5.576 | 0.029 | 3.636 |
| D2G0395 | 1150 | 1000 | 5.779 | 0.028 | 14.16 |

Table 5 shows that annealed samples possess elevated transition temperatures of approximately 10% higher than non-annealed samples. RRR varies between samples, with the sample experiencing the topographical change seen in Figure 61 reaching a RRR of over 14.

3.3 Niobium Nitride

3.3.1 Growth Process

NbN_x films were grown following the same wafer prep procedure as TiN films. Due to the higher temperature required to produce adequate niobium flux compared to titanium, an electron beam evaporator is used to generate the metal flux.

In Figure 68, the dip in chamber pressure beginning at hour 2 is due to the electron beam evaporator increasing in power above the nominal operational power to form a melt on the surface of the source material. This increase in power results in increased Nb flux, which acts as a getter for nitrogen and other gases in the chamber, lowering the pressure. The noise seen in the

Nb power is due to the EIES PID loop adjusting the evaporator power in real time to maintain a target EIES rate, shown in blue. This allows for precise generation of Nb flux, as maintaining the evaporator power manually or with a set power value results in significant drift of the EIES rate over time.

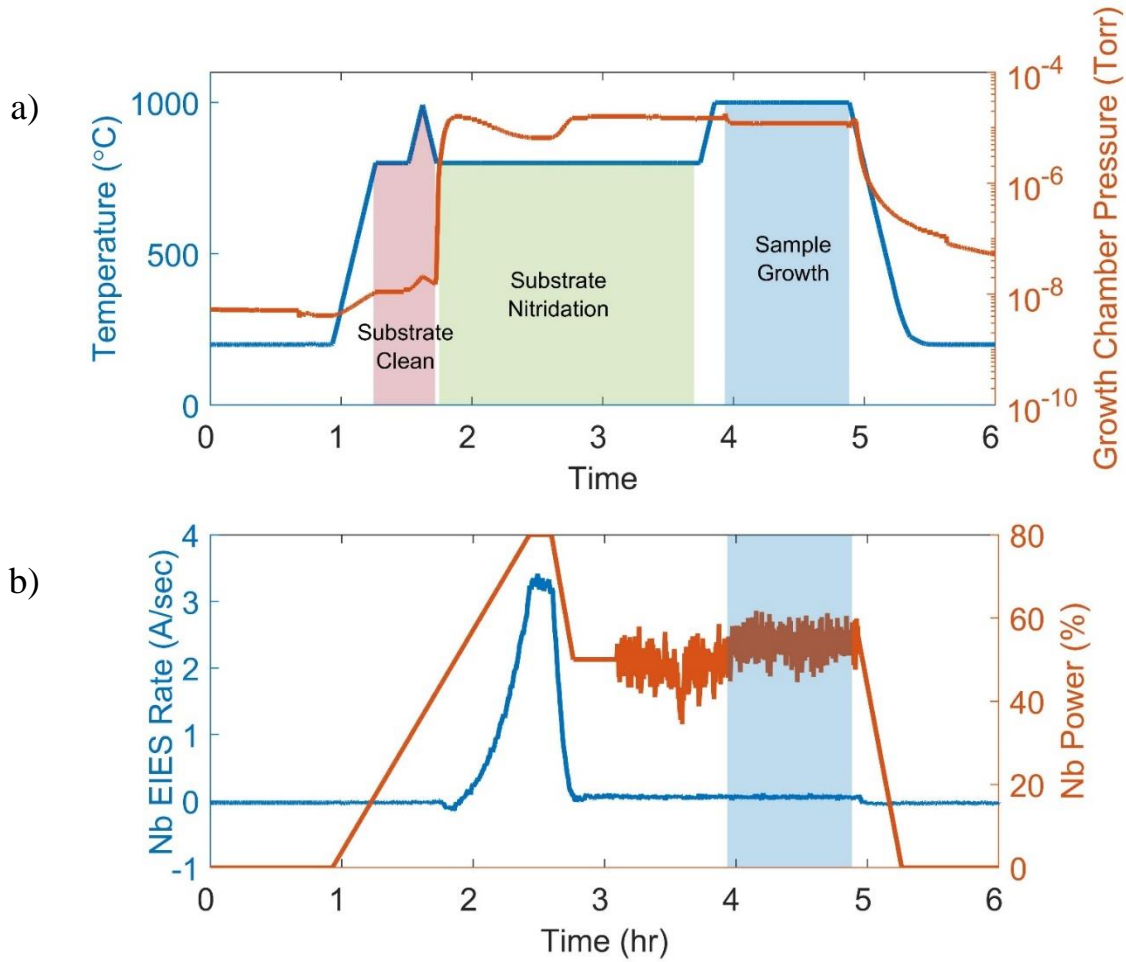


Figure 68: Growth process for a NbN_x sample. a) Typical temperature and pressure trends through the growth. b) EIES control and electron gun output power data during the growth.

The composition of NbN_x was determined using RBS as shown in Figure 69.

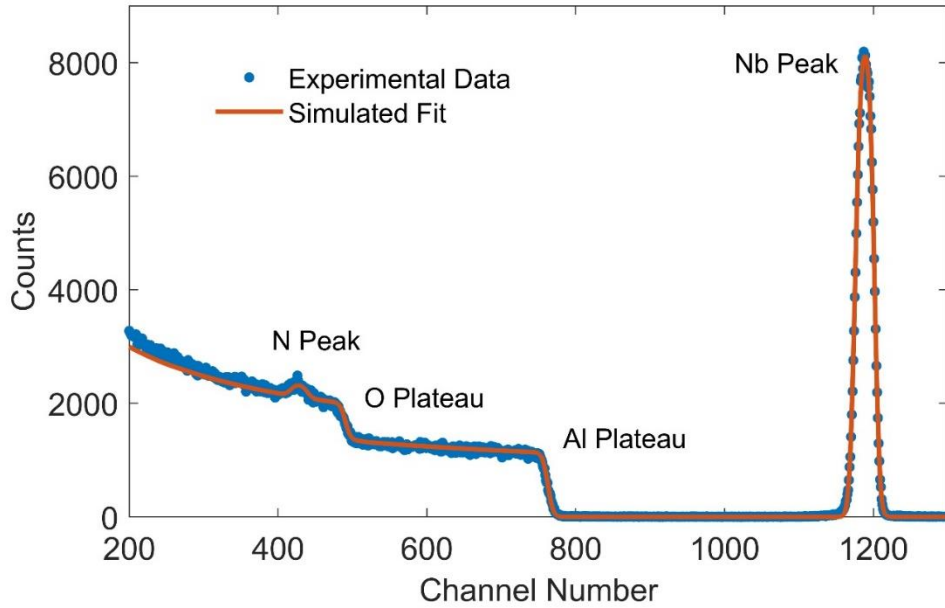


Figure 69: RBS data and simulated fit from a 30-nm thick NbN_x sample.

The RBS data is fit using a simulation where the main film is 29.3-nm-thick with a composition of $\text{Nb}_{0.52}\text{N}_{0.48}$. A thin oxide layer is added on the top of the heterostructure to improve the fit and converges to a thickness of 1.1 nm with a composition of $\text{Nb}_{0.45}\text{N}_{0.50}\text{O}_{0.05}$. Figure 70 shows the heterostructure used to produce the fit in Figure 69.

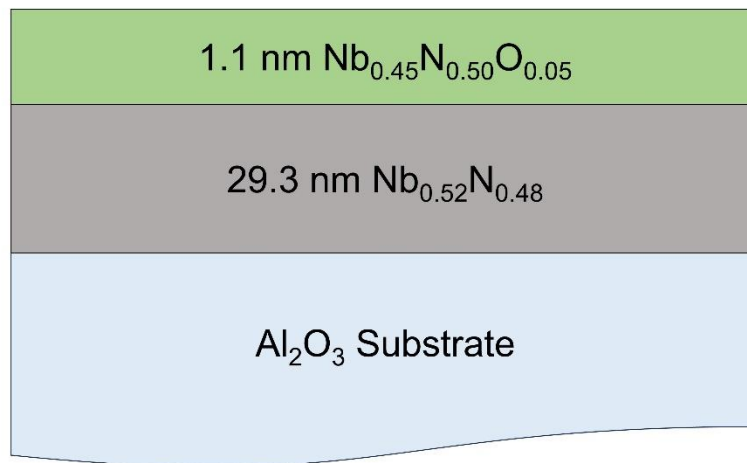


Figure 70: RBS simulation structure for a ~30 nm NbN_x sample.

XRR for the NbN_x sample is shown in Figure 71.

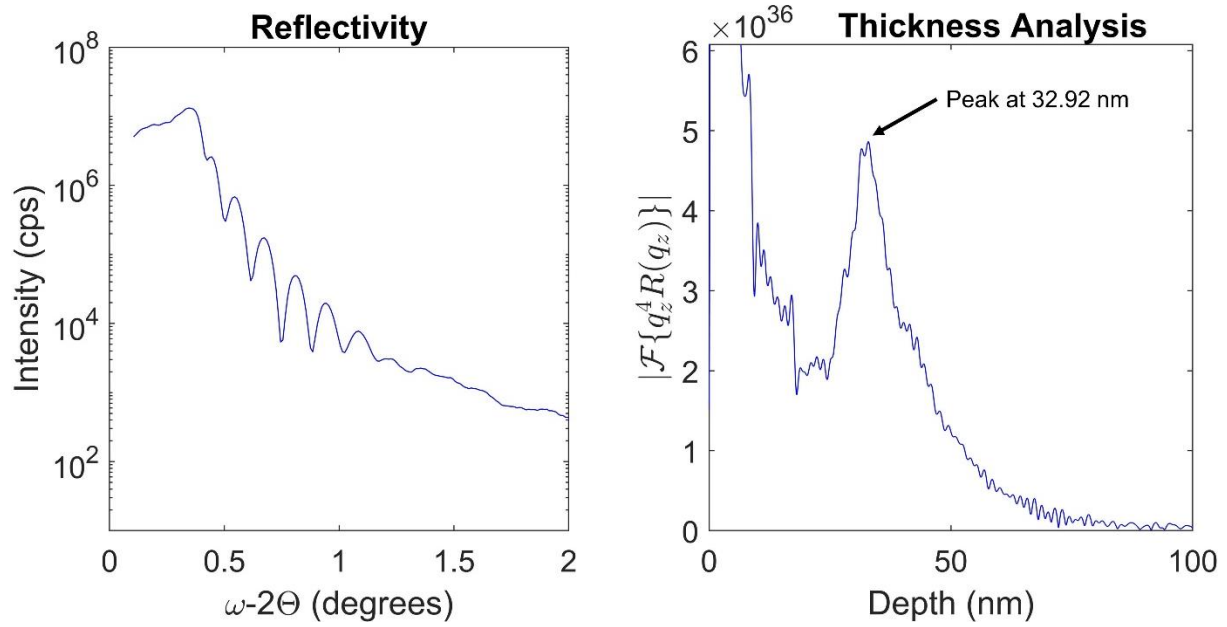


Figure 71: Reflectivity data (left) and thickness analysis (right) for a 32.92-nm thick NbN_x sample.

The added oxide layer of the RBS heterostructure brings the total thickness to 30.4 nm, which is close to the measurement performed using XRR, with a thickness of 32.92 nm.

3.3.2 Phase Identification

NbN_x films grown by PAMBE do not grow with the desired rock salt cubic structure, $\delta\text{-NbN}$, but instead form a hexagonal phase, $\varepsilon\text{-NbN}$, a nitrogen deficient tetragonal rock-salt-like phase, $\gamma\text{-Nb}_4\text{N}_3$, or a combination of both. The ratio of $\varepsilon\text{-NbN}$ to $\gamma\text{-Nb}_4\text{N}_3$ is dependent on the substrate temperature, the Nb flux, and the thickness of the film. The peaks expected from the NbN_x films grown are $\gamma\text{-Nb}_4\text{N}_3$ (111) at 17.8165° , and $\varepsilon\text{-NbN}$ (0004) at 15.9018° . The peak for $\delta\text{-NbN}$ (111) at 17.4711° is not evident in any samples grown. Figure 72 shows a 30-nm-thick NbN_x single phase film. Thickness fringes are evident around the clear $\gamma\text{-Nb}_4\text{N}_3$ (111) peak.

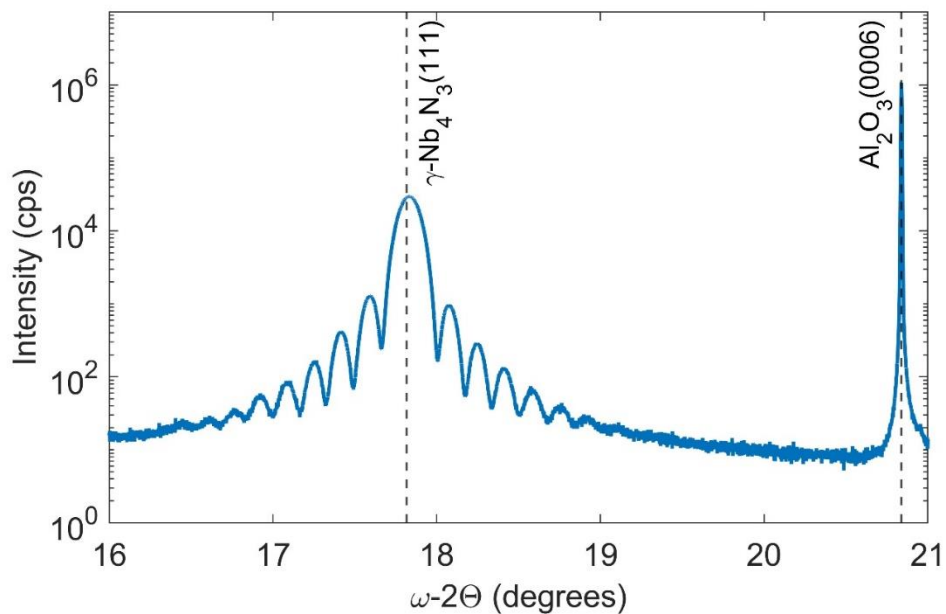


Figure 72: Symmetric XRD of a $\gamma\text{-Nb}_4\text{N}_3$ sample showing (111) orientation with no evidence of other phases or orientations.

Fitting the RBS data with a simulation where the NbN_x composition is forced to be Nb_4N_3 results in an overestimation of the Nb peak intensity, indicating that the crystal structure and composition implied by the XRD results for this sample do not entirely line up with the RBS

data collected from the same sample. Figure 73 shows the RBS fit with a set $\gamma\text{-Nb}_4\text{N}_3$ composition compared with the fitted solution used to determine the composition of the film.

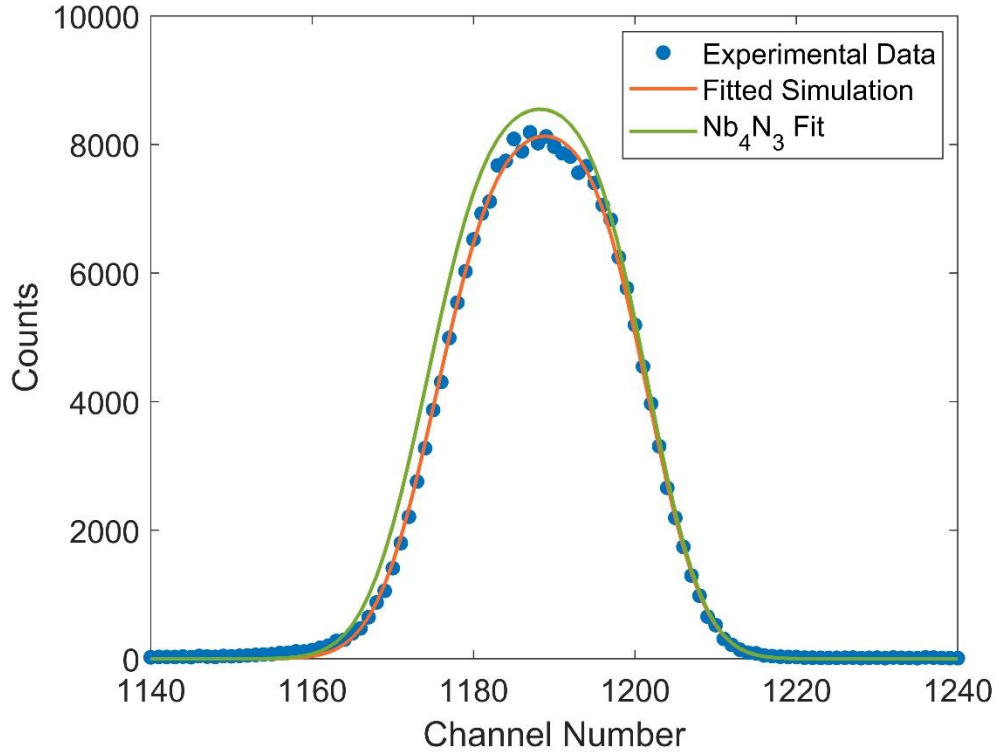


Figure 73: RBS data from a $\gamma\text{-Nb}_4\text{N}_3$ sample with fits using the composition of the gamma phase and the iteratively fit solution giving a composition of $\text{Nb}_{0.52}\text{N}_{0.48}$.

For samples grown to a nominal thickness of 100 nm, with Nb fluxes greater than 1×10^{17} atoms/ m^2s , three peaks emerge in the symmetric XRD data, $\epsilon\text{-NbN}$ (10 $\bar{1}0$), $\epsilon\text{-NbN}$ (0001), and $\gamma\text{-Nb}_4\text{N}_3$ (111). In Figure 74, these three peaks can be clearly seen, and the relative intensities of each of these peaks vary with changing growth conditions.

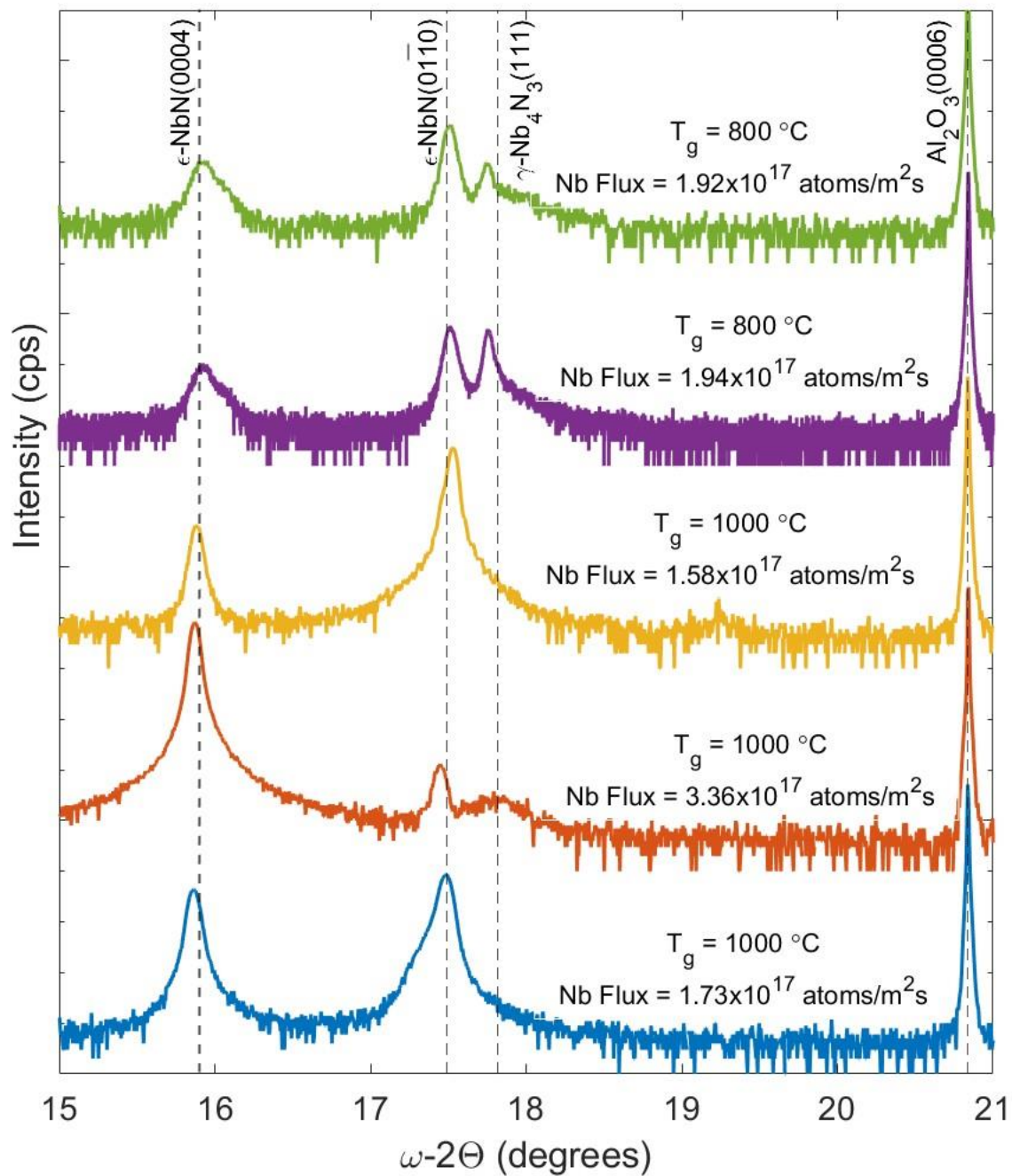


Figure 74: Symmetric XRD ω - 2θ data of several NbN_x films showing peaks from two phases, γ -Nb₄N₃, and ϵ -NbN. Data is offset vertically for clarity.

To quantify the relative composition of each phase in these samples, the relative intensity can be calculated by summing the area under each peak, and comparing against the other peaks.

A Gaussian is fit to each peak using

$$f(x) = \frac{1}{\sigma\sqrt{2\pi}} e^{-\frac{1}{2}\left(\frac{x-\mu}{\sigma}\right)^2}, \quad (49)$$

where σ is the Gaussian width, and μ is the Gaussian center. A baseline intensity is determined by averaging the intensity between 19.5 ° and 20.5 °, where NbN_x peaks do not occur. Using the fits, a peak area is found with

$$A_{peak} = \sum_{G_c - (n*G_w)}^{G_c + (n*G_w)} I - I_0. \quad (50)$$

Here, G_c is the fitted Gaussian peak center, G_w is the Gaussian peak FWHM, I_0 is the baseline intensity or noise floor, and n is a FWHM width adjustment. The full width half max (FWHM) of the Gaussian peak is modified using n to prevent significant overlap between the ϵ -NbN (10 $\bar{1}$ 0) and γ -Nb₄N₃ (111) peaks. The width modifier n is nearly always zero unless the peak intensities of overlapping peaks are exceptionally low. From this, a fractional area of each phase and orientation can be extracted by summing the intensities over the range, and taking the fraction of the phase or orientation of interest as

$$Fraction_{NbN_x} = \frac{A_{NbN_x}}{A_{\epsilon-NbN(0001)} + A_{\epsilon-NbN(10\bar{1}0)} + A_{\gamma-Nb_4N_3(111)}}. \quad (51)$$

This phase fraction is shown in a heat map with changing substrate temperature and Nb flux in Figure 75. A constant nitrogen flux is used for all samples captured in these figures.

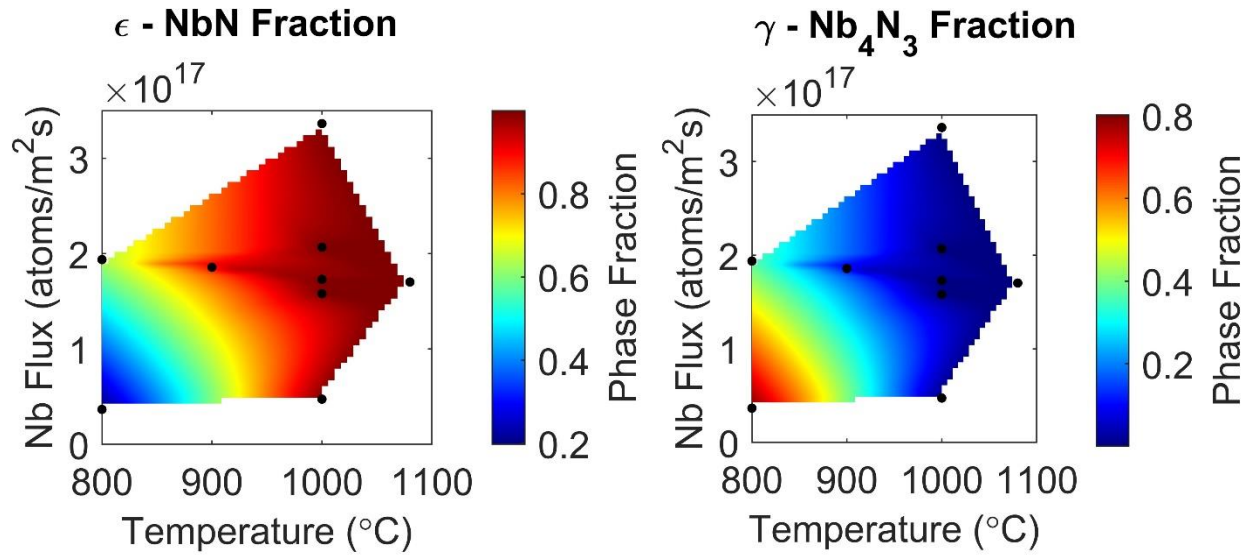


Figure 75: Heatmap of epsilon and gamma phases of NbN_x as substrate temperature and Nb flux are varied.

From these heatmaps, the epsilon phase grows preferentially at higher temperatures and Nb fluxes, while the tetragonal gamma phase is dominant at lower temperatures.

Diving further into the ϵ -NbN phase, two distinct growth regimes appear, with the ϵ -NbN (0001) orientation becoming more favorable at higher temperatures and metal fluxes, and the ϵ -NbN (10 $\bar{1}$ 0) orientation becoming the dominant phase at intermediate temperatures in the temperature range studied.

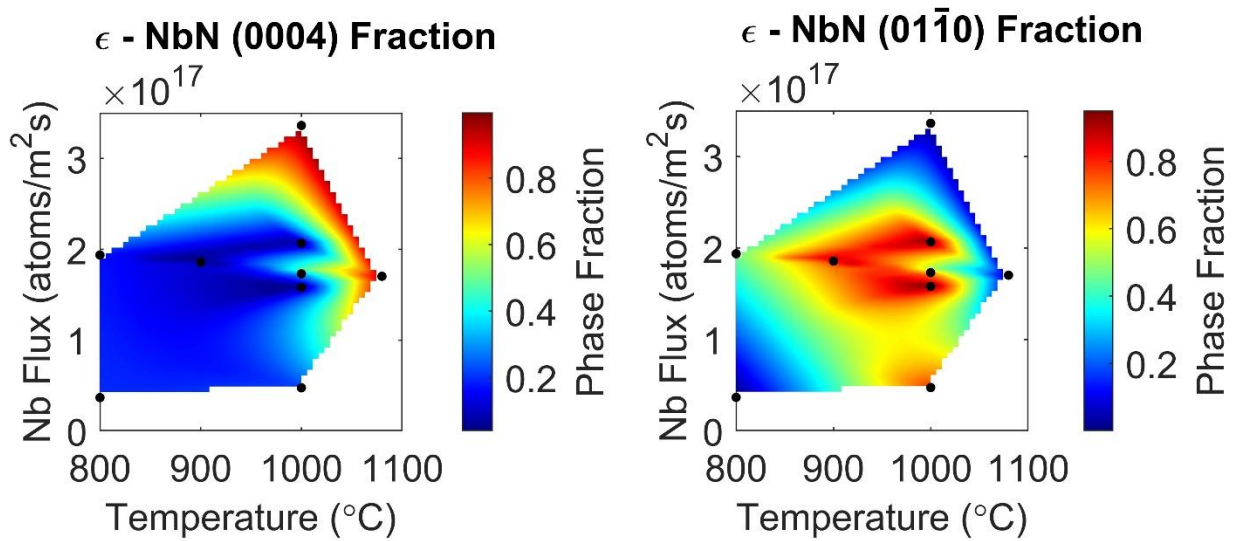


Figure 76: Heatmap comparing the two favorable orientations of ϵ -NbN as substrate temperature and Nb flux are varied.

Figure 77 compares XRD data from a 63-nm-thick NbN_x sample grown at 500 °C to a 30-nm-thick NbN_x sample grown at 800 °C, showing the effect of lower growth temperatures.

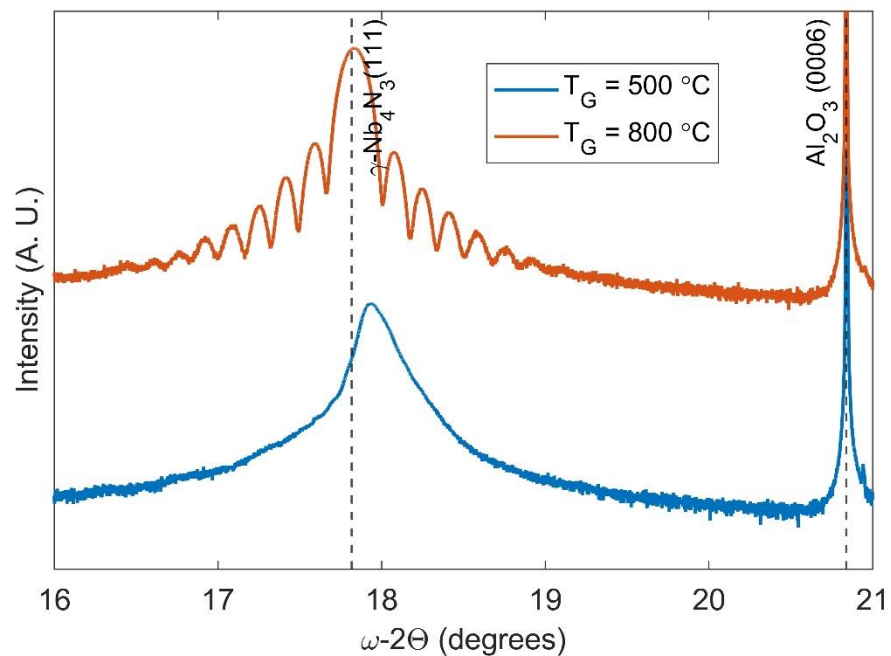


Figure 77: XRD of NbN_x samples grown at 500 °C and 800 °C. The lower growth temperature produces low quality films, setting the lower temperature bound for the phase fraction heatmaps.

3.3.3 Surface Topography

Surface topography of NbN_x samples is quite varied, with substrate temperature, metal flux, and film thickness having a significant effect on the final surface of NbN_x . For samples thinner than 40 nm, at a substrate temperature of 800 °C, and growth rates of 0.01 – 0.02 nm/sec, NbN_x grows primarily in the $\gamma\text{-Nb}_4\text{N}_3$ phase, forming a “river-rock” topography similar to TiN films. NbN_x with this river-rock surface generally possesses an R_q that is an order of magnitude less than TiN films of similar thickness, with the sample in Figure 78 possessing a surface roughness of 0.61 nm. RHEED for $\gamma\text{-Nb}_4\text{N}_3$ samples forms a streaky pattern with spots of higher intensity.

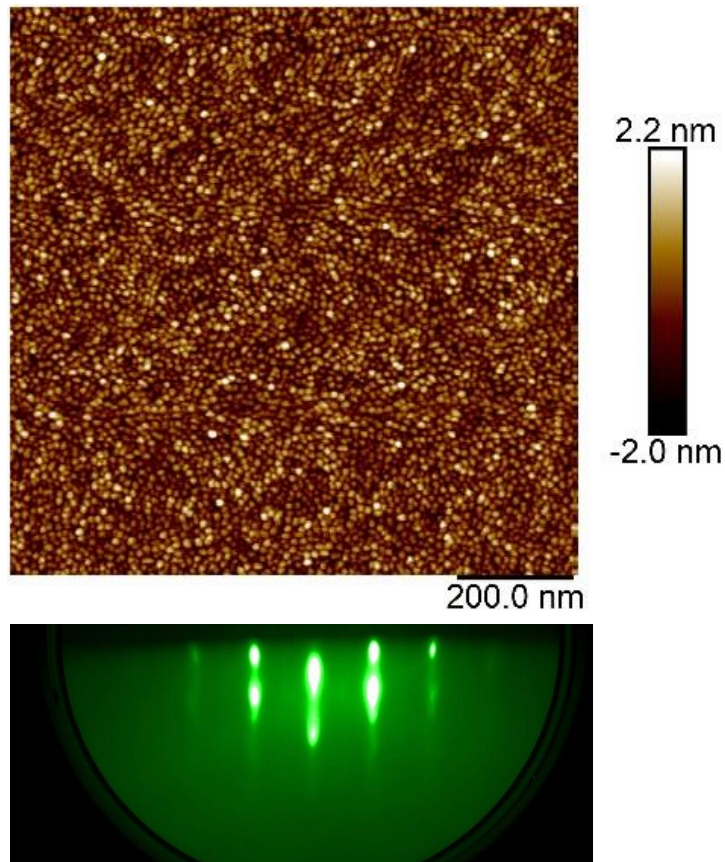


Figure 78: $\gamma\text{-Nb}_4\text{N}_3$ AFM (top) and RHEED (bottom), with a "river-rock" topography similar to TiN. $\gamma\text{-Nb}_4\text{N}_3$ surfaces have a lower R_q than TiN samples

For samples thicker than 40 nm and grown at temperatures above 800 °C, both ϵ -NbN and γ -Nb₄N₃ grow concurrently. Each phase and orientation possess a distinct surface morphology and RHEED pattern. In Figure 79, Sample A was grown at a substrate temperature of 800 °C with a Nb flux of 1.9×10^{17} atoms/m²s. Sample B was grown at a substrate temperature of 1000 °C with a Nb flux of 3.4×10^{17} atoms/m²s. Sample C was grown at a substrate temperature of 1000 °C with a Nb flux of 1.6×10^{17} atoms/m²s. All samples underwent the same wafer prep and had identical nitrogen plasma conditions.

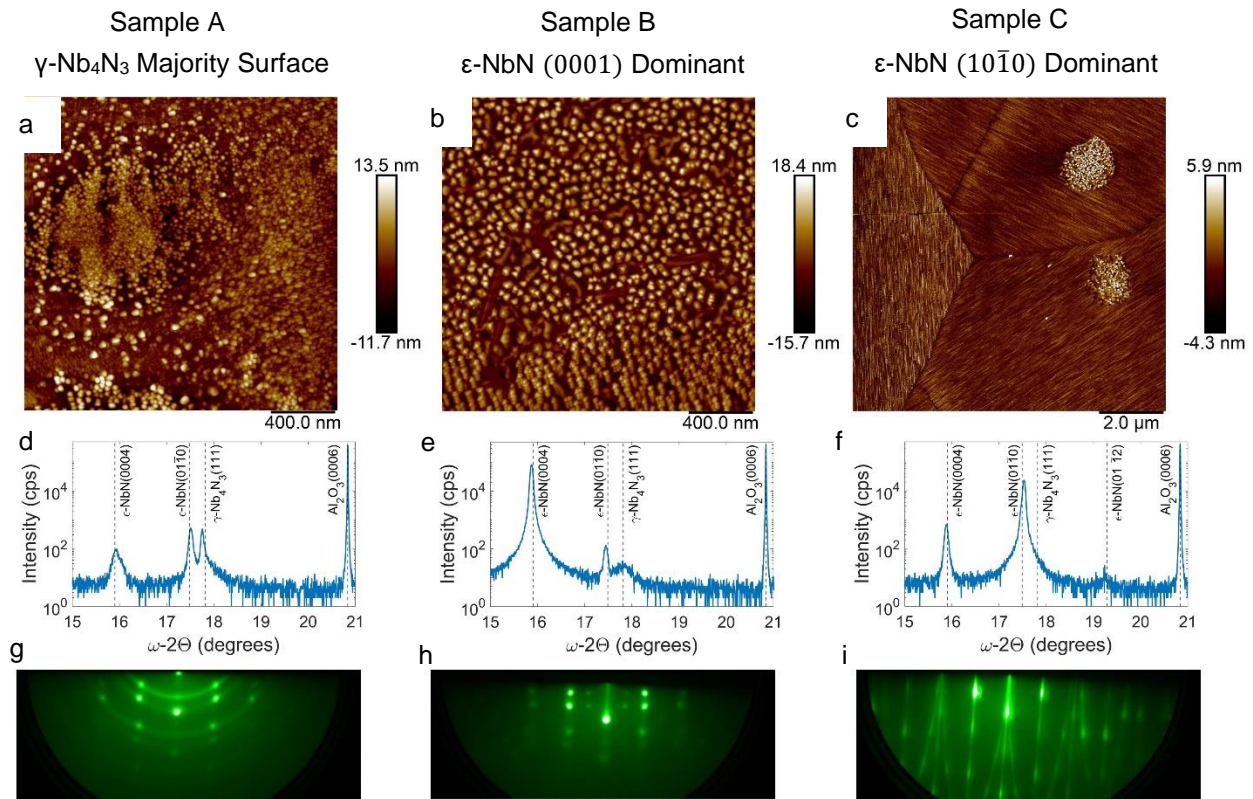


Figure 79: Comparison between NbN_x samples, each with a dominant phase and orientation.

RHEED of these multi-phase samples is complex, with a streaky pattern which begins to split as the streaks move farther from the specular spot. This splitting may be due to twinning of the ϵ -NbN (10 $\bar{1}$ 0) regions in the film, which is also seen in Figure 79(i), where visible directionality changes in the surface are seen. Spotty RHEED patterns indicate a rougher surface

with 3D-features, and this is evident in the AFM of each sample. Rings in the RHEED pattern, seen in the RHEED for the sample shown in Figure 79(g), are evident of polycrystallinity in the film, which is expected due to the multi-phase nature of the film.

AFM of these samples shows multiple domains on the surface and are identified by referencing the dominant XRD peak for each distinct surface. The areas with a river-rock appearance are identified as $\gamma\text{-Nb}_4\text{N}_3$, while the smooth striated regions and 3D peaks are identified as $\epsilon\text{-NbN}$ ($10\bar{1}0$) and $\epsilon\text{-NbN}$ (0001) respectively.

The RMS roughness (R_q) for sample A, a $\gamma\text{-Nb}_4\text{N}_3$ surface, in Figure 79(a) is 3.41 nm, with spots in the RHEED pattern surrounded by polycrystalline rings. The surface shown is a combination of the “river-rock” structure similar to $\gamma\text{-Nb}_4\text{N}_3$ samples, with interspersed regions of smoother $\epsilon\text{-NbN}$ ($10\bar{1}0$).

The R_q for sample B, a $\epsilon\text{-NbN}$ (0001) surface, in Figure 79(b) is 5.40 nm, and the RHEED pattern is exclusively spotty, indicative of the 3D-surface seen in the AFM for that sample. The 3D nodules are of similar density and size to the spherical nodules in the “river-rock” surface. Regions in between rougher sections of the film display $\epsilon\text{-NbN}$ ($10\bar{1}0$) character, which are smoother than the surrounding surface.

The R_q for sample C, a $\epsilon\text{-NbN}$ ($10\bar{1}0$) surface, in Figure 79(c) is 1.37 nm. This orientation is smoother than the other two, but still contains pockets of $\epsilon\text{-NbN}$ (0001), creating approximately 1- μm diameter regions of pyramidal structures. Both the RHEED, with its splitting of the streaky lines, as well as the AFM with its clear regions of directionality suggest twinning of the $\epsilon\text{-NbN}$ ($10\bar{1}0$) orientation. The twinning in the AFM has 6-fold symmetry, with 60° rotation between regions. In addition to the dominant $\epsilon\text{-NbN}$ ($10\bar{1}0$) peak, there is evidence

of the ϵ -NbN (01 $\bar{1}$ 2) peak in Figure 79(f), which is not prevalent enough to be observed in the AFM scans.

3.3.4 Superconducting Properties

Superconductivity of NbN_x samples changes drastically depending on whether the ϵ -NbN phase is predominant in the film grown. Figure 80 shows the superconducting transition for a γ -Nb₄N₃ sample and has a transition temperature of 9.7 K.

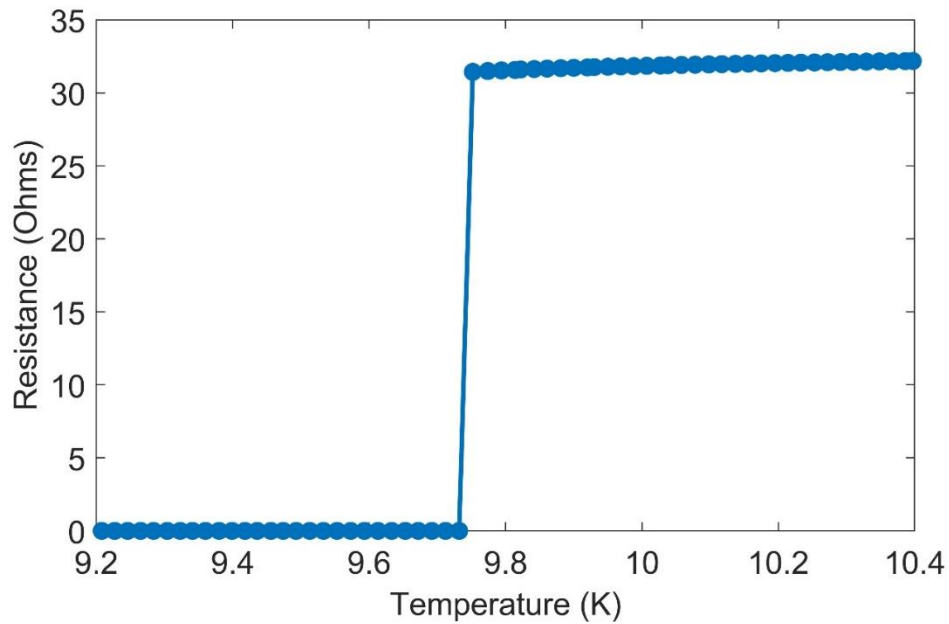


Figure 80: Superconducting transition for a γ -Nb₄N₃ sample with a thickness of 32-nm.

This transition is abrupt, with a maximum transition width of 0.019 K. This maximum is due to the sampling rate of the nanovoltmeter used to collect the data. The RRR for this sample is 0.45. The T_c of γ -Nb₄N₃ has been reported to be 11.5 K. [88]

For samples with some fraction, or entirely are ϵ -NbN, the superconducting transition occurs lower than 2 K, with a broad transition width. In Figure 81, sample A from Figure 79 with both γ -Nb₄N₃ and ϵ -NbN phases has a T_c of 2.27 K and a transition width of 1.66 K.

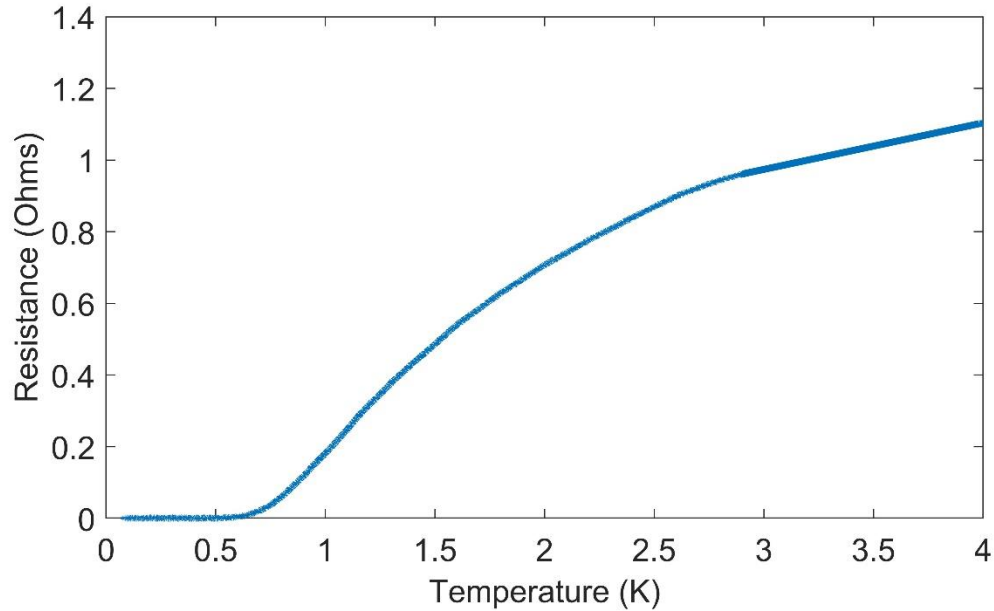


Figure 81: Superconducting transition for sample A from Figure 80, a multi-phase NbN_x sample.

In Figure 82, sample C from Figure 79 with exclusively ϵ -NbN phase has an estimated T_c of 0.20 K. The transition width is unknown. These uncertainties are due to the temperature floor of the ADR, as the 10 % resistance threshold would be 0.051 Ω , which was never reached. To calculate the T_c for this sample, a linear trendline was extrapolated through all data points below the normal state resistance, and the 10 % threshold was obtained from that trend.

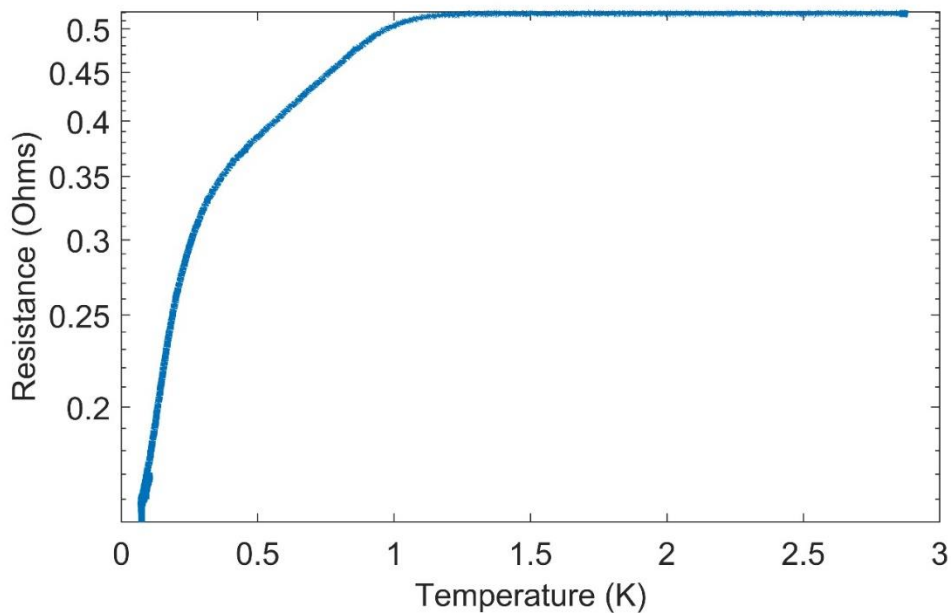


Figure 82: Superconducting transition for sample C from Figure 80, which is entirely ϵ -NbN.

Resonators were fabricated from the γ -Nb₄N₃ sample with the superconducting transition shown in Figure 80. Resonators from samples with ϵ -NbN phase were not tested due to the multi-phase nature of the films, as well as the low T_c . Resonators are initially found using a broad survey of the frequency range, looking at the forward transmission through the chip. Five co-planar waveguide resonators are fabricated on each chip, and five resonances are found in the survey. Figure 83 shows the frequency range from 3.3 GHz to 4.3 GHz. Resonances are marked in red and are found using peaks found in the derivative of the S_{21} data.

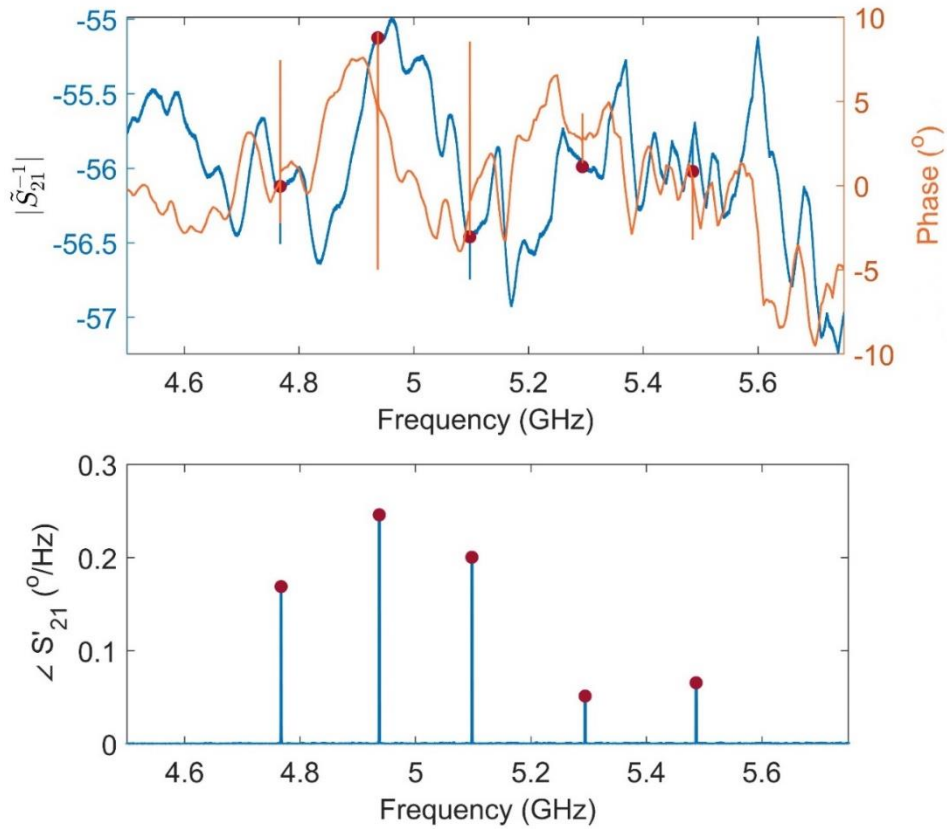


Figure 83: RF sweep of a γ -Nb₄N₃ chip featuring five resonators with a common feedline.

Resonators fabricated from PAMBE grown γ -Nb₄N₃ show high-power internal quality factors around 1 million but have a lower internal quality factor of between 100-500 thousand at a photon number of 10, shown in Figure 84. Resonator 4 is an outlier on this chip, where the quality factor does not saturate at higher powers like the other four resonators. Single photon levels were not able to be reached with these devices, as the noise described in the circle fitting was too much for a reliable fit.

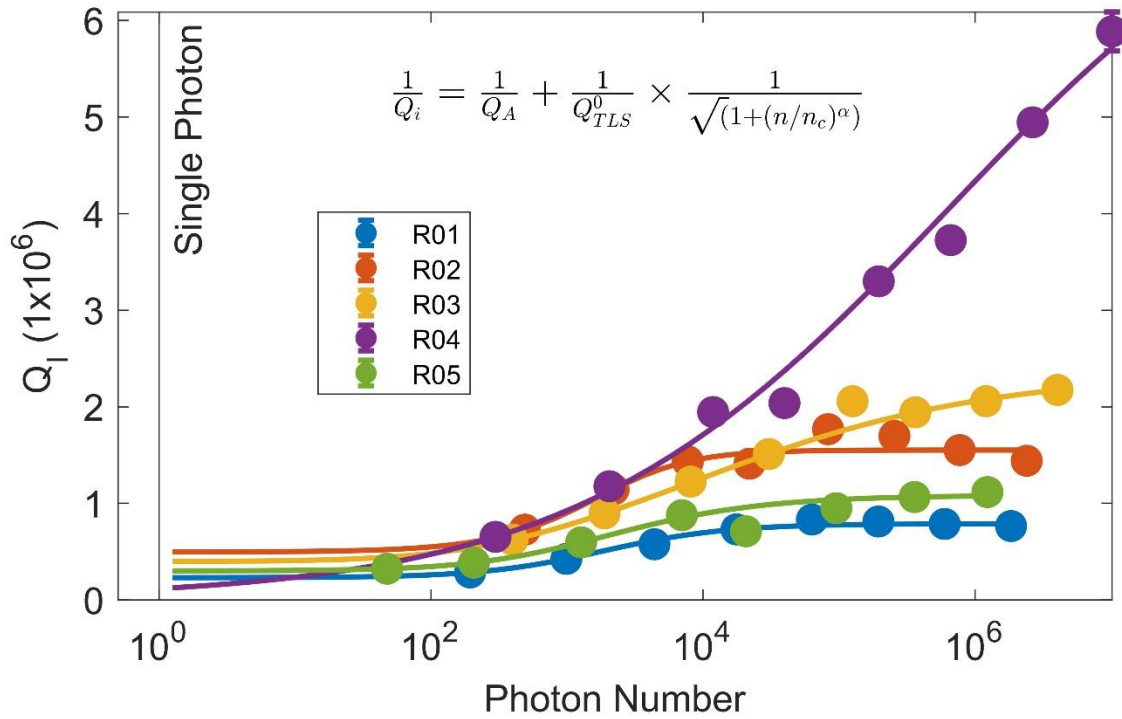


Figure 84: Power dependent internal quality factor plot for γ -Nb₄N₃ resonators.

Table 6 shows the resonant frequency for resonators fabricated from a sample composed of exclusively γ -Nb₄N₃, along with the variables used to fit the power dependence data. Unlike the resonators from the TiN sample seen in Table 5, the parameters in Table 6 have a larger variation. Alpha ranges from 0.32 to 1.43, which is an analysis artifact due to an incomplete dataset as alpha cannot be higher than one or lower than zero. While the low photon level quality factors are within the range of the TiN sample from Table 5, the maximum quality factors are an order of magnitude lower than those for TiN.

Table 6: Values used to construct power dependent resonator fitting, with the internal quality factors at single photon power as well as the maximum power during that measurement.

| Resonator | f_0 (GHz) | Q_A | Q_{TLS} | α | n_c | Q_i ($n = 1$) | Q_i (max) |
|-----------|-------------|-----------------------|-----------------------|----------|-------|--------------------|--------------------|
| 1 | 4.7672 | 1.27×10^{-6} | 3.07×10^{-6} | 0.95 | 494 | 2.31×10^5 | 8.33×10^5 |
| 2 | 4.9372 | 6.44×10^{-7} | 1.37×10^{-6} | 1.43 | 885 | 4.97×10^5 | 1.77×10^6 |
| 3 | 5.0977 | 4.26×10^{-7} | 2.09×10^{-6} | 0.39 | 120 | 3.99×10^5 | 2.17×10^6 |
| 4 | 5.2940 | 1.24×10^{-7} | 1.88×10^{-5} | 0.32 | 837 | 1.18×10^5 | 5.89×10^6 |
| 5 | 5.4862 | 9.22×10^{-7} | 2.40×10^{-6} | 0.71 | 312 | 3.02×10^5 | 1.12×10^6 |

3.4 Impact of Annealing Niobium Nitride

3.4.1 Topographical Changes

The topography for annealed NbN_x samples undergoes a dramatic change similar to TiN samples, where a significant decrease in RMS roughness and peak-to-peak roughness is seen. Figure 85 shows the comparison between as-grown and annealed NbN_x samples grown under similar growth conditions. The annealed sample underwent a 2-hour post-growth anneal at 850°C . The annealed surface in Figure 85(b) adopts a mottled appearance with an RMS roughness of 0.595 nm , which is an order of magnitude decrease from the roughness seen on the non-annealed sample in Figure 85(a). The distinct 3D character of the $\epsilon\text{-NbN}$ (0001) surface in Figure 85(a) is removed, as well as the distinct RHEED pattern in Figure 85(c) for the non-annealed sample.

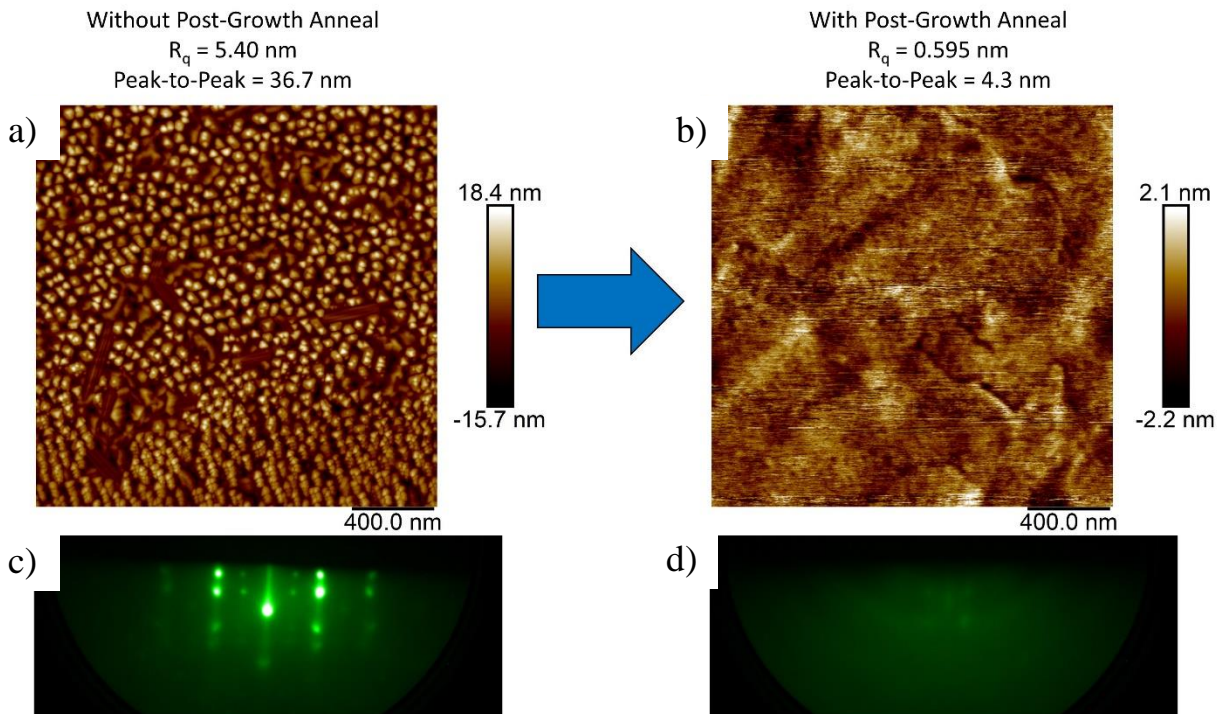


Figure 85: NbN_x samples with and without a post-growth anneal.

The faint spots seen in the annealed samples RHEED patterns are similar to the pattern from the non-annealed sample, indicating the dominant phase and orientation in the film remains ϵ -NbN (0001).

3.4.2 Structural Changes

Annealing of the NbN_x sample showed little change in the XRD ω - 2θ pattern, showing peaks from ϵ -NbN (0001), ϵ -NbN ($10\bar{1}0$), and γ - Nb_4N_3 (111) phases and orientations. Figure 86 shows the XRD from two samples, a non-annealed sample in blue, and an annealed sample in orange with $T_A = 850^\circ\text{C}$. Both samples are grown under nominally the same growth conditions, with a substrate temperature of 1000°C , a target Nb flux of 3×10^{17} atoms/ m^2s , under a nitrogen plasma overpressure of 1.8 sccm at 500 W forward power.

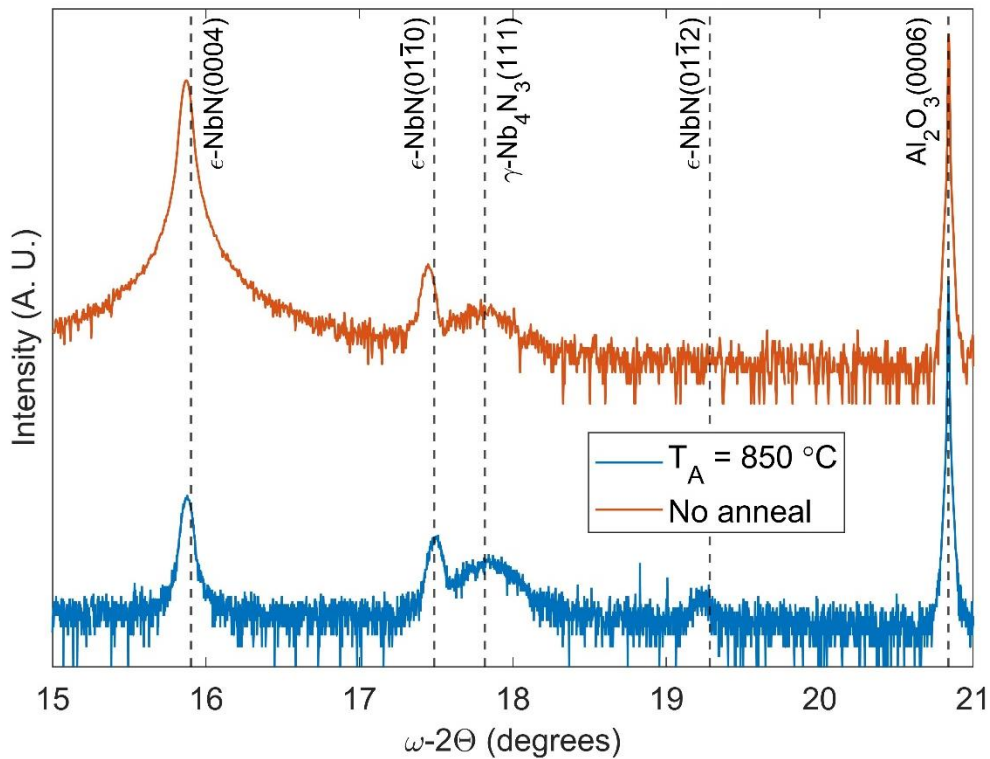


Figure 86: NbN_x samples with and without a post-growth anneal.

The intensity of the ϵ -NbN (0001) peak decreases with annealing, while the magnitude and location of ϵ -NbN (10 $\bar{1}$ 0) and γ -Nb₄N₃ (111) peaks remain nominally the same. A third ϵ -NbN orientation, ϵ -NbN (01 $\bar{1}$ 2) is evident in the annealed sample.

3.4.3 Impact on Superconductivity

The annealed NbN_x sample did not show signs of a superconducting transition down to approximately 90 mK, the base temperature of the ADR. Likely due to the dominant epsilon phase, the sample would superconduct lower than 1 K, similar to the unannealed samples.

3.5 Summary

Growth of TiN and NbN_x thin films on sapphire was accomplished using PAMBE. TiN samples follow the results in literature closely, with the surface morphology consisting of “river-rock” features with R_q of between 1 – 3 nm. [132] X-Ray results of the TiN films show a TiN (111) peak without evidence of any other orientations or phases of TiN. The peak location lines up well with literature values for the material, and thickness fringes on each side of the peak point to the film consisting of uniformly stacked unit cells of good crystal quality. Lattice constants calculated from TiN XRD data do not show a trend corresponding to expected strain due to CTE mismatch, indicating that the interface between the TiN film and the sapphire substrate may be metamorphic. [57] From pole figure measurements, it can be shown that TiN films grown using PAMBE may be twinned, with TiN (111) oriented domains rotated 60 ° from each other throughout the film. RBS simulations indicate that the composition best fitting the

TiN data shows a nitrogen rich sample, which may indicate interstitial nitrogen in the film. Figure 17, the phase diagram for TiN, indicates no phases of TiN_x where x is greater than 1, making interstitial nitrogen a possibility for describing the RBS results. Interstitial nitrogen may cause compressive stress in the film as the lattice is expanded beyond the lattice expected by a 1:1 stoichiometric film.

The superconducting properties of the unannealed TiN films are also consistent with literature, with critical temperatures near 5 K. [80] The transitions for this material are very abrupt, consistent with reported type I behavior of TiN. Resonators fabricated from the material show excellent high power internal quality factors near 20 million, with single photon power levels showing Q_i 's of several hundred thousand.

NbN_x films grown using PAMBE are not as consistent as TiN films, showing evidence of multiple phases growing concurrently within most films. These phases, $\epsilon\text{-NbN}$ and $\gamma\text{-Nb}_4\text{N}_3$, are documented in literature individually, but only a few groups have reported work on multi-phase growth. [88], [91] The high temperature formation of $\epsilon\text{-NbN}$ with the low temperature formation of $\gamma\text{-Nb}_4\text{N}_3$ in this work is contrary to some literature concerning multi-phase NbN_x films, where the opposite temperature dependence was found. [133] The desired phase, $\delta\text{-NbN}$ was not found to be stable for any growth conditions tested in this work. Superconductivity of samples containing $\epsilon\text{-NbN}$ demonstrates the low T_c of this phase, with samples transitioning at or below 2 K. The surface morphology of NbN_x samples is dependent on the relative fractions of the phases and orientations in the film, with three distinct surface features evident: smoother striated regions for $\epsilon\text{-NbN}$ ($10\bar{1}0$), rougher pyramidal features for $\epsilon\text{-NbN}$ (0001), and rocky features for $\gamma\text{-Nb}_4\text{N}_3$ (111).

Annealing of TiN and NbN_x films results in dramatic changes to the surface morphology. For TiN samples annealed at 1000 °C, the surface adopts a smooth triangular pattern, which may be indicative of the (111) oriented facet formation, along with trench-like features throughout the surface. Anneal temperatures less than 1000 °C failed to produce a noticeable change in TiN topography. The critical transition temperature of the annealed TiN films improves significantly, to nearly 5.8 K, with a RRR of over 14. Additionally, the crystalline quality improves, according to thickness fringes seen in XRD data. The reduction in FWHM of the RSM cross section indicates less variation in the lattice constant through the film when compared to an unannealed sample, implying that the anneal may improve the lattice uniformity. RBS measurements of both unannealed and annealed TiN films show nominally the same composition, indicating that possible changes in nitrogen content may not be causing the topography changes or crystallinity improvements. Annealing of NbN_x films results in a much smoother surface than an unannealed sample but does not result in a noticeable change in the critical temperature or the dominant phase of the film.

This chapter helps illuminate the difference between crystallographic and electrical characteristics of the NbN_x family of materials and provides the first evidence of phase control by varying the Nb flux and films thickness for MBE grown NbN_x thin films. In addition, the improvements in T_c and crystalline quality by annealing TiN samples may be beneficial in producing high quality materials for devices like Josephson junctions.

Chapter 4: NbTiN Alloy Development

The engineering of an alloy for epitaxial Josephson junctions requires careful characterization of the material properties throughout the composition range. In this chapter, NbTiN alloys are grown using PAMBE, and characterized with respect to their structural and electrical properties, as well as the surface morphology of the samples. Due to the variation in both the metal concentration and nitrogen content in these films, alloys will be denoted as $(\text{Nb}_x\text{Ti}_{1-x})_{1-y}\text{N}_y$ when appropriate, where x is the relative metal fraction, and y is the relative nitrogen content. Samples without nitrogen content data will omit the nitrogen fraction, y .

4.1 $(\text{Nb}_x\text{Ti}_{1-x})_{1-y}\text{N}_y$ Alloy Growth

Growth of $(\text{Nb}_x\text{Ti}_{1-x})_{1-y}\text{N}_y$ alloys follows the wafer preparation procedures used in the growth of binary NbN_x and TiN films. In Figure 87, the growth process is shown using both the high temperature effusion cell and the electron beam evaporator to co-deposit Nb and Ti.

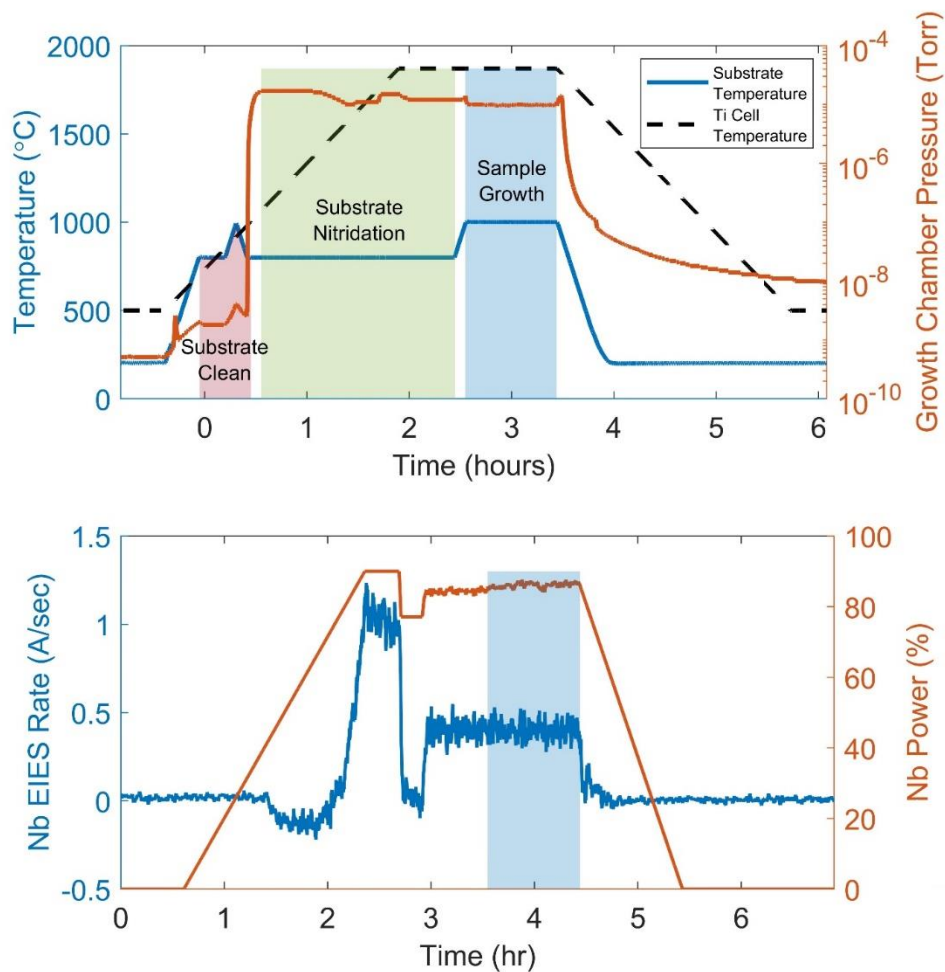


Figure 87: Growth process chart for a $(\text{Nb}_x\text{Ti}_{1-x})_{1-y}\text{N}_y$ alloy grown at 1000 °C with a two-hour substrate nitridation process.

$(\text{Nb}_x\text{Ti}_{1-x})_{1-y}\text{N}_y$ samples undergo the same substrate nitridation as the binary compounds.

Compositional control for Nb and Ti is accomplished by varying the relative metal fluxes. The BEP and EIES are impacted by the chamber environment, which can change from sample to sample. The presence of residual nitrogen in the growth chamber affects the titanium BEP reading, so care must be taken to measure the Ti calibration when the chamber pressure has recovered after a growth using nitrogen. Nitrogen does not affect the niobium source calibration due to the use of a gas compensation sensor. Alloy sample growth near the composition of interest is needed for proper calibration of ternary films.

Nitrogen incorporation during these growths was accomplished with an ultra-pure N₂ flow of 1.8 sccm through a Veeco Uni-Bulb plasma generator operating at 500 W forward power. For all samples grown, the total metal flux was targeted to be 1×10^{18} atoms/m²s. This total metal flux was used in combination with the plasma conditions listed prior because it provides a nitrogen rich-growth environment regardless of the composition of the sample.

(Nb_xTi_{1-x})_{1-y}N_y samples were grown at two substrate temperatures, 800 °C and 1000 °C. These growth temperatures were chosen due to the temperature dependence of NbN_x phase growth described in the previous chapter, and the expected increase in crystal quality based on literature concerning high-temperature growth of TiN. [132], [134] The upper bound on substrate temperature is placed to ensure safe operation of the SiC substrate heater and maximum output of the heater power supply.

4.2 Structural Analysis

4.2.1 X-Ray Analysis

Symmetric x-ray of $(\text{Nb}_x\text{Ti}_{1-x})_{1-y}\text{N}_y$ samples shows excellent crystal quality for samples with metal composition $x < 0.98$. Figure 88 shows symmetric ω - 2θ XRD plots for representative samples across the compositional range.

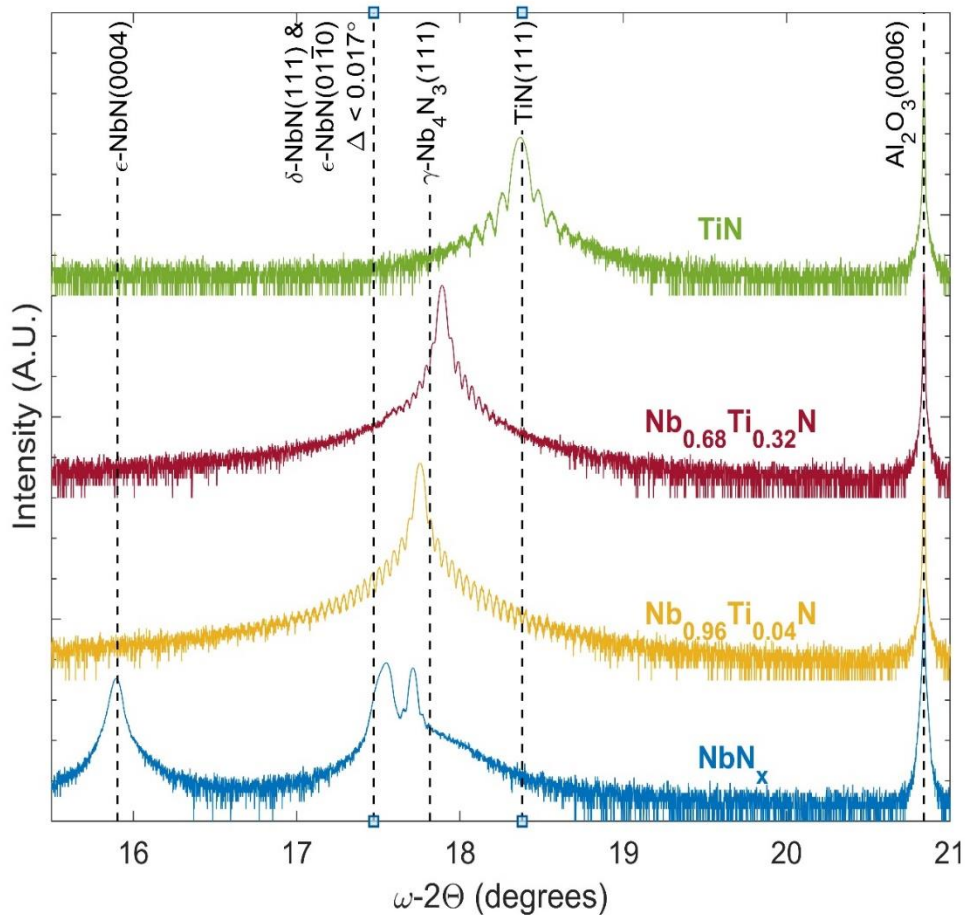


Figure 88: Waterfall of several XRD plots spanning the $(\text{Nb}_x\text{Ti}_{1-x})_{1-y}\text{N}_y$ composition range as indicated by labels. Reference Bragg angles are shown with vertical dashed lines for planes of interest.

Vertical dashed lines indicate reference planes of interest using literature lattice constants. The line at approximately 17.5° represents both the ϵ -NbN (0110) and the desired rock salt phase of δ -NbN (111).

The difference between the peak locations based on literature is less than 0.017° . Thickness fringes can be seen on samples with Nb composition less than 0.98 and can be used to calculate the approximate thickness.

As the composition becomes more niobium rich, the peak shifts from right to left. The desired peak shift is between the TiN and δ -NbN reference lines following a linear trend, as is typically seen in alloys. [135] By using the peak angle from the symmetric XRD data, the out-of-plane lattice constant can be calculated and plotted as a function of composition, as seen in Figure 89. The reference line for γ -Nb₄N₃ is calculated using a $\frac{1}{2}c$ parameter due to the identical metal lattice for both δ -NbN and γ -Nb₄N₃ so as to be comparable when comparing samples.

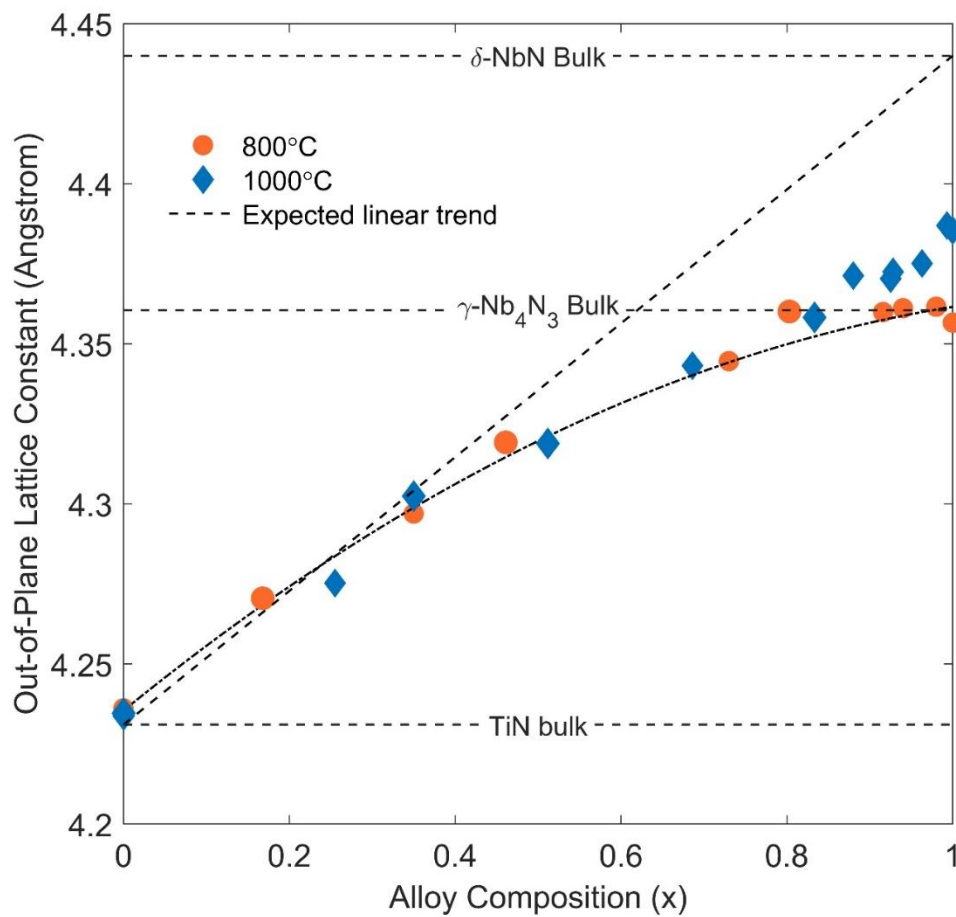


Figure 89: Out of plane lattice constant as a function of $(\text{Nb}_x\text{Ti}_{1-x})_{1-y}\text{N}_y$ composition with two temperature ranges. Reference lines for literature lattice constants are shown, as well as the expected linear and real trends.

Out-of-plane lattice constants for samples with high niobium content, or pure NbN_x films are calculated from the peak position of the rightmost peak corresponding to the γ -Nb₄N₃ (111) peak. Fitting a trend to the data reveals a bowing to Vegard's Law, with a bowing parameter $b = -0.085$. The upturn in the 1000 °C symmetric XRD data may be due to the presence of ϵ -NbN in the film, as this phase grows more predominantly at higher temperatures as discussed in the previous chapter. With multi-phase films, the γ -Nb₄N₃ (111) peak may be shifted due to strain caused by the phase distribution in the film. This increase in lattice constant at 1000 °C may suggest a tensile strain on the regions in the film of tetragonal crystal structure. This lattice mismatch strain is calculated to be 4.6 % using bulk values for in-plane ϵ -NbN lattice constant a and the in-plane atomic spacing of the γ -Nb₄N₃ (111) lattice from literature assuming the unit cells are stacked on top of each other with the relationship $((11\bar{2}0)_{\epsilon-NbN} || (110)_{\gamma-Nb_4N_3})$. [91]

This asymptotic behavior is unexpected and is explored in more detail using asymmetric reciprocal space maps. RSM data taken for each of the (Nb_xTi_{1-x})_{1-y}N_y samples is plotted in Figure 90 and Figure 91 for growth temperatures of 800 °C and 1000 °C.

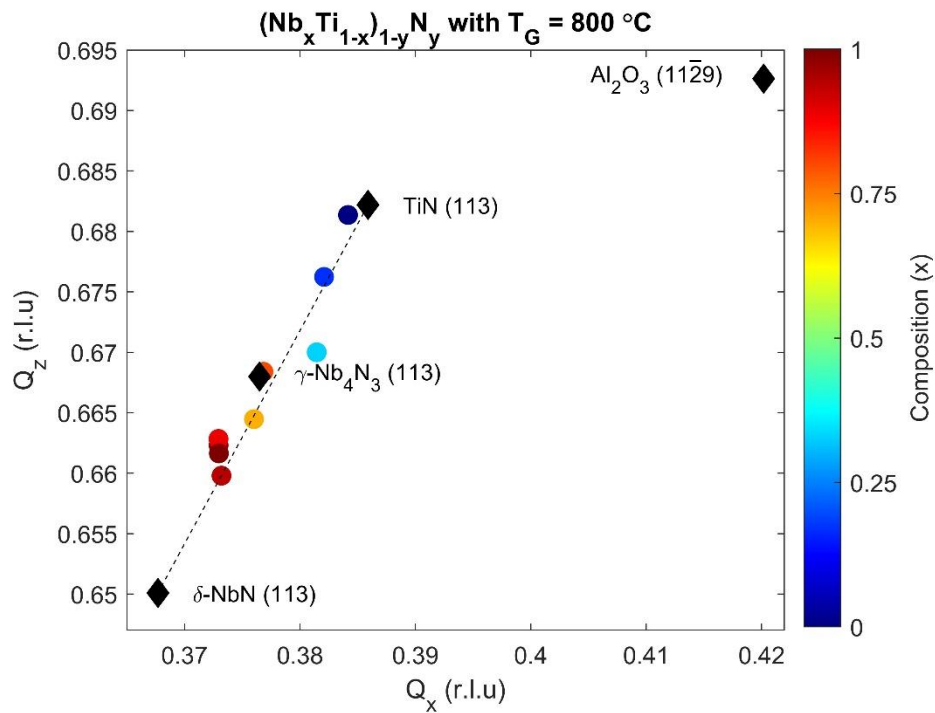


Figure 90: RSM peaks for (Nb_xTi_{1-x})_{1-y}N_y (113) and Al₂O₃ (11 $\bar{2}$ 9) planes from samples grown at 800 °C across the compositional range x .

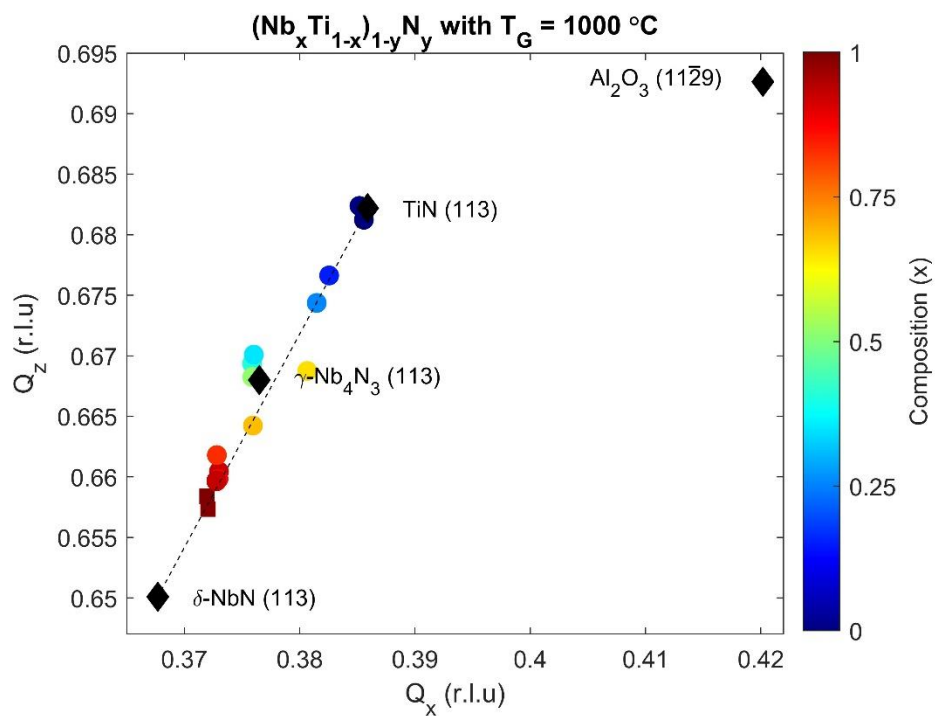


Figure 91: RSM peaks for (Nb_xTi_{1-x})_{1-y}N_y (113) and Al₂O₃ (11 $\bar{2}$ 9) planes from samples grown at 1000 °C across the compositional range x .

Reference points for each of the nitrides as well as the substrate are shown as black diamonds. The dotted line between TiN and δ -NbN provides a linear Vegard's law trend between the two rock-salt materials. The square data points represent multiphase growth, where ϵ -NbN begins to form.

4.2.2 Surface Morphology

The topology of $(\text{Nb}_x\text{Ti}_{1-x})_{1-y}\text{N}_y$ samples is dependent on the composition of the sample, and changes drastically when the Nb content exceeds 0.98. Surfaces of films with Nb-content less than 0.92 resemble a “river-rock” morphology. Surfaces of films with Nb-content between 0.92 and 0.97 change into pyramidal structures instead of spherical features. The RMS roughness of these samples ranges from 0.8 nm to 3.5 nm, with RMS roughness less than 1 nm seen in samples with Nb content between 0.92 and 0.97. When the Nb content is greater than 0.97, the surface drastically changes, forming a mottled surface with the emergence of the ϵ -NbN phase growing in conjunction with the cubic $(\text{Nb}_x\text{Ti}_{1-x})_{1-y}\text{N}_y$. Figure 92 illustrates this change in surface character with corresponding RHEED taken from various sample, as well as AFM representing all the surfaces discussed.

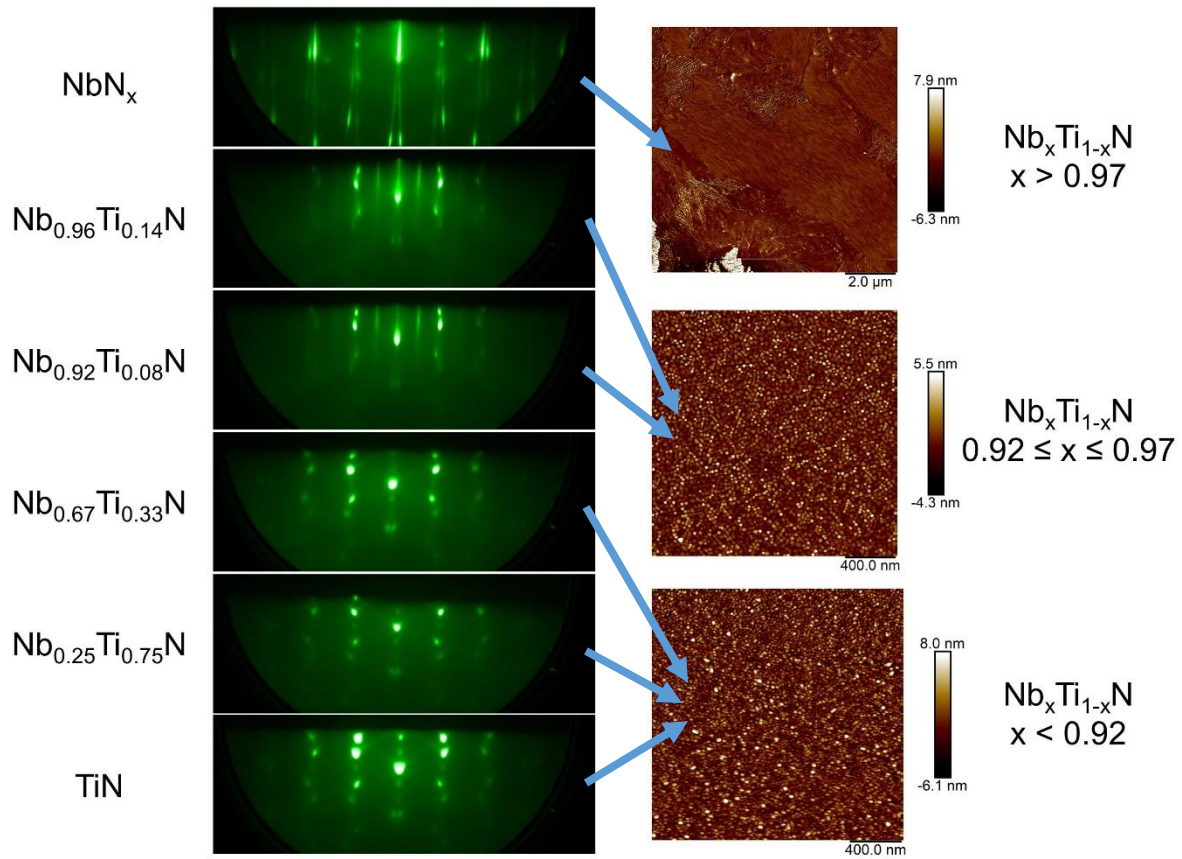


Figure 92: RHEED and AFM evolution as composition of $(\text{Nb}_x\text{Ti}_{1-x})_{1-y}\text{N}_y$ samples changes.

Spotty RHEED patterns are evidence of a 3D surface, and this is corroborated with the AFM scans of relatively low Nb content samples. This surface is reminiscent of TiN samples and $\gamma\text{-Nb}_4\text{N}_3$ samples described in Chapter 3. When the Nb-content is greater than 0.92, the RHEED becomes streakier, indicative of a smoother, 2D growth surface. This RHEED pattern never becomes wholly streaky, and always possesses spotty features and split lines for high Nb content samples.

Examining the AFM images for high Nb-content films provides insight into the RHEED pattern features where distinct regions of smoother $\epsilon\text{-NbN}$ ($10\bar{1}0$) interspersed with rougher $\gamma\text{-Nb}_4\text{N}_3$ (111). The splitting of the RHEED pattern when the Nb content is greater than 0.98 is

due to the twinning seen in ϵ -NbN ($10\bar{1}0$) regions. This twinning follows domains which are 60° apart from one another.

4.2.3 Transition Metal Compositional Analysis

Compositional determination of relative metal content, x , in $(\text{Nb}_x\text{Ti}_{1-x})_{1-y}\text{N}_y$ films was accomplished using both RBS and EDS for a subset of the samples grown, then exclusively with EDS after it was found that the atomic percentages produced using the two techniques agree to within 10 % error. Table 7 shows the compositions of a subset of samples which had both techniques used to calculate the composition of the samples.

Table 7: Subset of $(\text{Nb}_x\text{Ti}_{1-x})_{1-y}\text{N}_y$ samples showing the composition calculated by both RBS and EDS.

| Sample Number | x_{EDS} | x_{RBS} | $\frac{x_{EDS} - x_{RBS}}{x_{RBS}}$ |
|----------------------|-----------|-----------|-------------------------------------|
| D2G0184 | 1.00 | 1.00 | 0 |
| D2G0190 | 0.00 | 0.00 | 0 |
| D2G0191 | 0.30 | 0.32 | -0.06 |
| D2G0192 | 0.67 | 0.72 | -0.07 |
| D2G0193 | 0.89 | 0.92 | -0.03 |
| D2G0194 | 0.94 | 0.95 | -0.01 |
| D2G0195 | 0.98 | 0.99 | -0.01 |

The RBS compositions reported are with nitrogen artificially set to 1.0 to better compare with EDS, which has poor detection of N and can only be used to reliably compare the relative

metal content. EDS was chosen as the compositional technique of choice due to the tool being on-site, reducing cost and time spent waiting for results.

RBS analysis of the $(\text{Nb}_x\text{Ti}_{1-x})_{1-y}\text{N}_y$ samples shows both transition metal peaks as well as plateaus for substrate elements and nitrogen, similar to those spectra collected for TiN and NbN_x samples. Figure 93 shows this spectrum along with the simulated fit using SIMNRA. Plateaus are formed for the substrate elements due to the thickness of the substrate. Thicker layers form wider peaks during measurement, which helps to identify the thickness of the layer produced by fitting the data.

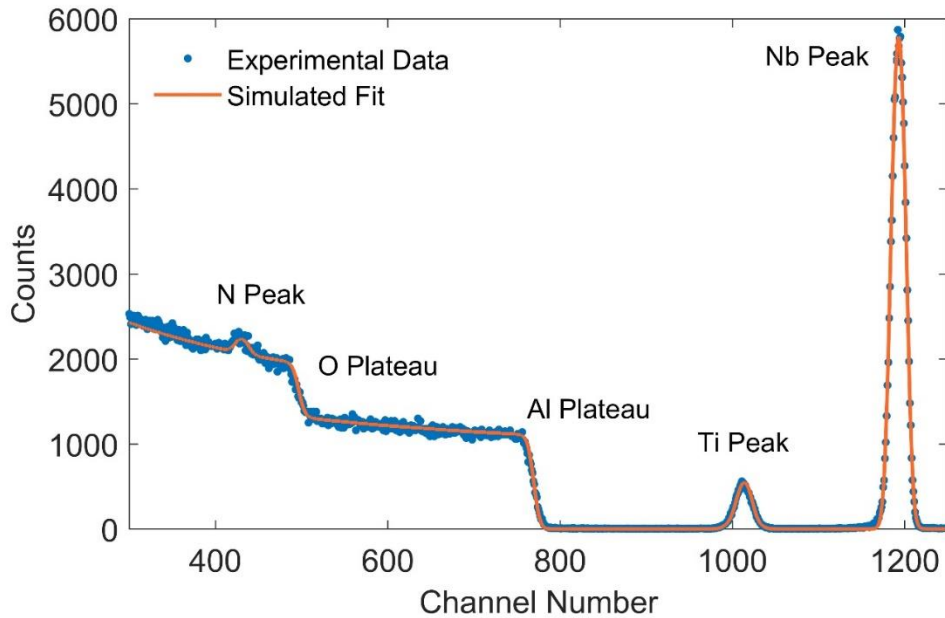


Figure 93: RBS spectra and simulated fit for a $(\text{Nb}_{0.72}\text{Ti}_{0.28})_{0.55}\text{N}_{0.45}$ sample.

A 1-nm surface oxide layer is included in the simulation to improve the fit. This oxide layer is allowed to change thickness and composition to better fit the data. Specifically, the fit is improved with the use of an oxide layer around the base of the metal peaks where it meets the noise floor. For the figure shown, the oxide layer is determined to be 1.0-nm thick, with an

oxygen fraction of 0.03. Figure 94 shows the representation of the heterostructure used to generate the simulated fit used in Figure 93.

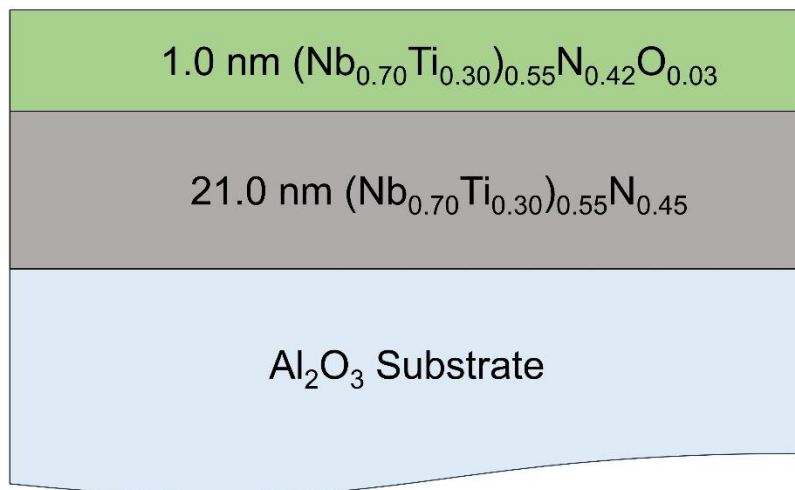


Figure 94: RBS simulated heterostructure for the fit of sample D2G0192, shown in Figure 93.

Compositions in Table 7 and Table 8 are taken from the nitride layer of the simulation, which did not include oxygen. Including the nitrogen content from the RBS simulations shows that all samples containing niobium in any amount are nitrogen deficient by 1-4 %. Table 8 shows the samples, RBS fitted compositions, and the error associated in the areal density of nitrogen.

Table 8: RBS fitted compositions for $(\text{Nb}_x\text{Ti}_{1-x})_{1-y}\text{N}_y$ samples including the nitrogen fraction.

| Sample Number | RBS Composition | χ_{RBS} Fit Error |
|---------------|--|------------------------|
| D2G0190 | $\text{Ti}_{0.45}\text{N}_{0.55}$ | 0.013 |
| D2G0191 | $(\text{Nb}_{0.33}\text{Ti}_{0.77})_{0.54}\text{N}_{0.46}$ | 0.026 |
| D2G0192 | $(\text{Nb}_{0.70}\text{Ti}_{0.30})_{0.55}\text{N}_{0.45}$ | 0.012 |
| D2G0193 | $(\text{Nb}_{0.89}\text{Ti}_{0.11})_{0.51}\text{N}_{0.49}$ | 0.003 |
| D2G0194 | $(\text{Nb}_{0.94}\text{Ti}_{0.06})_{0.52}\text{N}_{0.48}$ | 0.004 |
| D2G0195 | $(\text{Nb}_{0.98}\text{Ti}_{0.02})_{0.51}\text{N}_{0.49}$ | 0.005 |
| D2G0184 | $\text{Nb}_{0.52}\text{N}_{0.48}$ | 0.007 |

4.3 Superconducting Critical Temperature

The superconducting critical temperature of the $(\text{Nb}_x\text{Ti}_{1-x})_{1-y}\text{N}_y$ samples varies with composition but does not follow the linear trend expected between the binary endpoints of the composition range. Figure 95 shows a selection of representative samples from the $(\text{Nb}_x\text{Ti}_{1-x})_{1-y}\text{N}_y$ series.

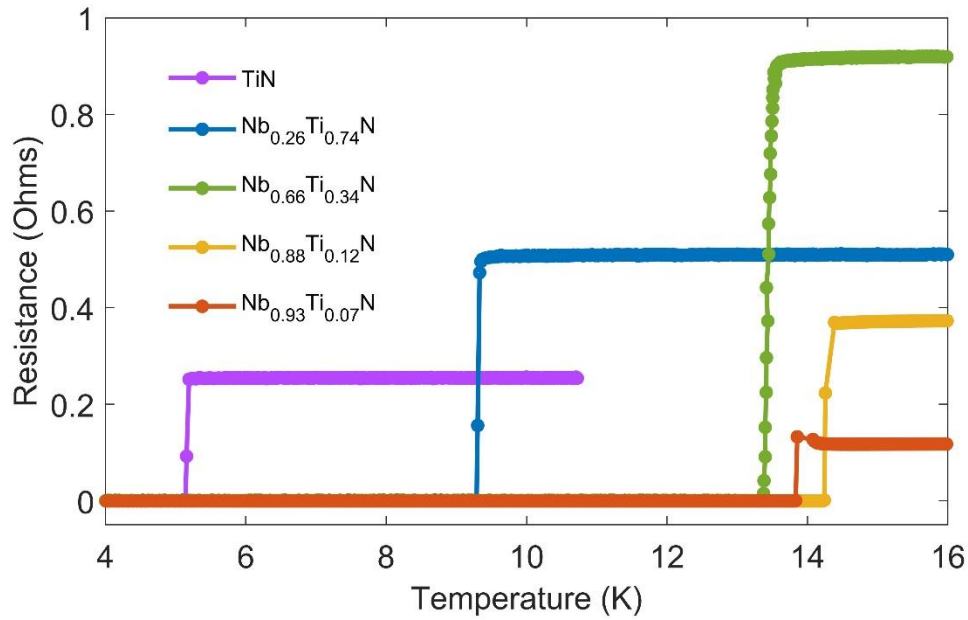


Figure 95: Selection of $\text{Nb}_x\text{Ti}_{1-x}\text{N}$ samples showing abrupt superconducting transitions.

Transition widths for the entire series are abrupt at less than 0.15 K. Triple R (RRR) for all samples range from 0.5 to 3.5. Higher titanium content films possess higher RRRs.

Figure 96 shows the trend of T_c with changing composition, including two substrate temperatures in blue and red.

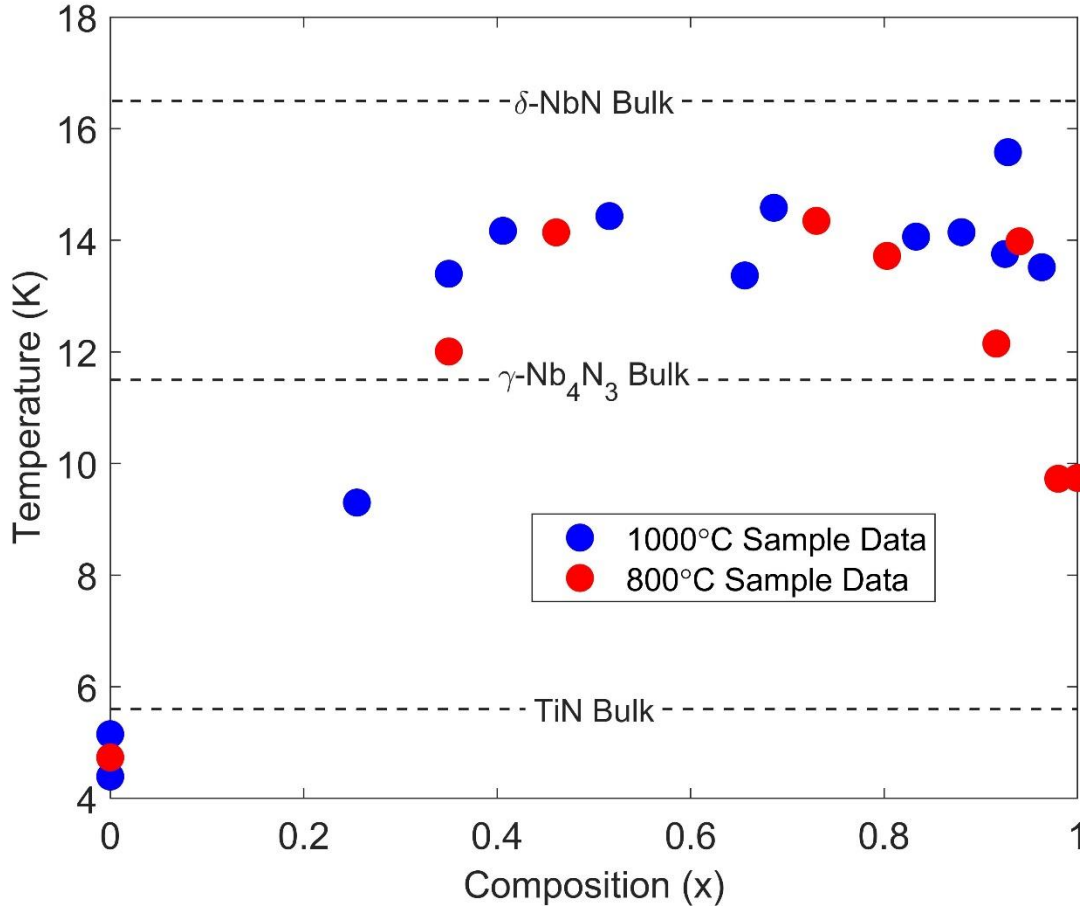


Figure 96: Superconducting critical temperature as a function of composition for two substrate temperatures.

The T_c rises at a steep rate as more Nb is introduced into the lattice, but plateaus at around a composition of $x = 0.5$. Increasing the Nb content after this point causes a slight reduction in T_c in samples grown at 1000 °C, and a more significant reduction in samples grown at 800 °C. Significant spread in the data is present and may be due to differences in sample thickness or changes in the growth environment causing subtle changes in the crystal quality.

Samples grown at 1000 °C have no collected data when composition is greater than 0.97, due to the growth of ϵ -NbN causing a significant drop in T_c to sub-Kelvin temperatures. The T_c

of such samples is phase dependent and depends on the metal flux as well as the sample thickness and substrate temperature as described in Chapter 3.

4.4 Resonator Analysis

Five resonators were fabricated from $(\text{Nb}_x\text{Ti}_{1-x})_{1-y}\text{N}_y$ samples as described in Methods section 2.7.2. Three of the resonators were fabricated using the repeatability design, while the other two samples were fabricated from the width variation design. The simulated resonant frequency is used to determine the frequency shift from the design frequency seen in physical devices. This frequency shift may be due to the kinetic inductance of the material used to fabricate the resonator. The fractional frequency shift is calculated using

$$\Delta f = \frac{f_m - f_0}{f_0}. \quad (52)$$

Here, f_0 is the ideal center frequency of the resonator simulated using Ansys, and f_m is the measured center frequency of the physical measured resonator. Figure 98 shows the frequency shift for all resonators fabricated from $(\text{Nb}_x\text{Ti}_{1-x})_{1-y}\text{N}_y$ samples.

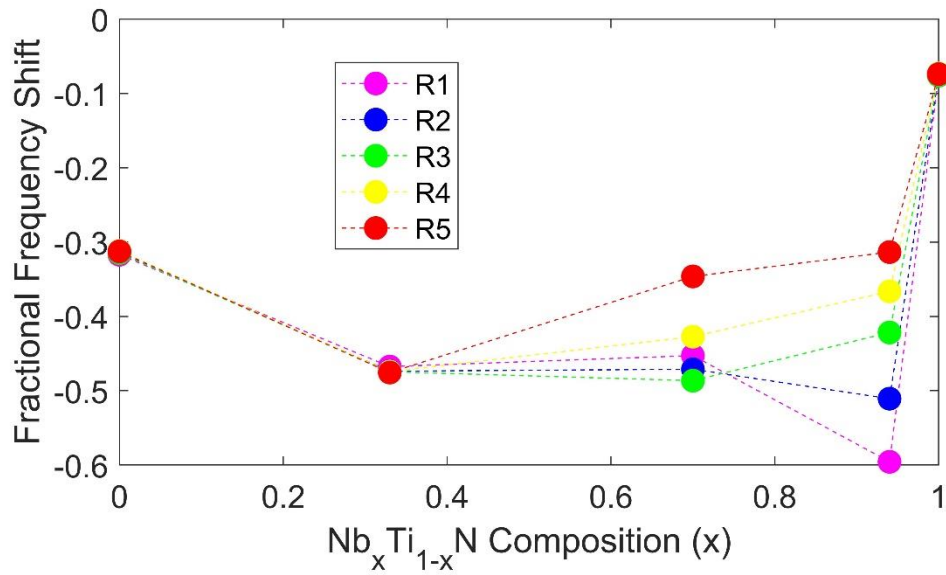


Figure 98: Fractional frequency shift as a function of composition. Two of the samples with significant variance between the resonators are due to fabrication with the width variation mask.

The samples fabricated using the width variation mask are clearly visible from the variation of frequency shift from the simulated center frequency, while the samples fabricated using the repeatability design have a tight spread. Figure 97 shows the resonator center trace width dependence of the fractional frequency shift for the resonators fabricated using the width variation design.

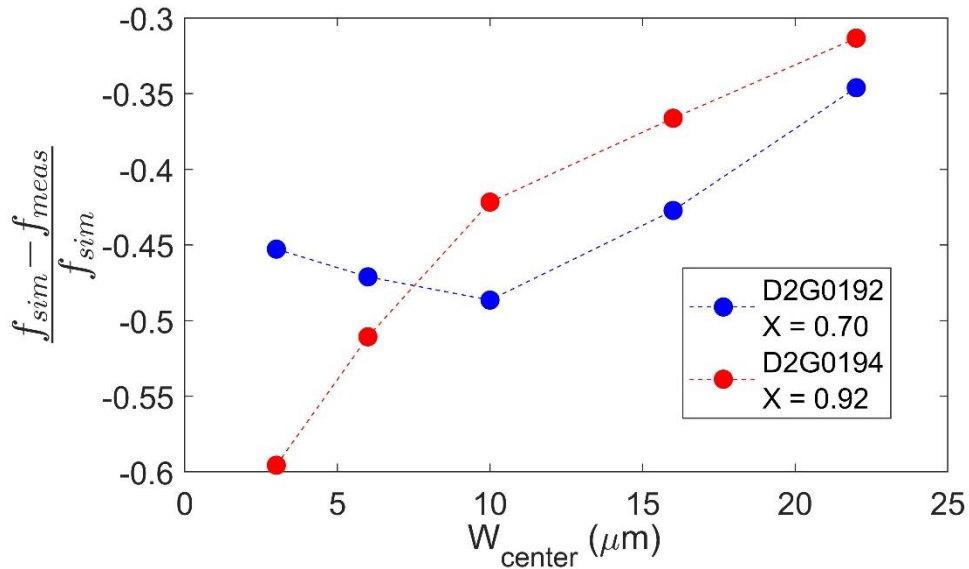


Figure 97: Fractional frequency shift due to changing W_{center} .

This variation may be due to losses at the changing metal-air, metal-substrate, or substrate-air interfaces, since the simulation and calculation both indicate that the frequency shift should be length dependent only for all resonators on a chip, and not affected by the cross-sectional geometry of the devices. Methods section 2.7 details the calculation of kinetic inductance from experimental data and is shown in Figure 99 for all $(\text{Nb}_x\text{Ti}_{1-x})_{1-y}\text{N}_y$ resonators measured.

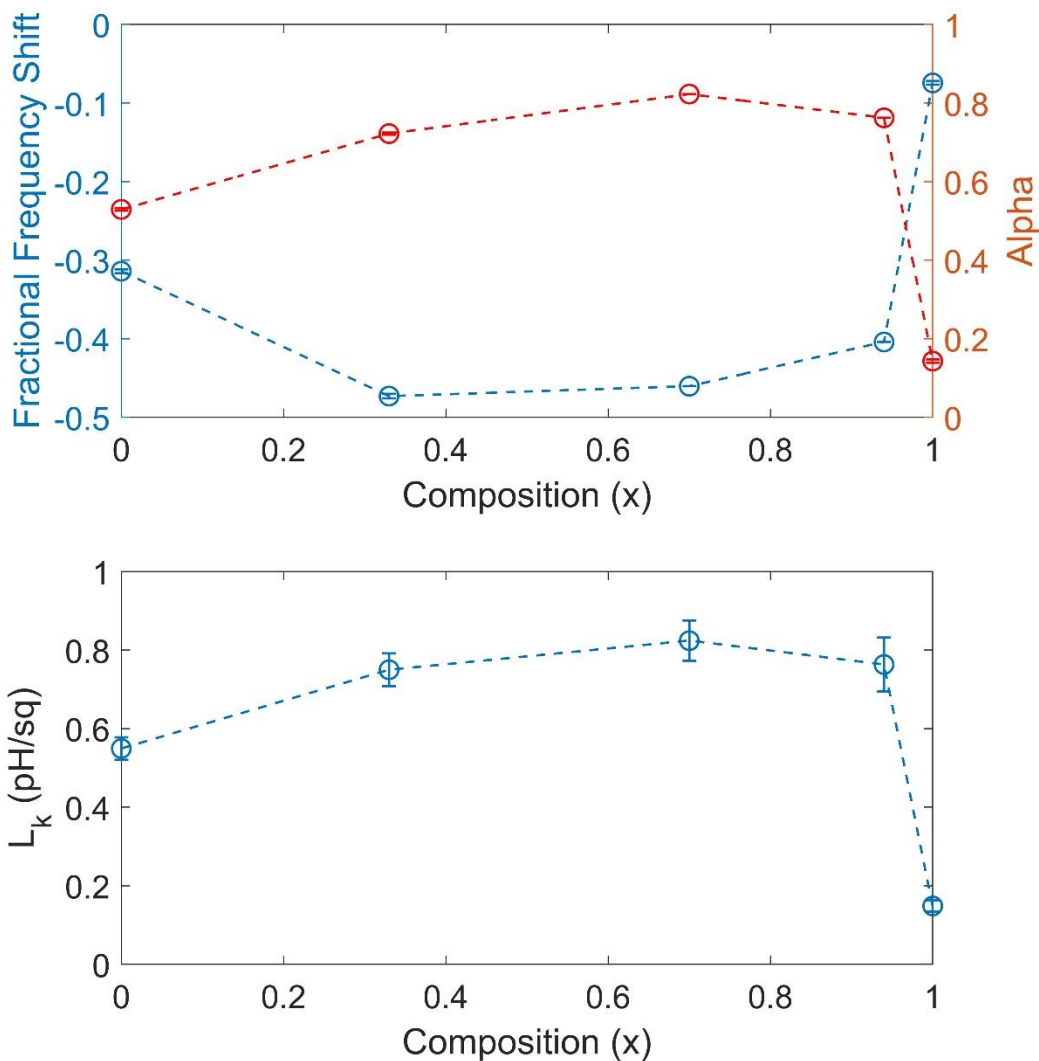


Figure 99: Average frequency shift, alpha values, and kinetic inductances for $(\text{Nb}_x\text{Ti}_{1-x})_{1-y}\text{N}_y$ resonators.

Figure 99 shows the average fractional frequency shift, the average alpha value, and the calculated kinetic inductance of each sample in the $(\text{Nb}_x\text{Ti}_{1-x})_{1-y}\text{N}_y$ series. The samples with the width variation design only use R2 (center width = 6 μm) for the plots in Figure 99 to eliminate the frequency variance due to uncontrolled losses with a changing W_{trace} .

Average fractional frequency shifts are negative, as the center frequency of each resonator in the series shifts to a lower frequency when compared to the design frequency simulated in Ansys. The frequency shift possesses a small increase in magnitude as Nb is added to the alloy, then shows a sudden decrease in shift magnitude for a purely NbN_x sample. The alpha value shows a similar trend, with an increase in alpha as Nb is added to the sample, then having a dramatic decrease in alpha for a purely NbN_x sample. Error bars are calculated from both the standard deviation of kinetic inductance and the variation in the etching process during the fabrication process, which can change the resonant frequency of a resonator by up to 0.46 % from Ansys simulations of the over-etched resonators.

This suggests that the kinetic inductance is increasing for samples of mixed composition and having a minimized kinetic inductance for the binary materials, TiN and $\gamma\text{-Nb}_4\text{N}_3$. When the kinetic inductance per square is calculated using Equation 42, the maximum L_k is seen at around $x \approx 0.7$. The error bars surrounding each sample are indicative of the standard deviation in the average frequency shift, as well as the effect of fabrication variation in the thickness of the center resonator line.

From BCS theory, the kinetic inductance can be calculated using a samples superconducting gap Δ , sheet resistance R_s , length of the resonator l and width of the center line w using

$$L_{ki} = \frac{l R_s h}{w 2\pi^2 \Delta} \frac{1}{\tanh\left(\frac{\Delta}{2k_B T}\right)}. \quad (53)$$

Figure 100 shows calculated kinetic inductances for $(\text{Nb}_x\text{Ti}_{1-x})_{1-y}\text{N}_y$ samples used for resonator fabrication at 90 mK, the base temperature of the ADR, using values from

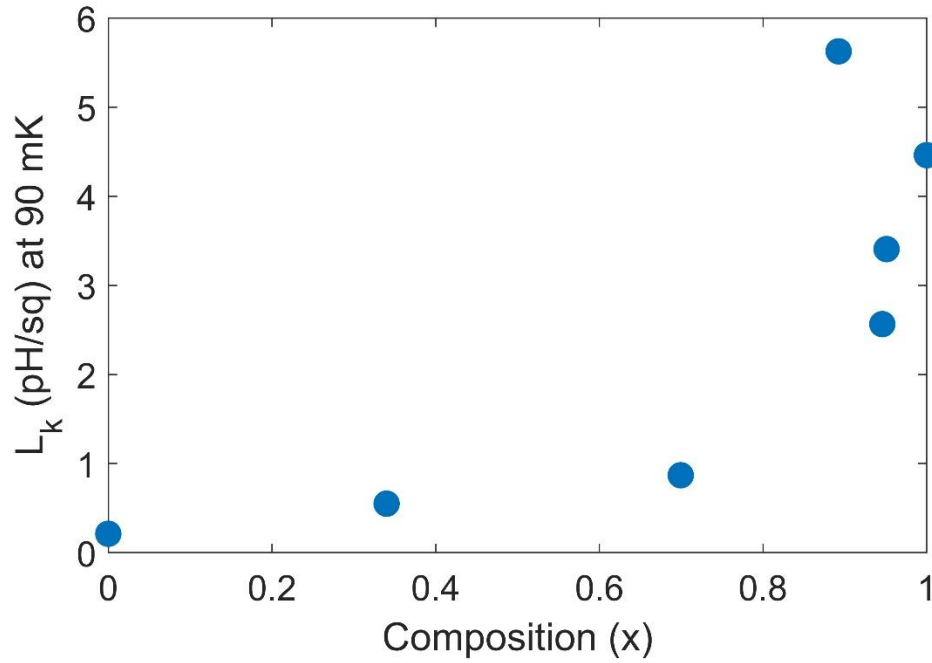


Table 9. [136]

Values used to create plots in this chapter are tabulated in

Table 9.

Table 9: Selection of $(\text{Nb}_x\text{Ti}_{1-x})_{1-y}\text{N}_y$ samples showing T_c , RRR, and transition width.

| Composition | T_G ($^{\circ}\text{C}$) | Thickness (nm) | T_c (K) | RRR | R_s (Ω) | Maximum Transition Width (K) |
|-------------|------------------------------|----------------|-----------|------|--------------------|------------------------------|
| TiN | 1000 | 60 | 5.17 | 3.43 | 0.255 | 0.047 |
| TiN | 1000 | 68 | 4.39 | 0.28 | 0.092 | 0.062 |

Figure 100: BCS theory predicted kinetic inductances for NbTiN samples using DC measurement results.

| | | | | | | |
|---|------|-----|-------|------|--------|-------|
| TiN | 800 | 29 | 4.73 | 2.79 | 0.754 | 0.098 |
| Nb _{0.26} Ti _{0.74} N | 1000 | 245 | 9.31 | 1.37 | 0.509 | 0.042 |
| Nb _{0.33} Ti _{0.67} N | 800 | 12 | 12.01 | 2.42 | 26.846 | 0.085 |
| Nb _{0.35} Ti _{0.65} N | 1000 | 59 | 13.40 | 1.40 | 1.621 | 3.270 |
| Nb _{0.41} Ti _{0.59} N | 1000 | 80 | 14.17 | 1.33 | 1.597 | 0.042 |
| Nb _{0.46} Ti _{0.54} N | 800 | 101 | 14.14 | 1.15 | 2.185 | 0.032 |
| Nb _{0.52} Ti _{0.48} N | 1000 | 130 | 14.43 | 1.24 | 1.053 | 0.066 |
| Nb _{0.66} Ti _{0.34} N | 1000 | 202 | 13.44 | 1.16 | 0.917 | 0.132 |
| Nb _{0.69} Ti _{0.31} N | 1000 | 108 | 14.58 | 1.12 | 0.229 | 0.108 |
| Nb _{0.70} Ti _{0.30} N | 800 | 23 | 14.35 | 0.96 | 9.672 | 0.050 |
| Nb _{0.80} Ti _{0.20} N | 800 | 108 | 13.72 | 0.98 | 2.646 | 0.036 |
| Nb _{0.83} Ti _{0.17} N | 1000 | 77 | 14.07 | 1.05 | 1.783 | 0.061 |
| Nb _{0.88} Ti _{0.12} N | 1000 | 113 | 14.25 | 1.05 | 0.374 | 0.012 |
| Nb _{0.89} Ti _{0.11} N | 800 | 44 | 12.15 | 0.65 | 52.732 | 0.130 |
| Nb _{0.93} Ti _{0.07} N | 1000 | 112 | 13.88 | 1.03 | 0.118 | 0.002 |
| Nb _{0.93} Ti _{0.07} N | 1000 | 128 | 15.61 | 1.09 | 1.15 | 0.263 |
| Nb _{0.94} Ti _{0.06} N | 800 | 39 | 13.98 | 0.87 | 26.948 | 0.737 |
| Nb _{0.96} Ti _{0.04} N | 1000 | 113 | 13.52 | 1.04 | 0.525 | 0.023 |
| Nb _{0.98} Ti _{0.02} N | 800 | 38 | 9.73 | 0.49 | 93.844 | 0.082 |
| NbN | 800 | 33 | 9.74 | 0.45 | 32.440 | 0.040 |

4.5 Summary

$(\text{Nb}_x\text{Ti}_{1-x})_{1-y}\text{N}_y$ samples were produced across the metal composition range $0 \leq x \leq 1$ using PAMBE, and the structural, electrical, and surface characteristics were investigated. The $(\text{Nb}_x\text{Ti}_{1-x})_{1-y}\text{N}_y$ alloy was found to have superconducting and structural dependences on the composition of the film. Alloys were grown at substrate temperatures of 800 °C and 1000 °C, with the growth in both cases of ϵ -NbN when Nb content is greater than 0.97. Both out-of-plane lattice constant and superconducting critical temperature experienced a plateauing when the Nb content is approximately 0.5 or higher

RBS results showed that TiN films grown under the conditions used in this thesis result in N rich films, with excess nitrogen likely in interstitial locations in the lattice. Inversely, when Nb was added to the alloy, the RBS results indicated N deficient material, which could be one of the causes of the T_c and XRD results plateauing when the Nb content is greater than 0.5. The RBS study does not consider larger amounts of oxygen being incorporated in the film due to the difficulty of determining an accurate oxygen concentration, which could influence the apparent nitrogen vacancy rate.

The small nitrogen deficiency may explain the asymptotic behavior of the XRD data, with the nitrogen deficiency causing a contraction of the lattice constant, and an increase in the peak angle. γ -Nb₄N₃ would have a theoretical nitrogen fraction $y = 0.43$, which places the niobium containing samples in Table 8 in between γ -Nb₄N₃ and δ -NbN in terms of nitrogen fraction. This deviation from the expected 1:1 stoichiometry may explain some of the shift in peak location in the XRD data in Figure 89 but would be expected to have a much more leftward shift of the peak based on the RBS data. Nitrogen deficiency may be accompanied by strain in the lattice causing a contraction of the out-of-plane lattice constant. Since the sapphire substrate

may create a tensile stress on the $(\text{Nb}_x\text{Ti}_{1-x})_{1-y}\text{N}_y$ layer, the out-of-plane lattice constant would be expected to contract in accordance with the Poisson's ratio of the material. This interfacial strain may pair with the nitrogen deficiency to cause the peak shift seen in the XRD data.

The T_c for these $(\text{Nb}_x\text{Ti}_{1-x})_{1-y}\text{N}_y$ samples fails to reach the value for $\delta\text{-NbN}$ seen in literature [137], but are consistently above the T_c for $\gamma\text{-Nb}_4\text{N}_3$, [88] which may be expected from the asymptotic behavior seen in the XRD data. Since the $\gamma\text{-Nb}_4\text{N}_3$ phase can be visualized as a nitrogen deficient rock salt unit cell, this critical temperature in between $\gamma\text{-Nb}_4\text{N}_3$ and $\delta\text{-NbN}$ may suggest a metastable film with a nitrogen content of $0.43 \leq y \leq 0.50$. This is corroborated by the RBS results, which may point to the inclusion of niobium in the film causing a nitrogen deficiency.

Since $(\text{Nb}_x\text{Ti}_{1-x})_{1-y}\text{N}_y$ is often used as a high kinetic inductance material for single photon detectors and similar devices, Ansys was used to simulate resonator devices with two different mask designs which were then used to create physical resonators from the $(\text{Nb}_x\text{Ti}_{1-x})_{1-y}\text{N}_y$ alloys. [138] Resonator measurements show a trend for frequency shift and kinetic inductance fraction that has minima at the binary endpoints, which increase when the alloy is of mixed composition. Kinetic inductance values extracted from the frequency shift of the resonators are less than 30X smaller than $\text{Nb}_x\text{Ti}_{1-x}\text{N}$ in literature, demonstrating the role of microstructure in kinetic inductance. Tzu-Ming Lu et al. reports a $L_k = 400$ pH/sq for their NbTiN samples produced using DC magnetron sputtering, as well as Vandersypen et al. reporting $L_k = 35$ pH/sq for their sputtered samples. [139], [140] It should be noted however that both groups were investigating intentionally high kinetic inductance materials like sputtered NbTiN.

RF measurements demonstrate a resonator center line width dependence on the fractional frequency shift, and is similar to the effect reported by Gao. [141] It was shown that variation in

the center line width changes the electric field strength and degree that TLS are saturated. Smaller resonator line widths were shown to have larger fractional frequency shifts, which is consistent with this work.

It can be shown that the measured kinetic inductances track well with BCS theory-predicted kinetic inductances for $(\text{Nb}_x\text{Ti}_{1-x})_{1-y}\text{N}_y$ samples with x less than 0.70. For high Nb content samples this agreement between theory and experiment fails, and the BCS theory predicted kinetic inductances rise an order of magnitude over those of the measured samples.

Chapter 5: Annealed NbTiN

Due to the thickness requirements for JJ fabrication and the surface roughness encountered when growing $(\text{Nb}_x\text{Ti}_{1-x})_{1-y}\text{N}_y$ alloys in the previous chapter, a new growth scheme is required to produce high quality material. In this chapter, a technique for in-situ annealing of transition metal nitrides is developed, showing improvements in crystal quality, superconducting critical temperature, and most importantly, surface roughness. All samples in this chapter have a target composition of $(\text{Nb}_{0.84}\text{Ti}_{0.16})_{0.50}\text{N}_{0.50}$, and so will be referred to as NbTiN for simplicity.

5.4 Impact on $\text{Nb}_x\text{Ti}_{1-x}\text{N}$ Alloys

All samples in the annealed $\text{Nb}_x\text{Ti}_{1-x}\text{N}$ series were grown to a target composition of $x = 0.84 \pm 0.02$, verified using EDS. This composition was chosen as the target since the interpolated atomic spacing of the $(\text{Nb}_{0.84}\text{Ti}_{0.16})_{0.50}\text{N}_{0.50}$ alloy would ideally be identical to the in-plane atomic spacing of AlN (0001), which may create a coherently bonded interface at the JJ barrier layer. This composition also affords good surface roughness when compared to higher Ti content films, while keeping a safe buffer preventing any growth of $\epsilon\text{-NbN}$, which would significantly decrease the T_c and decrease surface uniformity.

Figure 101 shows the progression of the anneal with RHEED, where the sample is grown at 1000 °C and annealed at 850 °C.

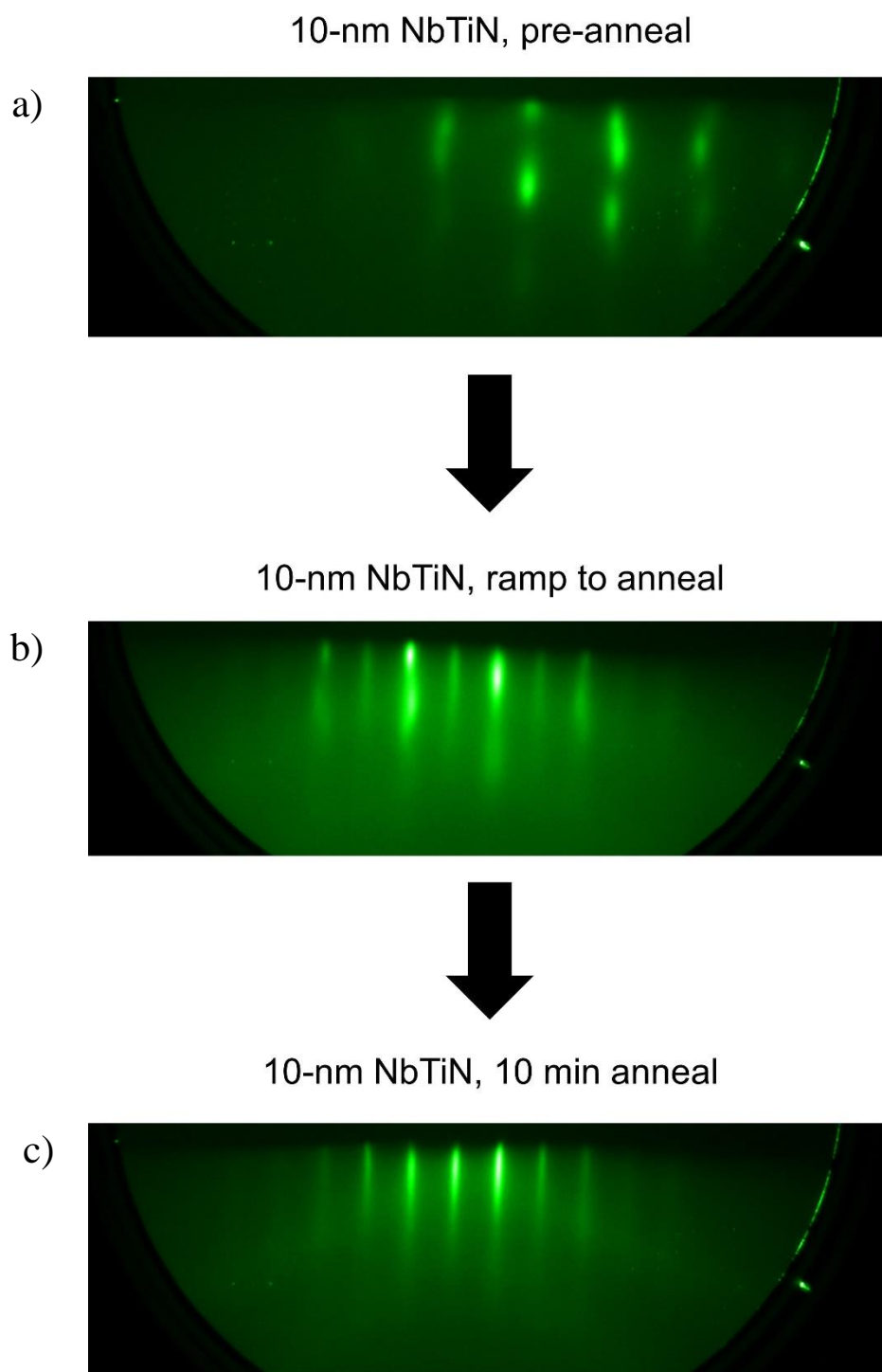


Figure 101: RHEED progression as the post-growth anneal progresses. Some images are offset due to rotation of the substrate and interaction of the RHEED beam with the electron beam positioning magnet.

Figure 101(a) begins immediately post growth and possesses a spotty pattern typical of NbTiN alloys, which indicates 3D growth with a “river-rock” surface morphology. The RHEED pattern in Figure 101(b) becomes streaky during the ramp to the anneal temperature. The final RHEED image in the progression occurs 10 minutes after the ramp to 850 °C has finished, and features nearly complete streakiness in the RHEED pattern, indicating a smooth 2D surface. Change in the RHEED pattern halts after 10 minutes and maintains this streakiness when cooled down to 200 °C, before removal from the chamber and exposure to air and room temperature.

The topography for the annealed samples undergoes a drastic change after an anneal, growing a very smooth 2D surface with RMS roughness less than 1 Å. Figure 102 shows the AFM and RHEED for an unannealed 76.9-nm thick NbTiN sample in Figure 102(a, c) and a 112-nm thick sample annealed at 850 °C for two hours in Figure 102(b, d).

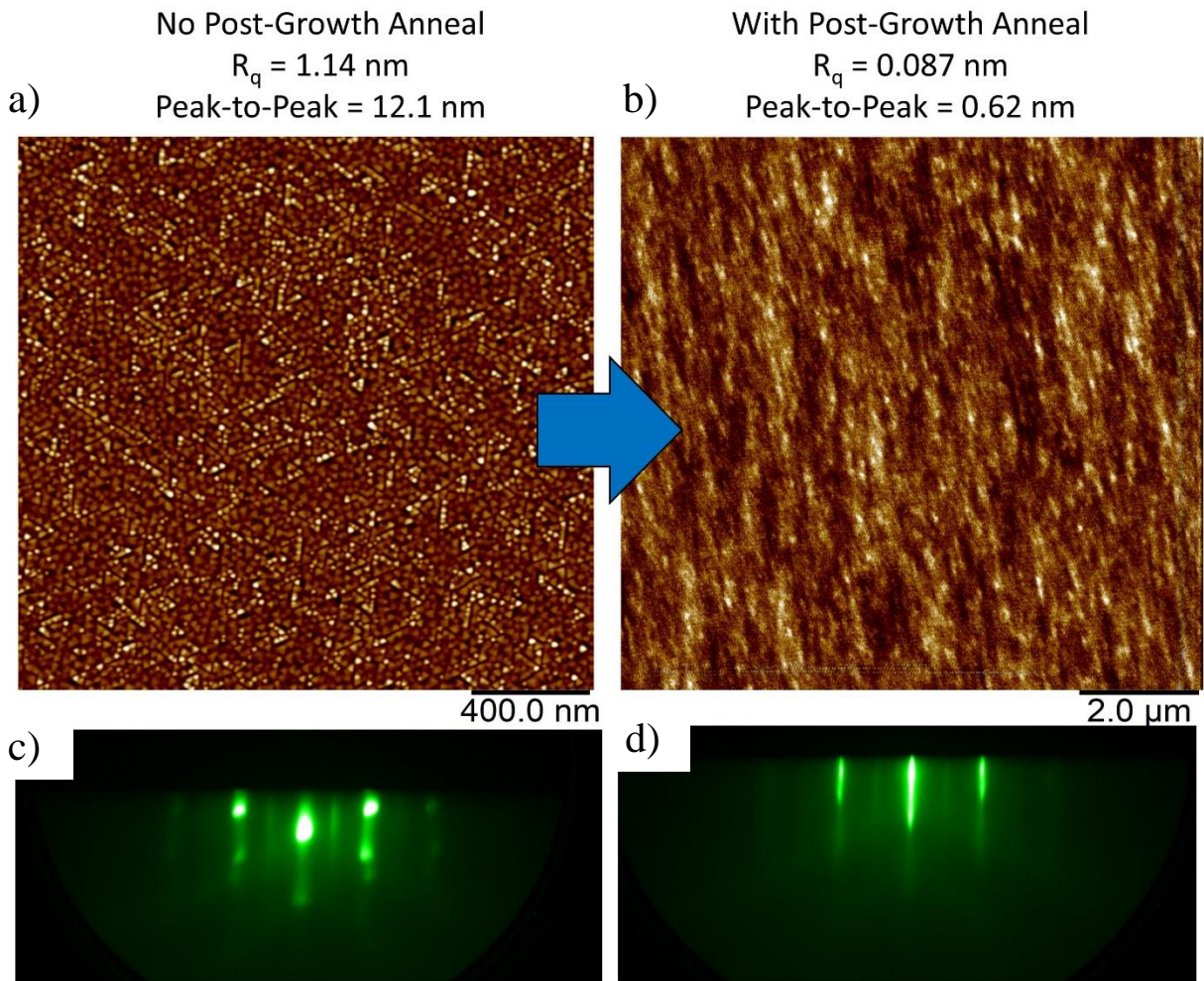


Figure 102: a) AFM of an unannealed NbTiN sample. b) AFM of a NbTiN sample annealed at 850 °C for 2-hours. c) RHEED of an unannealed NbTiN sample. d) RHEED of a NbTiN sample annealed at 850 °C for 2-hours.

Both samples in Figure 102 were grown with a substrate temperature of 1000 °C. The nitrogen overpressure for both samples was identical, with 1.8 sccm at a forward power of 500 W. The annealed surface consists of a streaky morphology with an excellent R_q for this material of less than 1 Å. The RHEED and surface shown develop after an anneal for two hours. This streaky RHEED pattern is void of spots, indicative of the smooth 2D surface grown.

The low peak-to-peak roughness is adequate for JJ fabrication, with a value of 0.62 nm. For a barrier layer of ~5-10 nm of AlN in the JJ heterostructure, this relatively low peak to peak

roughness should prevent pinhole defects which would otherwise have been created using a higher roughness material like the non-annealed sample in Figure 102.

This smooth surface persists for a limited time when exposed to air, after which the surface oxidizes into the surface shown in Figure 103.

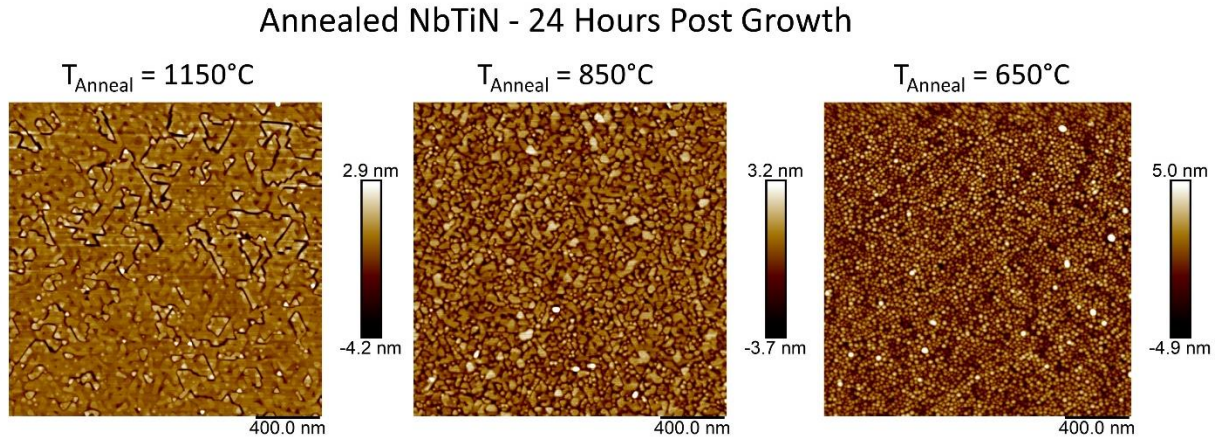


Figure 103: Oxidation effects of the NbTiN film after being annealed at 1150 °C, 850 °C, and 650 °C, then left at ambient conditions for 24 hours.

Ambient condition oxidation of the films over the course of 24 hours results in flat regions on the surface interspersed with trench-like features which are at least several nm deep, with measurement limited by the size of the AFM tip. The density of the trenches and flat islands is dependent on the anneal temperature, with the lower temperatures producing a surface similar to the “river-rock” style morphology seen in samples without an anneal step. Figure 103 shows AFM scans of several samples annealed at different temperatures after 24 hours in an ambient environment.

All samples annealed in Figure 103 had a $t_A = 2$ hours. The sample annealed at 1150 °C in Figure 103 has a $R_q = 0.816$ nm, with a peak-to-peak roughness of 17.6 nm, largely due to the trench depth. The sample annealed at 850 °C has a $R_q = 0.995$ nm and a peak-to-peak roughness

of 6.11 nm. The sample annealed at 650 °C has a $R_q = 1.43$ nm, and a peak-to-peak roughness of 17.0 nm, with a surface morphology similar to an unannealed sample.

5.4.1 Effect of Anneal Temperature Variation

Annealing the NbTiN samples affects the crystalline quality of the films and this effect can be seen in the symmetric XRD of each sample. In Figure 104, several annealed samples and a control sample without an anneal are shown. Anneal temperatures range from 1150 °C to 650 °C, all with a two-hour duration. The extensive thickness fringes are evident on all annealed samples, extending beyond the range typically seen on samples such as the control sample. In addition to the crystalline quality increasing, a peak shift can be identified, and is dependent on anneal temperature.

All samples shown in Figure 104 are grown with the same growth conditions, with a substrate temperature of 1000 °C during growth, and under a nitrogen flux of 1.8 sccm at a forward power of 500 W. The target thickness of all samples is 100 nm, and small deviations in thickness and composition are mainly due to inconsistencies in titanium flux.

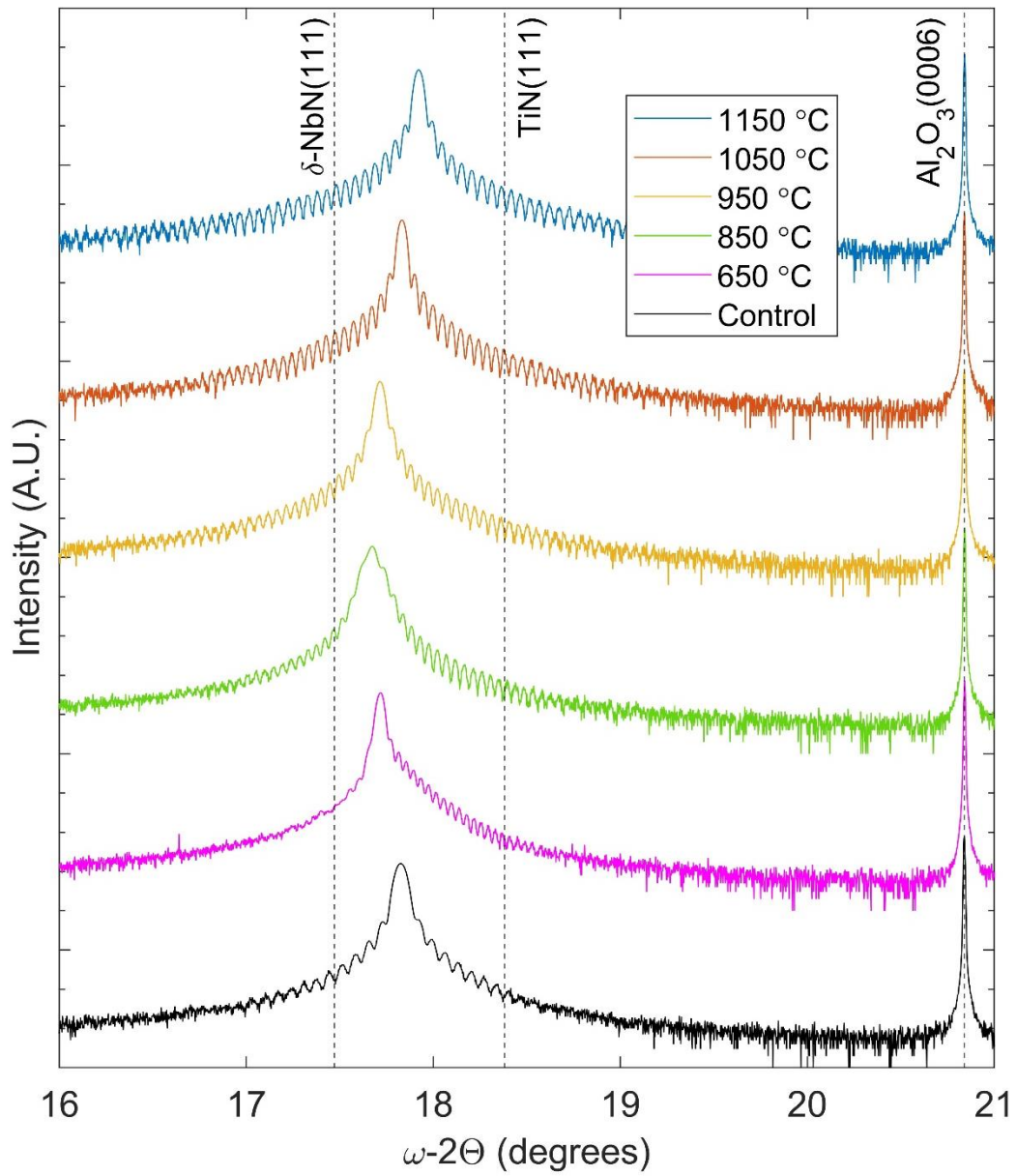


Figure 104: Symmetric XRD ω - 2θ data for annealed NbTiN samples with T_A ranging from 650 °C to 1150 °C

The peak angle of the NbTiN (111) peak is visualized in Figure 105, where a minimum peak angle is seen for the sample annealed at 850 °C. This indicates an expansion in the lattice of the NbTiN film. The peak angle increases for anneal temperatures greater or less than 850 °C, with anneal temperatures of 1050 °C and 1150 °C producing a peak from a smaller d spacing than the control sample, indicating a contraction of the lattice during the anneal step at high temperatures.

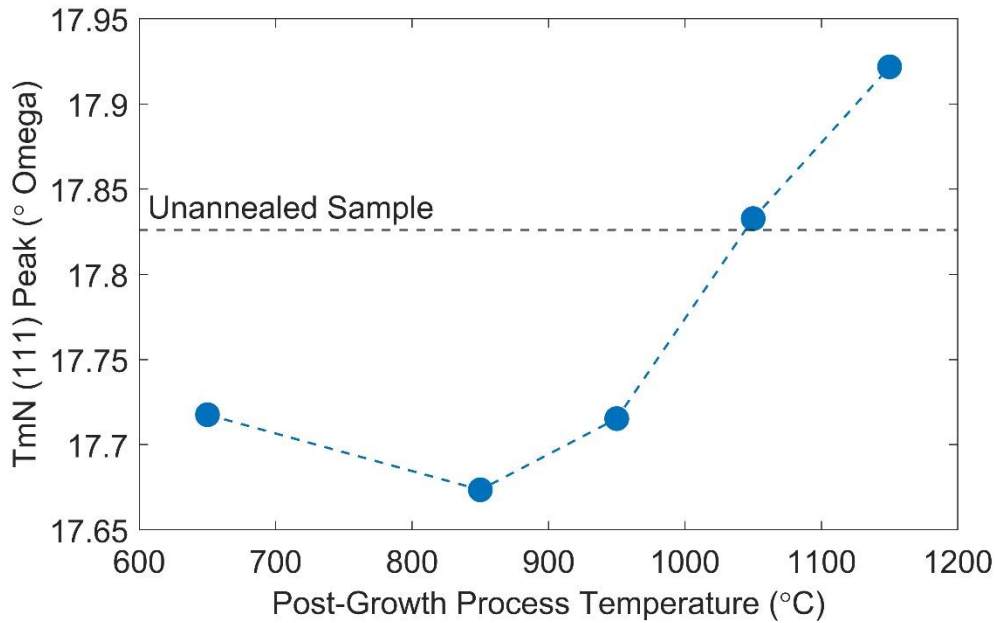


Figure 105: Peak shift for NbTiN samples annealed at temperatures varying from 650 °C to 1150 °C.

The improvement in the crystal quality can also be seen in the thickness measurements of annealed samples. The ratio of the thickness extracted from XRR data and the thickness extracted from XRD thickness fringes can be used to probe the amount of the film ordered into a homogenous crystal structure. The thickness from XRR is a measure of the entire film thickness from top interface to the interface with the substrate, while the XRD fringe thickness is a measure of the number of complete, perfect unit cells stacked up through the film. The ratio of the two gives an estimate of the film fraction that is well ordered. Figure 106 shows the trend of

XRD:XRR thickness ratio as a function of anneal temperature. All samples annealed show a higher ratio than the control sample by ~5 %, indicating a larger percentage of the film is coherently grown with complete unit cells when annealed.

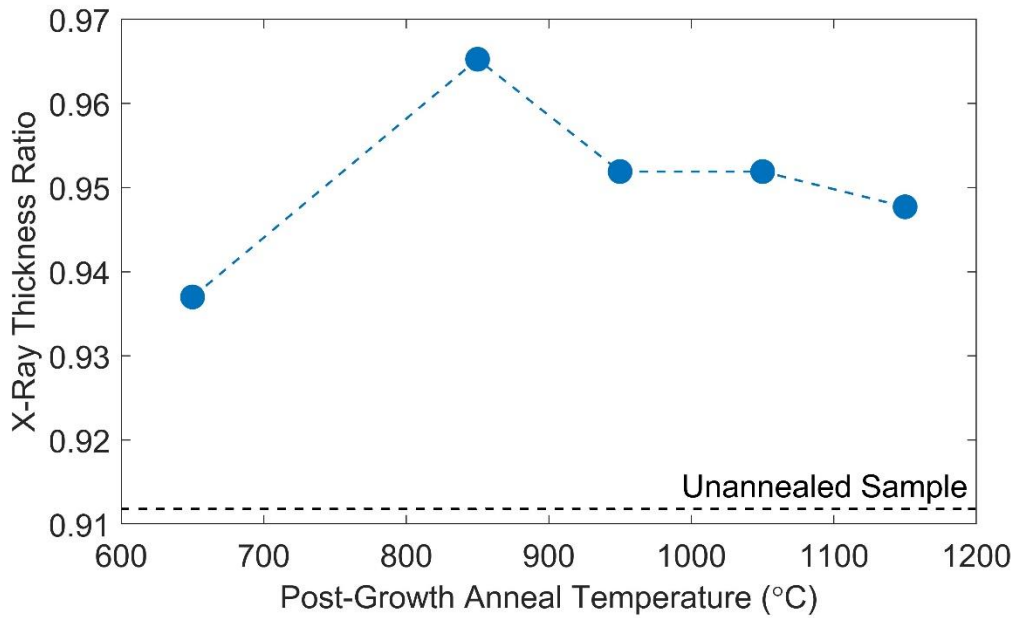


Figure 106: Ratio of thickness obtained from XRD fringes and extracted from XRR data of NbTiN samples annealed.

RBS results from annealed samples show a similar trend to the XRD peak shift. Figure 107 shows an increase in nitrogen content y in $(\text{Nb}_{0.84}\text{Ti}_{0.16})_{1-y}\text{N}_y$ for all samples above the control sample at anneal temperatures less than 1050 °C. For anneal temperatures greater than 1050 °C, the nitrogen content decreases, possibly indicating decomposition of the material, bringing the nitrogen content below 0.5 and into the nitrogen deficient range for this material. The error bars in Figure 107 represent the standard deviation of the nitrogen content allowed by

the simulated fit before the fit exceeds a χ^2 value of 1. This represents the point at which SIMNRA does not recognize the fitted solution as valid for the experimental data presented.

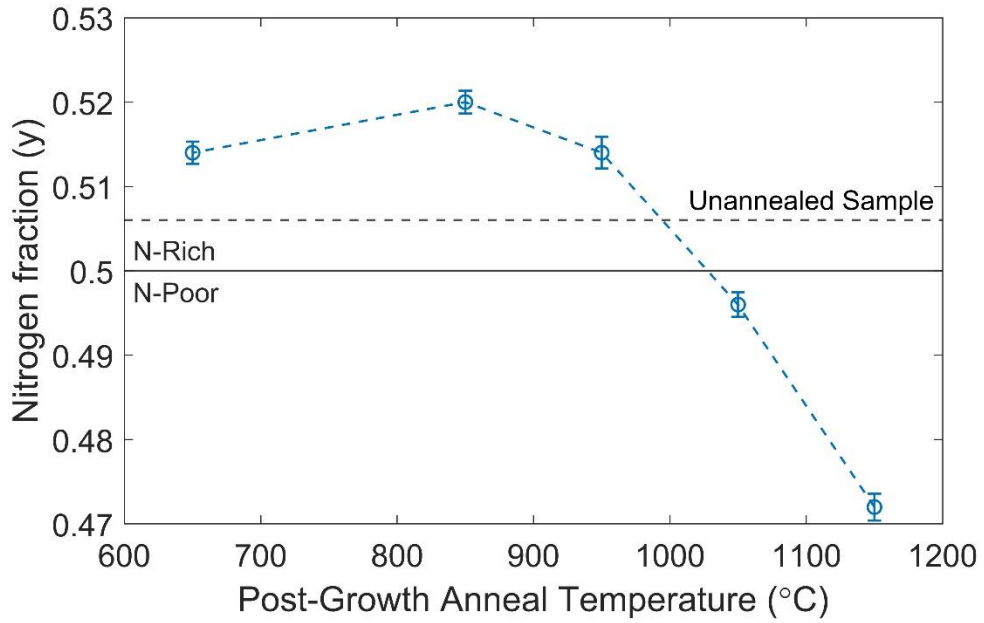


Figure 107: Nitrogen fraction of annealed $(\text{Nb}_{0.84}\text{Ti}_{0.16})_{1-y}\text{N}_y$ films from RBS simulated fits.

Anneal temperature affects the critical temperature of NbTiN films, in addition to changing the RRR and transition width of these films. Figure 108 shows several superconducting transitions for annealed samples.

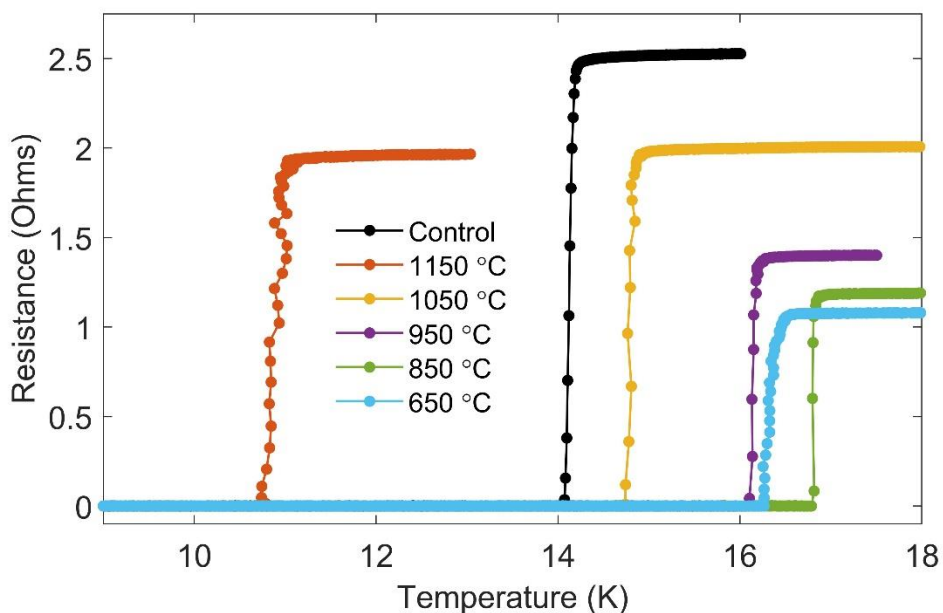


Figure 108: Superconducting transitions for NbTiN samples annealed at varying temperatures. A control sample with no anneal is shown in black.

Figure 109 shows the trend for critical temperature versus the temperature of the anneal, with improvement showing for all samples annealed at temperatures less than 1150 °C. In Chapter 3, the superconducting critical temperature plateaued near 14 K regardless of the composition of the film. With the anneal step performed on NbTiN samples, the critical temperature rises to 16.8 K, near the literature maximum value of 17.3 K of δ -NbN when annealed at 850 °C for 2 hours. [137] At 1150 °C, the sample experiences significant degradation of the critical temperature, being reduced to 10.9 K, well below the non-annealed sample T_c of 14.1 K.

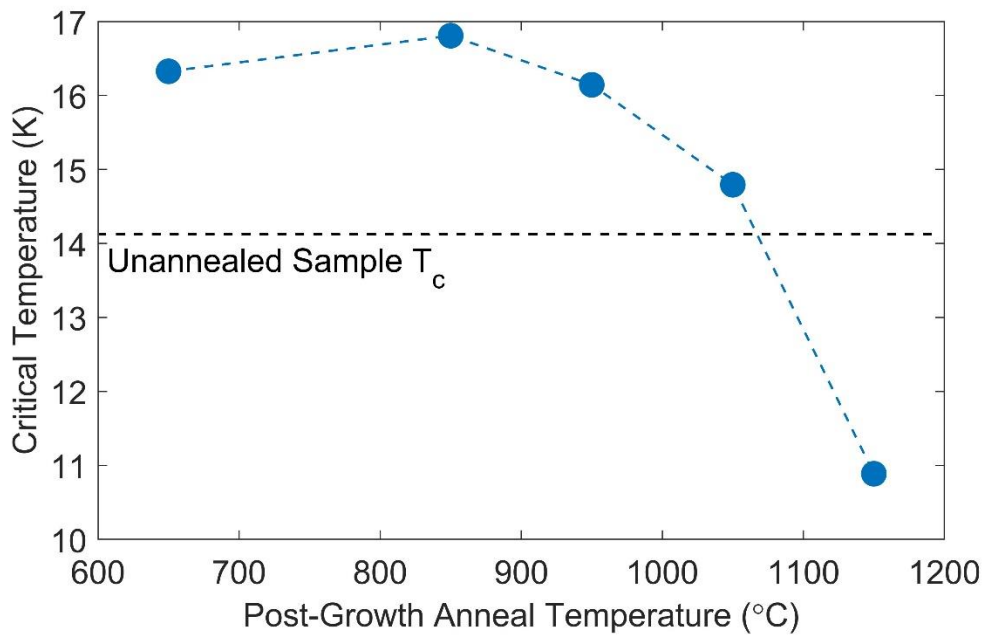


Figure 109: Superconducting critical temperature as a function of anneal temperature, with a control sample added as a horizontal line.

The transition width of these films is also affected by the anneal step. Figure 110 shows the transition width and RRR of NbTiN samples as a function of anneal temperature. While there is no significant impact to the RRR in Figure 110(a), the transition width shows a clear trend with anneal temperature in Figure 110(b), reaching a minimum for the anneal temperature of 850 °C, and becoming higher than the control sample when the anneal temperature was set to 650 °C or when the anneal temperature is greater than or equal to 1050 °C.

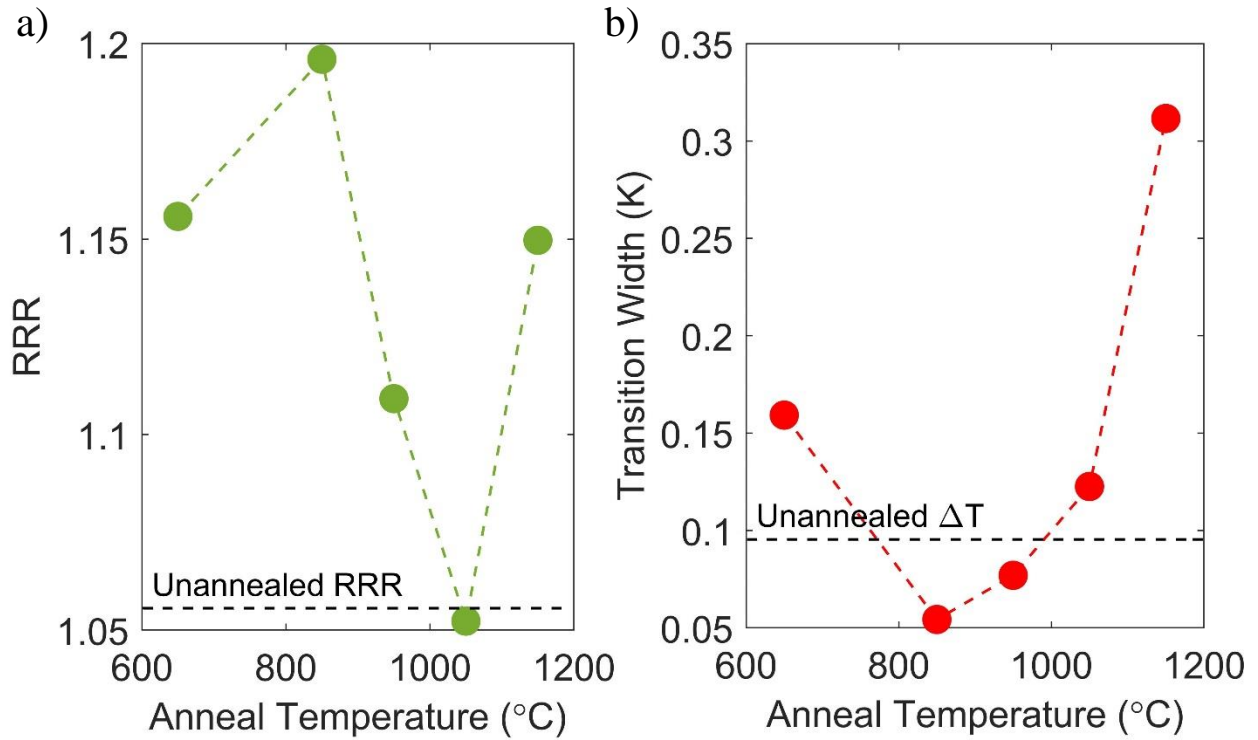


Figure 110: RRR and transition width for annealed NbTiN samples. An unannealed sample is shown as a horizontal line for reference.

The values for the nitrogen content, critical temperature, transition width, and RRR for annealed NbTiN samples are tabulated below in

Table 10. All samples listed are annealed for two hours.

Table 10: Compositional and electrical properties for NbTiN sample annealed at varying temperatures.

| T_A (°C) | Metal Composition (x) | Nitrogen Fraction (y) | T_c (K) | Maximum ΔT (K) | RRR |
|------------|-----------------------|-----------------------|-----------|------------------------|------|
| Control | 0.83 | 0.506 | 14.127 | 0.095 | 1.06 |
| 650 | 0.83 | 0.514 | 16.326 | 0.159 | 1.16 |
| 850 | 0.83 | 0.520 | 16.808 | 0.054 | 1.19 |
| 950 | 0.84 | 0.514 | 16.144 | 0.077 | 1.11 |
| 1050 | 0.84 | 0.496 | 14.793 | 0.123 | 1.05 |
| 1150 | 0.82 | 0.472 | 10.887 | 0.312 | 1.15 |

5.4.2 Effect of Anneal Time

The duration of the anneal step after sample growth also affects the final properties of the film. Samples were annealed at 850 °C for 30 minutes, 2 hours, and 4 hours, with a control sample forgoing the anneal step. 850 °C was chosen as the optimum anneal temperature due to the maximization of T_c , maximization of nitrogen content, with improvements in both crystal quality and surface roughness. Figure 111 shows the symmetric XRD for annealed samples, along with an unannealed control sample in black.

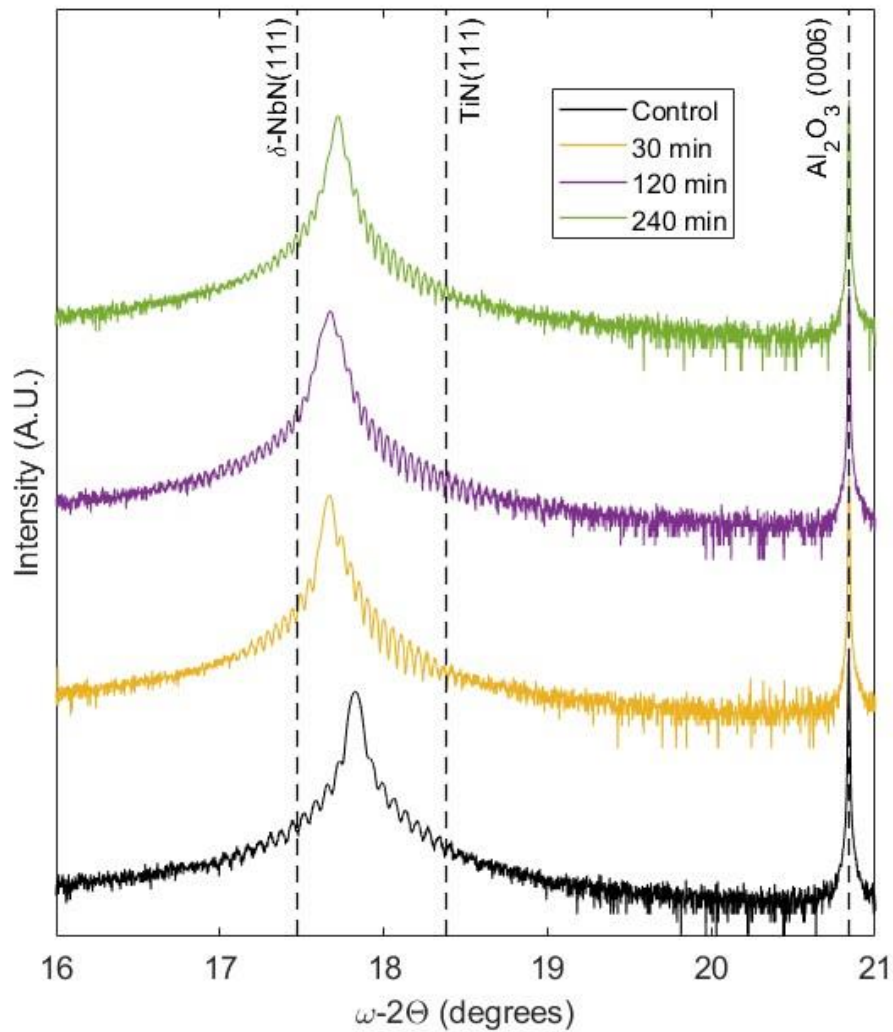


Figure 111: XRD for annealed samples of varying durations at 850 °C

Similar to Figure 104 showing XRD at varying anneal temperatures, all annealing times possess extensive thickness fringes which indicate excellent crystal quality. Some asymmetry is present in the annealed sample NbTiN (111) peak, which may be due to interference between the reflectivity fringes and the thickness fringes. The peak shift seen through the sample range is displayed in Figure 112.

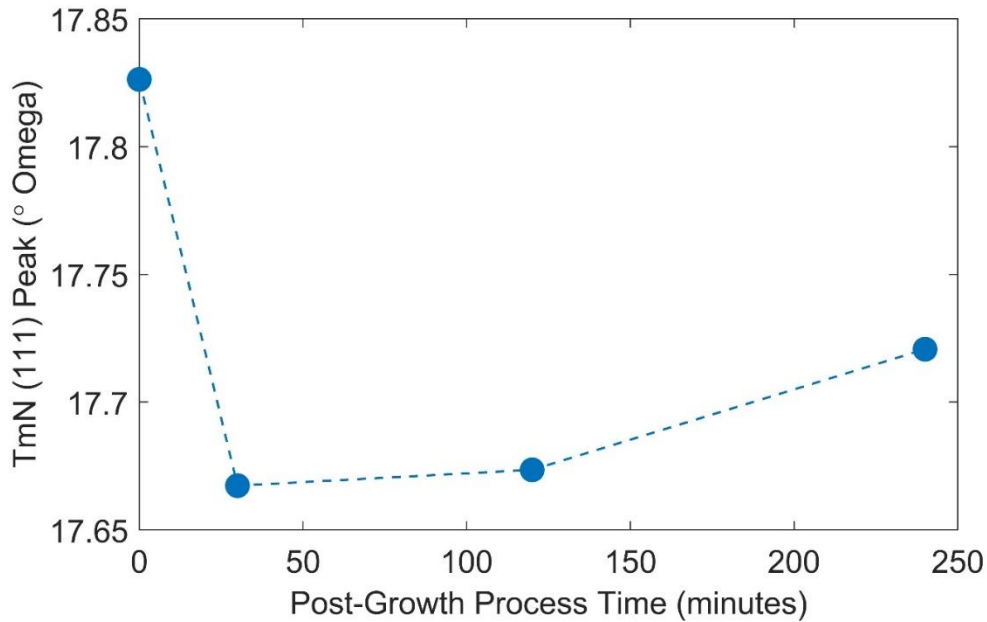


Figure 112: XRD peak shift as a function of t_{anneal} at $T_{\text{anneal}} = 850^{\circ}\text{C}$.

With an anneal time of 30 minutes, the symmetric XRD peak is shifted 0.158° from the control, which corresponds to an increase in lattice constant by 0.87 % assuming a cubic unit cell. The peak angle then begins to increase slightly as the anneal time increases.

Figure 113 shows the ratio of thickness calculated from XRD fringes and thickness extracted from XRR data for each sample. The ratio increases steadily from 0.91 to 0.98 at four hours of annealing time. This may indicate that as the sample is annealed, the crystal uniformity in the bulk of the material continually improves to an upper limit.

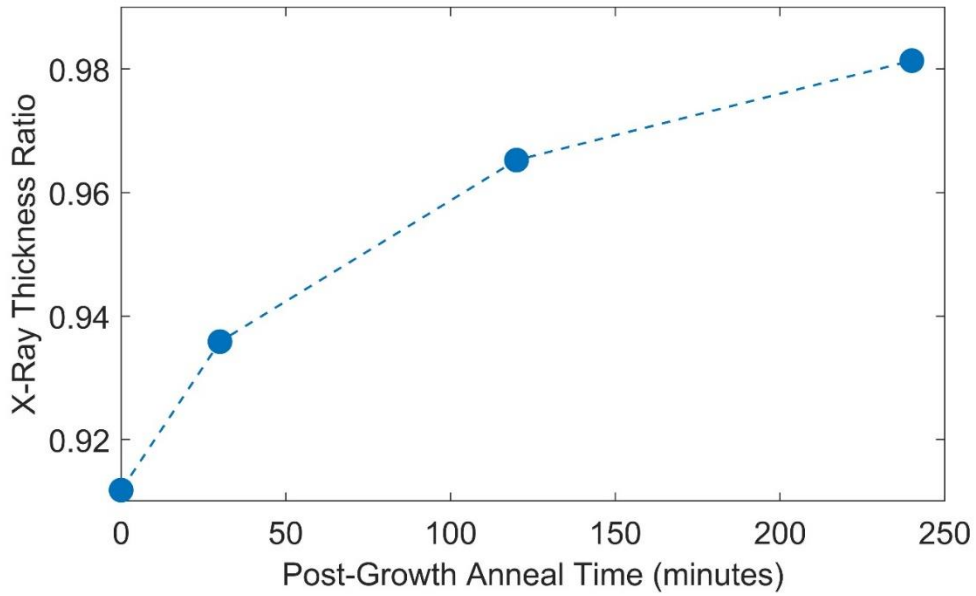


Figure 113: Thickness ratio of XRD: XRR measurements as a function of t_A .

The anneal time was not extended beyond 4 hours, where the thickness ratio may possess asymptotic behavior up to a ratio of 1.0. This trend in thickness ratio does not fit with the trend seen in both the peak location and the nitrogen content in Figure 114.

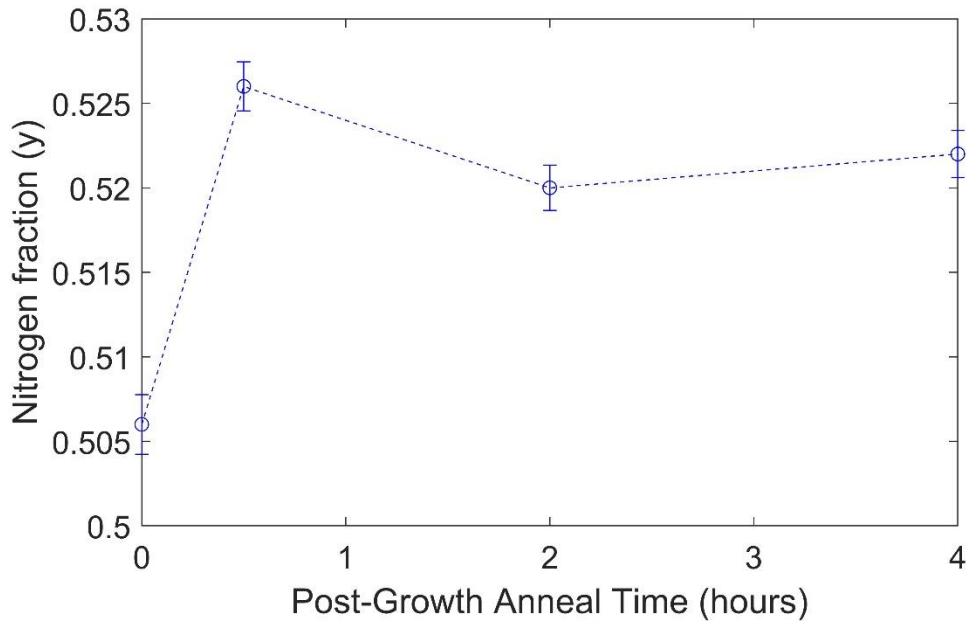


Figure 114: RBS measurements of nitrogen content extracted from simulated fits of the experimental data.

Both of these trends see a maximum lattice constant and nitrogen content after 30 minutes of annealing, then a slight decrease. The improvement over the control sample is consistent for all anneal times, however. Tying the results of these two data sets with the results of the thickness ratio may indicate that two responses to the annealing are occurring simultaneously. Nitrogen incorporation in the film may be initially increased, then saturates with a slight decrease as annealing time increases. This may be happening alongside an improvement in crystallinity of the sample.

Figure 115 below shows the superconducting transitions for NbTiN samples all grown at 1000 °C and annealed at 850 °C for varying lengths of time. All transitions are abrupt with improvement seen in the critical transition temperature for all anneal durations.

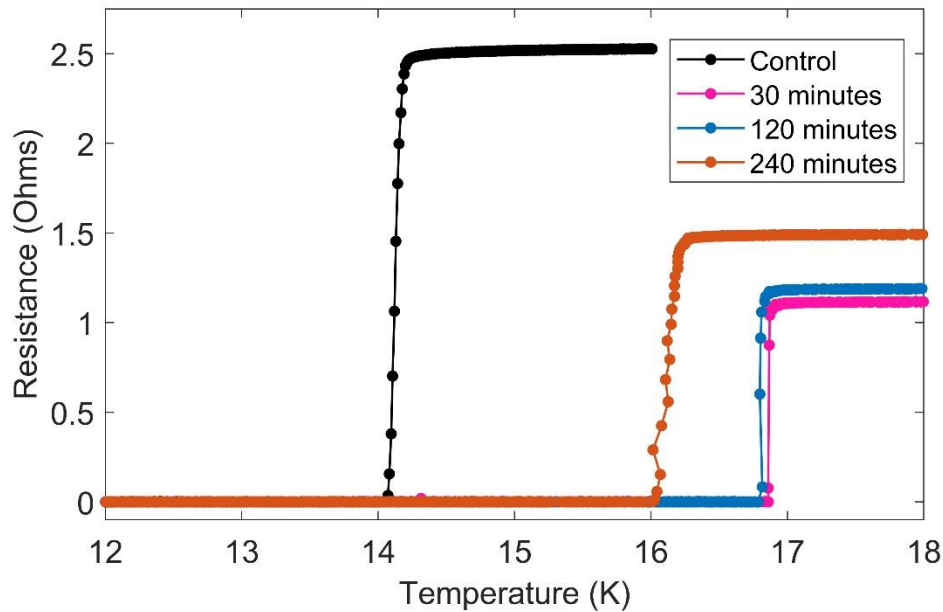


Figure 115: Superconducting transitions for NbTiN samples with varying t_A .

Figure 116 displays the critical temperature of the four samples above as a function of anneal time at 850 °C. Maximal T_c of 16.86 K is obtained at $t_{\text{anneal}} = 30$ minutes. Surface topography has little change after the first 30 minutes of anneal time, possessing a smooth 2D surface with R_q less than 1 Å.

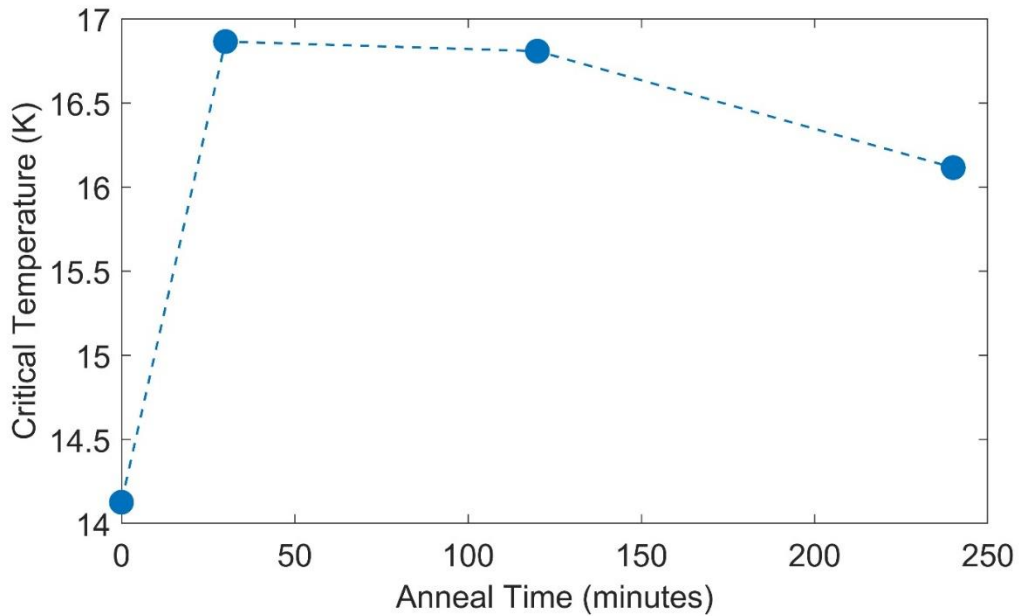


Figure 116: Critical temperature of NbTiN alloys as a function of anneal duration.

In Figure 117, the transition width and RRR are shown for the annealed samples and a control sample. After the initial 30 minute anneal, RRR quickly rises ~30 % higher than the non-annealed sample, while the transition width decreases by nearly an order of magnitude. RRR then sharply decreases with increasing anneal time, which indicates a transition to more insulating character. Transition width increases an order of magnitude over the course of four hours of anneal time, to nearly double the maximum transition width of the non-annealed sample.

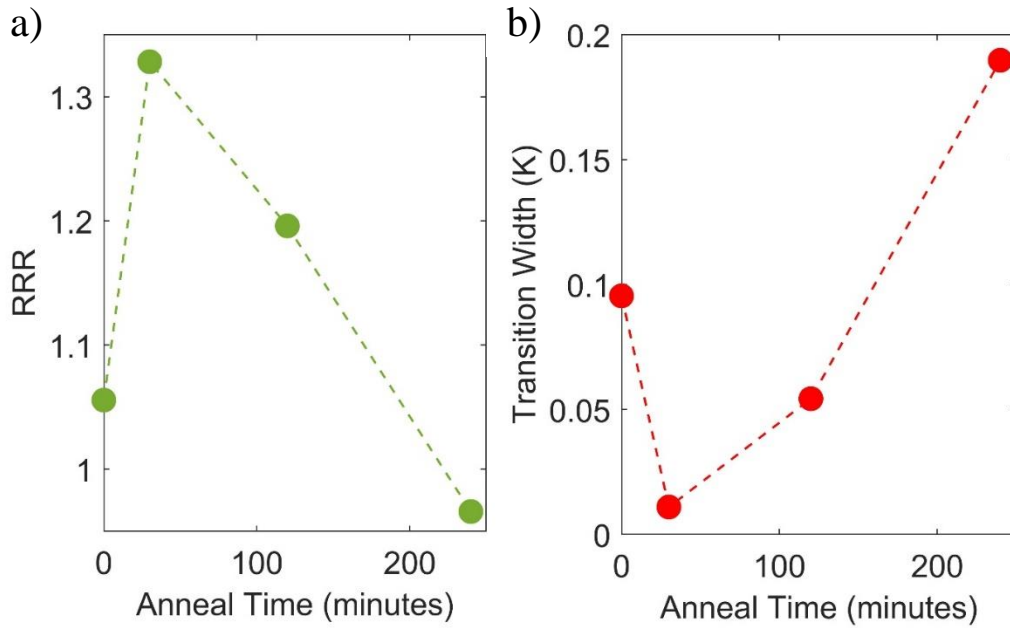


Figure 117: RRR and transition width for NbTiN samples of varying anneal times, at $T_A = 850\text{ }^\circ\text{C}$.

These results indicate changes in the electrical properties that are not reflected in the structural and compositional properties of the annealed films. Through the varying t_A , the nitrogen content does not change appreciably while the X-Ray results indicate that the film quality is improving with increasing anneal time.

The values for the nitrogen content, critical temperature, transition width, and RRR for annealed time dependent NbTiN samples are tabulated below in Table 11. All samples listed are annealed at $850\text{ }^\circ\text{C}$.

Table 11: Compositional and electrical properties for NbTiN sample annealed at varying durations.

| t_A (hours) | Metal Composition (x) | Nitrogen Fraction (y) | T_c (K) | Maximum ΔT (K) | RRR |
|------------------|-----------------------|-----------------------|-----------|------------------------|------|
| Control | 0.83 | 0.506 | 14.127 | 0.095 | 1.06 |
| 0.5 | 0.86 | 0.526 | 16.865 | 0.011 | 1.33 |
| 2 | 0.83 | 0.520 | 16.808 | 0.054 | 1.19 |
| 4 | 0.90 | 0.522 | 16.116 | 0.190 | 0.97 |

5.4.3 SIMNRA RBS Simulations

To examine the effect of changing nitrogen content on the RBS results for NbTiN samples, simulations were performed using the SIMNRA RBS software. To keep the simulations as comparable as possible, the niobium and titanium areal densities were kept constant, while the areal density of nitrogen in the film was adjusted to generate a simulated film with a range of nitrogen atomic percentages. Performing the simulations in this manner causes the thickness of the film to change in proportion to the nitrogen density, but the ratio of Nb:Ti as well as the density of both metals are kept constant. The simulation parameters are kept constant, with the energy offset $E_{\text{offset}} = 6.8 \text{ keV}$, the energy per channel $E_{\text{channel}} = 1.4 \text{ keV/ch}$, and the particle density value at 1.4×10^{12} . These values were chosen from averaging the values used in the automated fitting of the actual data from NbTiN samples.

Figure 118 shows the overview of the simulated data with plateaus seen from the substrate as well as peaks from the superconducting nitride film.

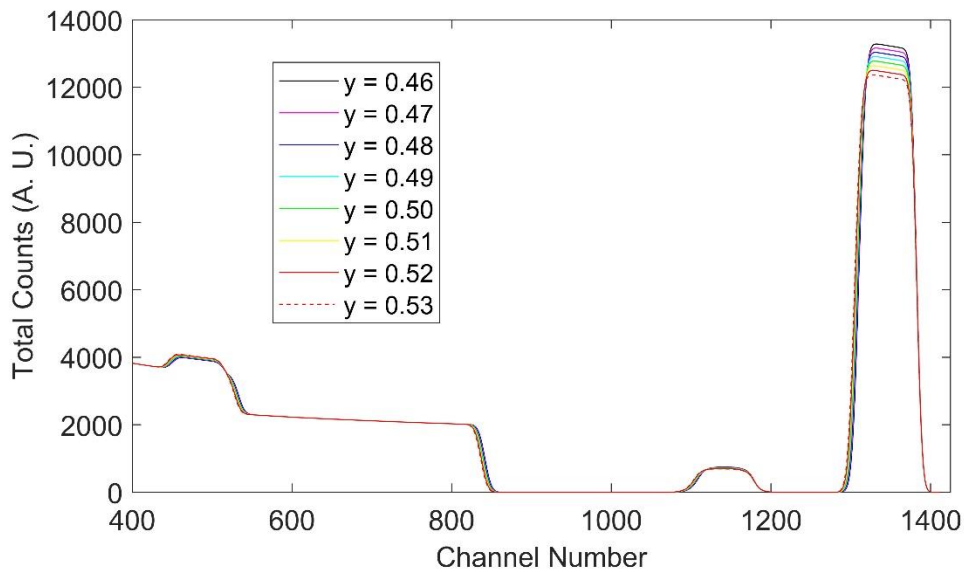


Figure 118: Simulations of $(\text{Nb}_{0.84}\text{Ti}_{0.16})_{1-y}\text{N}_y$ samples. Nitrogen content of the films is changed, with overall sample density floating and all other parameters fixed.

Variation is seen throughout the simulated data but is most prominent around the niobium peak. Isolating the component elements and zooming in on the nitrogen peak better reveals changes due to the nitrogen content. Nitrogen counts increases 22 % from $y = 0.46$ to $y = 0.53$, which are the extreme bounds from the experimental data. Niobium counts decrease by 7 % in the same range. The peak width change in this nitrogen content range is due to the simulated thickness of the sample changing with nitrogen areal density, as the two parameters are linked from the total areal density of all elements. The width change is not influenced significantly by the relative Tm:N ratio. The linked shift between the metal and nitrogen peaks makes manual fitting of RBS data difficult, as small changes to a single parameter greatly affect more than that element. Isolating the fit from the nitrogen and niobium peaks results in Figure 120, which more clearly shows the variation in peak height due to nitrogen content.

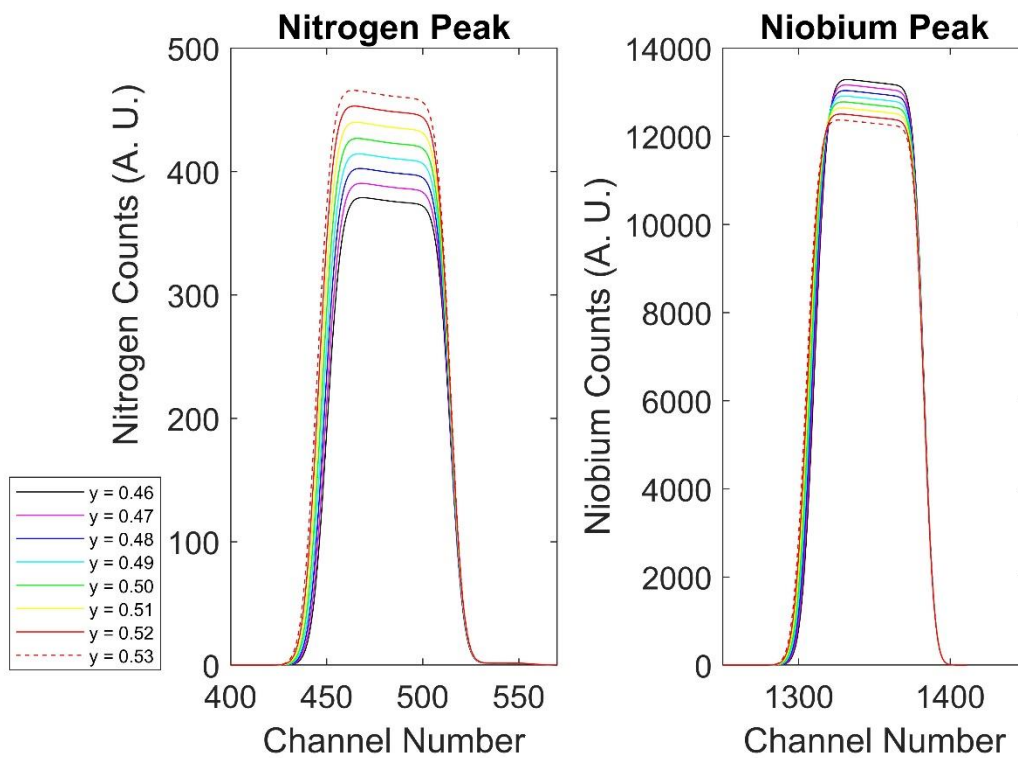


Figure 119: RBS simulations of isolated nitrogen and niobium peaks for a $\text{Nb}_{0.84}\text{Ti}_{0.16}\text{N}$ sample.

Figure 120 shows the fit and experimental data for an unannealed sample and annealed sample.

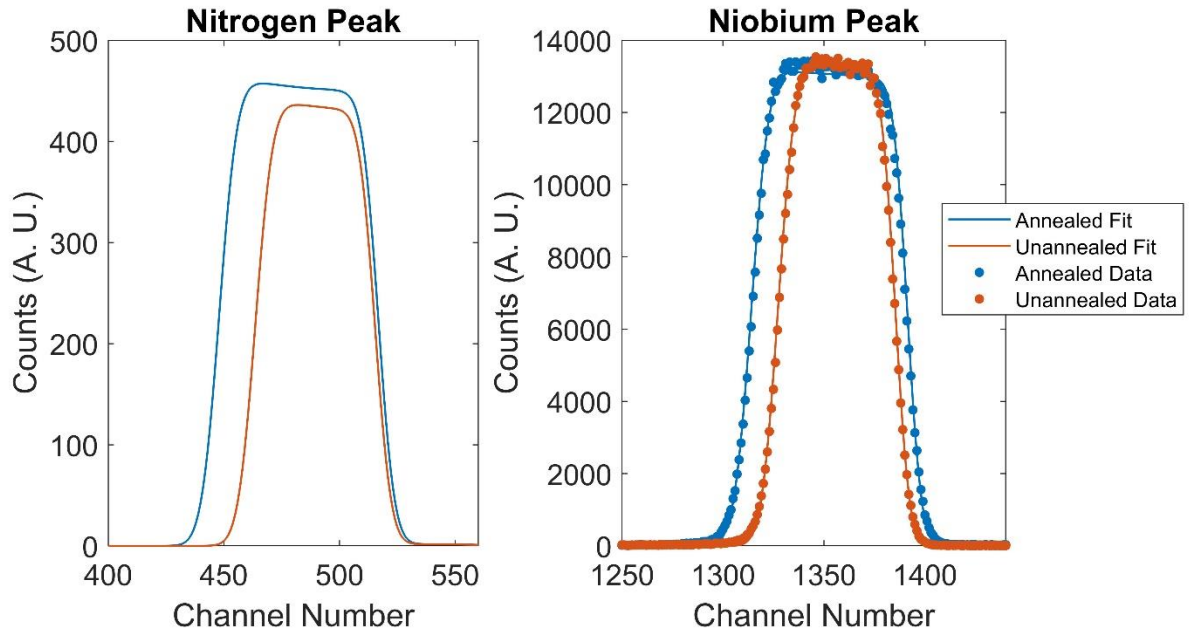


Figure 120: RBS fit and experimental data for the isolated nitrogen and niobium peaks. Experimental data is not shown for the nitrogen peaks due to influence of the substrate on the experimental data in that region.

Both NbTiN samples were grown at 1000 °C, with $T_A = 850$ °C and $t_A = 30$ minutes for the annealed sample. Fits are isolated components of the overall spectra fit, highlighting the variation seen in the nitrogen peak. Experimental data for the nitrogen peak is not shown due to the influence of the substrate plateau obscuring changes in the nitrogen peak.

5.5 Anneal Effects at Depth

Due to the dramatic surface morphology change when annealed, examination of the changes as purely a surface effect in NbTiN alloys was investigated. If the changes were simply due to a modified surface layer, whether due to nitrogen incorporation or increases in crystal quality, the T_c would be expected to decrease if a top portion of the sample was removed.

To investigate this, annealed samples grown at 1000 °C with T_A of 850 °C and 1150 °C for an annealing time of 2 hours, along with a non-annealed sample were thinned using an Oxford PlasmaPro 100 Cobra chlorine reactive ion etcher. Samples were etched an estimated 40-nm. The etch recipe consisted of a 2:1 Cl_2 : BCl_3 chlorine ratio with 2500 W forward power, and a substrate temperature of 40 °C.

Figure 121 shows the superconducting transitions for three samples etched using the recipe above. Solid lines indicate pre-etch measurements, while dashed lines indicate post-etch measurements.

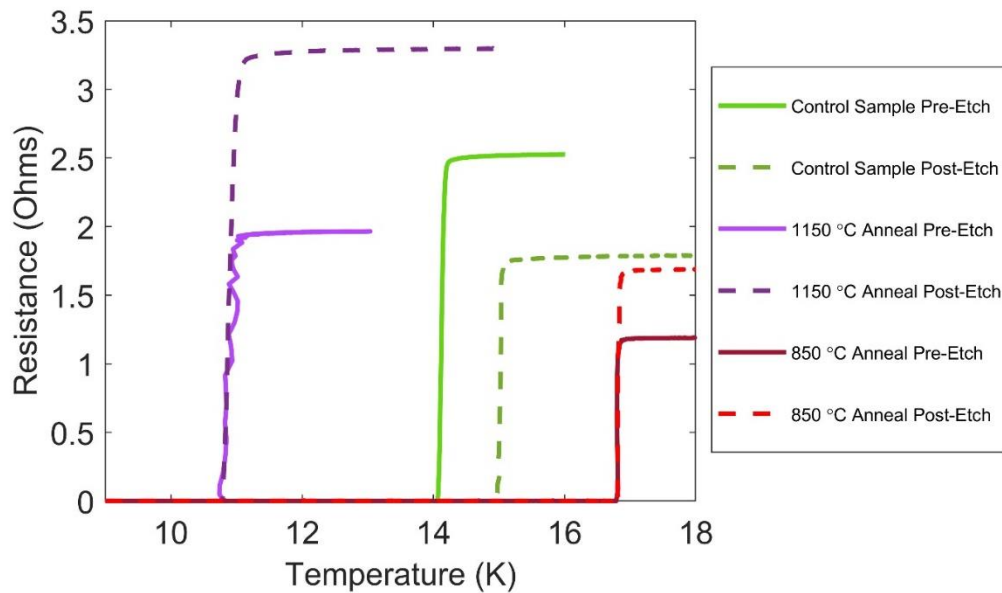


Figure 121: Effect of etching annealed and non-annealed NbTiN alloys.

Variation seen in the 1150 °C pre-etch sample is due to inadequate temperature averaging during the measurement, and not the sample itself. The annealed samples experience negligible change in the critical temperature, while the control sample increases T_c by over a Kelvin. The values are tabulated in Table 12.

Table 12: Tabulated values for etched annealed and unannealed NbTiN samples.

| T_A (°C) | T_c (K) | | ΔT (K) | | RRR | | XRR Thickness (nm) | |
|------------|-----------|-----------|----------------|-----------|----------|-----------|--------------------|-----------|
| | Pre-Etch | Post-Etch | Pre-Etch | Post-Etch | Pre-Etch | Post-Etch | Pre-Etch | Post-Etch |
| Unannealed | 14.12 | 15.02 | 0.095 | 0.061 | 1.056 | 1.049 | 76.9 | 32.0 |
| 850 | 16.81 | 16.82 | 0.054 | 0.042 | 1.192 | 1.290 | 112.5 | 64.1 |
| 1150 | 10.89 | 10.90 | 0.312 | 0.198 | 1.150 | 1.146 | 92.9 | 53.0 |

Considering the T_c of the annealed samples did not change significantly after etching, this indicates that the changes experienced by the sample during the anneal step are not purely surface effects. This is corroborated by the symmetric XRD for these samples which show enhancement of both the thickness fringes and XRD:XRR thickness ratio, which is consistent with a bulk affect during annealing.

5.6 Summary

An annealing scheme was used post-growth on 100-nm thick NbTiN samples with dramatic improvements in the surface roughness, critical temperature, and crystal quality. All samples had a metal composition, x , of 0.84. The anneal step occurred in-situ immediately

following growth under a nitrogen plasma overpressure. The tested parameters include anneals at 650 °C, 850 °C, 950 °C, 1050 °C, and 1150 °C. The duration of the anneal was tested at 30 minutes, 2 hours, and 4 hours.

The anneal was found to improve the crystal quality of the film at all temperatures and durations, evidenced by the enhancement of thickness fringes for each of these samples. The surfaces of these films were found to smoothen, shown by both a streaky post-anneal RHEED, and AFM of the samples within an hour of exposure to air. Interestingly, the surface drastically changes after approximately 24 hours in air due to the oxidation of this smooth surface, where the prevalence of trench-like features on the surface are dependent on the anneal temperature. The sample annealed at 650 °C establishes a lower bound on anneal temperature where the surface modification will occur. This oxidized surface is smoother than the “river-rock” surface, but the surface modification excludes it from being a viable base material for oxide barrier JJs.

Nitrogen content in the films was measured using RBS and found to follow the trend of critical temperature closely, with annealed samples with $T_A < 1050$ °C having a higher nitrogen content than unannealed samples, or those annealed at higher temperatures.

This anneal step also affects the critical temperature, where annealed samples show considerable improvement in T_c , reaching as high as 16.8 K. Critical temperature measurements after etching of the surface show that the annealing effect isn't due to a purely surface effect, but extends through the bulk of the film. The increase in T_c for the unannealed sample, considering the negligible change for the annealed samples, may suggest that there is a gradient of nitrogen concentration in the sample. The expectation for an etched sample is that the T_c would decrease compared to the full thickness sample, but Figure 121 shows an opposite effect. This may be due to the sample growing nitrogen deficient, with nitrogen diffusing downwards as the growth

progresses. By eliminating the upper nitrogen-deficient section of the sample, the superconductivity is now influenced by the relatively nitrogen rich lower section of the film. The annealed samples do not suffer from this effect due to the uniform distribution of nitrogen caused by the anneal step.

Chapter 6: Discussion and Future Work

6.1 Binary TiN and NbN_x

As shown in Chapter 3, using the binary transition metal nitrides TiN and NbN_x for Josephson junction fabrication results in films which are either too rough for a defect-free interface, or have multiple phases present which hinders both the surface uniformity and the superconducting critical temperature. TiN (111) produced using PAMBE typically has RMS surface roughness of 2-nm, with 1-nm roughness only possible for very thin TiN films (< 30 nm). Orientation of the TiN grown is stable, only deviating from a high-quality TiN (111) film in cases of high Ti flux where the α -Ti phase would begin to form.

For NbN_x, a novel phase control method was found by varying the substrate temperature and metal flux, which has some unintuitive results concerning nitrogen flow and nitrogen incorporation into the films. Looking at the heat maps of substrate temperature and niobium flux, while the nitrogen flux is constant throughout the growth series, the phase of NbN_x seen at higher Nb fluxes is of a higher nitrogen content than at lower metal fluxes. This may point to the ϵ -NbN phase being more stable than the γ -Nb₄N₃ phase at higher temperatures, as long as sufficient nitrogen is present. Based on nitridation studies of NbN_x, the phase progression typically follows α -Nb(N) \rightarrow β -Nb₂N \rightarrow γ -Nb₄N₃ \rightarrow δ -NbN, changing phase as the sample becomes more nitrogen rich. [92], [142], [143] This does not seem to be the case with PAMBE grown NbN_x, where thermodynamic stability of the phase is dominant, especially at higher temperatures.

In addition, the change in ϵ -NbN at high temperatures and high Nb fluxes is interesting in that a smoother surface is produced with the ϵ -NbN (10 $\bar{1}$ 0) orientation, indicating that a high surface temperature is required for sufficient surface diffusion to occur, and once reached results in this 2D growth mode of ϵ -NbN. Unfortunately, complete coverage of this smoother orientation of ϵ -NbN was not able to be grown and may require much higher substrate temperatures, or a different substrate orientation. Regardless of the surface features, the growth of ϵ -NbN results in a $T_c < 2$ K, and with a lattice constant far from matching with AlN, greatly reduces any benefit of using ϵ -NbN in a JJ structure over aluminum, a much more commonly used and well understood superconductor.

Only γ -Nb₄N₃ was able to be isolated, and only for low growth rates, lower substrate temperatures below 800 °C, and when grown thinner than 50-nm, which is too little for JJ fabrication. The originally desired phase, δ -NbN has been well documented in literature, but was unable to be grown within the growth conditions in this thesis, and on these substrates. Some literature indicates that the substrate has a significant effect on the orientation and possibly the phase of NbN_x thin films and this could be why the rock salt phase was unable to be grown. SiC and MgO substrates both offer a more closely matched cubic growth face and have resulted in cubic δ -NbN. [144]–[146]

Structural similarities between the δ -NbN rock salt structure and the γ -Nb₄N₃ tetragonal structure make identification difficult when using XRD or TEM. Both crystal structures have identical metal lattices, and only differ in the positioning of nitrogen vacancies. [88]

Identification is made more difficult in that δ -NbN_x is known to be stable in a wide range of stoichiometry from 0.72 to 1.06 [147], while the γ -Nb₄N₃ phase structure can be thought of as two rock salt unit cells stacked upon one another with ordered nitrogen vacancies. This makes

distinguishing between an off-stoichiometric rock-salt structure near indistinguishable from the tetragonal phase, as the nitrogen vacancies will compress the rock salt unit cell to have a lattice constant more reminiscent of the $\gamma\text{-Nb}_4\text{N}_3$ phase.

A 17 % reduction in FWHM of the cross sectional RSM along the line indicating changes in lattice constant of annealed TiN samples may indicate that the anneal step causes increased lattice uniformity through the thickness of the sample. The small increase in RBS nitrogen fraction for the annealed TiN sample in addition to the RSM data suggests that the change in lattice constant may be due to increased nitrogen incorporation into the lattice.

For JJ fabrication, the superconducting layers need to be grown relatively thick, approximately 100 nm or more, to allow for reliable and repeatable etching and lithography during fabrication. Unfortunately, growing NbN_x thicker with PAMBE seems to preferentially favor the growth of the hexagonal $\epsilon\text{-NbN}$ phase, which has a low T_c , and has a rough, nonuniform surface which makes coherent JJ interfaces impossible. With TiN, the high roughness creates a potential for pinhole defects in the tri-layer JJ structure, shorting the device and rendering it unusable.

6.2 NbTiN Alloys

To reduce the surface roughness of the nitride thin films while maintaining the rock salt crystal structure, alloying of TiN and NbN_x was performed. Initial results were positive, where the alloy maintained a single $(\text{Nb}_x\text{Ti}_{1-x})_{1-y}\text{N}_y$ (111) XRD peak for compositions of less than 0.97. For composition greater than 0.97, the $\epsilon\text{-NbN}$ becomes dominant. At this composition and higher, the surface would change from a “river-rock” style topography to having domains of

ϵ -NbN (0001) and ϵ -NbN ($10\bar{1}0$) as seen in Chapter 3. Fortunately, the theoretical ideal composition to lattice match in-plane with AlN is with an alloy $(\text{Nb}_{0.84}\text{Ti}_{0.16})_{0.50}\text{N}_{0.50}$, assuming a linear lattice constant shift between the binary endpoints, well below the transition point where ϵ -NbN is dominant. Analysis of the alloy range resulted in a peak shift between the TiN (111) peak and the γ -Nb₄N₃ (111) peak, which was unexpected as the stabilization of the rock-salt structure by the added titanium was originally thought to bridge the range to the δ -NbN (111) peak. This symmetric XRD based result implies that there is a change in crystal structure occurring as the niobium content of the film is increased. The tetragonal γ -Nb₄N₃ metal lattice and the δ -NbN metal arrangement should be identical according to Pickett et al., [88] so considering the metal-limited growth environment used to produce these films, the addition and elimination of nitrogen vacancies is left as a possible cause of the discrepancy in XRD peak shift.

Furthering the challenging analysis is the result from RBS measurements performed at Rutgers University. These show that Nb-containing Nb_xTi_{1-x}N_y samples have a nitrogen content of $0.46 \leq y \leq 0.49$. These films are slightly nitrogen deficient when compared to the rock salt crystal structure, but nitrogen rich when compared to the tetragonal rock-salt-like structure of γ -Nb₄N₃, which would have a nitrogen fraction $y = 0.43$. This lines up well for TiN samples but indicates that the final lattice of NbTiN should contain a nitrogen fraction between that of δ -NbN and γ -Nb₄N₃ at high niobium contents. The TiN film possesses a nitrogen fraction of $y = 0.55$, which would indicate excess nitrogen in the lattice, possibly in interstitial locations. Possible oxygen incorporated into the films is not accurately captured by RBS results.

The RBS results corroborate the superconducting critical transition temperatures seen in these samples, which have a maximum T_c of approximately 14 K, between γ -Nb₄N₃ (11.6 K) and

δ -NbN (17 K). Considering that these samples contain titanium, which should reduce the T_c in proportion to the titanium content, is testament to the good crystal quality of these alloys.

Nitrogen content has been shown to play a role in superconducting critical temperature, mainly by changing phase, but also within a phase by way of nitrogen vacancies. [86], [143]

Regardless of the nitrogen deficiency of the samples, all samples have very abrupt superconducting transitions and can be fabricated into resonators with low kinetic inductance when compared to literature. These results, in addition to the excellent quality fringes in the XRD, indicate good crystal quality. Unfortunately, use of these materials for JJ fabrication in their current state of optimization is limited by their surface roughness, which varies up to several nanometers. This roughness translates into pinhole defects in the JJ barrier layer, shorting devices.

Though poor candidates for epitaxial JJs, these films make adequate resonator devices, possessing high power internal quality factors in the several millions, and having kinetic inductances an order of magnitude less than sputtered NbTiN films used for single photon detectors and other devices. [138] It can be shown that the resonator center trace width has an effect on the fractional frequency shift that is not captured by the Ansys simulations or center width resonant frequency calculations.

The resonators fabricated in this work show a frequency shift dependence on the composition of the alloy, and subsequently a change in kinetic inductance as the composition is changed. The minimum frequency shift, and lowest kinetic inductance is seen at either end of the compositional range, with a maximum shift seen at around a composition of $x = 0.5$. The lack of agreement between BCS theory and the experimental results in Chapter 4 may indicate a change in superconducting character of the film as composition is varied. Since NbN_x behaves as a type

II superconductor, and BCS theory is mainly applicable to type I superconductors, the ability to predict the high Nb content film's kinetic inductance may suffer. As of this writing, this work is the first examination of the frequency shift in coplanar waveguides fabricated from NbTiN by PAMBE as a function of composition. While NbTiN as a low-loss material for resonators has been well studied, most literature uses a single composition of the alloy, and so the cause of the change in kinetic inductance with composition is unknown. [140]

6.3 Annealed NbTiN

Improvement in the surface roughness was necessary for epitaxial JJ material growth, so an annealed scheme was implemented based on research by Guziewicz et al. and Tian et al. [148], [149] Previous research shows marginal improvements in T_c , and some improvement in surface roughness, but the results were not as dramatic as the results found with the NbTiN films grown in this work.

Annealing immediately post growth in-situ offers several advantages compared to previous attempts to implement this scheme, namely reduced contaminants due to the cleanliness of the MBE chamber, and ability to generate nitrogen plasma during the anneal. In contrast, previous attempts at annealing NbN or NbTiN films often takes place in argon or air. In addition, for JJ material growth, the AlN barrier layer can then be grown directly on top of the annealed NbTiN surface without breaking vacuum, giving the opportunity to create a low-contaminant interface between the layers.

The alloy $(\text{Nb}_{0.84}\text{Ti}_{0.16})_{0.50}\text{N}_{0.50}$ was chosen as the constant composition for all the annealed samples, as this is the theoretical crossing point of the in-plane atomic spacing of both

AlN (0001) and NbTiN (111), as well as having a high enough niobium content to create a smooth surface, while still containing enough titanium to prevent the growth of ϵ -NbN. While the compositional control during this growth series was not perfect, a metal composition with variation of $x = 0.84 \pm 0.02$ across all samples demonstrates good control of the alloy growth. The results in Chapter 5 can then be meaningfully attributed to the annealing process and not from compositional changes between alloys.

NbTiN samples display three distinct changes due to the annealing step: a dramatic reduction in surface roughness (~ 2 orders of magnitude) to sub-angstrom levels, an increase in the intensity and number of thickness fringes on each side of the NbTiN (111) peak, and an increase in T_c from approximately 14 K to a maximum of 16.8 K. The optimal annealing scheme found for this alloy was 30 minutes at 850 °C immediately post growth. Interestingly, the T_c begins to drop once the annealing temperature is greater than 1000 °C, while the crystal quality according to XRD and the surface roughness remain similar to samples annealed at lower temperatures. This change in one of the three material properties while the others remained the same may indicate that post growth annealing material changes are due to two or more separate phenomena.

The shift in the symmetric ω -2 θ XRD peak in Chapter 5 may be due to strain in the lattice, formation of a higher quality, more uniform film, or potentially by incorporating more nitrogen into the lattice at intermediate temperatures, and desorbing nitrogen at high temperatures. Changes in crystal quality are likely not the cause of the peak shift, as the thickness fringes would be expected to reduce in intensity at the higher temperatures corresponding to a peak shift to a higher angle than the control sample.

RBS measurements show an increase in the nitrogen fraction of a few percent, and this trends well with the critical temperature data shown in Chapter 5. Since the transition metal nitrides are known to have stoichiometry dependent critical temperatures, it is likely that during the anneal step more nitrogen is being incorporated into the sample, causing the changes seen in lattice constant and critical temperature.

The increase in thickness fringes, surface restructuring, and increasing trend in XRR:XRD thickness ratio point to increases in crystal quality within the film. This trend in XRD:XRR ratio also supports the changes in T_c seen in the annealed samples. While the improved thickness fringes and surface roughness are present in all samples annealed above 650 °C, the XRR:XRD thickness ratio is dependent on anneal time, but has a negligible dependence on anneal temperature, which may be due to time-dependent diffusion within the bulk of the sample. Since the XRD and XRR measurements are dependent on the metal arrangement within the unit cells, the diffusion caused by the anneal step affects the rock-salt sub lattice. Additionally, the etching measurements in Chapter 5 where the top 40 nm of material was removed from the sample shows that critical temperature remains unchanged when the annealed sample is thinned, which may be due to nitrogen diffusion through the material during the annealing process. If the sample annealing affected only the top few layers of the sample, it should be expected that the critical temperature would drop as the layers were removed due to a nitrogen density gradient through the film. This is not the case, and nitrogen seems to be distributed evenly through the annealed samples. The etching tests also show that improvements in T_c are not due to the formation of an oxynitride or carbon containing layer during annealing as discussed in Tian et al. [148] The increase of nearly 1 K in the T_c of the non-annealed sample

may be the result of the elimination of a nitrogen deficient surface region that forms during growth, as the change in T_c would have been negative for a thinned sample.

Considering the annealed TiN results in Chapter 3 with a 17 % reduction in FWHM of the RSM cross section, the increased nitrogen incorporation during the anneal may be compensating for a nitrogen deficient growth, where the growth front is not 1:1 stoichiometric. This may create a gradient of nitrogen incorporation through the film thickness as nitrogen diffuses downward through the sample. By using the annealing step in a nitrogen plasma overpressure, this nitrogen deficiency at the top layers of the film may be remedied, causing the structural and superconducting changes seen in these films.

Due to results showing electrical, structural, and surface roughness improvements, the anneal step affects NbTiN alloys by way of both nitrogen incorporation and improving the crystal structure. These phenomena can be decoupled, with nitrogen content being independent of improvement in crystal quality as seen in the NbTiN samples annealed at temperatures above 1050 °C, where nitrogen content drops below that of a control sample while maintaining excellent quality XRD and surface roughness properties.

This work demonstrates the first study into in-situ annealing NbTiN grown using PAMBE, and the documentation of the electrical and structural improvements that emerge from annealed samples. This work also stands as an investigation into optimization of NbTiN for use in epitaxial, all-nitride Josephson junctions with AlN as a barrier layer.

6.4 Future Work

From an engineering standpoint, the future direction for this work is to incorporate annealed NbTiN into a tri-layer heterostructure with AlN grown all with PAMBE. With the optimization of the superconductor performed in this thesis, further research needs to be done concerning the AlN layer. Optimization of the stoichiometry, as well as the proper growth conditions for a smooth, uniform layer will be performed, then analysis of the surface created with a two-layer stack of AlN on NbTiN. Once the AlN layer grown on annealed NbTiN can be shown to have low surface roughness, a top layer can be added for the full heterostructure stack.

Proof that the all-nitride, epitaxial JJ is a better superconducting computing candidate than traditional Al based devices requires fabrication of entire qubits from this material. Results from the NbTiN material system can be compared to literature for NbN/AlN/NbN JJs as well as LPS produced TiN/AlN/TiN and Al/AIO_x/Al JJs. Measurement of J_c of the junction itself, as well as T_1 and T_2 times from the created qubit would help solidify the improvements that a coherent, crystalline interface at the JJ barrier offers, if any. Resonators in this thesis were only measured from non-annealed samples, and so any internal quality factor improvements due to the annealing step are not documented.

Measurement of resonators fabricated from annealed NbTiN samples would provide data regarding the kinetic inductance of the material, potentially giving another avenue for evaluating material quality, as well as providing data on the internal losses present in the material. If higher internal quality factors are seen with this alloy, NbTiN may be better suited to qubit development than traditionally used materials.

From a fundamental science standpoint, more research is required to understand the relationship between nitrogen vacancies and transition metal nitride phase, and the mass diffusion occurring during annealing at temperatures near the growth temperature. Additionally, the effect of strain on the JJ barrier layer needs to be understood better, as well as the effect of changing NbTiN composition in annealed thin films.

Based on results in this thesis, the introduction of niobium into the alloy reduces the nitrogen content when grown with PAMBE, preventing the ideal growth of δ -NbN. Instead, a nitrogen deficient phase of NbN_x begins to dominantly form. Onodera et al. theorized that the γ - Nb_4N_3 , δ -NbN, and Nb_4N_5 phases form a single continuous phase only differentiated by the number of nitrogen vacancies and interstitial nitrogen contained within the niobium superlattice. [86] As T_c increases with increasing nitrogen content, the instability of the rock salt phase δ -NbN causes a high likelihood of converting to the hexagonal ϵ -NbN under a wide range of growth conditions. The group found that this conversion could be forced by annealing in a nitrogen-poor H_2 overpressure, where the ϵ -NbN and γ - Nb_4N_3 forms may grow preferentially. By this reasoning, the annealing process in this thesis with a nitrogen plasma overpressure may have the opposite effect, incorporating more nitrogen into the lattice. A thermodynamically driven model created with this material system in mind, such as with density functional theory (DFT) may elucidate the relationship between NbN_x phase and stability, allowing for better prediction of certain phase growth at specific growth conditions. Slight differences in a particular phase between multi-phase and single-phase samples may require different models in order to accurately capture the growth behavior and phase stability. In addition, modeling of multiphase samples may become complicated due to the simultaneously occurring effects from nitrogen concentration as well as the competition between phases and crystal orientations. While these

phenomena may be accurately modeled independently from each other, it may be difficult to separate the effects in multiphase samples. Similarly, a model based around hopping frequency and likelihood of adsorption of nitrogen into the metal lattice would help the understanding of nitrogen incorporation during growth, versus the incorporation seen during annealing. It is interesting to note that the growth of annealed NbN_x did not possess the characteristic improvements in T_c and crystal quality as seen in annealed TiN and NbTiN films.

A high-resolution study using TEM or XPS may help identify the regions of the film which are nitrogen deficient, and whether it is a uniform Tm:N ratio throughout the film, or if the film grows nitrogen deficient, but with diffusion causing the lower regions of the film to become more stoichiometrically 1:1. The addition of electron energy loss spectroscopy (EELS) may also be beneficial for nitrogen analysis in NbTiN thin films. This technique can be considered complementary to EDS, where the energy lost due to inelastic scattering of electrons in the material is measured. Interpreting the energy loss spectra can reveal information about elemental composition, and is particularly sensitive to light elements, which is a limitation of the EDS results discussed in this work. The improved sensitivity to nitrogen may allow for more accurate Tm:N ratio analysis, as well as possibly providing information on contaminant concentrations in the thin films such as carbon or oxygen. These techniques would improve the understanding of the mechanism behind the annealing step, and the material property improvements that come with it.

The use of titanium as a stabilizing alloy constituent makes sense as the rock salt phase of TiN_x is very stable, occurring over a wide range of nitrogen fractions, as well as titanium functioning as an excellent getter of nitrogen, oxygen, and carbon. However, in a DFT based model, it would be prudent to examine the relationship of titanium content and the overall

stability of the rock salt structure when compared to the hexagonal and tetragonal NbN_x structures. The addition of titanium has also been shown to shift the lattice constant of the samples and could be used to apply strain on the AlN barrier layer in the JJ heterostructure. Some evidence has shown that growth of cubic AlN can be accomplished in thin layers or under higher pressures. [150] The engineered lattice constant of NbTiN can be matched to the in-plane atomic spacing of the cubic phase of AlN as well as the wurtzite phase, with the cubic phase possessing higher thermal conductivity and hardness than the hexagonal phase. In addition, wurtzite AlN is well known to be piezoelectric, which could interfere with reliable operation of a JJ using this material as the barrier layer. Investigation into using the cubic phase of AlN alongside $\text{Nb}_x\text{Ti}_{1-x}\text{N}$ may be a better solution for coherent interfaces in this all-nitride system.

Lastly, investigation into other transition metal nitrides such as VN and ScN may result in better candidates for alloyed superconducting with engineered lattice constant. Both of these materials have known rock salt crystal structures and may be more suited for use in these nitride JJs than NbN, which has multiple phases shown to be stable at similar growth conditions, causing non-uniformity in the films produced.

Conferences and Posters

- Austin Thomas, Nick Grabon, Alan Kramer, and Christopher J. K. Richardson “*Nb_xTi_{1-x}N Development for Epitaxial All Nitride Josephson Junctions*”, LPS Quantum Computing Program Review, 2022.
- Austin Thomas, Alan Kramer, and Christopher J. K. Richardson “*Investigation of Phase Composition in PAMBE Grown NbN_x Thin Films*”, International Conference on Molecular Beam Epitaxy, 2021.
- Austin Thomas, Nick Grabon, Alan Kramer, and Christopher J. K. Richardson “*Growth of PAMBE grown TiN//AlN//TiN Josephson junctions*”, American Physical Society Spring Conference, 2021.
- Austin Thomas, Alan Kramer, and Christopher J. K. Richardson “*Characterization of the Structure and Superconducting Properties of Plasma Assisted Molecular Beam Epitaxy Grown Nb_xTi_{1-x}N Alloy Thin Films*”, Materials Research Society Fall Meeting, 2020.

Works in Progress

- Austin Thomas, and Christopher J. K. Richardson “*Phase Competition in Plasma Assisted Molecular Beam Epitaxy Grown NbN_x Thin Films*”
 - Based on Chapter 3 of this thesis.
- Austin Thomas, and Christopher J. K. Richardson “*Effects of Annealing on Nitrogen Vacancies in Plasma Assisted Molecular Beam Epitaxy Grown TiN Thin Films*”
 - Based on Chapter 3 of this thesis.
- Austin Thomas, Ashish Alexander, Alan Kramer, and Christopher J. K. Richardson “*Characterizing the structural and superconducting properties of Plasma Assisted Molecular Beam Epitaxy Grown Nb_xTi_{1-x}N Alloy Thin Films*”
 - Based on Chapter 4 of this thesis.
- Austin Thomas, and Christopher J. K. Richardson “*Post-Growth Annealing Effects on Plasma Assisted Molecular Beam Epitaxy Grown Nb_{0.84}Ti_{0.16}N Thin Films*”
 - Based on Chapter 5 of this thesis.

Bibliography

- [1] G. E. Moore, “Cramming more components onto integrated circuits,” *Electronics*, vol. 38, no. 8, 1965, doi: 10.1109/n-ssc.2006.4785860.
- [2] “Intel’s Journey From 100 Billion To 1 Trillion Transistors Was Painted At The IntelON 2022 Event,” *Forbes*, 2022.
<https://www.forbes.com/sites/patrickmoorhead/2022/10/04/intels-journey-from-100-billion-to-1-trillion-transistors-was-painted-at-the-intelon-2022-event/?sh=63d319e92b3e> (accessed Jul. 22, 2023).
- [3] J. I. Latorre and G. Sierra, “Quantum computation of prime number functions,” *Quantum Inf. Comput.*, vol. 14, no. 7–8, pp. 577–588, 2014, doi: 10.26421/qic14.7-8-3.
- [4] M. Schuld, I. Sinayskiy, and F. Petruccione, “An introduction to quantum machine learning,” *Contemp. Phys.*, vol. 56, no. 2, pp. 172–185, 2015, doi: 10.1080/00107514.2014.964942.
- [5] J. R. Petta *et al.*, “Applied physics: Coherent manipulation of coupled electron spins in semiconductor quantum dots,” *Science (80-.)*, vol. 309, no. 5744, pp. 2180–2184, 2005, doi: 10.1126/science.1116955.
- [6] C. H. B. & D. P. DiVincenzo, “Quantum Information and Computation,” *Nature*, vol. 404, pp. 247–255, 2000, doi: 10.3390/e25030463.
- [7] C. J. K. Richardson, “ENMA613: Materials Science of Quantum Computing - QCOverview.” Unpublished, 2020.
- [8] R. Youssef and A. Lyon, “Measuring and Simulating T1 and T2 for Qubits,” *Nucl. Spin Relax. Liq.*, vol. 60510, pp. 139–152, 2018, doi: 10.1201/9781351264600-8.
- [9] W. Paul, “Electromagnetic Traps for Charged and Neutral Particles (Nobel Lecture),” *Rev. Mod. Phys.*, vol. 62, no. 3, pp. 531–540, 1990, doi: 10.1002/anie.199007391.
- [10] E. Kawakami *et al.*, “Electrical control of a long-lived spin qubit in a Si/SiGe quantum dot,” *Nat. Nanotechnol.*, vol. 9, no. 9, pp. 666–670, 2014, doi: 10.1038/nnano.2014.153.
- [11] K. J. Satzinger *et al.*, “Realizing topologically ordered states on a quantum processor,” *Science (80-.)*, vol. 374, no. 6572, pp. 1237–1241, 2021, doi: 10.1126/science.abi8378.
- [12] P. Krantz, M. Kjaergaard, F. Yan, T. P. Orlando, S. Gustavsson, and W. D. Oliver, “A quantum engineer’s guide to superconducting qubits,” 2019. doi: 10.1063/1.5089550.
- [13] F. London, H. London, and F. A. Lindemann, “The electromagnetic equations of the supraconductor,” *Proc. R. Soc. London. Ser. A - Math. Phys. Sci.*, vol. 149, no. 866, pp. 71–88, 1935, doi: 10.1098/rspa.1935.0048.
- [14] P. Patsalas and S. Logothetidis, “Optical, electronic, and transport properties of nanocrystalline titanium nitride thin films,” *J. Appl. Phys.*, vol. 90, no. 9, pp. 4725–4734, 2001, doi: 10.1063/1.1403677.
- [15] V. L. Ginzburg, “On Superconductivity and Superfluidity,” *Nobel Lect.*, pp. 96–127,

- 2003, doi: 10.1007/978-3-540-68008-6.
- [16] C. Kittel, *Introduction To Solid State Physics*, 8th Editio. Singapore, SINGAPORE: Wiley, 2005.
- [17] C. J. K. Richardson, “ENMA613: Materials Science of Quantum Computing - Josephson Junctions.” 2020.
- [18] P. Joyez, A. Cottet, D. Esteve, M. H. Devoret, M. E. Huber, and J. M. Martinis, “Direct measurement of the josephson supercurrent in an ultrasmall josephson junction,” *Phys. Rev. Lett.*, vol. 87, no. 13, pp. 11–14, 2001, doi: 10.1103/PhysRevLett.87.137003.
- [19] I. Giaever, “Electron tunneling between two superconductors,” *Phys. Rev. Lett.*, vol. 5, no. 10, pp. 464–466, 1960, doi: 10.1103/PhysRevLett.5.464.
- [20] A. Anferov, K.-H. Lee, F. Zhao, J. Simon, and D. I. Schuster, “Improved Coherence in Optically-Defined Niobium Trilayer Junction Qubits,” pp. 1–16, 2023, [Online]. Available: <http://arxiv.org/abs/2306.05883>.
- [21] A. P. M. Place *et al.*, “New material platform for superconducting transmon qubits with coherence times exceeding 0.3 milliseconds,” *Nat. Commun.*, vol. 12, no. 1, 2021, doi: 10.1038/s41467-021-22030-5.
- [22] E. J. Patiño and D. Lozano-Gómez, “Quantum tunneling theory of Cooper pairs as bosonic particles,” *Sci. Rep.*, vol. 11, no. 1, pp. 1–8, 2021, doi: 10.1038/s41598-021-88228-1.
- [23] R. McDermott, “Materials origins of decoherence in superconducting qubits,” *IEEE Trans. Appl. Supercond.*, vol. 19, no. 1, pp. 2–13, 2009, doi: 10.1109/TASC.2008.2012255.
- [24] S. Oh *et al.*, “Low-leakage superconducting tunnel junctions with a single-crystal Al 2O₃ barrier,” 2005. doi: 10.1088/0953-2048/18/10/026.
- [25] C. J. K. Richardson, V. Lordi, and S. Misra, “Materials science for quantum information science and technology,” pp. 485–498, 2020, doi: 10.1557/mrs.2020.147.
- [26] J. M. Sage, V. Bolkhovskiy, W. D. Oliver, B. Turek, and P. B. Welander, “Study of loss in superconducting coplanar waveguide resonators,” *J. Appl. Phys.*, vol. 109, no. 6, pp. 0–10, 2011, doi: 10.1063/1.3552890.
- [27] J. M. Kreikebaum, A. Dove, W. Livingston, E. Kim, and I. Siddiqi, “Optimization of infrared and magnetic shielding of superconducting TiN and Al coplanar microwave resonators,” *Supercond. Sci. Technol.*, vol. 29, no. 10, 2016, doi: 10.1088/0953-2048/29/10/104002.
- [28] J. Lisenfeld, G. J. Grabovskij, C. Müller, J. H. Cole, G. Weiss, and A. V. Ustinov, “Observation of directly interacting coherent two-level systems in an amorphous material,” *Nat. Commun.*, vol. 6, pp. 1–6, 2015, doi: 10.1038/ncomms7182.
- [29] S. E. de Graaf *et al.*, “Two-level systems in superconducting quantum devices due to trapped quasiparticles,” *Sci. Adv.*, vol. 6, no. 51, pp. 1–9, 2020, doi: 10.1126/SCIADV.ABC5055.
- [30] D. F. Ogletree *et al.*, “Localization and mitigation of two-level system (TLS) and non-

- TLS losses at interfaces of niobium superconducting quantum resonators,” in *APS March Meeting Abstracts*, Jan. 2022, vol. 2022, p. Q41.003.
- [31] A. A. Murthy *et al.*, “Developing a Chemical and Structural Understanding of the Surface Oxide in a Niobium Superconducting Qubit,” *ACS Nano*, vol. 16, no. 10, pp. 17257–17262, Oct. 2022, doi: 10.1021/acsnano.2c07913.
- [32] P. Kumar *et al.*, “Origin and Reduction of 1/f Magnetic Flux Noise in Superconducting Devices,” *Phys. Rev. Appl.*, vol. 6, no. 4, pp. 1–5, 2016, doi: 10.1103/PhysRevApplied.6.041001.
- [33] Z. Ding *et al.*, “A stable and low loss oxide for superconducting qubits,” *arXive*, no. 110, pp. 1–17, 2023, [Online]. Available: <https://arxiv.org/abs/2305.11395v1>.
- [34] M. Alghadeer, A. Banerjee, A. Hajr, H. Hussein, H. Fariborzi, and S. G. Rao, “Surface Passivation of Niobium Superconducting Quantum Circuits Using Self-Assembled Monolayers,” *ACS Appl. Mater. Interfaces*, vol. 15, no. 1, pp. 2319–2328, 2023, doi: 10.1021/acsmi.2c15667.
- [35] M. Schmelz and R. Stolz, “Superconducting quantum interference device (SQUID) magnetometers,” 2017. doi: 10.1007/978-3-319-34070-8_10.
- [36] K. K. Likharev and V. K. Semenov, “RSFQ Logic/Memory Family: A New Josephson-Junction Technology for Sub-Terahertz-Clock-Frequency Digital Systems,” 1991. doi: 10.1109/77.80745.
- [37] A. Kraft, C. Rupprecht, and Y.-C. Yam, “Superconducting Quantum Interference Device Magnetometry,” *UBC Physics*. 2017, doi: 10.1002/9783527636839.ch25.
- [38] J. Clarke, M. Hatridge, and M. Möbke, “SQUID-Detected Magnetic Resonance Imaging in Microtesla Fields,” *Annu. Rev. Biomed. Eng.*, vol. 9, no. 1, pp. 389–413, 2007, doi: 10.1146/annurev.bioeng.9.060906.152010.
- [39] A. Blais, A. L. Grimsmo, S. M. Girvin, and A. Wallraff, “Circuit quantum electrodynamics,” *Rev. Mod. Phys.*, vol. 93, no. 2, p. 25005, 2021, doi: 10.1103/RevModPhys.93.025005.
- [40] M. H. Volkmann, A. Sahu, C. J. Fourie, and O. A. Mukhanov, “Implementation of energy efficient single flux quantum digital circuits with sub-aJ/bit operation,” 2013. doi: 10.1088/0953-2048/26/1/015002.
- [41] M. H. Devoret and J. M. Martinis, “Implementing qubits with superconducting integrated circuits,” in *Experimental Aspects of Quantum Computing*, vol. 3, no. 5, 2005, pp. 163–203.
- [42] F. Jazaeri, A. Beckers, A. Tajalli, and J. M. Sallese, “A Review on quantum computing: From qubits to front-end electronics and cryogenic mosfet physics,” 2019. doi: 10.23919/MIXDES.2019.8787164.
- [43] K. M. Lang, S. Nam, J. Aumentado, C. Urbina, and J. M. Martinis, “Banishing quasiparticles from Josephson-junction qubits: Why and how to do it,” 2003. doi: 10.1109/TASC.2003.814121.
- [44] D. Lee, J. L. Dubois, and V. Lordi, “Identification of the Local Sources of Paramagnetic

- Noise in Superconducting Qubit Devices Fabricated on-Al₂O₃ Substrates Using Density-Functional Calculations,” 2014, doi: 10.1103/PhysRevLett.112.017001.
- [45] Z. Wang, A. Kawakami, Y. Uzawa, and B. Komiyama, “Superconducting properties and crystal structures of single-crystal niobium nitride thin films deposited at ambient substrate temperature,” *J. Appl. Phys.*, vol. 79, no. 10, pp. 7837–7842, 1996, doi: 10.1063/1.362392.
- [46] M. Brink, J. M. Chow, J. Hertzberg, E. Magesan, and S. Rosenblatt, “Device challenges for near term superconducting quantum processors: Frequency collisions,” in *Technical Digest - International Electron Devices Meeting, IEDM, 2019*, vol. 2018-Decem, pp. 6.1.1-6.1.3, doi: 10.1109/IEDM.2018.8614500.
- [47] Y. L. Wu *et al.*, “Fabrication of Al/AlOx/Al Josephson junctions and superconducting quantum circuits by shadow evaporation and a dynamic oxidation process,” *Chinese Phys. B*, vol. 22, no. 6, 2013, doi: 10.1088/1674-1056/22/6/060309.
- [48] H. Paik *et al.*, “Observation of high coherence in Josephson junction qubits measured in a three-dimensional circuit QED architecture,” *Phys. Rev. Lett.*, vol. 107, no. 24, pp. 1–5, 2011, doi: 10.1103/PhysRevLett.107.240501.
- [49] G. J. Dolan, “Offset masks for lift - off photoprocessing,” *Appl. Phys. Lett.*, vol. 31, no. 5, pp. 337–339, 1977.
- [50] C. J. K. Richardson, V. Lordi, S. Misra, and J. Shabani, “Materials science for quantum information science and technology,” *MRS Bull.*, vol. 45, no. 6, pp. 485–497, 2020, doi: 10.1557/mrs.2020.147.
- [51] S. Kim *et al.*, “Enhanced coherence of all-nitride superconducting qubits epitaxially grown on silicon substrate,” *Commun. Mater.*, vol. 2, no. 1, pp. 1–7, 2021, doi: 10.1038/s43246-021-00204-4.
- [52] Z. Wang, H. Terai, A. Kawakami, Y. Uzawa, and K. Advanced, “Characterization of NbN / AlN / NbN Tunnel Junctions,” vol. 9, no. 2, pp. 3259–3262, 1999.
- [53] M. Cyberey, T. Farrahi, J. Lu, A. Kerr, R. M. Weikle, and A. W. Lichtenberger, “NbTiN/AlN/NbTiN SIS junctions realized by reactive bias target ion beam deposition,” *IEEE Trans. Appl. Supercond.*, vol. 29, no. 6, 2019, doi: 10.1109/TASC.2018.2884967.
- [54] A. W. Lichtenberger, D. M. Lea, and F. L. Lloyd, “SUPERCONDUCTIVE Nb / Al-A1203 / Nb FABRICATION,” *Lloydia (Cincinnati)*, vol. 3, no. 1, 1993.
- [55] H. Akaike, S. Sakamoto, K. Munemoto, and A. Fujimaki, “Fabrication of NbTiN/Al-A1NX/NbTiN Josephson Junctions for Superconducting Circuits Operating Around 10 K,” *IEEE Trans. Appl. Supercond.*, vol. 26, no. 5, pp. 1–5, 2016, doi: 10.1109/TASC.2016.2565613.
- [56] C. J. K. Richardson *et al.*, “MBE grown nitride heterostructures for superconducting quantum circuits,” 2019.
- [57] C. J. K. Richardson and M. L. Lee, “Metamorphic epitaxial materials,” *MRS Bull.*, vol. 41, no. 3, pp. 193–198, Mar. 2016, doi: 10.1557/mrs.2016.7.
- [58] Y. K. Kuo, B. T. Liou, S. H. Yen, and H. Y. Chu, “Vegard’s law deviation in lattice

- constant and band gap bowing parameter of zincblende $\text{In}_{x}\text{Ga}_{1-x}\text{N}$,” *Opt. Commun.*, vol. 237, no. 4–6, pp. 363–369, 2004, doi: 10.1016/j.optcom.2004.04.012.
- [59] S. Ouendadji, S. Ghemid, H. Meradji, and F. E. H. Hassan, “Density functional study of $\text{CdS}_{1-x}\text{Se}_x$ and $\text{CdS}_{1-x}\text{Te}_x$ alloys,” *Comput. Mater. Sci.*, vol. 48, no. 1, pp. 206–211, 2010, doi: 10.1016/j.commatsci.2009.12.029.
- [60] M. Aoyagi, H. Nakagawa, I. Kurosawa, and S. Takada, “NbN/MgO/NbN Josephson Junctions for Integrated Circuits,” *Jpn. J. Appl. Phys.*, vol. 31, no. 6 R, pp. 1778–1783, 1992, doi: 10.1143/JJAP.31.1778.
- [61] Z. H. Barber and M. G. Blamire, “Niobium nitride / aluminium nitride superconductor / insulator multilayers and tunnel junctions,” *IEEE Trans. Appl. Supercond.*, vol. 7, no. 2 PART 3, pp. 3609–3612, 1997, doi: 10.1109/77.622186.
- [62] A. Alexander, C. G. Weddle, and C. J. K. Richardson, “Power and temperature dependent model for High Q superconductors,” *arXiv*, 2022, [Online]. Available: <http://arxiv.org/abs/2205.06291>.
- [63] P. J. Koppinen, L. M. Väistö, and I. J. Maasilta, “Complete stabilization and improvement of the characteristics of tunnel junctions by thermal annealing,” *Appl. Phys. Lett.*, vol. 90, no. 5, 2007, doi: 10.1063/1.2437662.
- [64] N. Biunno, J. Narayan, A. R. Srivatsa, and O. W. Holland, “Laser deposition of epitaxial titanium nitride films on (100) MgO,” *Appl. Phys. Lett.*, vol. 55, no. 4, pp. 405–407, 1989, doi: 10.1063/1.101881.
- [65] M. A. Hein, R. G. Humphreys, P. J. Hirst, S. H. Park, and D. E. Oates, “Nonlinear microwave response of epitaxial YBaCuO films of varying oxygen content on MgO substrates,” *J. Supercond. Nov. Magn.*, vol. 16, no. 5, pp. 895–904, 2003.
- [66] A. P. Read *et al.*, “Precision Measurement of the Microwave Dielectric Loss of Sapphire in the Quantum Regime with Parts-per-Billion Sensitivity,” *Phys. Rev. Appl.*, vol. 19, no. 3, p. 1, 2023, doi: 10.1103/PhysRevApplied.19.034064.
- [67] M. Checchin, D. Frolov, A. Lunin, A. Grassellino, and A. Romanenko, “Measurement of the Low-Temperature Loss Tangent of High-Resistivity Silicon Using a High-Superconducting Resonator,” *Phys. Rev. Appl.*, vol. 18, no. 3, p. 1, 2022, doi: 10.1103/PhysRevApplied.18.034013.
- [68] C. J. K. Richardson, A. Alexander, C. G. Weddle, B. Arey, and M. Olszta, “Low-loss superconducting titanium nitride grown using plasma-assisted molecular beam epitaxy,” *J. Appl. Phys.*, vol. 127, no. 23, 2020, doi: 10.1063/5.0008010.
- [69] C. Ndoye, K. Tapily, M. Orłowski, H. Baumgart, and D. Gu, “Silicidation of Niobium Deposited on Silicon by Physical Vapor Deposition,” *J. Electrochem. Soc.*, vol. 158, no. 9, p. H897, 2011, doi: 10.1149/1.3609845.
- [70] D. Eley and P. Wilkinson, “Kinetics of oxidation of aluminum films,” in *Structure and Properties of Thin Films*, Wiley, 1959.
- [71] J. R. Rairden and C. A. Neugebauer, “Critical Temperature of Niobium and Tantalum Films,” *Proc. IEEE*, vol. 52, no. 10, pp. 1234–1238, 1964, doi: 10.1109/PROC.1964.3311.

- [72] O. G. D'yachenko, S. Y. Istomin, A. M. Abakumov, and E. V. Antipov, "Synthesis, structure, and properties of mixed niobium(IV, V) oxides," *Inorg. Mater.*, vol. 36, no. 3, pp. 247–259, 2000, doi: 10.1007/BF02757930.
- [73] P. Kofstad, "The Oxidation Behavior of Tantalum at 700 - 1000 C," *J. Electrochem. Soc.*, vol. 110, no. 491, 1963.
- [74] M. V. P. Altoé *et al.*, "Localization and Mitigation of Loss in Niobium Superconducting Circuits," *PRX Quantum*, vol. 3, no. 2, p. 1, 2022, doi: 10.1103/PRXQuantum.3.020312.
- [75] S. M. Anton *et al.*, "Low-frequency critical current noise in Josephson junctions induced by temperature fluctuations," *Appl. Phys. Lett.*, vol. 101, no. 9, p. 92601, 2012, doi: 10.1063/1.4749282.
- [76] A. J. Elliot *et al.*, "Controlling the thickness of Josephson tunnel barriers with atomic layer deposition," 2014, Accessed: Apr. 30, 2020. [Online]. Available: <http://arxiv.org/abs/1408.3077>.
- [77] K. Inumaru, T. Ohara, and S. Yamanaka, "Pulsed laser deposition of epitaxial titanium nitride on MgO(001) monitored by RHEED oscillation," *Appl. Surf. Sci.*, vol. 158, no. 3, pp. 375–377, 2000, doi: 10.1016/S0169-4332(00)00038-6.
- [78] J. M. Martinis *et al.*, "Decoherence in Josephson qubits from dielectric Loss," *Phys. Rev. Lett.*, vol. 95, no. 21, pp. 1–4, 2005, doi: 10.1103/PhysRevLett.95.210503.
- [79] E. Santecchia, A. M. S. Hamouda, F. Musharavati, E. Zalnezhad, M. Cabibbo, and S. Spigarelli, "Wear resistance investigation of titanium nitride-based coatings," *Ceram. Int.*, vol. 41, no. 9, pp. 10349–10379, 2015, doi: 10.1016/j.ceramint.2015.04.152.
- [80] Y. Krockenberger, S. I. Karimoto, H. Yamamoto, and K. Semba, "Coherent growth of superconducting TiN thin films by plasma enhanced molecular beam epitaxy," *J. Appl. Phys.*, vol. 112, no. 8, pp. 1–6, 2012, doi: 10.1063/1.4759019.
- [81] H. G. Leduc *et al.*, "Titanium nitride films for ultrasensitive microresonator detectors," *Appl. Phys. Lett.*, vol. 97, no. 10, pp. 1–4, 2010, doi: 10.1063/1.3480420.
- [82] J. Zmuidzinas, "Superconducting Microresonators: Physics and Applications," *Annu. Rev. Condens. Matter Phys. is Annu. Rev. Condens. Matter Phys.*, vol. 3, pp. 169–214, 2012, doi: 10.1146/annurev-conmatphys-020911-125022.
- [83] C. Vahlas, B. Drouin Ladouce, P. Y. Chevalier, C. Bernard, and L. Vandenbulcke, "A thermodynamic evaluation of the Ti-N system," *Thermochim. Acta*, vol. 180, pp. 23–37, 1991, doi: [https://doi.org/10.1016/0040-6031\(91\)80371-O](https://doi.org/10.1016/0040-6031(91)80371-O).
- [84] B. Soundiraraju and B. K. George, "Two-Dimensional Titanium Nitride (Ti₂N) MXene: Synthesis, Characterization, and Potential Application as Surface-Enhanced Raman Scattering Substrate," *ACS Nano*, vol. 11, no. 9, pp. 8892–8900, 2017, doi: 10.1021/acsnano.7b03129.
- [85] D. Hazra *et al.*, "Superconducting properties of very high quality NbN thin films grown by high temperature chemical vapor deposition," *Supercond. Sci. Technol.*, vol. 29, no. 10, pp. 2–6, 2016, doi: 10.1088/0953-2048/29/10/105011.
- [86] G. I. Oya and Y. Onodera, "Transition temperatures and crystal structures of single-crystal

- and polycrystalline NbN_x films,” *J. Appl. Phys.*, vol. 45, no. 3, pp. 1389–1397, 1974, doi: 10.1063/1.1663418.
- [87] G. Brauer, “Nitrides, carbonitrides and oxynitrides of niobium,” *J. Less Common Met.*, vol. 2, no. 2, pp. 131–137, 1960, doi: [https://doi.org/10.1016/0022-5088\(60\)90008-4](https://doi.org/10.1016/0022-5088(60)90008-4).
- [88] E. Ethridge, S. Erwin, and W. Pickett, “Polymorphism in crystalline niobium nitrides,” *Phys. Rev. B - Condens. Matter Mater. Phys.*, vol. 53, no. 19, pp. 12563–12565, 1996, doi: 10.1103/PhysRevB.53.12563.
- [89] R. Sanjinés, M. Benkahoul, C. S. Sandu, P. E. Schmid, and F. Lévy, “Electronic states and physical properties of hexagonal β -Nb 2N and δ' -NbN nitrides,” *Thin Solid Films*, vol. 494, no. 1–2, pp. 190–195, 2006, doi: 10.1016/j.tsf.2005.07.185.
- [90] N. Nepal *et al.*, “Characterization of molecular beam epitaxy grown β -Nb₂N films and AlN/ β -Nb₂N heterojunctions on 6H-SiC substrates,” *Appl. Phys. Express*, vol. 9, no. 2, 2016, doi: 10.7567/APEX.9.021003.
- [91] Y. Zou *et al.*, “Discovery of superconductivity in hard hexagonal ϵ -NbN,” *Sci. Rep.*, vol. 6, 2016, doi: 10.1038/srep22330.
- [92] W. Lengauer, M. Bohn, B. Wollein, and K. Lisak, “Phase reactions in the Nb-N system below 1400°C,” *Acta Mater.*, vol. 48, no. 10, pp. 2633–2638, 2000, doi: 10.1016/S1359-6454(00)00056-2.
- [93] Y. Zou *et al.*, “Hexagonal-structured ϵ -NbN: Ultra-incompressibility, high shear rigidity, and a possible hard superconducting material,” *Sci. Rep.*, vol. 5, no. February, pp. 1–11, 2015, doi: 10.1038/srep10811.
- [94] X. Wang, L. Bao, Y. Wang, Y. Wu, Y. Duan, and M. Peng, “Explorations of electronic, elastic and thermal properties of tetragonal TM₄N₃ (TM=V, Nb and Ta) nitrides,” *Mater. Today Commun.*, vol. 26, no. August 2020, pp. 1–11, 2021, doi: 10.1016/j.mtcomm.2020.101723.
- [95] A. D. Pogrebnyak *et al.*, “Structural and mechanical properties of NbN and Nb-Si-N films: Experiment and molecular dynamics simulations,” *Ceram. Int.*, vol. 42, no. 10, pp. 11743–11756, 2016, doi: 10.1016/j.ceramint.2016.04.095.
- [96] T. Namazu, S. Inoue, H. Takemoto, and K. Koterazawa, “Mechanical Properties of Polycrystalline Titanium Nitride Films Measured by XRD Tensile Testing,” *IEEJ Trans. Sensors Micromachines*, vol. 125, no. 9, pp. 374–379, Jan. 2005, doi: 10.1541/ieejsmas.125.374.
- [97] J. S. Thorp, D. Evans, M. Al-Naief, and M. Akhtaruzzaman, “The dielectric properties of aluminium nitride substrates for microelectronics packaging,” *J. Mater. Sci.*, vol. 25, no. 12, pp. 4965–4971, 1990, doi: 10.1007/BF00580114.
- [98] K. Miwa and A. Fukumoto, “First-principles calculation of the structural, electronic, and vibrational properties of gallium nitride and aluminum nitride,” *Phys. Rev. B*, vol. 48, no. 11, pp. 7897–7902, 1993, doi: 10.1103/PhysRevB.48.7897.
- [99] J. S. Lundh *et al.*, “Residual stress analysis of aluminum nitride piezoelectric micromachined ultrasonic transducers using Raman spectroscopy,” *J. Appl. Phys.*, vol.

- 130, no. 4, 2021, doi: 10.1063/5.0056302.
- [100] R. Elfrink *et al.*, “Vibration energy harvesting with aluminum nitride-based piezoelectric devices,” *J. Micromechanics Microengineering*, vol. 19, no. 9, 2009, doi: 10.1088/0960-1317/19/9/094005.
- [101] M. A. Dubois and P. Muralt, “Properties of aluminum nitride thin films for piezoelectric transducers and microwave filter applications,” *Appl. Phys. Lett.*, vol. 74, no. 20, pp. 3032–3034, 1999, doi: 10.1063/1.124055.
- [102] R. Hull, R. M. Osgood, J. H. Sakaki, and A. Zunger, *Springer Series in MATERIALS SCIENCE Molecular Beam Epitaxy - Fundamentals and Current Status*. 2008.
- [103] E. Al-Dmour, *Fundamentals of Vacuum Physics and Technology*. 2017.
- [104] M. Pérez-Caro *et al.*, “Optical studies of nitrogen plasma for molecular beam epitaxy of InN,” *J. Appl. Phys.*, vol. 128, no. 21, 2020, doi: 10.1063/5.0029138.
- [105] R. P. Vaudo, Z. Yu, J. W. C. Jr, and J. F. Schetzina, “Atomic-nitrogen production in a radio-frequency plasma source,” *Opt. Lett.*, vol. 18, no. 21, pp. 1843–1845, 1993, Accessed: May 01, 2020. [Online]. Available: <https://pubs.acs.org/sharingguidelines>.
- [106] DCA Instruments, “High Temperature Effusion Cell Manual.” .
- [107] R. F. C. Farrow, *1.5.1 K-Cells (also Known as Thermal Effusion Sources or MBE Furnaces)*. William Andrew Publishing/Noyes, 1995.
- [108] M. Ohring, *Materials Science of Thin Films : Depositon and Structure*, vol. 2nd ed. San Diego, CA: Academic Press, 2002.
- [109] B. D. (Bernard D. Cullity and S. R. Stock, *Elements of x-ray diffraction LK* - <https://umaryland.on.worldcat.org/oclc/46437243>, 3rd ed. Upper Saddle River, NJ SE - xviii, 664 pages : illustrations ; 25 cm: Prentice Hall, 2001.
- [110] A. Liljas, “Background to the Nobel Prize to the Braggs,” *Acta Crystallogr. Sect. A Found. Crystallogr.*, vol. 69, no. 1, pp. 10–15, 2013, doi: 10.1107/S0108767312031133.
- [111] P. F. Fewster, *Reciprocal space mapping*, vol. 22, no. 2. 1997.
- [112] F. Bridou, J. Gautier, F. Delmotte, M. F. Ravet, O. Durand, and M. Modreanu, “Thin multilayers characterization by grazing X-ray reflectometry and use of Fourier transform,” *Appl. Surf. Sci.*, vol. 253, no. 1 SPEC. ISS., pp. 12–16, 2006, doi: 10.1016/j.apsusc.2006.05.122.
- [113] N. A. Geisse, “AFM and combined optical techniques,” *Mater. Today*, vol. 12, no. 7–8, pp. 40–45, 2009, doi: 10.1016/S1369-7021(09)70201-9.
- [114] J. I. Goldstein, D. E. Newbury, J. R. Michael, N. W. M. Ritchie, J. H. J. Scott, and D. C. Joy, *Scanning electron microscopy and x-ray microanalysis*. 2017.
- [115] M. Mayer, “SIMNRA User’s Guide,” *MAX-PLANCK-INSTITUT FÜR Plasmaphys.*, 1997.
- [116] M. S. Caceci and W. P. Cacheris, “Fitting curves to data. The Simplex algorithm is the answer.,” *Byte*, vol. 9, no. 1, pp. 340–362, 1984.
- [117] High Precision Devices, “ADR Cryostat Installation and Operation Manual.” 2016.

- [118] R. N. Simons, “Conventional Coplanar Waveguides,” in *Coplanar Waveguide Circuits, Components, and Systems*, John Wiley & Sons, Ltd, 2001, pp. 11–86.
- [119] W. G. Hurley and M. C. Duffy, “Calculation of self- and mutual impedances in planar sandwich inductors,” *IEEE Trans. Magn.*, vol. 33, no. 3, pp. 2282–2290, 1997, doi: 10.1109/20.573844.
- [120] J. Gao, J. Zmuidzinis, B. A. Mazin, P. K. Day, and H. G. Leduc, “Experimental study of the kinetic inductance fraction of superconducting coplanar waveguide,” *Nucl. Instruments Methods Phys. Res. Sect. A Accel. Spectrometers, Detect. Assoc. Equip.*, vol. 559, no. 2, pp. 585–587, 2006, doi: 10.1016/j.nima.2005.12.075.
- [121] J. A. Cuenca *et al.*, “Superconducting boron doped nanocrystalline diamond microwave coplanar resonator,” *Carbon N. Y.*, vol. 201, pp. 251–259, 2023, doi: 10.1016/j.carbon.2022.08.084.
- [122] E. J. G. Santos and E. Kaxiras, “Electric-field dependence of the effective dielectric constant in graphene,” *Nano Lett.*, vol. 13, no. 3, pp. 898–902, 2013, doi: 10.1021/nl303611v.
- [123] F. R. Fickett, “Standards for Measurement of the Critical Fields of Superconductors.,” *J. Res. Natl. Bur. Stand. (United States)*, vol. 90, no. 2, pp. 95–113, 1985, doi: 10.6028/jres.090.007.
- [124] F. R. Fickett, “Standards for Measurement of the Critical Fields of Superconductors.,” *J. Res. Natl. Bur. Stand. (United States)*, vol. 90, no. 2, pp. 95–113, 1985, doi: 10.6028/jres.090.007.
- [125] A. Yamamoto, M. Tsujino, M. Ohkubo, and A. Hashimoto, “Nitridation effects of substrate surface on the metalorganic chemical vapor deposition growth of InN on Si and α -Al₂O₃ substrates,” *J. Cryst. Growth*, vol. 137, no. 3–4, pp. 415–420, 1994, doi: 10.1016/0022-0248(94)90979-2.
- [126] K. Uchida, A. Watanabe, F. Yano, M. Kouguchi, T. Tanaka, and S. Minagawa, “Nitridation process of sapphire substrate surface and its effect on the growth of GaN,” *J. Appl. Phys.*, vol. 79, no. 7, pp. 3487–3491, 1996, doi: 10.1063/1.361398.
- [127] A. R. Kramer, “Unpublished Work.” 2020.
- [128] A. Howie and U. Valdrè, *Surface and interface characterization by electron optical methods*. New York: Plenum Press, 1988.
- [129] H. Holleck, “Material selection for hard coatings,” *J. Vac. Sci. Technol. A Vacuum, Surfaces, Film.*, vol. 4, no. 6, pp. 2661–2669, 1986, doi: 10.1116/1.573700.
- [130] N. Daneu and A. Recnik, “The atomic-scale aspects of twinning and polytypism in minerals,” *Acta Mineral.*, vol. 7, no. April 2012, pp. 32–37, 2012.
- [131] A. M. Abakumov, A. A. Tsirlin, I. Bakaimi, G. Van Tendeloo, and A. Lappas, “Multiple twinning as a structure directing mechanism in layered rock-salt-type oxides: NaMnO₂ polymorphism, redox potentials, and magnetism,” *Chem. Mater.*, vol. 26, no. 10, pp. 3306–3315, 2014, doi: 10.1021/cm5011696.
- [132] W. P. Guo *et al.*, “Titanium Nitride Epitaxial Films as a Plasmonic Material Platform:

- Alternative to Gold,” *ACS Photonics*, vol. 6, no. 8, pp. 1848–1854, 2019, doi: 10.1021/acsp Photonics.9b00617.
- [133] J. G. Wright, H. G. Xing, and D. Jena, “Growth windows of epitaxial NbN_x films on c-plane sapphire and their structural and superconducting properties,” *arXiv*, pp. 18–20, 2022, doi: 10.1103/PhysRevMaterials.7.074803.
- [134] R. Chowdhury, R. D. Vispute, K. Jagannadham, and J. Narayan, “Characteristics of titanium nitride films grown by pulsed laser deposition,” *J. Mater. Res.*, vol. 11, no. 6, pp. 1458–1469, 1996, doi: 10.1557/JMR.1996.0182.
- [135] S. T. Murphy, A. Choneos, C. Jiang, U. Schwingenschlögl, and R. W. Grimes, “Deviations from Vegard’s law in ternary III-V alloys,” *Phys. Rev. B - Condens. Matter Mater. Phys.*, vol. 82, no. 7, pp. 7–10, 2010, doi: 10.1103/PhysRevB.82.073201.
- [136] J. A. Anthony *et al.*, “Tunable superconducting nanoinductors,” *Nanotechnology*, vol. 21, no. 44, p. 445202, 2010, [Online]. Available: <http://stacks.iop.org/0957-4484/21/i=44/a=445202>.
- [137] K. S. Keskar, T. Yamashita, and Y. Onodera, “Superconducting transition temperatures of r. F. sputtered nbn films,” *Jpn. J. Appl. Phys.*, vol. 10, no. 3, pp. 370–374, 1971, doi: 10.1143/JJAP.10.370.
- [138] P. D. Mauskopf, “Transition edge sensors and kinetic inductance detectors in astronomical instruments,” *Publications of the Astronomical Society of the Pacific*, vol. 130, no. 990, 2018, doi: 10.1088/1538-3873/aabaf0.
- [139] N. Samkharadze *et al.*, “High-Kinetic-Inductance Superconducting Nanowire Resonators for Circuit QED in a Magnetic Field,” *Phys. Rev. Appl.*, vol. 5, no. 4, pp. 1–10, 2016, doi: 10.1103/PhysRevApplied.5.044004.
- [140] T. M. Bretz-Sullivan *et al.*, “High kinetic inductance NbTiN superconducting transmission line resonators in the very thin film limit,” *Appl. Phys. Lett.*, vol. 121, no. 5, 2022, doi: 10.1063/5.0100961.
- [141] J. Gao, “The Physics of Superconducting Microwave Resonators Thesis by,” vol. 2008, 2008.
- [142] A. H. Farha, A. O. Er, Y. Ufuktepe, G. Myneni, and H. E. Elsayed-Ali, “Influence of nitrogen background pressure on structure of niobium nitride films grown by pulsed laser deposition,” *Surf. Coatings Technol.*, vol. 206, no. 6, pp. 1168–1174, 2011, doi: 10.1016/j.surfcoat.2011.08.012.
- [143] A. V. Linde, R. M. Marin-Ayral, D. Granier, F. Bosc-Rouessac, and V. V. Grachev, “Synthesis of cubic niobium nitride by reactive diffusion under nitrogen pressure,” *Mater. Res. Bull.*, vol. 44, no. 5, pp. 1025–1030, 2009, doi: 10.1016/j.materresbull.2008.11.008.
- [144] S. Chaudhuri, M. R. Nevala, T. Hakkarainen, T. Niemi, and I. J. Maasilta, “Infrared pulsed laser deposition of niobium nitride thin films,” *IEEE Trans. Appl. Supercond.*, vol. 21, no. 3 PART 1, pp. 143–146, 2011, doi: 10.1109/TASC.2010.2081656.
- [145] N. Hayashi, I. H. Murzin, I. Sakamoto, and M. Ohkubo, “Single-crystal niobium nitride thin films prepared with radical beam assisted deposition,” *Thin Solid Films*, vol. 259, no.

- 2, pp. 146–149, 1995, doi: 10.1016/0040-6090(94)06436-9.
- [146] T. Roch, M. Gregor, S. Volkov, M. Čaplovičová, L. Satrapinskyy, and A. Plecenik, “Substrate dependent epitaxy of superconducting niobium nitride thin films grown by pulsed laser deposition,” *Appl. Surf. Sci.*, vol. 551, no. February, 2021, doi: 10.1016/j.apsusc.2021.149333.
- [147] Y. Ufuktepe *et al.*, “Structural, electronic, and mechanical properties of niobium nitride prepared by thermal diffusion in nitrogen,” *Mater. Chem. Phys.*, vol. 141, no. 1, pp. 393–400, 2013, doi: 10.1016/j.matchemphys.2013.05.029.
- [148] L. Tian *et al.*, “Improved critical temperature of superconducting plasma-enhanced atomic layer deposition of niobium nitride thin films by thermal annealing,” *Thin Solid Films*, vol. 709, no. May 2019, p. 138232, 2020, doi: 10.1016/j.tsf.2020.138232.
- [149] M. Guziewicz *et al.*, “Technology of ultrathin NbN and NbTiN films for superconducting photodetectors,” *Acta Phys. Pol. A*, vol. 120, no. 6, pp. A76–A79, 2011, doi: 10.12693/aphyspola.120.a-76.
- [150] T. Schupp, K. Lischka, and D. J. As, “MBE growth of atomically smooth non-polar cubic AlN,” *J. Cryst. Growth*, vol. 312, no. 9, pp. 1500–1504, 2010, doi: 10.1016/j.jcrysgr.2010.01.040.